INHIBITING THE GALVANIC CORROSION OF ALUMINUM ALLOYS WHEN COUPLED WITH CARBON FIBER COMPOSITES AND LOCALIZED CORROSION OF ADVANCED TITANIUM ALLOYS THROUGH SURFACE TREATMENT

By

Isuri Nirmani Dammulla

A DISSERTATION

Submitted to
Michigan State University
in partial fulfillment of the requirements
for the degree of

Chemistry – Doctor of Philosophy

2024

ABSTRACT

Carbon fiber reinforced polymer (CFRP) composites are rapidly replacing metallic structural components in aerospace and automotive applications owing to their high strength to weight ratio and other excellent mechanical properties. Even though the general practice is to keep CFRP composites electrically isolated from aluminum alloys in aircraft structures, they can become connected when a layer of moisture condenses over their surfaces creating a galvanic couple. In such cases, the more noble carbon fibers of the composite material will act as the cathode and aid the reduction of dissolved oxygen. The less noble aluminum alloy will become the anode and get oxidized at an accelerated rate– so-called galvanic corrosion which can be catastrophic and is a significant challenge encountered in aerospace and automotive assets. Corrosion of the aluminum alloy can be inhibited by decreasing the rate of aluminum oxidation, decreasing the rate of cathodic reaction, or decreasing the rate of both. The cathodic reaction rate can be reduced by blocking the active sites of exposed carbon fibers for O_2 chemisorption-the first step of oxygen reduction reaction (ORR). This is accomplished by chemically modifying the exposed carbon fiber surfaces of the composites.

The first part of research described herein focuses on exploring the influence of chemical modification of carbon fiber epoxy composite edges with substituted phenyl diazonium adlayers on the electrochemical reduction of dissolved oxygen, how stable the modified surface is and how much the rate of galvanic corrosion of aluminum alloy is reduced during accelerated degradation tests. The electrochemically assisted and spontaneous formation of diazonium molecular adlayers on the exposed fibers of a carbon fiber reinforced polymer (CFRP) composites were investigated. The formation of stable adlayers was confirmed and adlayer coverage was determined by Raman spectroscopy and cyclic voltammetry. The influence of diazonium surface treatment on the ORR

kinetics was assessed by measuring the voltammetric curves for dissolved oxygen reduction on unmodified and chemically modified composites in naturally aerated 0.5 M Na_2SO_4. Two accelerated degradation test paradigms were investigated: (i) neutral salt spray (ASTM B117) and (ii) thin layer mist spray. Galvanic corrosion on the aluminum alloy was evaluated by weight change measurements, visual observation with digital optical microscopy and scanning electron microscopy, and surface topographical analysis by digital optical microscopy, confocal laser microscopy, and optical profilometry. The stability of the adlayer after accelerated degradation tests was determined by Raman spectroscopy observing for the presence of the adlayer.

Due to the growing demand for titanium alloys in the aviation sector and the high cost associated with conventional subtractive manufacturing methods for titanium components, there has been a significant focus on utilizing additive manufacturing (AM) techniques for fabricating titanium components. Fundamental research is needed to better understand how the fabrication parameters influence the material density, microhardness, microstructure, and electrochemical corrosion susceptibility of such AM titanium alloys. The second part of this dissertation work focuses on investigating the material and electrochemical properties of titanium alloys prepared by selective laser melting (SLM). The surface morphology and microstructure of the as-processed and surface-pretreated titanium alloy (Ti-5553) specimens were investigated employing scanning electron microscopy. The surface pretreatment involved abrading and polishing to reduce the surface roughness and smooth the surface texture. The electrochemical corrosion behavior of the as-processed and surface-pretreated titanium specimens were studied by performing open circuit potential and electrochemical impedance spectroscopy (EIS) measurements and recording potentiodynamic polarization curves.

ACKNOWLEDGEMENTS

I would like to extend my sincere thanks to my advisor, Professor Greg Swain, and committee members, Professor Gary Blanchard, Professor Lawrence Drzal, and Professor Andre Lee for their invaluable advice and guidance navigating my dissertation journey. Thank you to my fellow lab mates, Skye Henderson, Jack Walton, Zack Smith, Nick Knowles, Sarah McFall-Boegeman, and Fatemeh Parvis for their friendship during my time at Michigan State University.

I am deeply grateful to my parents and my sister for their unwavering support over the years. Thank you for believing in me and doing all you could every step of the way to help me achieve my dreams as a first-generation college student. A very special thank you to my amazing husband Shashika, for being my rock through all the highs and lows. You were my source of strength and stability during this journey. I could not have done this without you by my side. Thank you for all the sacrifices you have made and words cannot express my gratitude to you.

Thank you to Chloe and Cannoli, my pet cats, for their unconditional love and emotional support. Their playful spirits and joyful companionship made this these past few years much more tolerable and I wish they could read these words to understand the impact their comforting presence has had on my journey through graduate school.

Many thanks to Dr. Ciera Lewis for teaching me to advocate for myself and my needs. I am grateful for your advice and support. To Malini and Saroopa, thank you for being there for me, from the very beginning, helping me as I navigated life as an international student in the United States. I sincerely appreciate your friendship and guidance.

Lastly, I would like to acknowledge the Office of Naval Research, Sea-Based Aviation Program (Grant #N00014-21-1-2686) and Honeywell Federal Manufacturing and Technologies, LLC for providing the financial support to conduct this dissertation research.

TABLE OF CONTENTS

CHAPTER 1. INTRODUCTION

1.1 ALUMINUM AND ALUMINUM ALLOYS

Aluminum is the most abundant metal element in Earth's crust with a silver-white metallic appearance and ranks only second to steel and iron in terms of tonnage used annually.[1-3] Pure aluminum exhibits superior corrosion resistance due to the formation of native, self-healing oxide films.[4,5] The high ductility of aluminum allows it to be easily shaped and formed into products by casting, forming, and powder metallurgy.[6] The electrical and thermal conductivity of aluminum is second only to copper.[7] Aluminum is therefore used extensively in electrical transmission lines, heat exchangers, evaporators, electrically heated appliances, and automotive cylinder heads and radiators.[8,9] Aluminum has a low density of 2.7 $g.cm^3$ which is about one-third of that of steel making it a primary choice of material in automotive, aviation, and construction sectors where lightweight structures are desirable.[10-18]

The alloys of aluminum are formed by mixing metallic or semi-metallic elements in small amounts with pure molten aluminum to achieve unique combinations of properties.[4,19] Aluminum alloys have become one of the most versatile and economical metal alloy categories, and there are more than 530 registered aluminum alloy compositions as of today, according to the Aluminum Association.[20,21] Aluminum alloys have been predominantly used in the aerospace and automotive industries owing to their low density and high strength.[22,23] AA2024-T3 and AA7075-T6 are two of the most sought-after aluminum alloys in aerospace applications. The four-digit number followed by the letter "T" denotes that both are wrought alloys subjected to a series of thermal treatments during manufacturing.[19,24] The registered elemental composition of AA 2024-T3 and AA7075-T6 are presented in Table 1.1.[25] AA2024-T3 contains copper (Cu) as the primary alloying element, while zinc (Zn) is the principal alloying element of AA7075-T6. AA2024-T3 is typically

employed in the manufacturing of aircraft fuselages, wings, and roofs. Conversely, AA7075-T6 is mainly used in the construction of horizontal and vertical stabilizers of aircraft tails. [22,23]

Table 1.1. The elemental composition of AA 2024-T3 and AA 7075-T6.

Wt.%	Si	Fe	Cu	Mn	Mg	Cr	Zn	Ti	Al
2024-T3	0.5	0.5	3.8-4.9	0.3-0.9	1.2-1.8	0.1	0.2	0.2	Rem.
7075-T6	0.4	0.5	1.2-2.0	0.3	2.1-2.9	0.2-0.3	5.1-6.1	0.2	Rem.

1.2 CARBON FIBER REINFORCED POLYMER COMPOSITES

A composite is a combination of two or more components with notably different physical and chemical characteristics from those of its constituent components.[26,27] In a composite, the constituents remain physically separate and distinct from each other.[28,29] Carbon fiber reinforced polymer (CFRP) composites, as the name suggests, embody a polymer matrix reinforced by carbon fibers. Carbon fibers contain at least 92 wt.% of elemental carbon and are commercially manufactured using pitch and polyacrylonitrile (PAN) precursors.[30-32] The excellent mechanical properties of CFRP composites, including lightweight, high strength, superior corrosion resistance, and outstanding fatigue and damage tolerance, have made them an attractive choice as structural materials in the aerospace and automotive industries.[33-40] CFRP composites have been successfully employed in the manufacturing of Boeing 787 and Airbus A380 civilian aircraft,[34,40-43] F35 and Typhoon military aircraft[44-46] and BMW and Audi automobiles.[47-48] The lightweight CFRP composites are widely used in various sections of aircraft including wings, fuselages, tails, and doors to reduce structural weight and fuel consumption. [34,40-43]

1.3 GALVANIC CORROSION

Corrosion is a universal phenomenon and a billion dollar problem annually. Although its pervasiveness may often go unnoticed in our daily lives, it has severe consequences and can lead

to catastrophic events when proper control and prevention measures are not implemented. Corrosion is not only detrimental but also costly. In 2013, the worldwide cost of corrosion was estimated at US $2.5 trillion, constituting approximately 3.4% of the global Gross Domestic Product (GDP). The profound impact of corrosion extends to the aviation and automotive sectors. According to the 2019 report from the LMI Department of Defense on the cost of corrosion, the United States Navy and Marine Corps spends approximately US $3.7 billion annually to address corrosion-related issues within their aircraft systems. In 2016, a survey revealed that the US automobile owners spent approximately US $15.4 billion to repair damage due to corrosion from 2011 to 2016.

Galvanic corrosion is one of the most common and aggressive form of corrosion that occurs when two (or more) dissimilar conductive materials are in direct electrical contact in the presence of an electrolyte facilitating ion conduction. When direct electrical contact is made, a galvanic couple is formed changing the self-corrosion rates of the two dissimilar materials. Upon galvanic coupling, one material becomes the anode and corrodes faster than it would otherwise be in isolation, while the other material becomes the cathode with a decelerated corrosion rate.[49,50] The three critical elements required for the formation of a galvanic couple are,

(i) at least two dissimilar conductive materials with different corrosion potentials

(ii) direct electrical contact between the materials

(iii) an electrolyte solution (i.e. water, moisture)

It is crucial to note that galvanic corrosion cannot occur if any one of these elements is absent.

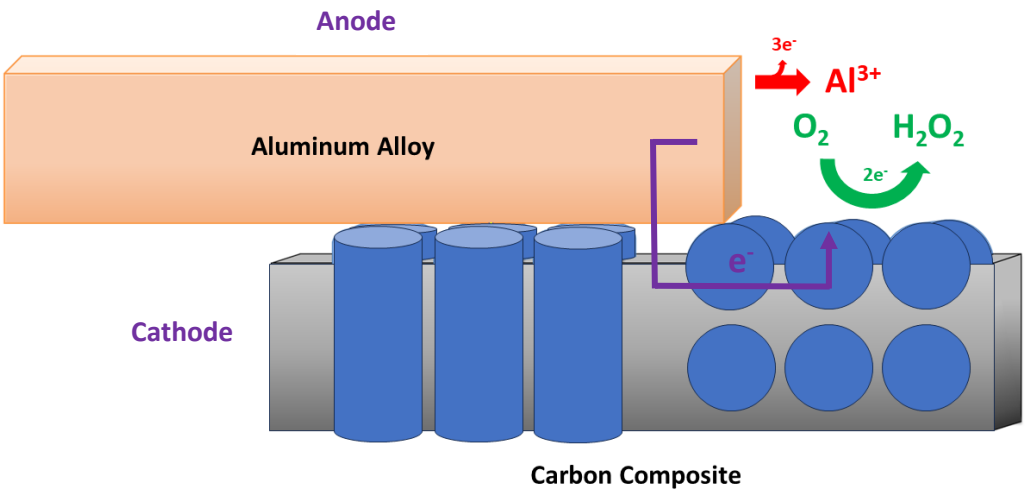

Figure 1.1. Schematic diagram showing the anodic and cathodic reactions taking place at an aluminum alloy-CFRP composite couple.

The carbon fibers in CFRP composites are electrically conductive and electrochemically more noble than aluminum in the galvanic series.[51-52] Hence, when used together in aircraft and automotive structures, the CFRP composites and aluminum alloys can become electrically connected through a condensed layer of atmospheric moisture forming a galvanic cell. In such cases, the more noble carbon fibers of the composite will act as a cathode and support the oxygen (O_2) reduction reaction thereby accelerating the oxidation or the so-called galvanic corrosion of the less noble aluminum alloy.[53-56] Figure 1.1 presents a schematic diagram of the galvanic coupling between an aluminum alloy and a CFRP composite. The anodic and cathodic reactions taking place respectively at the aluminum alloy and CFRP composite during galvanic coupling at neutral pH are as follows.

Anodic Reaction,

$$Al \rightarrow \quad Al^{3+} + 3e^{-} \qquad (1)$$

Cathodic Reaction,

$$O_2 + 2H_2O + 2e^{-} \rightarrow H_2O_2 + 2OH^{-} \qquad (2)$$

The anodic reaction is the oxidation of the aluminum alloy (Reaction 1). This metal dissolution reaction produces Al^{3+} ions and electrons. The cathodic reaction at the exposed carbon fiber surfaces of the composite is the reduction of atmospheric O_2 dissolved in the moisture/electrolyte layer consuming the electron liberated by the metal oxidation. At neutral pH, the oxygen reduction reaction typically occurs at carbon cathodes via a two-electron pathway generating hydrogen peroxide (H_2O_2). Since the ORR kinetics are considerably slower at carbon electrodes compared to active metal electrodes such as platinum and gold, the four-electron reduction pathway is not supported at carbon electrodes unless a catalyst is introduced.[156] The following mechanism has been proposed for the reduction of O_2 at carbon electrodes.[156-159] The first step of oxygen reduction reaction (ORR) mechanism is the adsorption of O_2 molecules onto the active sites of exposed carbon fibers (Reaction 3). During the two-electron pathway, O_2 adsorption occurs "end-on" and the reaction proceeds to form H_2O_2 following the protonation of HO_2^- intermediate (Reaction 6).[160]

$$O_2 \rightarrow O_{2\,(ads)} \quad (3)$$

$$O_{2\,(ads)} + e^- + H_2O \rightarrow HO_{2\,(ads)} + OH^- \quad (4)$$

$$HO_{2\,(ads)} + e^- \rightarrow HO_2^- \quad (5)$$

$$HO_2^- + H_2O \rightarrow H_2O_2 + OH^- \quad (6)$$

The prolonged consumption of electrons released by metal dissolution in the cathodic reaction escalates the oxidation or galvanic corrosion rate of the nearby aluminum (Figure 1.2) and can initiate CFRP composite degradation due to the gradual accumulation of H_2O_2.[57-59] Galvanic corrosion adversely affects the structural integrity of both materials and may lead to massive safety risks if left unattended. Hence, it has become a well-known and expensive issue in aviation, automotive, and marine applications where aluminum alloy-CFRP composite hybrid components

are extensively used. The standard practice to mitigate the galvanic corrosion of aluminum alloys in aircraft structures involves the elimination of direct contact between the two materials by inserting insulation layers[60–63]. Additionally, galvanic corrosion of the aluminum alloy can be inhibited by decreasing the rate of the metal oxidation, decreasing the rate of the cathodic reaction, or decreasing the rate of both. The inhibition of the rate of anodic metal oxidation is often achieved by the application of coating systems on the alloy surface[64-65] and is discussed in detail under sections 1.4 and 1.5. The rate of cathodic reaction can be decreased for reduced galvanic corrosion by coatings and or surface treatments that reduce the rate of oxygen reduction at the exposed carbon fibers of the composite. The presence of a coating or an adlayer on CFRP composite surfaces inhibits the first step of ORR mechanism (Reaction 3) through blockade of active sites on exposed carbon fibers for O_2 chemisorption. In this dissertation work, we employ a widely adopted carbon surface treatment technique known as diazonium modification (Section 1.6) to form organic adlayers on CFRP composites and investigate the efficacy of the chemical modification in decreasing the rate of oxygen reduction, thereby reducing the rate of aluminum alloy oxidation in joined test specimens.

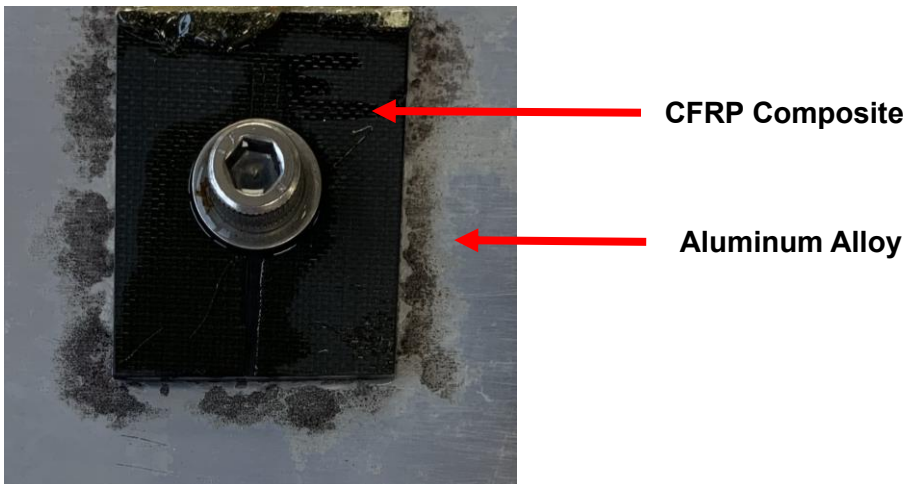

Figure 1.2. Galvanic corrosion damage on an aluminum alloy panel (AA2024-T3) joined to an unmodified CFRP composite after a 14-day neutral salt spray exposure. Corrosion damage is localized near the edges of the CFRP composite since the edge plane sites are more kinetically active for O_2 reduction.

1.4 CORROSION PREVENTION

When exposed to the atmosphere, aluminum and its alloys spontaneously react with oxygen and generate a thin, passive oxide film that is typically ~2 nm thick on their surface.[66] The self-healing native oxide films protects the aluminum alloy from further oxidation providing a barrier layer between the atmosphere and underlying metal and improves the resistance of the metal to general corrosion.[4,67,68] They, however, possess many defects through which ions such as chloride (Cl^-) can penetrate inducing localized corrosion attacks on the metal and promote the breakdown of the passive oxide film.[69,70] The aerospace industry routinely employs a multilayer coating system for corrosion mitigation of aluminum and its alloys in the field.[71,72]

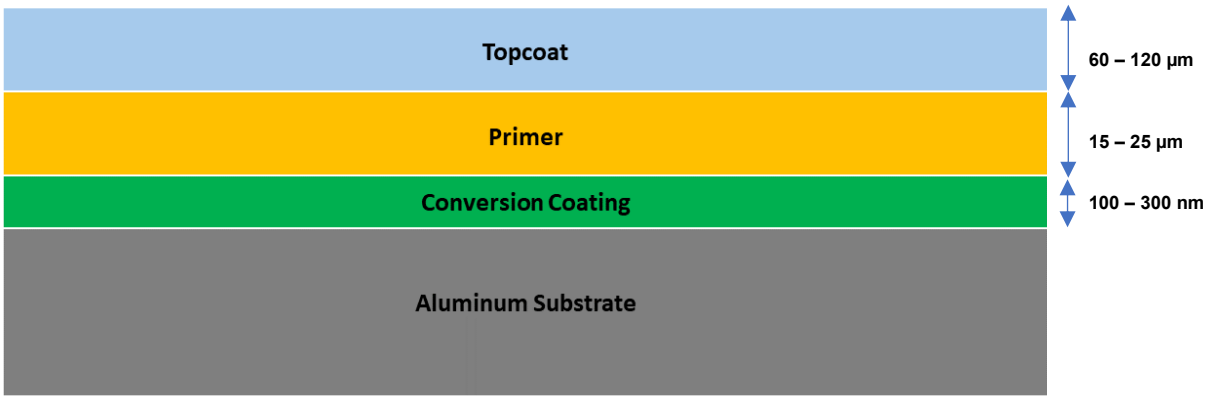

Figure 1.3. Schematic diagram of a multilayer coating system used in aerospace applications on aluminum substrates for corrosion mitigation.[71, 79]

A multilayer coating system consists of an initial inorganic conversion coating followed by a primer, and a topcoat. Figure 1.3 presents a schematic diagram of a multilayer coating system. The thin inorganic conversion coating furnishes anti-corrosion properties to the base metal and provides improved adhesion for the subsequent primer layer.[73,74] The function of the primer is to promote the adhesion with the topcoat as well as to impart corrosion protection.[75] The topcoat is the final layer and is exposed to the outside environment. It predominantly serves as a barrier and protects the underlying layers and the metal from ultraviolet radiation, harsh chemicals, and

moisture.[75,76] The topcoat is also used for aesthetic purposes.[72,75] Each layer plays a vital role and contributes to the overall performance of the coating system. Multilayer coating systems protect the aluminum alloy components against corrosion, extending their lifespan in the field.

1.5 CONVERSION COATINGS

Conversion coatings, when applied on aluminum alloys, provide improved corrosion resistance properties to the underlying metal, and activate the metal surface for better primer receptivity.[77] They are thin hydrated metal oxide films formed on aluminum alloy components either by immersion or spraying.[78] Conversion coatings are typically 100 – 300 nm in thickness, depending on the formation conditions and constitute the first layer of a multilayer coating system.[79] In the past, the metal processing and surface finishing industries relied heavily on chromate conversion coatings composed of hexavalent chromium - Cr^{6+}/Cr(VI) corrosion inhibitors.[80-82] Chromate conversion coatings offer an excellent active corrosion protection to aluminum alloys by facilitating the release of chromate (CrO_4^{2-}) ions from the coating, which then migrate to the nearby corroding areas of the alloy. Upon reaching these sites, CrO_4^{2-} undergoes reduction forming a passivating and chemically inert chromium hydroxide - $Cr(OH)_3$ film.[83-84] The major drawback associated with chromate conversion coatings lies in the toxicity and carcinogenicity of the active chrome species, Cr^{6+}/Cr(VI).[85-87] Consequently, the use of hexavalent chromium species has been limited through numerous acts and regulations enforced by the Environmental Protection Agency (EPA) despite their outstanding corrosion protection.[86]

The aerospace and automotive industries have transitioned away from using chromate conversion coatings to more environmentally sustainable and equally effective conversion coatings. The trivalent chromium process (TCP) coating formulated and developed by the Naval Air Systems Command (NAVAIR) for aerospace aluminum alloys is one of the promising

replacements for chromate conversion coatings.[88-89] TCP is a non-chromate, trivalent chromium (Cr^{3+}) and zirconium (Zr)-based conversion coating.[90] Cr^{3+}/Cr(III) is considerably a weaker oxidizer and possesses a lower health risk as compared to Cr^{6+}/Cr(VI).[91,92] TCP is a leading chromate-free conversion coating in the market and has been licensed and vended by several companies under different names such as Bonderite® M-CR T 5900 AERO also known as Alodine T 5900 (Henkel Corporation), CHEMEON TCP-HF™ (CHEMEON Surface Technology), and Luster-On® Aluminescent (Luster-On Products Inc.). While these TCP coating baths have chemical compositions that vary from the original NAVAIR TCP composition to some extent, they typically contain hexafluorozirconate (ZrF_6^{2-}), Cr^{3+}/Cr(III), sulfate (SO_4^{2-}), and fluoroborate (BF_4^-) salts and an acid with a pH between 3.8 and 4.0.[90,93]

TCP coating formation on aluminum alloys can be achieved by immersion or spray.[94] The metal surface should be cleaned and properly prepared prior to coating application to ensure uniform coverage and good adhesion. The TCP coating has a biphasic structure comprised of an inner potassium fluoroaluminate (K_xAlF_{3+x}) interfacial layer and an outer hydrated zirconia ($ZrO_2.2H_2O$) layer and grows up to a thickness of ~100 nm.[93] A well-formed TCP coating provides aluminum alloys with protection against corrosion through both anodic and cathodic protection mechanisms.[95-101] The TCP coating furnishes anodic protection by forming a barrier layer over the aluminum (Al) rich sites of the alloy, thereby inhibiting the metal oxidation reaction and cathodic protection by blocking the Cu and Fe containing intermetallic particles to inhibit the surface-sensitive ORR. [95-101]

1.6 REDUCTION OF ARYLDIAZONIUM SALTS

Aryldiazonium salts are organic compounds with a common formula, R-N_2^+ X^-, where R is an aryl group and X is an anion such as chloride (Cl^-) or tetrafluoroborate (BF_4^-). The aryldiazonium salts are formed by a process known as diazotization (Scheme 1.1).Diazotization is carried out by addition of nitrous acid (HNO_2) to aromatic amines at about 0 °C. HNO_2 is usually generated in situ from sodium nitrite ($NaNO_2$) and inorganic acid (i.e., hydrochloric [HCl] or tetrafluoroboric [HBF_4] acid).

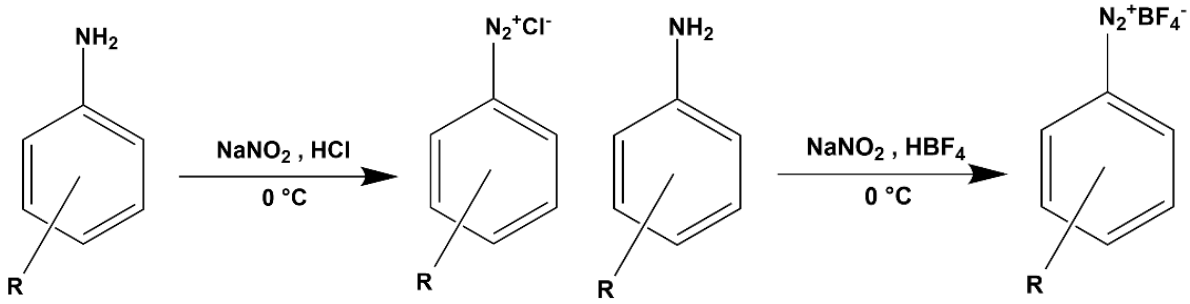

Scheme 1.1 Formation of aryldiazonium salt by diazotization.[104]

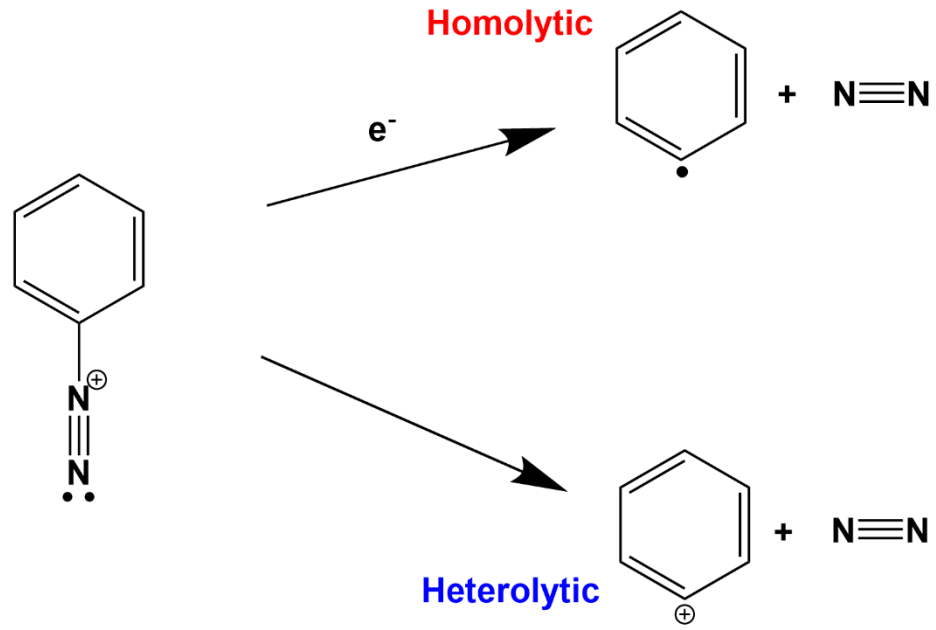

Scheme 1.2. Homolytic and heterolytic dediazoniation pathways.[102,105]

Aryldiazonium cations can displace the diazo group as stable dinitrogen (N_2). This process is called "Dediazoniation". Dediazoniation occurs in two pathways: homolytic and heterolytic (Scheme 1.2). The homolytic dediazoniation pathway involves an electron transfer to the diazonium cation resulting in aryl radical. The electron transfer can be achieved electrochemically, photochemically, or chemically using a reducing agent.[102-104] The heterolytic pathway generates an aryl cation via thermal decomposition.[105] Many diazonium salts are commercially available and stable for months at low temperatures.[106]

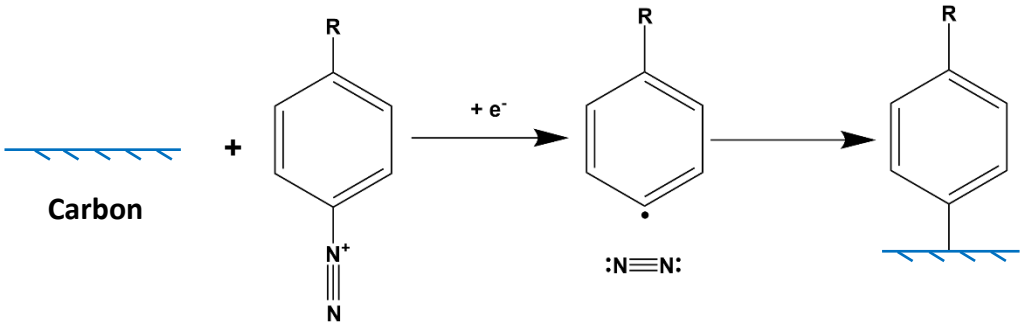

Scheme 1.3. Electrochemically-assisted reduction of aryldiazonium cations.

The electrochemically-assisted reduction of aryldiazonium salts (Scheme 1.3) originally reported by Savéant and coworkers is one of the most common and versatile methods used to functionalize carbon electrode surfaces.[107] This simple and well-established technique modifies carbon surfaces by generating aryl radicals through electrochemical reduction of aryldiazonium salts that then can covalently bind with nearby surface carbon atoms forming a adlayer as shown in Figure 1.4.[108-114] These covalently attached adlayers are generally stable to harsh environments and high temperatures.[112,115] Compared to surface modification methods such as anodization in aqueous medium in which corrosion of the carbon surface can be observed, the diazonium method is advantageous owing to its non-corrosive and reproducible nature.[108] Multilayers can also be formed depending on the electrodeposition conditions such as diazonium cation concentration and

reduction time employed for the derivatization.[108,114] Further, this surface modification method allows the formation of a wide variety of organic adlayers with unique chemical properties on carbon utilizing commercially available aryldiazonium salts with different substituents on the phenyl group.

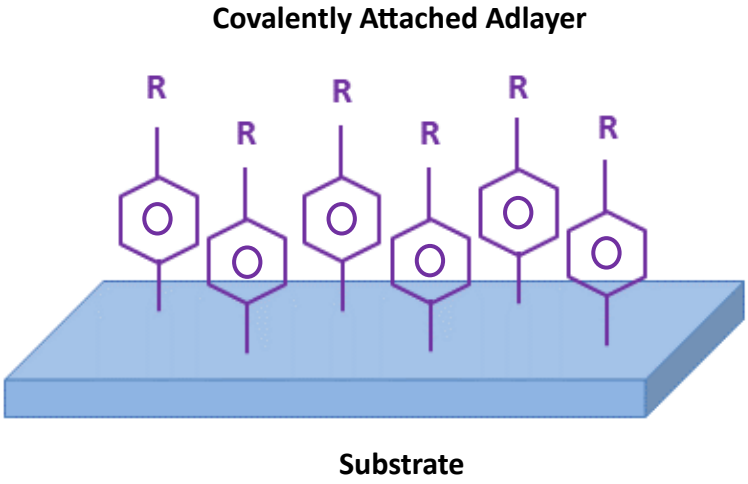

Figure 1.4. Formation of the covalently attached adlayer.

Spontaneous grafting of aryl groups to carbon and metallic surfaces by immersing the substrate in an appropriate diazonium salt solution has been extensively reported in literature.[116-118] Spontaneous grafting occurs under open circuit conditions and does not require any electrochemical induction. Spontaneous modification generates covalently attached, stable adlayers similarly to the electrochemically-assisted modification but at a slower rate. The uniformity and thickness of the spontaneously grafted adlayers depend on the deposition conditions such as immersion time, concentration of the diazonium salt solution, and temperature as well as the condition of the substrate surface.[116] Spontaneous grafting offers a simpler and more adaptable approach for compared to electrochemical grafting and its straightforward implementation holds a considerable appeal in the industrial field.

Organic adlayers formed on carbon surfaces through electrochemically assisted and spontaneous reduction of aryldiazonium cations exhibit barrier properties by acting as an insulating spacer that separates the redox molecule from the electrode surface.[110,119,120] More importantly, glassy carbon electrodes electrochemically grafted by this method with phenyl, 4-methylphenyl, naphthyl and anthracenyl adlayers have been proven to inhibit the oxygen reduction reaction by hindering the electron transfer process.[121,122] It is hypothesized that the electrochemically assisted and spontaneous diazonium surface treatment yields stable adlayers on exposed carbon fiber surfaces of the CFRP composites and that these adlayers will inhibit the oxygen reduction reaction kinetics by blocking the active sites on the carbon fibers for O_2 chemisorption; the first step in the ORR. Inhibiting the oxygen reduction reaction kinetics will inhibit galvanic corrosion of the joined aluminum alloy and the adlayers will be stable during environmental exposure.

1.7 TITANIUM AND TITANIUM ALLOYS

Titanium and its alloys are another popular metal category that offers many advantages, including outstanding mechanical properties and high corrosion endurance, making them a widely used material in aerospace,[123,124] marine,[125,126] automotive[127-129] and biomedical applications.[130,131] When exposed to the atmosphere, similarly to aluminum and its alloys, titanium and its alloys spontaneously react with oxygen and generate passive oxide (mainly TiO_2) films that are typically 2-5 nm thick on their surface.[132-134] These ultra-thin native oxide films exert superior resistance to general corrosion. Due to the growing demand for titanium alloys and the high cost associated with conventional top-down or subtractive manufacturing methods for titanium components, there has been a significant focus on utilizing additive manufacturing or bottom-up techniques for fabricating titanium components.[135,136]

1.8 ADDITIVE MANUFACTURING

Additive manufacturing (AM), commonly known as 3D printing, is a process by which parts and components are fabricated one layer at a time directly from a three-dimensional computer-aided design (3D CAD) as opposed to conventional subtractive and formative manufacturing technologies.[137-140] Over the past years, AM has gained a significant interest owing to its promising potential to accelerate the advancement of next generation manufacturing processes and unveil novel design opportunities. The noteworthy advantages AM offers over traditional manufacturing and fabrication techniques, such as extrusion, forging, shape casting, and machining, include the ability to design and fabricate geometrically intricate, lightweight structures with improved performance, reduced design-to-manufacture time, minimized waste production, and lower cost.[141,142]Powder bed fusion (PBF) and directed energy deposition (DED) are two broad classes of metal AM technologies. PBF involves the scanning of metal powders laid down on a build platform with an intense heat source (laser or electron beam) and are better suited to fabricate smaller structures with complex geometries.[135,143,144] In contrast, DED dispenses the metal powders to a substrate where a high energy density heat source, such as a laser, electron beam or plasma electric arc, is focused and these are more appropriate for manufacturing larger parts with a coarser finish.[135,145,146] Selective laser melting (SLM) is a rapidly evolving PBF AM technique that employs a high-power laser beam to melt and fuse metallic powders preplaced on a build platform.[147-150] The melting of the regions of interest in a layer-by-layer manner fuses the molten metal into the desired structure upon solidification. The process is repeated until the final geometry is achieved. Recent advancements in SLM have enabled the bottom-up fabrication of geometrically complex titanium and titanium alloy components.

A relatively new titanium alloy is Ti-5Al-5Mo-5V-3Cr (Ti-5553 wt.%); a variation of the Russian alloy VT22 (Ti-5Al-5Mo-5V-1Cr-1Fe) developed for improved processability with excellent mechanical properties.[151] Ti-5553 is a near-β alloy with a nominal density of 4.67 g/cm^3 and an ultimate tensile strength up to 1300 MPa.[152] This high strength alloy is used in aircraft landing gears (i.e. Boeing 787 Dreamliner), where the structural parts are subjected to heavy takeoff weight and high impact loads on landing. [152-155] While several studies have explored the microstructure and mechanical properties of Ti-5553 prepared by SLM, there is comparatively limited research dedicated to the electrochemical characterization of this alloy.

1.9 RESEARCH MOTIVATION AND SIGNIFICANCE OF THE WORK

With the increased usage of CFRP composites with aluminum alloys in the aerospace industry, environmentally friendly surface treatments are needed more than ever to solve the galvanic corrosion issue. The first part of research presented herein explores a fundamental surface modification technique that holds the potential to evolve into a novel approach for mitigating the galvanic corrosion rate of aluminum alloys when integrated with carbon fiber reinforced (CFRP) composites in aircraft structures. It is hypothesized that the electrochemically assisted and spontaneous diazonium surface treatment yields stable adlayers on exposed carbon fiber surfaces of the CFRP composites and that these adlayers will inhibit the oxygen reduction reaction kinetics by blocking the active sites on the carbon fibers for O_2 chemisorption; the first step in the ORR. Inhibiting the oxygen reduction reaction kinetics will inhibit galvanic corrosion of the joined aluminum alloy. Furthermore, it is hypothesized that the adlayers will be stable during environmental exposure and will support adhesion of primer overlayers. This leads to two specific aims.

(i) To investigate the electrochemically assisted and spontaneous derivatization of CFRP composite edges with aryldiazonium salts, characterize the modified surfaces and assess the influence of diazonium surface modification of CFRP composite electrodes on the kinetics of oxygen reduction reaction.

(ii) To determine how effectively the diazonium surface treatment inhibits the galvanic corrosion on the wrought aluminum alloys surface treated with TCP coating, when joined by metal fasteners, during accelerated degradation testing designed to mimic conditions of the service environment.

The AM processing conditions influence the grain size and shape, porosity, defects, alloying elemental distribution within the matrix and intermetallic phase formation. From a corrosion perspective, these are all important factors. Although numerous studies have delved into the microstructure and mechanical properties of Ti-5553 alloy produced by SLM, there is a notable scarcity of research focused on the electrochemical corrosion behavior of this alloy. To bridge this gap in knowledge fundamental research is needed to better understand how the microstructure, porosity/defects, and intermetallic phases affect the electrochemical corrosion behavior of SLM Ti alloy 5553 with and without surface treatment. The second part of this dissertation thus presents an investigation into the material characterization and electrochemical properties of Ti-5553 prepared by SLM in its as-processed state, as well as after abrading and polishing treatments.

Overall, this dissertation aspires to contribute to the development and advancement of environmentally and economically sustainable material processing technologies within the aviation industry.

REFERENCES

1. Martin, R. B. Chemistry of aluminum. (1990). In *Aluminum and renal failure* (pp. 7-26). Dordrecht: Springer Netherlands.

2. Kvande, H. (2015). Occurrence and production of aluminum. *The Lightest Metals: Science and Technology from Lithium to Calcium*, 13.

3. Liu, G., & Müller, D. B. (2012). Addressing sustainability in the aluminum industry: a critical review of life cycle assessments. *Journal of Cleaner Production*, *35*, 108.

4. Davis, J. R. (Ed.). (2001). *Alloying: understanding the basics*. ASM international.

5. Rooy, E. L. (1990). Introduction to aluminum and aluminum alloys.

6. Gándara, M. F. (2013). Aluminium: the metal of choice. *Mater. Tehnol*, *47*(3), 261.

7. Sanders Jr, R. E. (2000). Aluminum and aluminum alloys. *Kirk-Othmer Encyclopedia of Chemical Technology*.

8. Jawalkar, C. S., & Kant, S. (2015). A review on use of aluminium alloys in aircraft components. *i-manager's Journal on Material Science*, *3*(3), 33.

9. Kissell, J. R., Pantelakis, S. G., & Haidemenopoulos, G. N. (2004). Aluminum and aluminum alloys. *Handbook of Advanced Materials: Enabling New Designs*, 321.

10. Miller, W. S., Zhuang, L., Bottema, J., Wittebrood, A., De Smet, P., Haszler, A., & Vieregge, A. J. M. S. (2000). Recent development in aluminium alloys for the automotive industry. *Materials Science and Engineering: A*, *280*(1), 37.

11. Fridlyander, I. N., Sister, V. G., Grushko, O. E., Berstenev, V. V., Sheveleva, L. M., & Ivanova, L. A. (2002). Aluminum alloys: promising materials in the automotive industry. *Metal science and heat treatment*, *44*(9), 365.

12. Long, R. S., Boettcher, E., & Crawford, D. (2017). Current and future uses of aluminum in the automotive industry. *Jom*, *69*(12), 2635.

13. Starke Jr, E. A., & Staley, J. T. (1996) Application of modern aluminum alloys to aircraft. *Progress in aerospace sciences*, *32*(2-3), 131.

14. Dursun, T., & Soutis, C. Recent developments in advanced aircraft aluminum alloys. *Materials & Design,* 2014, *56*, 862.

15. Li, S. S., Yue, X., Li, Q. Y., Peng, H. L., Dong, B. X., Liu, T. S., ... & Jiang, Q. C. (2023). Development and applications of aluminum alloys for aerospace industry. *Journal of Materials Research and Technology*.

16. Hung, F. S. (2020). Design of lightweight aluminum alloy building materials for corrosion and wear resistance. *Emerging Materials Research*, *9*(3), 750.

17. Dokšanović, T., Džeba, I., & Markulak, D. (2017). Applications of aluminium alloys in civil engineering. *Tehnički vjesnik*, *24*(5), 1609.

18. Wahid, M. A., Siddiquee, A. N., & Khan, Z. A. (2020). Aluminum alloys in marine construction: characteristics, application, and problems from a fabrication viewpoint. *Marine Systems & Ocean Technology*, *15*(1), 70.

19. Kaufman, J. G. (2000). *Introduction to aluminum alloys and tempers*. ASM international.

20. *Industry Standards.* https://www.aluminum.org/industry-standards

21. Pfeiffer, O. P., Liu, H., Montanelli, L., Latypov, M. I., Sen, F. G., Hegadekatte, V., ... & Homer, E. R. (2022). Aluminum alloy compositions and properties extracted from a corpus of scientific manuscripts and US patents. *Scientific Data*, *9*(1), 128.

22. Staley, J. T., & Lege, D. J. (1993). Advances in aluminium alloy products for structural applications in transportation. *Le Journal de Physique IV*, *3*(C7), C7-179.

23. Froes, F. H. (1994). Advanced metals for aerospace and automotive use. *Materials Science and Engineering: A*, *184*(2), 119.

24. Weritz, J. (2018). Aluminum alloy nomenclature and temper designations.

25. Alloys, W. A. (2015). International Alloy Designations and Chemical Composition Limits for Wrought Aluminum and Wrough Aluminum Alloys.

26. Altenbach, H., Altenbach, J., Kissing, W., & Altenbach, H. (2004). *Mechanics of composite structural elements* (pp. 122-297). Berlin: Springer-Verlag.

27. Rajak, D. K., Pagar, D. D., Kumar, R., & Pruncu, C. I. (2019). Recent progress of reinforcement materials: a comprehensive overview of composite materials. *Journal of Materials Research and Technology*, *8*(6), 6354.

28. Jose, J. P., & Joseph, K. (2012). Advances in polymer composites: macro-and microcomposites–state of the art, new challenges, and opportunities. *Polymer composites*, 1-16.

29. Fan, J., & Njuguna, J. (2016). An introduction to lightweight composite materials and their use in transport structures. In *Lightweight Composite Structures in Transport* (pp. 3-34). Woodhead Publishing.

30. Chung, Deborah DL. *Carbon Composites: composites with carbon fibers, nanofibers, and nanotubes*. Butterworth-Heinemann, 2016.

31. Park, Soo-Jin, and Gun-Young Heo. *Carbon Fibers*, pp. 31-66. Springer, Dordrecht, 2015. 9.

32. Aldosari, S. M., Khan, M., & Rahatekar, S. (2020). Manufacturing carbon fibres from pitch and polyethylene blend precursors: a review. *Journal of Materials Research and Technology*, *9*(4), 7786.

33. Soutis, C. (2005). Carbon fiber reinforced plastics in aircraft construction. *Materials Science and Engineering: A*, *412*(1-2), 171.

34. Kesarwani, S. (2017). Polymer composites in aviation sector. *Int. J. Eng. Res*, *6*(10).

35. Aamir, M., Tolouei-Rad, M., Giasin, K., & Nosrati, A. (2019). Recent advances in drilling of carbon fiber–reinforced polymers for aerospace applications: A review. *The International Journal of Advanced Manufacturing Technology*, *105*, 2289.

36. Ozkan, D., Gok, M. S., & Karaoglanli, A. C. (2020). Carbon fiber reinforced polymer (CFRP) composite materials, their characteristic properties, industrial application areas and their machinability. *Engineering Design Applications III: Structures, Materials and Processes*, 235.

37. Ahmad, H., Markina, A. A., Porotnikov, M. V., & Ahmad, F. (2020, November). A review of carbon fiber materials in automotive industry. In *IOP Conference Series: Materials Science and Engineering* (Vol. 971, No. 3, p. 032011). IOP Publishing.

38. Das, T. K., Ghosh, P., & Das, N. C. (2019). Preparation, development, outcomes, and application versatility of carbon fiber-based polymer composites: a review. *Advanced Composites and Hybrid Materials*, *2*, 214.

39. Kesarwani, S. (2017). Polymer composites in aviation sector. *Int. J. Eng. Res*, *6*(10).

40. Aamir, M., Tolouei-Rad, M., Giasin, K., & Nosrati, A. (2019). Recent advances in drilling of carbon fiber–reinforced polymers for aerospace applications: A review. *The International Journal of Advanced Manufacturing Technology*, *105*, 2289.

41. Joshi, S. (2012). Processing science for polymeric composites in aerospace. *Aerospace Materials Handbook*, 461.

42. Mrazova, M. (2013). Advanced composite materials of the future in aerospace industry. *Incas bulletin*, *5*(3), 139.

43. van Grootel, A., Chang, J., Wardle, B. L., & Olivetti, E. (2020). Manufacturing variability drives significant environmental and economic impact: The case of carbon fiber reinforced polymer composites in the aerospace industry. *Journal of cleaner production*, *261*, 121087.

44. Charitidis, P. J. (2018). Criteria for the selection of carbon fiber composite materials for fighter aircraft. *Advances in Materials Science and Engineering: An International Journal (MSEJ)*, *5*(2/3/4), 1-13.

45. Soutis, C. (2020). Aerospace engineering requirements in building with composites. In *Polymer composites in the aerospace industry* (pp. 3-22). Woodhead Publishing.

46. Siengchin, S. (2023). A review on lightweight materials for defence applications: A present and future developments. *Defence Technology*.

47. Ishikawa, T., Amaoka, K., Masubuchi, Y., Yamamoto, T., Yamanaka, A., Arai, M., & Takahashi, J. (2018). Overview of automotive structural composites technology developments in Japan. *Composites Science and Technology*, *155*, 221.

48. Zhang, J., Lin, G., Vaidya, U., & Wang, H. (2023). Past, present and future prospective of global carbon fibre composite developments and applications. *Composites Part B: Engineering*, *250*, 110463.

49. Taylor, C., & Sours, A. S. (2022). *Corrosion management for a sustainable future*.

50. Pedeferri, P., & Pedeferri, P. (2018). Galvanic corrosion. *Corrosion Science and Engineering*, 183.

51. Whitman, B. W., Miller, D., Davis, R., Brennan, J., & Swain, G. M. (2017). Effect of galvanic current on the physicochemical, electrochemical, and mechanical properties of an aerospace carbon fiber reinforced epoxy composite. *Journal of The Electrochemical Society*, *164*(13), C881.

52. Hur, S. Y., Kim, K. T., Yoo, Y. R., & Kim, Y. S. (2020). Effects of NaCl concentration and solution temperature on the galvanic corrosion between CFRP and AA7075T6. *Corros. Sci. Technol.*, *19*(2), 75.

53. Liu, Z., Curioni, M., Jamshidi, P., Walker, A., Prengnell, P., Thompson, G. E., & Skeldon, P. (2014). Electrochemical characteristics of a carbon fibre composite and the associated galvanic effects with aluminium alloys. *Applied surface science*, *314*, 233.

54. Håkansson, E., Hoffman, J., Predecki, P., & Kumosa, M. (2017). The role of corrosion product deposition in galvanic corrosion of aluminum/carbon systems. *Corrosion Science*, *114*, 10.

55. Li, S., Khan, H. A., Hihara, L. H., Cong, H., & Li, J. (2018). Corrosion behavior of friction stir blind riveted Al/CFRP and Mg/CFRP joints exposed to a marine environment. *Corrosion Science*, *132*, 300.

56. Srinivasan, R., Nelson, J. A., & Hihara, L. H. (2015). Development of guidelines to attenuate galvanic corrosion between mechanically-coupled aluminum and carbon-fiber reinforced epoxy composites using insulation layers. *Journal of the Electrochemical Society*, *162*(10), C545.

57. Whitman, B. W., Miller, D., Davis, R., Brennan, J., & Swain, G. M. (2017). Effect of galvanic current on the physicochemical, electrochemical and mechanical properties of an aerospace carbon fiber reinforced epoxy composite. *Journal of The Electrochemical Society*, *164*(13), C881.

58. Dammulla, I. N., & Swain, G. M. (2022). Inhibiting the oxygen reduction reaction kinetics on carbon fiber epoxy composites through diazonium surface modification-impacts on the

galvanic corrosion of coupled aluminum alloys. *Journal of the electrochemical society*, *169*(7), 071501.

59. Dammulla, I. N., & Swain, G. M. (2023). Inhibiting Metal Galvanic and Carbon Corrosion in Aluminum Alloy-Carbon Fiber Reinforced Composite Joints by Spontaneous Deposition of Diazonium Adlayers on Exposed Carbon Fibers. *Journal of The Electrochemical Society*, *170*(9), 091503.

60. N. Faisal, O. N. Cora, M. L. Becki, R. E. Silwa, Y. Sternberg, S. Pant, R. Degenhardt, and A. Prathuru, "Defect types. In structural health monitoring damage detection systems for aerospace." Springer Aerospace Technology., ed. M. G. R. Sause and E. Jasiūnienė (Springer, Cham) pp. 15 (2021)978-3-030-72191-6.

61. Srinivasan, R., Nelson, J. A., & Hihara, L. H. (2015). Development of guidelines to attenuate galvanic corrosion between mechanically-coupled aluminum and carbon-fiber reinforced epoxy composites using insulation layers. *Journal of the Electrochemical Society*, *162*(10), C545.

62. Peng, Z., & Nie, X. (2013). Galvanic corrosion property of contacts between carbon fiber cloth materials and typical metal alloys in an aggressive environment. *Surface and coatings technology*, *215*, 85.

63. R. Srinivasan and L. H. Hihara, (2016). Utilization of hydrophobic coatings on insulative skirts to attenuate galvanic corrosion between mechanically-fastened aluminum alloy and carbon-fiber reinforced polymer-matrix composites. *Electrochem. Commun.,* 72, 96.

64. Feng, Z., Boerstler, J., Frankel, G. S., & Matzdorf, C. A. (2015). Effect of surface pretreatment on galvanic attack of coated Al alloy panels. *Corrosion*, *71*(6), 771.

65. Feng, Z., Frankel, G. S., Abbott, W. H., & Matzdorf, C. A. (2016). Galvanic attack of coated Al alloy panels in laboratory and field exposure. *Corrosion*, *72*(3), 342.

66. Gorobez, J., Maack, B., & Nilius, N. (2021). Growth of Self-Passivating Oxide Layers on Aluminum—Pressure and Temperature Dependence. *physica status solidi (b)*, *258*(5), 2000559.

67. Revie, R. W. (Ed.). (2011). *Uhlig's corrosion handbook* (Vol. 51). John Wiley & Sons.

68. Evertsson, J., Bertram, F., Zhang, F., Rullik, L., Merte, L. R., Shipilin, M., Soldemo, M., Ahmadi, S., Vinogradov, N., Carla, F., Weissenrieder, J., Göthelid, M., Pan, J., Mikkelsen, A., Nilsson, J. -O., & Lundgren, E. (2015). The thickness of native oxides on aluminum alloys and single crystals. *Applied Surface Science*, *349*, 826.

69. Serebrennikova, I., & White, H. S. (2000). Scanning electrochemical microscopy of electroactive defect sites in the native oxide film on aluminum. *Electrochemical and Solid-State Letters*, *4*(1), B4.

70. Natishan, P. M., & O'grady, W. E. (2014). Chloride ion interactions with oxide-covered aluminum leading to pitting corrosion: a review. *Journal of the electrochemical society*, *161*(9), C421.

71. Visser, P., Terryn, H., & Mol, J. M. (2016). Aerospace coatings. *Active protective coatings: New-generation coatings for metals*, 315.

72. Duarte, T., Meyer, Y. A., & Osório, W. R. (2022). The holes of Zn phosphate and hot dip galvanizing on electrochemical behaviors of multi-coatings on steel substrates. *Metals*, *12*(5), 863.

73. Kiyota, S., Valdez, B., Stoytcheva, M., Zlatev, R., & Schorr, M. (2009). Electrochemical study of corrosion behavior of rare earth based chemical conversion coating on aerospace aluminum alloy. *ECS Transactions*, *19*(29), 115.

74. Buchheit, R. G., & Hughes, A. E. (2003). Chromate and chromate-free conversion coatings.

75. Kaysser, W. (2001). Surface modifications in aerospace applications. *Surface engineering*, *17*(4), 305.

76. Asmatulu, R., Khan, S. I., & Jenkinson, M. L. (2016). 30 Improving Corrosion Resistance via Graphene Nanocomposite Coatings.

77. Hesamedini, S., & Bund, A. (2019). Trivalent chromium conversion coatings. *Journal of Coatings Technology and Research*, *16*, 623.

78. Becker, M. (2019). Chromate-free chemical conversion coatings for aluminum alloys. *Corrosion Reviews*, *37*(4), 321.

79. Twite, R. L., & Bierwagen, G. P. (1998). Review of alternatives to chromate for corrosion protection of aluminum aerospace alloys. *Progress in organic coatings*, *33*(2), 91.

80. Kendig, M. W., & Buchheit, R. G. (2003). Corrosion inhibition of aluminum and aluminum alloys by soluble chromates, chromate coatings, and chromate-free coatings. *Corrosion*, *59*(5), 379.

81. Zhao, J., Xia, L., Sehgal, A., Lu, D., McCreery, R. L., & Frankel, G. S. (2001). Effects of chromate and chromate conversion coatings on corrosion of aluminum alloy 2024-T3. *Surface and Coatings Technology*, *140*(1), 51.

82. Campestrini, P., Goeminne, G., Terryn, H., Vereecken, J., & De Wit, J. H. W. (2004). Chromate conversion coating on aluminum alloys: I. formation mechanism. *Journal of the Electrochemical Society*, *151*(2), B59.

83. Kendig, M. W., Davenport, A. J., & Isaacs, H. S. (1993). The mechanism of corrosion inhibition by chromate conversion coatings from X-ray absorption near edge spectroscopy (XANES). *Corrosion Science*, *34*(1), 41.

84. Xia, L., Akiyama, E., Frankel, G., & McCreery, R. (2000). Storage and release of soluble hexavalent chromium from chromate conversion coatings equilibrium aspects of Cr VI concentration. *Journal of the Electrochemical Society*, *147*(7), 2556.

85. Costa, M. (1997). Toxicity and carcinogenicity of Cr (VI) in animal models and humans. *Critical reviews in toxicology*, *27*(5), 431.

86. Baral, A., & Engelken, R. D. (2002). Chromium-based regulations and greening in metal finishing industries in the USA. *Environmental Science & Policy*, *5*(2), 121.

87. Gharbi, O., Thomas, S., Smith, C., & Birbilis, N. (2018). Chromate replacement: what does the future hold? *npj Materials Degradation*, *2*(1), 12.

88. W. C. Nickerson and E. Lipnickas, (2003) Proceedings of the 2003 Tri Service Corrosion Conference, Las Vegas, NV, Nov. 17–21.

89. C. Matzdorf, M. Kane, and J. Green, U.S. Patent Appl. 09/702,225, Patent # U.S. 6375726 B1, April 23, 2002.

90. Guo, Y., & Frankel, G. S. (2012). Characterization of trivalent chromium process coating on AA2024-T3. *Surface and Coatings Technology*, *206*(19-20), 3895.

91. Berger, R., Bexell, U., Grehk, T. M., & Hörnström, S. E. (2007). A comparative study of the corrosion protective properties of chromium and chromium free passivation methods. *Surface and Coatings Technology*, *202*(2), 391.

92. Suib, S. L., La Scala, J., Nickerson, W., Fowler, A., & Zaki, N. (2009). Determination of hexavalent chromium in NAVAIR trivalent chromium process (TCP) coatings and process solutions. *Metal Finishing*, *107*(2), 28.

93. Li, L., Kim, D. Y., & Swain, G. M. (2012). Transient formation of chromate in trivalent chromium process (TCP) coatings on AA2024 as probed by Raman spectroscopy. *Journal of the Electrochemical Society*, *159*(8), C326.

94. Munson, C. A., & Swain, G. M. (2017). Structure and chemical composition of different variants of a commercial trivalent chromium process (TCP) coating on aluminum alloy 7075-T6. *Surface and Coatings Technology*, *315*, 150.

95. L. Li, K. P. Doran, and G. M. Swain. (2013). Electrochemical characterization of trivalent chromium process (TCP) coatings on aluminum alloys 6061 and 7075. *J. Electrochem. Soc.*, 160, C396

96. S. Dardona, L. Chen, M. Kryzman, and M. Jaworowski, (2011). Polarization controlled kinetics and composition of trivalent chromium process coatings on aluminum. *Anal. Chem.*, 83, 6127

97. A. Iyer, W. Willis, S. Frueh, W. Nickerson, A. Fowler, J. Bames, L. Hagos, J. Escarsega, J. La Scala, and S. L. Suib. (2010). Characterization of NAVAIR trivalent chromium process (TCP) coatings and solutions. *Plat. Surf. Finish.*, 5, 32.

98. X. C. Dong, P. Wang, S. Argekar, and D. W. Schaefer. (2010). Structure and composition of trivalent chromium process (TCP) films on Al alloy. *Langmuir*, 26, 10833.

99. Li, L., Swain, G. P., Howell, A., Woodbury, D., & Swain, G. M. (2011). The formation, structure, electrochemical properties and stability of trivalent chrome process (TCP) coatings on AA2024. *Journal of The Electrochemical Society*, *158*(9), C274.

100. Guo, Y., & Frankel, G. S. (2012). Active corrosion inhibition of AA2024-T3 by trivalent chrome process treatment. *Corrosion, The Journal of Science and Engineering*, *68*(4), 045002-1.

101. J. Qi, L. Gao, Y. Li, Z. Wang, G. E. Thompson, and P. Skeldon. (2017). An optimized trivalent chromium conversion coating process for AA2024-T351 Alloy. *J. Electrochem. Soc.*, 164, C390

102. Elofson, R. M., & Gadallah, F. F. (1969). Substituent effects in the polarography of aromatic diazonium salts. *The Journal of Organic Chemistry*, *34*(4), 854.

103. Ando, W. (1978). Photochemistry of the diazonium and diazo groups. *Diazonium and Diazo Groups (1978) Part 1*, *1*, 341.

104. Kornblum, N., Cooper, G. D., & Taylor, J. E. (1950). The Chemistry of Diazo Compounds. II. Evidence for a Free Radical Chain Mechanism in the Reduction of Diazonium Salts by Hypophosphorous Acid1, 2. *Journal of the American Chemical Society*, *72*(7), 3013.

105. DeTar, D. F., & Ballentine, A. R. (1956). The Mechanisms of Diazonium Salt Reactions. II. A Redetermination of the Rates of the Thermal Decomposition of Six Diazonium Salts in Aqueous Solution1. *Journal of the American Chemical Society*, *78*(16), 3916.

106. Filimonov, V. D., Krasnokutskaya, E. A., Kassanova, A. Z., Fedorova, V. A., Stankevich, K. S., Naumov, N. G., ... & Kataeva, V. A. (2019). Synthesis, structure, and synthetic potential of arenediazonium trifluoromethanesulfonates as stable and safe diazonium salts. *European Journal of Organic Chemistry*, *2019*(4), 665.

107. Delamar, M., Hitmi, R., Pinson, J., & Saveant, J. M. (1992). Covalent modification of carbon surfaces by grafting of functionalized aryl radicals produced from electrochemical reduction of diazonium salts. *Journal of the American Chemical Society*, *114*(14), 5883.

108. Downard, A. J. (2000). Electrochemically assisted covalent modification of carbon electrodes. *Electroanalysis: An International Journal Devoted to Fundamental and Practical Aspects of Electroanalysis*, *12*(14), 1085.

109. Allongue, P., Delamar, M., Desbat, B., Fagebaume, O., Hitmi, R., Pinson, J., & Savéant, J. M. (1997). Covalent modification of carbon surfaces by aryl radicals generated from the electrochemical reduction of diazonium salts. *Journal of the american chemical society*, *119*(1), 201.

110. Ortiz, B., Saby, C., Champagne, G. Y., & Bélanger, D. (1998). Electrochemical modification of a carbon electrode using aromatic diazonium salts. 2. Electrochemistry of 4-nitrophenyl modified glassy carbon electrodes in aqueous media. *Journal of Electroanalytical Chemistry*, *455*(1-2), 75.

111. Ray, K., & McCreery, R. L. (1997). Spatially resolved Raman spectroscopy of carbon electrode surfaces: Observations of structural and chemical heterogeneity. *Analytical Chemistry*, *69*(22), 4680.

112. Delamar, M., Desarmot, G., Fagebaume, O., Hitmi, R., Pinsonc, J., & Savéant, J. M. (1997). Modification of carbon fiber surfaces by electrochemical reduction of aryl diazonium salts: Application to carbon epoxy composites. *Carbon*, *35*(6), 801.

113. M. Dequaire, C. Degrand, and B. Limoges. (1999). Biotinylation of screen-printed carbon electrodes through the electrochemical reduction of the diazonium salt of paminobenzoyl biocytin. *J. Am. Chem. Soc*., 121, 6946.

114. Anariba, F., DuVall, S. H., & McCreery, R. L. (2003). Mono-and multilayer formation by diazonium reduction on carbon surfaces monitored with atomic force microscopy "scratching". *Analytical Chemistry*, *75*(15), 3837.

115. D'Amours, M., & Bélanger, D. (2003). Stability of substituted phenyl groups electrochemically grafted at carbon electrode surface. *The Journal of Physical Chemistry B*, *107*(20), 4811.

116. Adenier, A., Cabet-Deliry, E., Chaussé, A., Griveau, S., Mercier, F., Pinson, J., & Vautrin-Ul, C. (2005). Grafting of nitrophenyl groups on carbon and metallic surfaces without electrochemical induction. *Chemistry of Materials*, *17*(3), 491.

117. Adenier, A., Barré, N., Cabet-Deliry, E., Chaussé, A., Griveau, S., Mercier, F., Pinson, J., & Vautrin-Ul, C. (2006). Study of the spontaneous formation of organic layers on carbon and metal surfaces from diazonium salts. *Surface Science*, *600*(21), 4801.

118. Chamoulaud, G., & Belanger, D. (2007). Spontaneous derivatization of a copper electrode with in situ generated diazonium cations in aprotic and aqueous media. *The Journal of Physical Chemistry C*, *111*(20), 7501.

119. Downard, A. J., & Prince, M. J. (2001). Barrier properties of organic monolayers on glassy carbon electrodes. *Langmuir*, *17*(18), 5581.

120. Saby, C., Ortiz, B., Champagne, G. Y., & Bélanger, D. (1997). Electrochemical modification of glassy carbon electrode using aromatic diazonium salts. 1. Blocking effect of 4-nitrophenyl and 4-carboxyphenyl groups. *Langmuir*, *13*(25), 6805.

121. Yang, H. H., & McCreery, R. L. (2000). Elucidation of the mechanism of dioxygen reduction on metal-free carbon electrodes. *Journal of the Electrochemical Society*, *147*(9), 3420.

122. Kullapere, M., Jürmann, G., Tenno, T. T., Paprotny, J. J., Mirkhalaf, F., & Tammeveski, K. (2007). Oxygen electroreduction on chemically modified glassy carbon electrodes in alkaline solution. *Journal of Electroanalytical Chemistry*, *599*(2), 183.

123. Peters, M., Kumpfert, J., Ward, C. H., & Leyens, C. (2003). Titanium alloys for aerospace applications. *Advanced engineering materials*, *5*(6), 419.

124. Boyer, R. R. (1996). An overview on the use of titanium in the aerospace industry. *Materials Science and Engineering: A*, *213*(1-2), 103.

125. Williams, W. L. (1969). Development of structural titanium alloys for marine applications. *Ocean Engineering*, *1*(4), 375.

126. Gorynin, I. V. (1999). Titanium alloys for marine application. *Materials Science and Engineering: A*, *263*(2), 112.

127. Destefani, J. D. (1990). Introduction to titanium and titanium alloys.

128. Nyamekye, P., Golroudbary, S. R., Piili, H., Luukka, P., & Kraslawski, A. (2023). Impact of additive manufacturing on titanium supply chain: Case of titanium alloys in automotive and aerospace industries. *Advances in Industrial and Manufacturing Engineering*, *6*, 100112.

129. Takahashi, K., Mori, K., & Takebe, H. (2020). Application of titanium and its alloys for automobile parts. In *MATEC web of conferences* (Vol. 321, p. 02003). EDP Sciences.

130. Veiga, C., Davim, J. P., & Loureiro, A. J. R. (2012). Properties and applications of titanium alloys: a brief review. *Rev. Adv. Mater. Sci*, *32*(2), 133.

131. Jarosz, M., Grudzień, J., Kapusta-Kołodziej, J., Chudecka, A., Sołtys, M., & Sulka, G. D. (2020). Anodization of titanium alloys for biomedical applications. In *Nanostructured Anodic Metal Oxides* (pp. 211-275). Elsevier.

132. Rafieerad, A. R., Zalnezhad, E., Bushroa, A. R., Hamouda, A. M. S., Sarraf, M., & Nasiri-Tabrizi, B. (2015). Self-organized TiO_2 nanotube layer on Ti–6Al–7Nb for biomedical application. *Surface and Coatings Technology*, *265*, 24.

133. İzmir, M., & Ercan, B. (2019). Anodization of titanium alloys for orthopedic applications. *Frontiers of Chemical Science and Engineering*, *13*, 28.

134. Jáquez-Muñoz, J. M., Gaona-Tiburcio, C., Méndez-Ramírez, C. T., Baltazar-Zamora, M. Á., Estupinán-López, F., Bautista-Margulis, R. G., ... & Almeraya-Calderón, F. (2023). Corrosion of Titanium Alloys Anodized Using Electrochemical Techniques. *Metals*, *13*(3), 476

135. Dutta, B., & Froes, F. S. (2017). The additive manufacturing (AM) of titanium alloys. *Metal powder report*, *72*(2), 96.

136. Townsend, A., Senin, N., Blunt, L., Leach, R. K., & Taylor, J. S. (2016). Surface texture metrology for metal additive manufacturing: a review. *Precision Engineering*, *46*, 34.

137. Frazier, W. E. (2014). Metal additive manufacturing: a review. *Journal of Materials Engineering and performance*, *23*, 1917.

138. Lathabai, S. (2018). Additive manufacturing of aluminium-based alloys and composites. *Fundamentals of aluminium metallurgy*, 47-92.

139. Bahnini, I., Rivette, M., Rechia, A., Siadat, A., & Elmesbahi, A. (2018). Additive manufacturing technology: the status, applications, and prospects. *Int. J. Adv. Manuf. Technol. 97*, 147.

140. Bandyopadhyay, A., Zhang, Y., & Bose, S. (2020). Recent developments in metal additive manufacturing. *Curr. Opin. Chem. Eng*. *28*, 96.

141. Blakey-Milner, B., Gradl, P., Snedden, G., Brooks, M., Pitot, J., Lopez, E., Leary, M., Berto, F., & Du Plessis, A. (2021). Metal additive manufacturing in aerospace: A review. *Materials & Design*, *209*, 110008.

142. Sames, W. J., List, F. A., Pannala, S., Dehoff, R. R., & Babu, S. S. (2016). The metallurgy and processing science of metal additive manufacturing. *International materials reviews*, *61*(5), 315.

143. Bhavar, V., Kattire, P., Patil, V., Khot, S., Gujar, K., & Singh, R. (2017). A review on powder bed fusion technology of metal additive manufacturing. *Additive manufacturing handbook*, 251.

144. Singh, R., Gupta, A., Tripathi, O., Srivastava, S., Singh, B., Awasthi, A., Rajput, S. K., Sonia, P., Singhal, P., & Saxena, K. K. (2020). Powder bed fusion process in additive manufacturing: An overview. *Materials Today: Proceedings*, *26*, 3058.

145. Saboori, A., Gallo, D., Biamino, S., Fino, P., & Lombardi, M. (2017). An overview of additive manufacturing of titanium components by directed energy deposition: microstructure and mechanical properties. *Applied Sciences*, *7*(9), 883.

146. Svetlizky, D., Das, M., Zheng, B., Vyatskikh, A. L., Bose, S., Bandyopadhyay, A., Schoenung, J. M., Lavernia, E. J., & Eliaz, N. (2021). Directed energy deposition (DED) additive manufacturing: Physical characteristics, defects, challenges and applications. *Materials Today*, *49*, 271.

147. Yadroitsev, I., Gusarov, A., Yadroitsava, I., & Smurov, I. (2010). Single track formation in selective laser melting of metal powders. *Journal of Materials Processing Technology*, *210*(12), 1624.

148. Yadroitsev, I., & Smurov, I. (2011). Surface morphology in selective laser melting of metal powders. *Physics Procedia*, *12*, 264.

149. Yap, C. Y., Chua, C. K., Dong, Z. L., Liu, Z. H., Zhang, D. Q., Loh, L. E., & Sing, S. L. (2015). (2015) Review of selective laser melting: Materials and applications. *Appl. Phys. Rev. 2*(4), 041101.

150. Aboulkhair, N. T., Simonelli, M., Parry, L., Ashcroft, I., Tuck, C., & Hague, R. (2019) 3D printing of Aluminium alloys: Additive Manufacturing of Aluminium alloys using selective laser melting. *Prog. Mater. Sci. 106*, 100578.

151. Gerday, A. F. (2009). Mechanical behavior of Ti-5553 alloy. Modeling of representative cells.

152. Schwab, H., Palm, F., Kühn, U., & Eckert, J. (2016). Microstructure and mechanical properties of the near-beta titanium alloy Ti-5553 processed by selective laser melting. *Materials & Design*, *105*, 75.

153. Sabol, J. C., Pasang, T., Misiolek, W. Z., & Williams, J. C. (2012). Localized tensile strain distribution and metallurgy of electron beam welded Ti–5Al–5V–5Mo–3Cr titanium alloys. *Journal of Materials Processing Technology*, *212*(11), 2380.

154. Matsumoto, H., Kitamura, M., Li, Y., Koizumi, Y., & Chiba, A. (2014). Hot forging characteristic of Ti–5Al–5V–5Mo–3Cr alloy with single metastable β microstructure. *Materials Science and Engineering: A*, *611*, 337.

155. Kar, S. K., Ghosh, A., Fulzele, N., & Bhattacharjee, A. (2013). Quantitative microstructural characterization of a near beta Ti alloy, Ti-5553 under different processing conditions. *Materials characterization*, *81*, 37.

156. Yang, H. H., & McCreery, R. L. (2000). Elucidation of the mechanism of dioxygen reduction on metal-free carbon electrodes. *Journal of the Electrochemical Society*, *147*(9), 3420.

157. Xu, J., Huang, W., & McCreery, R. L. (1996). Isotope and surface preparation effects on alkaline dioxygen reduction at carbon electrodes. *Journal of Electroanalytical Chemistry*, *410*(2), 235.

158. Tammeveski, K., Kontturi, K., Nichols, R. J., Potter, R. J., & Schiffrin, D. J. (2001). Surface redox catalysis for O2 reduction on quinone-modified glassy carbon electrodes. *Journal of Electroanalytical Chemistry*, *515*(1-2), 101.

159. Yano, T., Tryk, D. A., Hashimoto, K., & Fujishima, A. (1998). Electrochemical behavior of highly conductive boron-doped diamond electrodes for oxygen reduction in alkaline solution. *Journal of the Electrochemical Society*, *145*(6), 1870.

160. Byeon, A., Yun, W. C., Kim, J. M., & Lee, J. W. (2023). Non-precious Metal Catalysts for Two-Electron Oxygen Reduction Reaction. *ChemElectroChem*, *10*(17), e202300234.

CHAPTER 2. INHIBITION OF THE OXYGEN REDUCTION KINETICS ON CARBON FIBER REINFORCED POLYMER COMPOSITES TROUGH ELECTROCHEMICALLY ASSISTED DIAZONIUM SURFACE MODIFICATION – IMPACTS ON THE GALVANIC CORROSION OF COUPLED AA2024-T3 ALUMINUM ALLOYS

Chapter adapted from *J. Electrochem. Soc. 169*(7) 071501 (2022).© The Electrochemical Society. Reproduced with permission. All rights reserved.

Article: Isuri N. Dammulla and Greg M. Swain. *Inhibiting the Oxygen Reduction Kinetics on Carbon Fiber Epoxy Composites Through Diazonium Surface Modification-Impacts on the Galvanic Corrosion of Coupled Aluminum Alloys.*

2.1 INTRODUCTION

Aluminum alloys are one of the most popular metal alloys and have been used in the aerospace industry since 1930 owing to their low density, high strength, and corrosion resistance.[1-4] Although a plethora of aluminum alloys exist, only a few such as AA 2024, 6061 and 7075 are most utilized as structural components of aircraft. To increase fuel efficiency by reducing the aircraft weight, the aerospace industry is now employing carbon fiber reinforced polymer (CFRP) composites in military (ex: F35, Typhoon) and civilian (ex: Boeing 787, Airbus A380) aircraft.[5] The desirable mechanical properties of CFRP composites include high strength-to-weight ratio, high fatigue resistance, high corrosion resistance, and high damage tolerance.[6-9] The use of CFRP composites as a structural component of aircraft wings, fuselages, tails, and doors also minimizes the number of costly inspections over the aircraft's lifespan.[10] CFRP composite parts are commonly joined to aluminum alloy structural components via mechanical fastening (e.g. bolting).[11]

When a CFRP composite and an aluminum alloy become electrically connected through a layer of condensed moisture, a galvanic couple is created with the more noble exposed carbon fibers of the composite acting as a cathode supporting the reduction of dissolved oxygen. The less

noble aluminum alloy will become the anode and undergo oxidation at an accelerated rate – so-called galvanic corrosion.[12-14] This corrosion can be catastrophic since it would greatly reduce the mechanical strength of the aluminum alloy and can lead to massive safety risks if left unattended. The general practice to mitigate the galvanic corrosion of aluminum alloys in aircraft structures involves the elimination of direct contact between the two materials by inserting insulation layers [15-17] and application of coating systems on the alloy surface.[18-20] In principle, the rate of galvanic corrosion can also be reduced by decreasing the rate of the oxygen reduction reaction (ORR) at the exposed carbon fibers of the CFRP composite. We hypothesize that the ORR can be reduced by blocking the active sites on exposed carbon fibers for O_2 chemisorption, the proposed first step of oxygen reduction reaction (ORR)[21-23], by surface modification.

The electrochemically-assisted reduction of aryl diazonium salts is a versatile and well-established surface modification method for carbon materials first introduced by Savéant *et al.* in the early 1990s.[24] The reduction of aryl diazonium salts leads to covalent attachment of aryl radicals onto the carbon surface. Grafting of substituted aryl moieties on a wide variety of carbon substrates including glassy carbon (GC),[24, 25] highly ordered pyrolytic (HOPG),[26,27] carbon fibers,[28,29] porous graphitic carbon (PGC),[30] screen printed carbon films,[31,32] pyrolyzed photoresist films (PPF),[33,34] carbon black,[35] carbon nanotubes,[36,37] and boron-doped diamond (BDD)[38] by employing diazonium chemistry has been described in previous reports. This field has been nicely reviewed by Downard.[40] Several studies have investigated the influence of diazonium-derived monolayers on interfacial electron transfer rates of solution species. Organic adlayers generated on carbon surfaces by this derivatization method exhibit barrier properties by acting as an insulating spacer that separates the redox molecule from the electrode surface.[39-41] More importantly, glassy carbon electrodes electrografted by this method with phenyl, 4-methylphenyl,

naphthyl and anthracenyl adlayers have proven to inhibit the oxygen reduction reaction by influencing the electron transfer process.[22,42]

The work reported herein is a part of an effort to devise an approach to attenuate the galvanic corrosion of aluminum alloys coupled to CFRP composites by inhibiting the cathodic oxygen reduction reaction kinetics. In the present work, we demonstrate the generality of the method by reacting diversely substituted phenyl radicals and other aryl radicals with CFRP composites and the influence of diazonium surface modification on the reduction of dissolved oxygen.

2.2 EXPERIMENTAL METHODS

Chemical and Reagents. Acetonitrile (Sigma Aldrich) was distilled (1x) and stored over activated 5 Å molecular sieves prior to use. Tetrabutylammonium tetrafluoroborate (NBu_4BF_4), 4-nitrophenyl diazonium tetrafluoroborate, potassium chloride (KCl), sodium sulfate (Na_2SO_4), and potassium ferrocyanide ($K_4Fe(CN)_6$) were all purchased from a commercial supplier (Sigma Aldrich) and used as received. Turco 6849 (20% v/v, Henkel Corp., Madison Heights, MI) was the commercial degreasing solution used. Turco Liquid Smut-Go (20% v/v, Henkel Corp., Madison Heights, MI) served as the commercial deoxidizing solution. Bonderite T-5900 RTU (Henkel Corp., Madison Heights, MI) was the commercial TCP coating bath studied. All aqueous solutions were prepared with ultrapure water (> 17 MΩ-cm) from a Barnstead E-Pure water purification system.

Carbon Fiber Reinforced Epoxy (CFRP) Composite Electrodes. A standard airframe composite panel (AS4/3501-6) was provided courtesy of the Polymer and Composites Division at the Naval Air Systems Command (Patuxent River, MD). The panel was a cross-ply [0/90]4s laminate, which is useful for resin-dominated tests of compression, flexure, and shear. It was prepared with an intermediate modulus PAN carbon fiber and a toughened epoxy prepreg (3501-6) from Hexcel.

The layup was an orthogonally oriented ply (0/90-degree direction 4 times). A symmetric layup at the mid-plane was used to keep the composite from warping due to differences in thermal expansion coefficients of the epoxy and the carbon. The total layup was 16 plys (0/90/0/90/0/90/0/90/90/0/90/0/90/0/90/0). A phenolic sizing material was applied to the carbon fibers before preparing the composite in order to promote stronger bonding with the epoxy matrix. The composite thickness was 0.25 cm. The CFRP composite panels were cut into 2.4 cm × 1.8 cm pieces and the electrodes were prepared as shown in Figure 2.1 by inserting a copper wire into a hole drilled on the topside of the CFRP specimen for electrical connection with the carbon fibers. The composite electrode design was validated in a previous work by verifying that the carbon fibers on the CFRP composite are electrically connected to the copper wire current collector at the top side through electrodeposition of Ag particles.[43] The edge of the composite is where the exposed and electrochemically active carbon exists. The geometric area of the exposed edge (a single edge) used in the electrochemical measurements was 0.45 cm^2. Currents and surface coverages were normalized to this area.

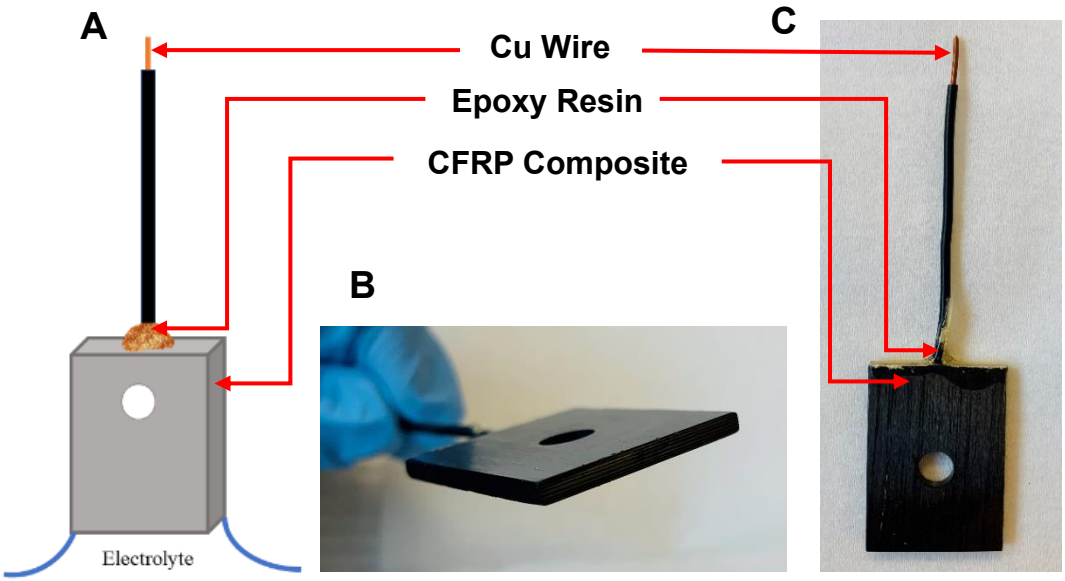

Figure 2.1. (A) Diagram of the CFRP composite electrode configuration for the electrochemical tests. One polished and cleaned edge of the composite was exposed to the electrolyte solution and served as the working electrode. (B) Photograph of the actual CFRP specimen.

Pretreatment of CFRP Composite Electrodes. The edge of the CFRP composite electrode was first abraded on a wet P1500 grit aluminum oxide sandpaper for 3 minutes. This was followed by a 10-minute ultrasonic cleaning in ultrapure water. The composite edge was then mechanically polished with decreasing grades of alumina powder (1, 0.3, and 0.05 μm) slurried in ultrapure water on separate felt polishing pads to smooth the surface. After each polishing step, the composite was rinsed with and ultrasonically cleaned in ultrapure water for 15 minutes to remove polishing residue. A final ultrasonic cleaning was then performed in pure acetonitrile for 10 minutes.

Surface Modification of CFRP Composite Electrodes. The surface modification was performed in an electrochemical-assisted mode using a three-compartment, three-electrode glass cell with a platinum (Pt) flag counter electrode, a silver quasi-reference electrode (AgQRE), and the pretreated CFRP composite working electrode. The aryldiazonium salts utilized in this study were (i) 4-nitrophenyldiazonium tetrafluoroborate (NP), (ii) 4-nitroazobenzene tetrafluoroborate (NAB) and (iii) 2-fluorenediaazonium tetrafluoroborate (FL) and are presented in Figure 2.2. The electrochemical surface modification of the exposed carbon fibers was performed by cyclic voltammetry in deaerated acetonitrile containing a solution of 5 mM of the diazonium salt dissolved in 0.1 M tetrabutylammonium tetrafluoroborate (NBu_4BF_4) supporting electrolyte. The applied potential was scanned from 0.6 to -0.5 V (vs Ag QRE) at 50 mV/s to electrochemically reduce NP and NAB and form the organic adlayer. In an effort to form a dense adlayer, 25 potential cycles were used. After the modification, the CFRP composite electrode was thoroughly rinsed with water and acetonitrile. The derivatized electrode was then placed in deaerated 0.1 M NBu_4BF_4 dissolved in acetonitrile and background cyclic voltammograms were recorded at 50 mV/s. These curves were compared with curves recorded for the composite electrode prior to derivatization. Raman spectroscopy was performed to confirm the presence of the adlayer.

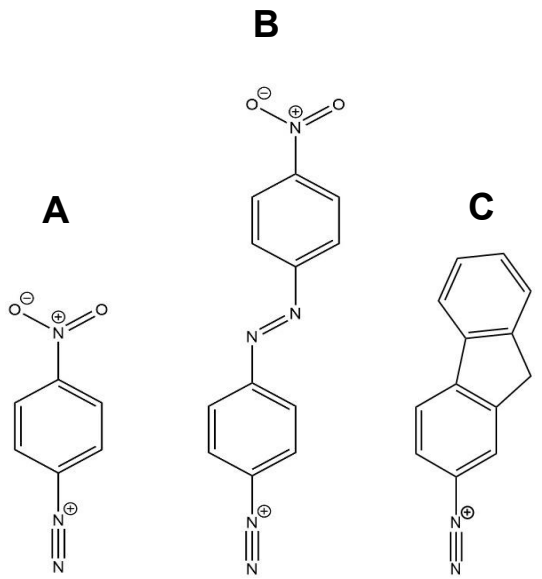

Figure 2.2. Chemical structures of the (A) 4-Nitrophenyl, (B) 4-nitroazobenzene and (C) 2-fluorene diazonium cations.

Material Characterization. Scanning electron microscopy was performed at the Center for Advanced Microscopy (MSU) using a JSM-6610LV (JEOL USA) general purpose microscope. Accelerating voltages used were between 10-15 kV with a working distance 10 – 13 mm. Raman spectroscopy was performed using a inVia™ confocal Raman microscope (Renishaw). The instrument consisted of a confocal microscope connected to a continuous wave, diode-pumped solid-state laser (100 mW with 10 mW applied at the sample) having a fundamental emission at 532 nm. The CFRP composite specimen was positioned under the laser light using a motorized stage. The stage position was controlled, and spectral data acquired with instrument's software (WiREInterface). This software allows for control of the laser power, integration time, spectral range covered, and stage positioning for mapping a sample. A Leica (50×/0.75 N.A.) objective lens was used for focusing the excitation light and collecting the scattered radiation. A notch filter was used to remove the Rayleigh scattered laser light. Each spectrum was acquired using a 1 μm spot size with an integration time of 10 s. Each spectrum presented represents the average of 5 spectral

acquisitions at each point. An 1800 lines mm^{-1} holographic grating was used for separating the Raman scattered light into its component wavelengths.

Electrochemical Measurements. All the electrochemical measurements were performed in a three-compartment, three-electrode glass cell with a platinum (Pt) flag counter electrode, a silver chloride reference electrode (Ag/AgCl, 4M KCl) and the chemically modified CFRP composite working electrode. The CFRP electrode preparation and electrochemical measurements with it were described elsewhere.[43] Only the edge opposite of that of the electrical contact was utilized in these measurements. The electrochemical measurements were made using a computer-controlled workstation (Model 900, CH Instruments, Austin, TX). Cyclic voltammograms were recorded in a 1M KCl solution at 50 mV/s to study the influence of diazonium modification on the magnitude of the background charging current and capacitance. Open circuit potential (OCP) measurements were recorded for at least 30 min until stabilization. Electrochemical impedance spectroscopy measurements (EIS) measurements were then performed at the OCP from 10^6 to 10^{-2} Hz (10 mV sine wave) in naturally aerated 0.5 M Na_2SO_4. The blocking properties of the NP and NAB adlayers were investigated by cyclic voltammetry in naturally aerated 0.5 mM $K_4Fe(CN)_6$ + 0.5 M Na_2SO_4. Some electrochemical measurements were made in naturally aerated 0.5 M Na_2SO_4 (pH 5-6) at room temperature to assess the impact of the surface functionalization on the background voltametric current and oxygen reduction reaction kinetics.

Aluminum Alloy Preparation. Wrought aluminum alloy 2024-T3 was obtained as a 1 mm-thick sheet (www.onlinemetals.com) and cut into 5.5 cm × 3.6 cm pieces. The specimens were mechanically abraded with a 1500 grit sandpaper for 4 minutes and ultrasonically cleaned in ultrapure water for 20 minutes. The specimens were then fine polished with 0.3 μm alumina powder (Buehler) slurried in ultrapure water on a felt polishing pad for 4 minutes and ultrasonically

cleaned in ultrapure water for another 20 minutes to remove polishing debris. This was followed by a degreasing step at 55 °C for 10 minutes in Turco 6849 (Henkel) alkaline degreaser. The specimens were then gently rinsed with flowing city tap water for 2 minutes. The specimens were then deoxidized by immersing in Turco Liquid Smut-Go NC (Henkel) at room temperature for 2 minutes. This will be followed by another 2-minute tap water rinse. The alloy specimens were then surface treated with trivalent chromium process (TCP) conversion coating by immersion in Alodine T5900 (Henkel) at room temperature for 10 minutes. Finally, the coated specimens were immersion rinsed in a beaker full of city tap water for 2 minutes, a beaker of ultrapure water for 30 seconds, and air dried for at least 12 hours in a covered container before further use.

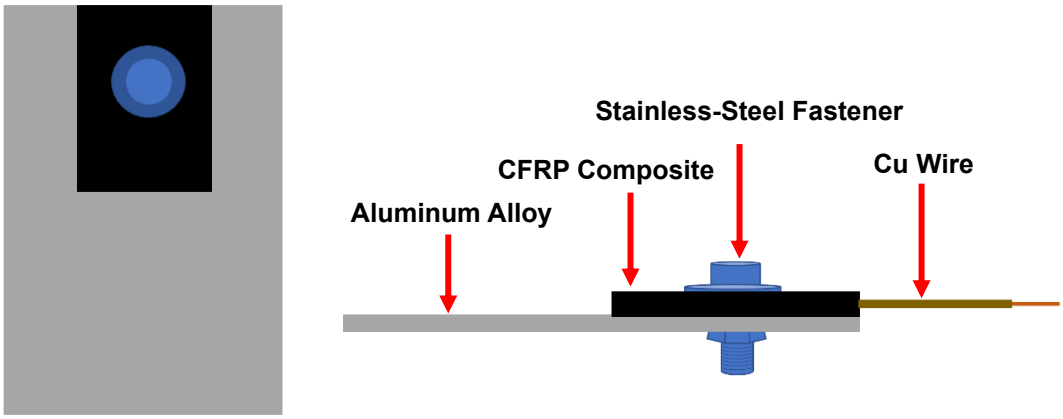

Figure 2.3. Configuration of the joined aluminum alloy-CFRP composite specimen (A) top view (B) side view. The geometric ratio of the cathode to anode exposed areas was 0.3 (5.3 cm^2 for the CFRP and 19.8 cm^2 for the aluminum alloy).

Neutral Salt Spray Testing (ASTM B117) Coated aluminum alloy specimens were joined with diazonium modified or unmodified CFRP composite specimens, as shown in Figure 2.3, using a stainless-steel fastener. The composites were derivatized by immersing the specimens (bottom and two sides) and applying 25 potential cycles in a solution of 5 mM of the diazonium salt dissolved in 0.1 M tetrabutylammonium tetrafluoroborate (NBu_4BF_4) supporting electrolyte. In this way, the three polished and cleaned edges, as well as the fastener hole, were functionalized at the same

time. The top side of the composite specimens with the attached Cu wire was not derivatized. The stainless-steel fastener threads were covered with Teflon tape to prevent electrical connection with the hole wall. The bolt head and nut were covered with a commercial siliconized sealant (DAP KWIK SEAL ULTRA) to repel moisture and electrically isolate the metal from the solution mist. The back side of the aluminum alloy specimens was covered with corrosion tape (Corrosion-Protection, 3M™, Scotchrap™) so that only the front surface and the edges were exposed to the salt fog environment.

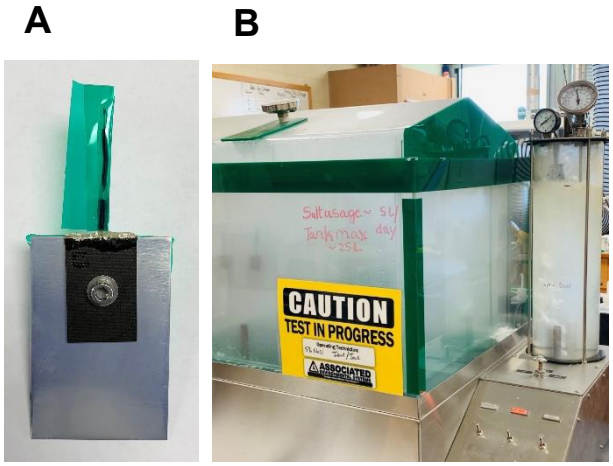

Figure 2.4. Photographs of (A) a joined aluminum alloy-CFRP composite specimen couple and (B) the salt spray chamber (Associated Environmental Systems-MX 9204).

Mechanically fastened aluminum alloy-CFRP composite specimens (Figure 2.4A), joined with a torque of 45 lb.-in, were exposed to a continuous salt fog generated with 5 wt. % NaCl at 35 ± 1 °C in a commercial salt spray chamber (Figure 2.4B, Associated Environmental Systems-MX 9204) for 7 days according to ASTM B117 (Standard Practice for Operating Salt Spray (Fog) Apparatus). At the end of the 7-day test period, the coupled specimens were removed, disassembled, and rinsed thoroughly with and ultrasonically cleaned in ultrapure water for 30 minutes to remove salt deposits. They were then ultrasonically cleaned in concentrated HNO_3 for 10 minutes to dissolve corrosion product, dried thoroughly with N_2 gas, and weighed. Ultrasonic

cleaning in HNO_3 was repeated until the mass change of a specimen was negligible ($\leq$ 0.002 g).[44] This was followed by a through rinsing in ultrapure water and drying under a stream of N_2 gas prior to any weight measurement or additional analysis. The cleaned specimens were analyzed by digital optical and scanning electron microscopy to determine the surface texture, pit dimensions, and other corrosion damage.

Corrosion Damage Evaluation. The following scale, developed by the U.S. Army Material Command, was used to grade the alloy specimens after the neutral salt-spray exposure: Stage 0 – shows no visible corrosion; Stage 1 – sample discoloration and staining; Stage 2 – loose isolated rust or corrosion product and early stage pitting of the surface along with minor etching; Stage 3 – more extensive rust or corrosion product, minor etching, pitting and more extensive surface damage; Stage 4 – extensive rust or corrosion product formation, extensive etching, blistering, deadhesion and pitting that has progressed to the point where the life of the specimen has been affected.[45]

2.3 RESULTS

Material Characterization. Figure 2.5 presents SEM micrographs of the abraded and polished composite electrode edge prior to derivatization. Micrographs at two different magnifications are presented, 140× (Figure 2.5A) and 750× (Figure 2.5B), showing the orthogonal arrangement of carbon fiber bundles in the laminate. The diameter of the carbon fibers is ca. 6 μm. Full polishing followed by ultrasonic cleaning produced a clean surface suitable for electrochemically assisted surface modification (Figure 2.5C and D). The surface is devoid of any detectable polishing debris (e.g., alumina powder or carbon particles) meaning that the ultrasonic cleaning in ultrapure water and acetonitrile is effective at cleaning the surface. Surface debris, if present, would interfere with the surface modification. Previous work revealed a similar morphology of the CFRP composite

edges.[50]

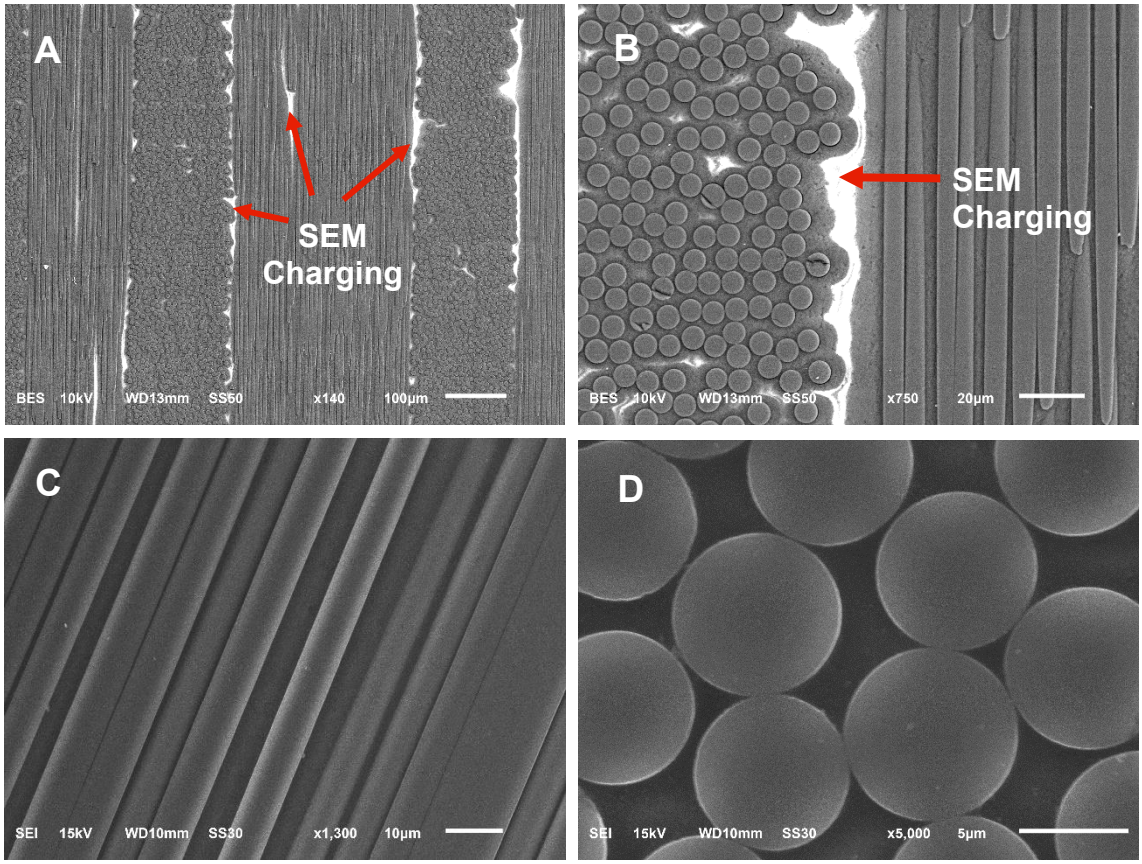

Figure 2.5. Backscattered electron SEM micrographs of the CFRP composite edge showing the orthogonal arrangement of carbon fiber bundles in the laminate at (A) 140×, (B) 750× magnifications. Higher magnification secondary electron SEM micrographs showing regions of the composite edge after wet abrading with P1500 grit aluminum oxide**,** polishing with decreasing grades of alumina powder, and ultrasonic cleaning in ultrapure water where the cylindrical carbon fibers (C) and the distal ends (D) are exposed.

A Raman spectrum of the carbon fibers on a polished and unmodified CFRP composite edge is shown in Figure 2.6. The Raman spectrum was obtained on a region of the composite edge where the cylindrical carbon fibers were exposed. Raman spectral features are sensitive to the microstructure of the carbon.[53-56] The a-and c-axis coherence lengths, L_a and L_c, as well as the interlayer d_{002} spacing all affect the spectral features.[53,55] The spectrum for highly ordered pyrolytic graphite (HOPG; single crystal sp^2-bonded carbon) consists of a single narrow peak at *ca.* 1580 cm^{-1}.[54] This is the so-called G-band with E_{2g} symmetry and arises from the in-plane stretching of

the C−C bonds of the aromatic rings (*i.e.*, lattice vibrational mode). As the amount of microstructural disorder in HOPG increases (*i.e.*, the size of the graphite crystallites decreases (< 1000 Å)), the Raman intensity increases for a so-called D-band or A_{1g} mode at *ca.* 1350 cm^{-1}. The D band corresponds to scattering from local defects or microstructurally disordered regions.[53-56]

A linear relationship between the 1350 cm^{-1} intensity and increasing values of the quantity, $1/L_a$, is well established.[53,55] This is reflective of the decreased microcrystallite size (*i.e.*, increased microstructural disorder). This A_{1g} vibrational mode becomes active near crystallite edges or defects, as discussed by Tuinstra and Koenig.[53] The Raman spectrum for the CFRP carbon fibers presented in Figure 2.6 consists of two distinct peaks at 1355 cm^{-1} and 1590 cm^{-1}. The ratio of the D/G band intensities is 0.28 indicating that the carbon fibers are of intermediate modulus with a relatively low faction of exposed graphitic edge plane (*i.e.*, a more graphitized exterior microstructure).

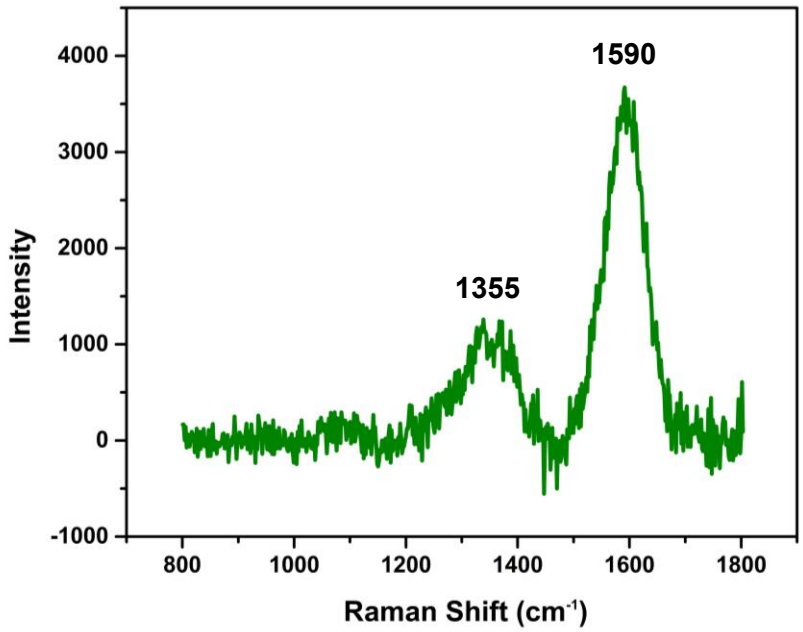

Figure 2.6. First-order Raman spectrum for the carbon fibers exposed on an abraded and polished CFRP edge.

Surface Functionalization. Three diazonium salts were used to modify the CFRP composite edges, NP and NAB. Both molecular structures are presented in Figure 2.2. The diazonium surface modification is based on the reductive formation of a para-substituted phenyl radical followed by covalent attachment with radical sites on the carbon surface according to the general reaction scheme:

$$X\text{-}C_6H_4N_2^+ + e^- \rightarrow X\text{-}C_6H_4\bullet + N_2 \qquad (1)$$

$$X\text{-}C_6H_4\bullet + CF \rightarrow CF\text{-}C_6H_4\text{-}X \qquad (2)$$

in which X is the functional group in the para position on the phenyl ring (e.g., NO_2 or nitroazobenzene) and CF is the exposed carbon fiber surface.

Figure 2.7 shows typical cyclic voltammograms recorded during the reduction of 4-nitrophenyl diazonium tetrafluoroborate (Figure 2.7A), 4-nitroazobenzene diazonium tetrafluoroborate (Figure 2.7B) and 2-fluorene diazonium tetrafluoroborate (Figure 2.7C) salts, all dissolved in acetonitrile containing 0.1 M NBu_4BF_4. The solution was deaerated with a 15-minute N_2 purge prior to the derivatization. The CFRP edge was abraded and polished, as described above, prior to derivatization. A well-defined, irreversible reduction peak is seen at -0.1 V for 4-nitrophenyl diazonium, at 0.1 V for 4-nitroazobenzene diazonium and at -0.2 V for 2-fluorene diazonium on the first scan, which is attributed to the $1e^-$ reduction of the aryl diazonium molecule to the corresponding aryl radical.[28-31,57-59] The potential at which the reduction of each aryldiazonium precursor occurs depends on the stability of the aryl radical product. The charge passed during the first scan is largest and progressively decreases with cycle number. In other words, the irreversible reduction peak disappears after the first scan. This reflects an inhibition of the electron transfer reaction due to surface passivation that follows from the attachment of nitrophenyl (NP), nitroazobenzene (NAB), and fluorene (FL) molecules on the exposed carbon

fibers.[28-31,57-59]

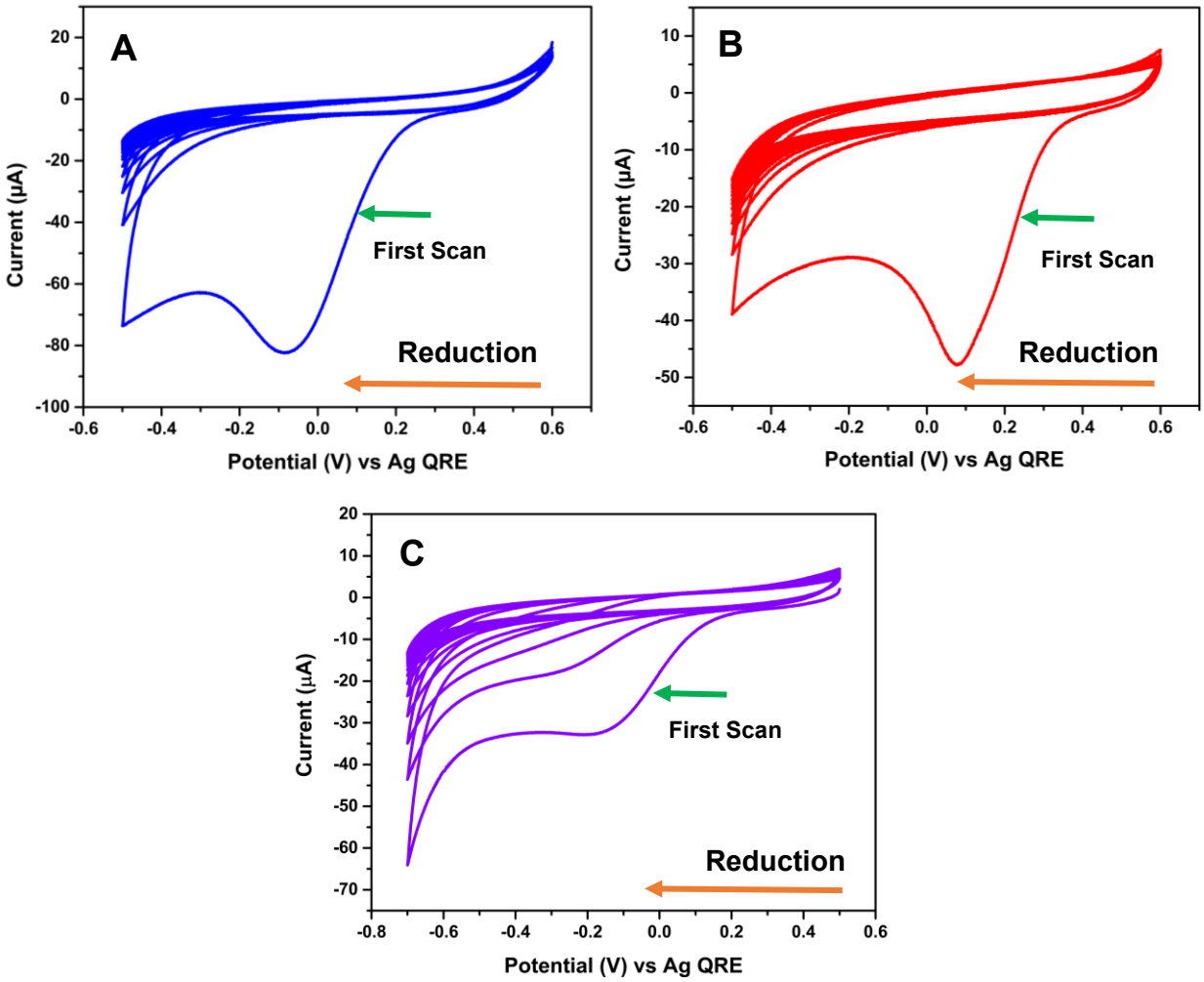

Figure 2.7. Repetitive cyclic voltammetric *i-E* curves recorded for a CFRP composite electrode edge in deaerated acetonitrile + 0.1 M NBu_4BF_4 containing (A) 5 mM 4-nitrophenyldiazonium tetrafluoroborate (NP), (B) 5 mM 4-nitroazobenzenediazonium tetrafluoroborate (NAB) and (C) 5 mM 2-fluorenediazonium tetrafluoroborate. Scan rate = 50 mV/s. Total potential cycles = 25.

Prior to grafting the NP, NAB and FL groups, the CFRP composite edge was pretreated by performing a few cyclic voltammetric scans over the same potential range in a deaerated solution containing only the solvent, acetonitrile, and the supporting electrolyte, NBu_4BF_4. These observations point to the covalent attachment of the para-substituted aryl radicals (AR) onto the carbon surface. The success of carbon surface derivatization hinges upon the fact that the aryl radicals produced by the above reaction are generated in the interfacial region and can immediately

react with the surface. The results observed for the CFRP are consistent with what has been previously reported for glassy carbon,[28] highly oriented pyrolytic graphite[30] and carbon fibers.[33] For example, it has been reported that the electrochemical reduction of nitrophenyl or other substituted phenyl diazonium molecules leads to a monolayer film of substituted phenyl groups on the surface[28,30,57,58] and that the binding is non-selective for basal or edge plane sites on the carbon surface[28,45,57]. Multilayers can also be formed depending on the electrodeposition conditions employed for the derivatization.[59-61]

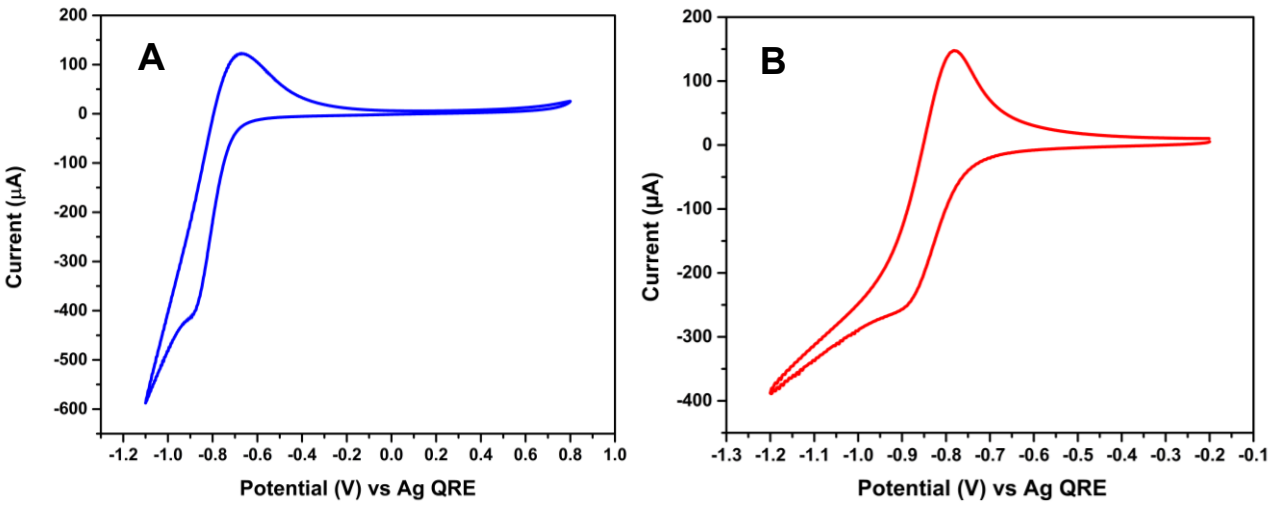

Figure 2.8. Cyclic voltammetric *i-E* curves of a CFRP composite electrode modified with (A) 4-nitrophenyl diazonium and (B) 4-nitroazobenzene diazonium adlayers in acetonitrile + 0.1 M NBu_4BF_4. Scan rate = 50 mV/s. Adlayers were formed using 25 potential cycles.

The electrochemically active admolecule coverage can be determined by recording cyclic voltammetric *i-E* curves for the modified surface in the pure electrolyte solution. Figure 2.8A and B present representative curves for (A) NP- and (B) NAB- modified CFRP surfaces. The measurements were made in deaerated 0.1 M NBu_4BF_4 in acetonitrile. The curves for both adlayers reveal a reduction peak prior to the onset of solvent/electrolyte reduction and a corresponding oxidation peak. The redox couple is the one-electron reduction of the nitro group to the radical anion and oxidation back to the neutral nitro group ($R\text{-}NO_2 + e^- \rightarrow R\text{-}NO_2^{\bullet -}$).[57] The reduction peak

potential for the NP- and NAB-modified CFRP specimens is -0.9 V. The oxidation peak potentials are -0.8 to -0.7 V. The oxidation peak current increased linearly with the scan rate consistent with a surface-confined redox species ($R^2 = 0.9954$).

Integration of the oxidation peak charge yields the electrochemically active surface coverage, $Q = nFAN$, where Q is the peak area or charge in coulombs, n is the number of electrons transferred per molecule, F is the Faraday constant, A is the geometric area of the composite edge in cm^2 and N is the number of moles electrolyzed. The results from integration of the oxidation peaks in Figure 2.8 reveal apparent surface coverages of 14.2 ± 1.7 nmol/cm^2 for the NP and 8.7 ± 1.8 nmol/cm^2 for the NAB adlayers. These surface coverage values are reported as mean ± std. dev. for three composite specimens. The theoretical monolayer coverages of NP and NAB admolecules have been calculated for the case of close packing on a flat surface. Assuming bonding at the edge of the phenyl ring, the theoretical coverages are 1.2 nmol/cm^2 and 1 nmol/cm^2, respectively, for NP and NAB.[57,62] Both calculated surface coverages on the modified CFRPs are larger than the theoretical monolayer coverage. The is because the geometric area of the CFRP edge used to normalize the data is significantly lower than the true carbon fiber surface area. Another possible explanation is the formation of multilayers because of scanning the potential from 0.6 to -0.5 V (vs Ag QRE) at 50 mV/s for 25 potential cycles during the derivatization.[59-61] Control measurements involving immersion of a CFRP edge in the diazonium solution for an equivalent time to that used for the electrochemically assisted derivatization (ca. 5-10 min) revealed no evidence for surface adsorption or any NO_2 group electrochemical activity. This observation indicates that the aryl adlayers are in fact grafted to and not just physisorbed on the surface. The grafted adlayers are extremely stable and difficult to remove from the CFRP surface, like other diazonium modified carbon electrodes.[33,40,63-65] Rinsing and ultrasonic cleaning of the

composites for up to 30 min in acetonitrile produced no change in the cyclic voltammetric response (e.g., Figure 2.8) for the modified CFRP. The adlayer was also stable during a 7-day neutral salt spray exposure, as discussed below. The only way to effectively remove the adlayer is by mechanical abrading and polishing. It should be noted that the admolecule coverage for FL-modified CFRP composite surfaces cannot be determined this way due to the absence of the electrochemically active -NO_2 groups in the structure.

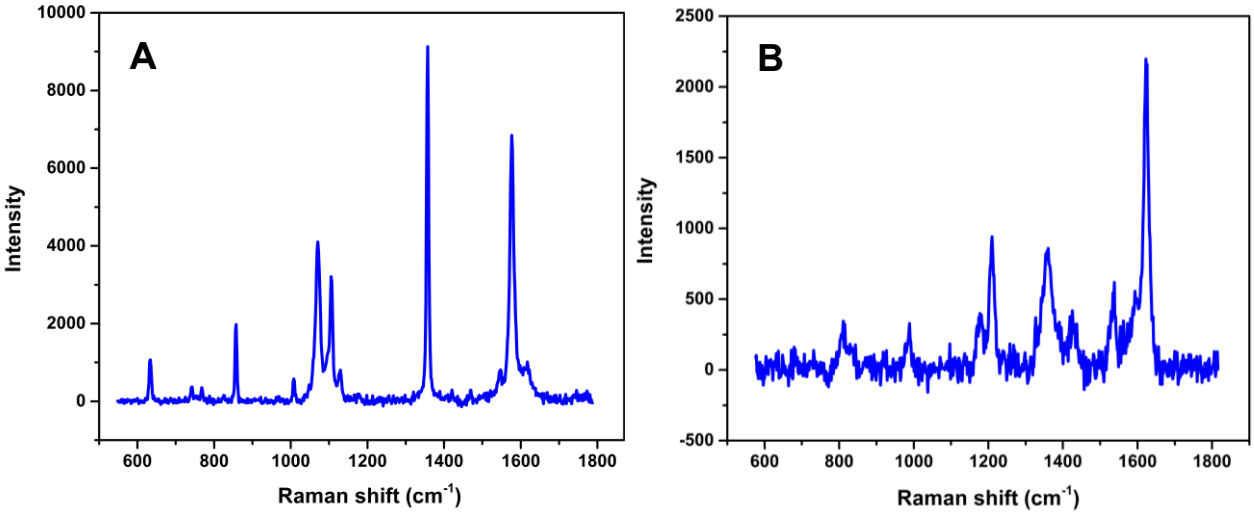

Figure 2.9. Visible Raman spectra of (A) solid 4-nitrophenyl diazonium salt and (B) a 4-nitrophenyl-modified CFRP composite edge. The spectrum in B has been background corrected using the spectral features for the unmodified carbon.

Raman spectroscopy was also used to confirm the presence of the adlayer on the CFRP surface. The spectrum of a 4-nitrophenyl diazonium tetrafluoroborate salt particle and a CFRP surface modified with an NP adlayer are presented in Figure 2.9. The Raman bands were assigned to vibrational modes based on assignments reported in the literature.[57,62] The Raman band positions and assignments for the nitrophenyl solid and NP adsorbate are listed in Table 2.1. In some cases, the adsorbate bands were downshifted relative to the nitrophenyl diazonium solid, and others were upshifted. In general, the band positions were reproducible for the modified CFRP specimens. The spectral features are largely conserved between those of the reference salt and the modified CFRP

surface. Primary peaks seen are for the phenyl ring C=C stretching mode at 1610 cm^{-1}, the NO_2 symmetric stretching mode at 1360 cm^{-1}, aromatic ring C-H bending modes at 988, 1180 and 1210 cm^{-1}, and an NO_2 bending mode at 811 cm^{-1}. These spectra features were not detected on a CFRP surface simply immersed in the diazonium solution for a time like that needed for the electrochemically assisted derivatization and rinsed in acetonitrile. Taken together, the results confirm the grafting of the NP adlayer on the carbon fiber surfaces.

Figure 2.10 presents Raman spectra for 4-nitroazobenzene diazonium tetrafluoroborate salt and a CFRP surface modified with a NAB adlayer. The Raman band positions and assignments for the nitroazobenzene solid and the NAB adsorbate are listed in Table 2.1.[57,62] In some cases, the adsorbate bands were downshifted relative to the nitroazobenzene diazonium solid, and others were upshifted. Primary peaks seen are for the phenyl ring C=C stretching mode at 1598 cm^{-1}, the N=N stretching mode at 1450 cm^{-1}, the phenyl-NN stretch at 1130 cm^{-1}, and the NO_2 symmetric stretching mode at 1340 cm^{-1}. Taken together, the Raman spectra for both the NP and NAB modified surfaces are consistent with covalently bonded organic adlayers on the CFRP surface.

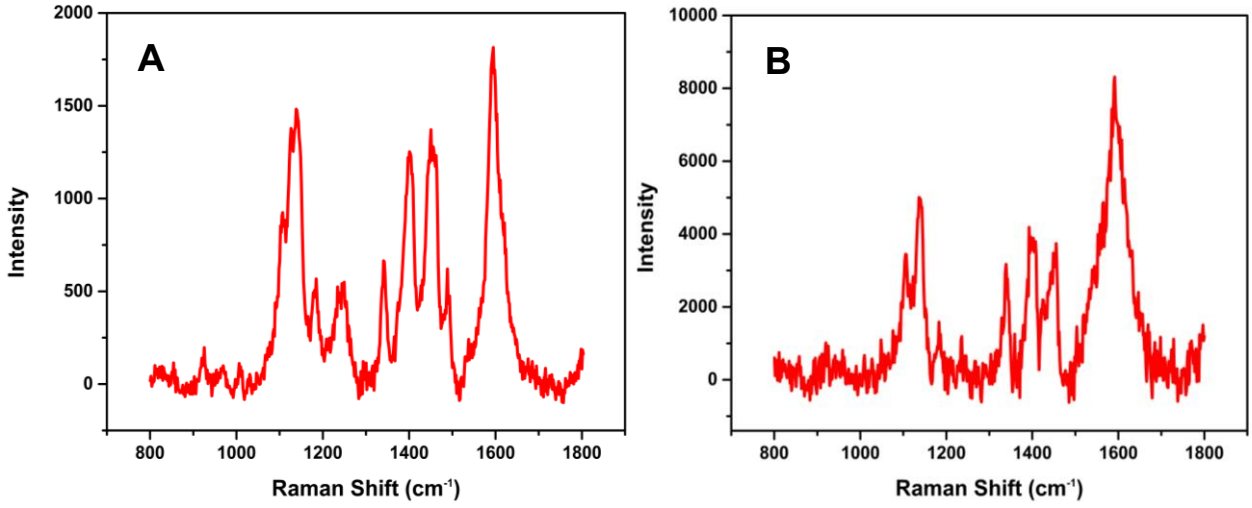

Figure 2.10. Visible Raman spectra of (A) solid 4-nitroazobenzene diazonium salt and (B) a 4-nitroazobenzene-modified CFRP composite edge. The spectrum in B has been background corrected using the spectral features for the unmodified carbon.

Raman spectra for 2-fluorene diazonium tetrafluoroborate salt and a CFRP surface modified with a FL adlayer are shown in Figure 2.11. The Raman spectrum of 2-fluorene diazonium (Figure 2.11A) salt exhibits Raman peaks for the -CH_2 valence and deformation vibrations at 1471 cm^{-1} and 1494 cm^{-1}, the -CH_2 hydrogen bending mode at 1178 cm^{-1}, and the bending of benzene hydrogen at 1149 and 1184 cm^{-1}. Additionally, the Raman bands between 800 and 1100 cm^{-1} can be attributed to the C-C vibrations and the Raman band at ~1229 cm^{-1} originates from the vibration of the direct C-C linkage between the two benzene rings. All these prominent Raman peaks are present on the Raman spectrum of the FL-modified electrode (Figure 2.11B) confirming the formation of a FL adlayer on the carbon fiber surface. The absence of the Raman peak at ~1540 cm^{-1} corresponding to the N=N stretching mode is ascribed to the elimination of N_2 during the reduction of the diazonium cation.

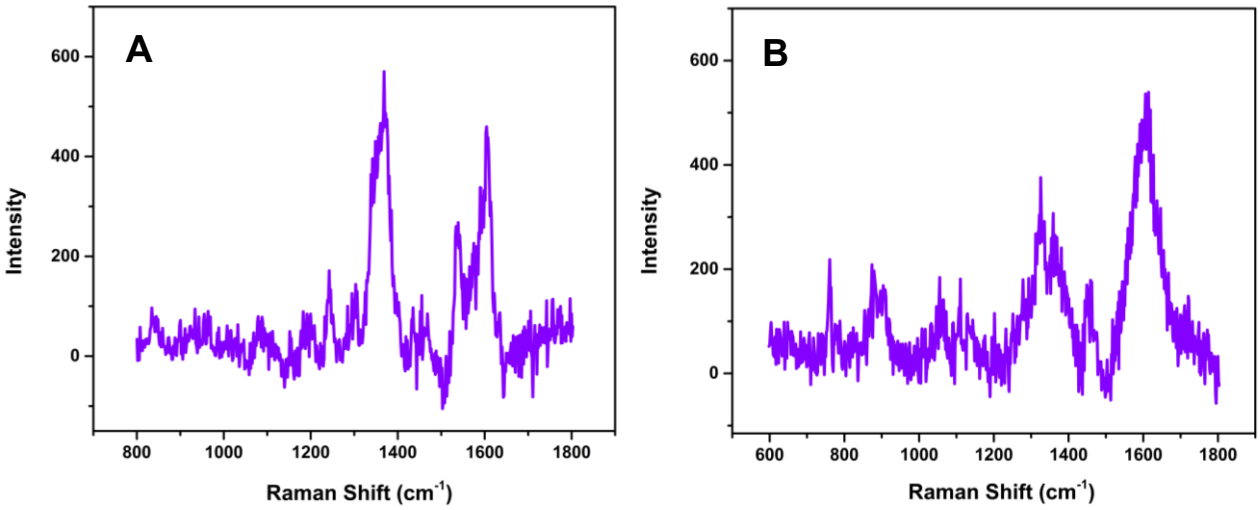

Figure 2.11. Visible Raman spectra of (A) solid 2-fluorene diazonium salt and (B) a 2-fluorene-modified CFRP composite edge. The spectrum in B has been background corrected using the spectral features for the unmodified carbon.

Table 2.1. Assignment of the Raman spectral bands observed for the diazonium-modified CFRP specimens.[57,62.]

Solid NP Raman shift /cm^{-1}	**NP Modified Raman shift /cm^{-1}**	**Vibrational Mode**
857	812 ± 1	NO_2 bend
1070	988 ± 4	Phenyl in plane C-H bend
1105	1179 ± 2	Phenyl in plane C-H bend
1129	1211 ± 2	Phenyl in plane C-H bend
1357	1358 ± 3	NO_2 symmetric stretch
1576	1615 ± 2	Phenyl C=C stretch
Solid NAB Raman shift /cm^{-1}	**NAB Modified Raman shift /cm^{-1}**	**Vibrational Mode**
1110	1105 ± 2	Phenyl ring - NO_2
1150	1140 ± 2	Phenyl ring - N=N stretch
1336	1341 ± 1	NO_2 symmetric stretch
1412	1401 ± 1	N=N stretch + Phenyl ring with NO_2
1450	1450 ± 1	N=N stretch
1594	1596 ± 2	Phenyl C=C stretch
Solid FL Raman shift /cm^{-1}	**FL Modified Raman shift /cm^{-1}**	**Vibrational Mode**
850	874 ± 3	C-C vibrations
1149	1057 ± 2	Phenyl ring H bending
1178	1110 ± 2	H bending -CH_2
1184	1139 ± 2	Phenyl ring H bending
1229	1324 ± 1	Direct C-C between phenyl rings
1471	1452 ± 3	Valence vibrations -CH_2
1494	1471 ± 1	Deformation Vibrations -CH_2
1540	-	N=N stretch

Electrochemical Properties. The effect of the diazonium adlayers on the electrochemical behavior of the CFRP edge was investigated (see Figure 2.1). Figure 2.12 presents background cyclic voltammetric *i-E* curves for unmodified and modified composites in 1M KCl. The background

current and charge within the voltametric envelope decrease in the following order: unmodified >> NP modified > NAB modified.

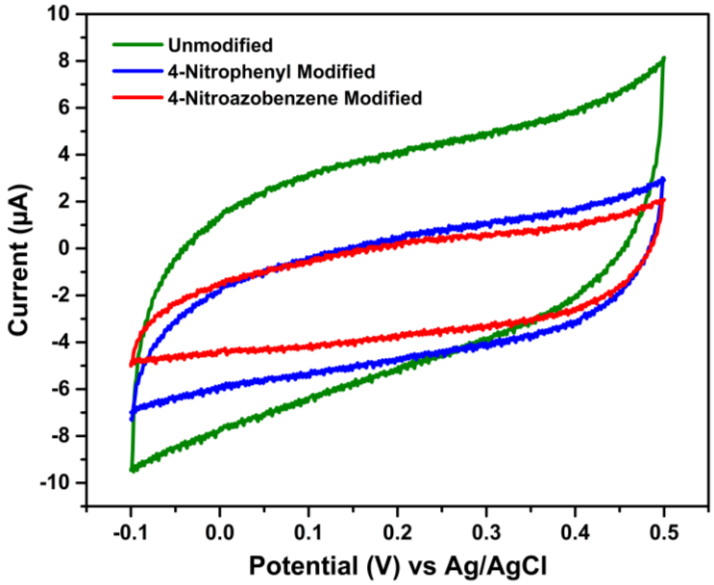

Figure 2.12. Background cyclic voltammetric *i-E* curves in 1 M KCl for unmodified, 4-nitrophenyl-modified, 4-nitroazobenzene-modified and 2-FL modified CFRP composite specimens. Scan rate = 50 mV/s. The diazonium adlayers were formed using 25 potential cycles.

The passivation of the composite surface by the diazonium adlayers is the reason for the lower current and charge. The adlayer essentially extends the counterbalancing charge on the solution side of the interface further away from the charged electrode surface and this results in a reduced capacitance. The passivation of the composite surface by the diazonium adlayers is the reason for the lower current and charge. The adlayer essentially extends the counterbalancing charge on the solution side of the interface further away from the charged electrode surface and this results in a reduced capacitance. The background current at several potentials in this range increased linearly with the scan rate for both the unmodified and modified composite specimens indicating the current is capacitive or pseudocapacitive in nature. The charge within the voltammetric envelope is *ca.* 2× lower for the NP modified and *ca.* 3× lower for the NAB modified specimens, as compared to the unmodified control. The apparent capacitance, C_{dl}, based on the current measured at 0.2 V, is 197, 104 and 70 μF/cm^2, respectively, for the unmodified, the NP,

and the NAB modified specimens. These values are normalized to the geometric area of the CFRP edge, which is much lower than the true surface area of the carbon fibers exposed. This leads to a relatively large apparent C_{dl} value. We do not have a good measure of the real surface are exposed. Additionally, the background current measured for the CFRP specimen likely contains a contribution from pseudocapacitance arising from redox-active and ionizable carbon-oxygen functional groups that populate the exposed edge plane sites of the carbon fibers.[66-68] This, along with the uncertainty in the real surface area of the carbon fibers exposed on the composite edge, leads to the larger apparent capacitance values. For low oxygen glassy carbon, for example, a capacitance of 20-30 μF/cm^2 is expected.[67,68] The key take-home message is still clear though and that is the reduced background current and charge arises from the presence of the covalently attached adlayer.

The electrochemically assisted modification of carbon material surfaces with diazonium molecule adlayers is straightforward and the modified electrode response toward various solution-based redox systems has been reported previously.[45-47,58,65,69] Experiments were performed in this work to probe for the blocking layer effect of the diazonium adlayers using the ferri/ferrocyanide redox system. Figure 2.13 presents cyclic voltammetric *i-E* curves for 0.5 mM $Fe(CN)_6^{-3/-4}$ in 0.5 M Na_2SO_4 under deaerated conditions at 0.05 V/s for the unmodified and diazonium-modified CFRP specimens. The $Fe(CN)_6^{-3/-4}$ redox system exhibits a heterogeneous electron-transfer rate constant that strongly depends on the surface cleanliness and exposed microstructure of sp^2 carbon electrodes.[58,70,71] Diazonium adlayers generally totally block electron transfer for this redox system.[45-47] The data presented here indicate this too is the case for the diazonium-modified CFRP specimens. For the unmodified specimen, a well resolved, quasi-reversible redox response is observed with an oxidation peak at *ca.* 0.31 V and a reduction peak at *ca.* 0.23 V. The ΔE_p is 83

mV. Quasi-reversibility was determined from the observation that the peak splitting increased with scan rate over the range of 0.05 to 0.25 V/s. The oxidation peak current on the forward sweep was *ca.* 118 μA. The oxidation peak current increased linearly with the scan rate$^{1/2}$ over the scan rate range probed. This indicates the oxidation reaction kinetics are limited by diffusion of $Fe(CN)_6^{-4}$ to the CFRP surface. Importantly, both diazonium adlayers totally inhibit the redox reaction. Surface interactions of this redox system with the electrode surface are blocked by the adlayer, and apparent the electron tunneling probability through the adlayer is low. [45-47,58,70,71]

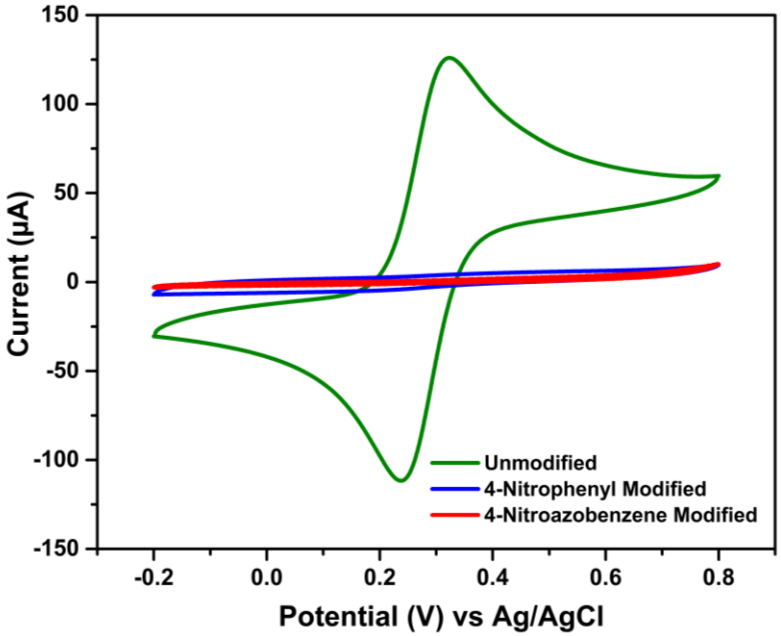

Figure 2.13. Cyclic voltammetric *i-E* curves recorded for 0.5 mM $Fe(CN)_6^{-3/-4}$ in 0.5 M Na_2SO_4 at unmodified, 4-nitrophenyl-modified, and 4-nitroazobenzene-modified CFRP composite specimens. Scan rate = 50 mV/s. The diazonium adlayers were formed using 25 potential cycles.

Inhibition of the Oxygen Reduction Reaction. Figure 2.14 shows cyclic voltammetric *i-E* curves for an unmodified CFRP specimen in 0.5 M Na_2SO_4 with and without dissolved oxygen. Clearly, in this electrolyte solution at ~pH 6, dissolved oxygen reduction commences at -0.2 V. A reduction current of *ca.* -90 μA is seen at the most negative potential, -0.8 V.

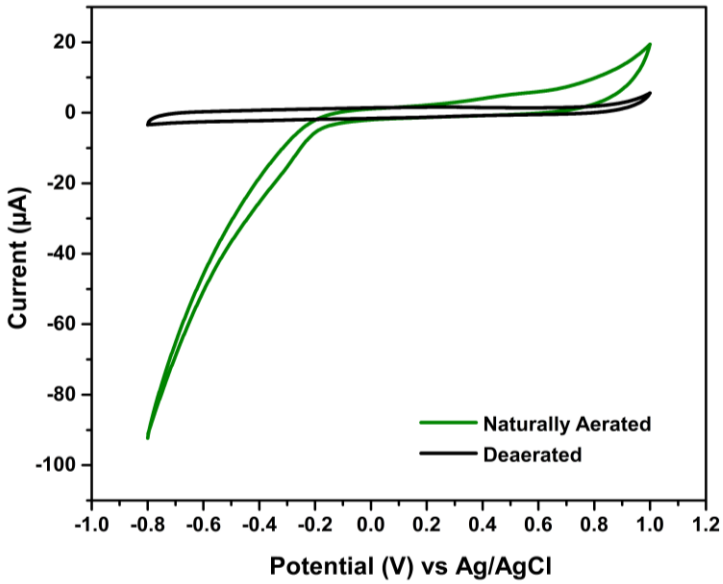

Figure 2.14. Cyclic voltammetric *i-E* curves for an unmodified CFRP composite specimen in naturally aerated and deaerated 0.5 M Na_2SO_4. Scan rate = 0.01 V/s.

Figure 2.15 presents cyclic voltammetric *i-E* curves for dissolved oxygen reduction at unmodified and diazonium-modified CFRP specimens. The curves were recorded in naturally aerated 0.5 M Na_2SO_4 at 0.01 V/s. The least negative onset potential is seen for the unmodified specimen with a value of *ca.* -0.2 V. The largest current for dissolved oxygen reduction is also seen for the unmodified specimen with a value of *ca.* -90 μA at -0.8 V. For the nitrophenyl and nitroazobenzene modified composite specimens, the onset potential for the dissolved oxygen reduction current is shifted to more negative potentials of *ca.* -0.4 V and the current at -0.8 V is reduced by close to 50%, as compared to the unmodified specimen. The more negative onset potential for the oxygen reduction current at the diazonium-modified specimens is consistent with the electron transfer kinetics being inhibited by the adlayer. FL modified composite specimen reduced the current by about 34%. However, there is not total inhibition of the current for the small, neutral O_2 molecule like there is for the anionic $Fe(CN)_6^{-3/-4}$. Ideally, near total current inhibition would be desired for maximum suppression of the aluminum alloy galvanic corrosion

rate. The fact that there is some reduction current means that there are likely defects in the adlayers or incomplete adlayer coverage such that the O_2 molecule can penetrate and reach the underlying carbon. Apparently, the anionic $Fe(CN)_6^{-3/-4}$ is unable to penetrate these defects. Data for three specimens of each type are summarized in Table 2.2. Preliminary results, not reported herein, indicate that spontaneously formed (24 h immersion) NAB diazonium adlayers on the CFRP specimens more effectively inhibit the current for dissolved oxygen reduction than do the electrochemically assisted formed adlayers suggesting a more complete, less defective adlayer coverage is possible. These results will be reported on separately.

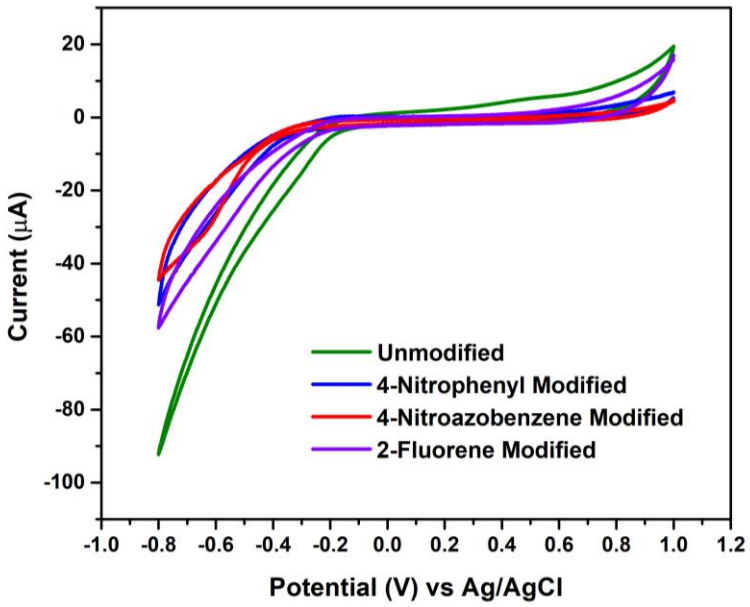

Figure 2.15. Cyclic voltammetric *i-E* curves for an unmodified CFRP composite specimen (green) and CFRP specimens modified with 4-nitrophenyl (blue), 4-nitroazobenzene (red) and 2-fluorene adlayers in naturally aerated 0.5 M Na_2SO_4. Scan rate = 0.01 V/s.

Table 2.2. Summary of electrochemical data for the dissolved oxygen reduction reaction (ORR) at unmodified and diazonium-modified CFRP specimens.

	Unmodified	NP Modified	NAB Modified	FL Modified
ORR Onset Potential (V)	-0.143 ± 0.022	-0.329 ± 0.043	-0.398 ± 0.065	-0.235 ± 0.035
ORR Current at -0.8 V (μA)	-112.2 ± 19.3	-56.3 ± 5.7	-47.7 ± 4.5	-58.1 ± 5.6

Data are presented as mean ± std. dev. for n=3 specimens of each type.

The nominal open circuit potential (OCP) values for unmodified and diazonium-modified CFRP composite specimens recorded vs. Ag/AgCl in 0.5 M Na_2SO_4 are presented in Table 2.3. The nominal OCP values for unmodified, NP-modified, NAB-modified and FL-modified CFRP composites are 0.149 ± 0.025 V, 0.275 ± 0.013 V, 0.274 ± 0.017 V and 0.263 0.015 V respectively. The positive shift in OCP after the surface modification is reflective of the passivation of exposed carbon fiber surfaces on the composite edge due to adlayer formation. The table also presents OCP data for TCP-coated AA2024-T3 specimens in the same electrolyte solution.[72] The values for the CFRPs are 375 to 500 mV more noble than the value for the TCP-coated aluminum alloy. Therefore, when a galvanic or contact cell is formed between the two materials, the CFRP will serve as the cathode and support the reduction of dissolved oxygen while the aluminum alloy will serve as the anode and undergo oxidation and dissolution.

Table 2.3. Summary of the nominal open circuit potential (OCP) values for unmodified and diazonium-modified CFRP specimens in naturally aerated 0.5 M Na_2SO_4.

Material	OCP (V) vs. Ag/AgCl
Unmodified CFRP	0.149 ± 0.025
NP-modified CFRP	0.275 ± 0.013
NAB-modified CFRP	0.274 ± 0.017
FL-modified CFRP	0.263 ± 0.015
TCP-coated AA2024-T3	-0.225 ± 0.020 (from ref. 72)

Data are presented as mean ± std. dev. for n=3 specimens of each type.

Neutral Salt-Spray Exposure. The degree to which galvanic corrosion of TCP-coated AA2024-T3 alloys is inhibited when coupled with CFRP specimens modified with diazonium adlayers was assessed during a 7-day neutral salt spray exposure. The two materials were mechanically joined using a stainless-steel fastener, as described in the Experimental section. Figure 2.16 presents digital micrographs of aluminum alloys before and after exposure to the salt spray environment. A

TCP-coated AA2024-T3 alloy specimen before the salt spray exposure shows no visible defects, surface imperfections or discolorations (Figure 2.16A). The uncoated AA2024-T3 alloy coupled with an unmodified CFRP composite (Figure 2.16B) shows severe and widespread corrosion damage (stage 4) after just 3 days into the salt spray test, even under the area where the composite was attached. This indicates that galvanic corrosion, crevice corrosion, and general corrosion all occurred on this specimen.

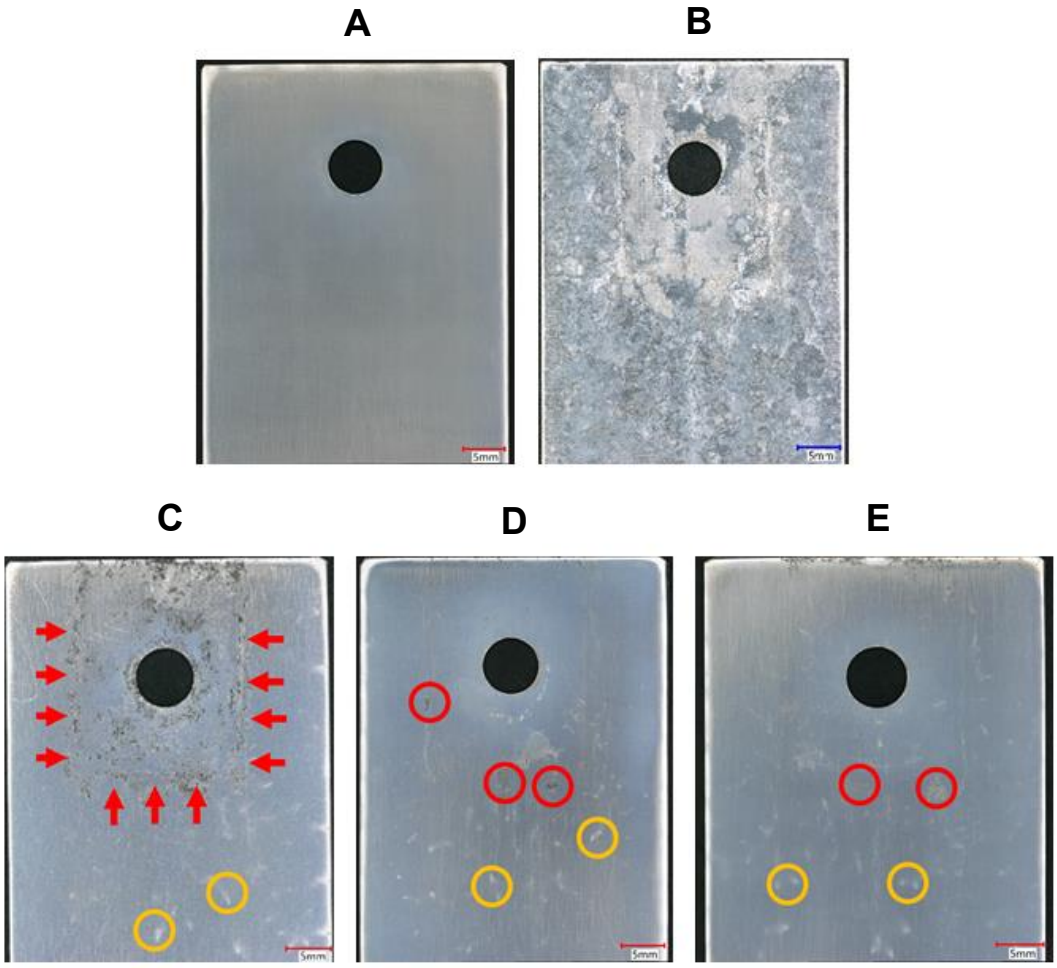

Figure 2.16. Digital optical micrographs of the AA2024-T3 panels (5.5 cm × 3.6 cm) (A) with a TCP coating and before salt spray exposure, (B) uncoated and joined with an unmodified CFRP composite after just 3 days of neutral salt spray exposure, (C) TCP coated and joined with an unmodified CFRP composite after 7 days of neutral salt spray exposure, (D) TCP coated and joined with a 4-nitrophenyl diazonium adlayer after 7 days of neutral salt spray exposure, and (E) TCP coated and joined with a 4-nitroazobenzene diazonium adlayer after 7 days of neutral salt spray exposure. TCP coated AA panels joined with 2-FL diazonium were tested for 14 days and the test results are reported in Chapter 3.

TCP is a non-chromated, trivalent chromium (Cr^{3+}) and zirconium-based conversion coating that provides aluminum alloys with protection against corrosion through anodic protection, cathodic protection, or both.[72,74-80] The TCP coating furnishes anodic protection by coating the Al rich sites of the alloy (physical blocking) thereby inhibiting the metal oxidation reaction and cathodic protection by blocking the Cu-containing intermetallics.[74-80] Significant corrosion damage (stage 3) is observed on TCP-coated AA2024-T3 specimen that was joined with an unmodified CFRP composite after 7 days (Figure 2.16C). The TCP coating adheres well to the alloy and provides good protection on the panel away from where the CFRP was joined. A few discolored areas are seen, as indicated by the yellow circles. The corrosion damage was limited to the alloy adjacent to the unmodified composite, mainly in the form of trenching. There was no evidence for undercutting of the TCP coating suggestive of strong adhesion with the alloy. The red arrows identify the damaged areas. There was also damage in and around the fastener hole on the alloy and some corrosion damage underneath the area where the composite was joined. This indicates that both galvanic and crevice corrosion occurred on the alloy specimen. The TCP coating prohibited general corrosion of the outer panel. The micrographs of TCP-coated alloy specimens joined with NP and NAB modified CFRP composites (Figure 2.16D and E), on the other hand, reveal much less corrosion damage (stage 2) after 7 days. The trenching degradation near the composite edge was greatly reduced by the modified CFRP edges. Crevice corrosion underneath the composite was also greatly reduced. Additionally, there was minimal degradation in and around the fastener hole. There is some minor discoloration seen, as identified with the yellow circles, and some isolated pitting corrosion on the outer panel, as demarked with the red circles. Overall, though, the NP and NAB surface modifications greatly reduced the galvanic, crevice and general corrosion of the TCP-coated alloy. The SEM-EDS spectra not reported herein showed that the

discolored areas (circled in yellow) on the TCP-coated alloy specimens are the regions where the coating coverage has been compromised during the neutral salt spray exposure.

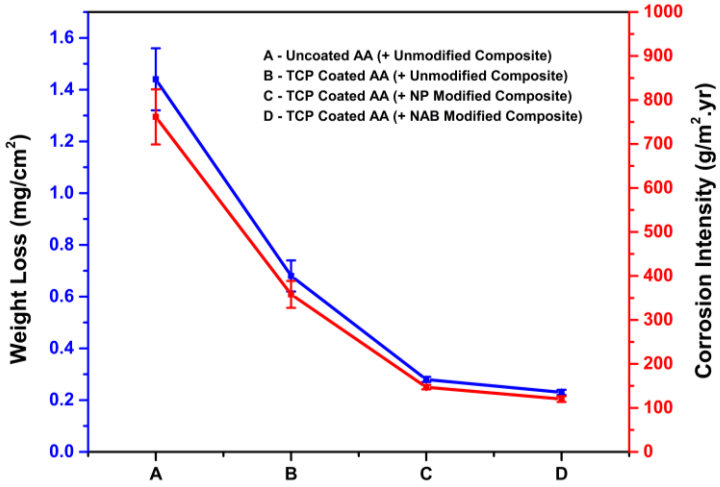

Figure 2.17. Weight loss (blue curve) and corrosion intensity (red curve) data for AA2024-T3 panels joined with unmodified/diazonium modified CFRP composites after a (A) 3 or (B,C,D) 7-day neutral salt spray exposure. Data are presented as mean ± std. dev. for n=3 specimens of each type. Blue curve is the weight loss data. Red curve is the corrosion intensity data.

A more quantitative corrosion damage assessment was performed by comparing the weight loss and corrosion intensity data. The resulting data are presented in Figure 2.17. The uncoated AA2024-T3 joined with an unmodified CFRP composite exhibited the largest weight loss per cm^2 because of the extensive corrosion damage after just 3 days. Since the TCP conversion coating provides an anodic protection to the aluminum alloy, the weight loss due to corrosion damage after 7 days was 2× lower as compared to the uncoated aluminum alloy even when joined with an unmodified CFRP composite specimen. TCP-coated AA2024-T3 joined with NP and NAB modified CFRP composites exhibited the smallest weight loss values. The corrosion intensity, defined as the weight loss of the aluminum alloy per m^2 per year, decreased in the same order as weight loss. Uncoated AA2024-T3 coupled to unmodified CFRP composite > TCP-coated AA2024-T3 coupled to unmodified CFRP composite > TCP-coated AA2024-T3 coupled to diazonium modified CFRP composites.

Aluminum alloy corrosion can be greatly accelerated when electrically coupled with a CFRP composite consisting of exposed and electrically conducting carbon fibers.[15-17,81-84]The corrosion damage on the TCP-coated alloy when joined with an unmodified CFRP edge (see Figure 2.16C) is primarily in the form of localized trenching near the edge of the composite and in the fastener hole. Since the TCP coating adhesion is strong, there is no delamination or coating lift off, rather the oxidation of the alloy proceeds inward with depth into the alloy right around the edge of the composite.

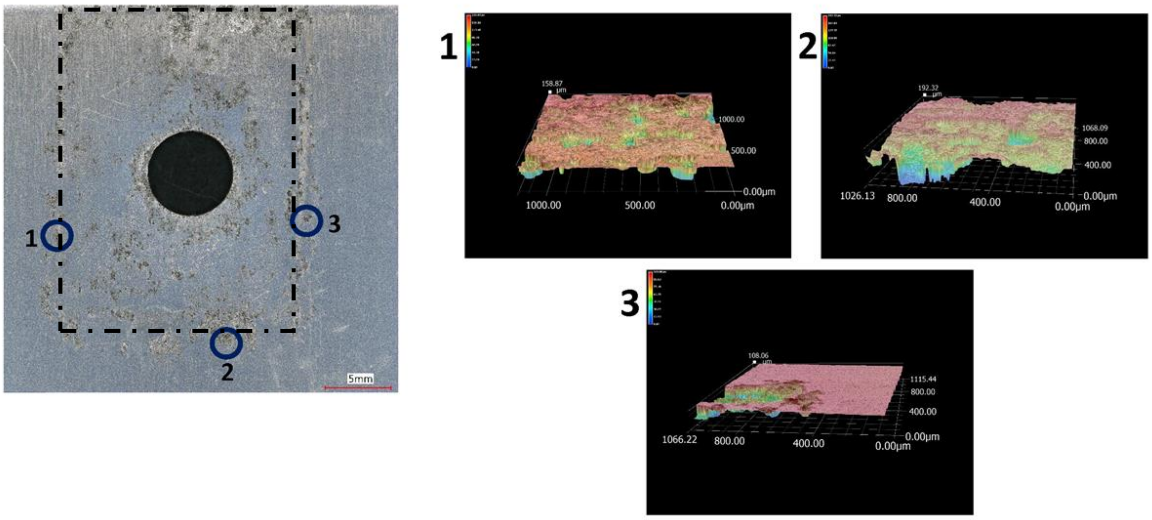

Figure 2.18. Plan view digital optical micrograph of a TCP-coated AA2024-T3 panel coupled to an unmodified CFRP composite specimen after 7 days of continuous neutral salt spray exposure (left). 3D contour plots generated from optical microscopy data at points 1-3 along the corrosion trench adjacent to the CFRP edges.

Figure 2.18 presents an optical micrograph of the TCP-coated AA2024-T3 specimen where an unmodified composite was joined (left, dashed outline). The outline reveals the region where the CFRP specimen was joined. There is clearly some significant alloy degradation and dissolution around the fastener hole and the hole wall (as evidenced in other microscopy data in Figure 2.16).[22,23,83] Even though the fastener was electrically isolated with insulating tape and sealant, moisture was apparently able to penetrate the hole of the CFRP composite and reach the alloy surface such that some galvanic corrosion occurred in and around the hole. Clearly, if the alloy

degradation was caused by galvanic corrosion, then mass transport of oxygen to the interior was not inhibited in a major way. There is clearly corrosion damage underneath the CFRP composite, so crevice corrosion was also a degradation mechanism.[15-17,83] Moisture and dissolved oxygen intrusion under the composite may have been the pathway to the hole. At points 1-3 along the alloy corrosion trench, digital optical microscopy was used in the 3D contour plot mode to depict the alloy dissolution. The degradation was discontinuous in the damaged area ranging from isolated pits in region 1 that were 50-100 μm in diameter and 10's of μm in depth, to coalesced pits in region 2, to a large area of metal dissolution 100's of μm across and 10's of μm in depth in region 3. This kind of material loss was not seen near the edges of the diazonium- modified CFRP specimens.

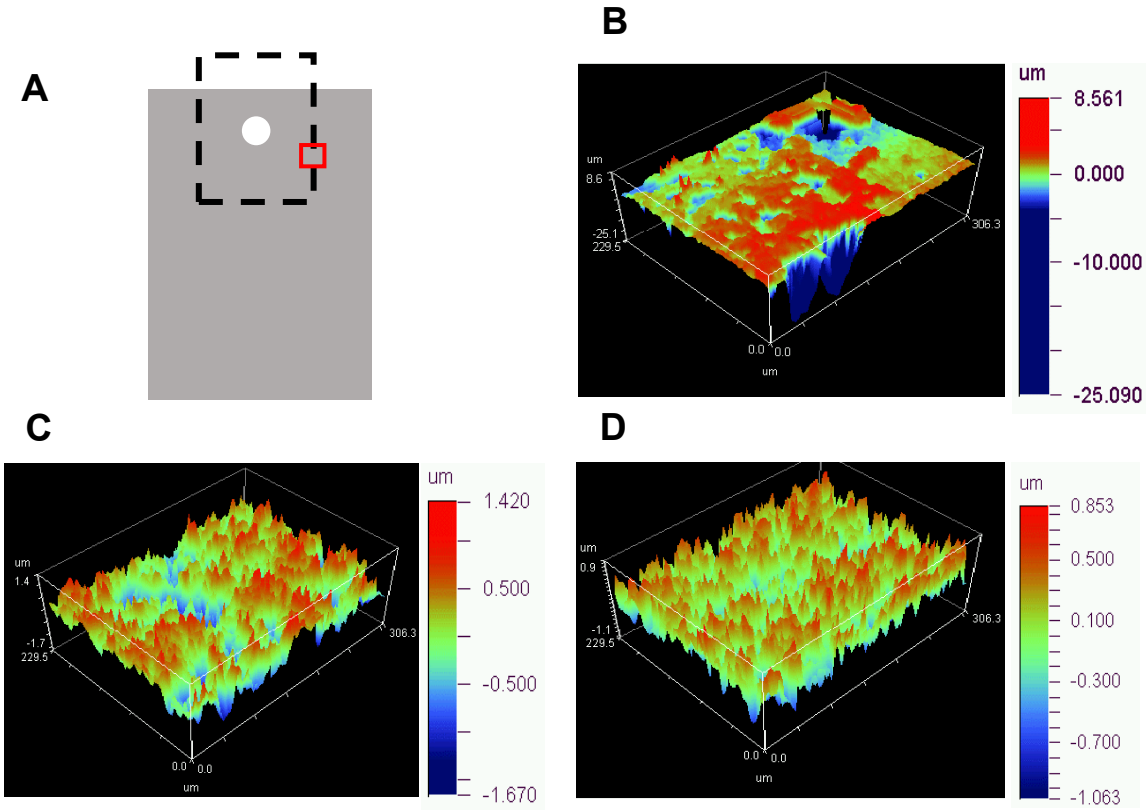

Figure 2.19. (A) Schematic diagram of a TCP-coated AA2024-T3 panel showing where the CFRP composite was joined and where the 3D contour plots were collected. Optical profilometry 3D contour plots of TCP-coated AA22024-T3 panels joined to (B) unmodified, (C) NP modified, and (D) NAB modified composites after 7 days of salt spray exposure.

Figure 2.19 presents the optical profilometry 3D contour plots obtained for TCP-coated AA panels joined to unmodified, NP modified, and NAB modified CFRP composites after exposing them to salt spray for 7 days. Clearly, the average surface roughness and pit depth is greater for the alloy panel joined with unmodified composite. In contrast, the 3D contour plots for alloy panels joined with electrochemically modified composites reveal relatively smoother surface texture due to reduced galvanic corrosion.

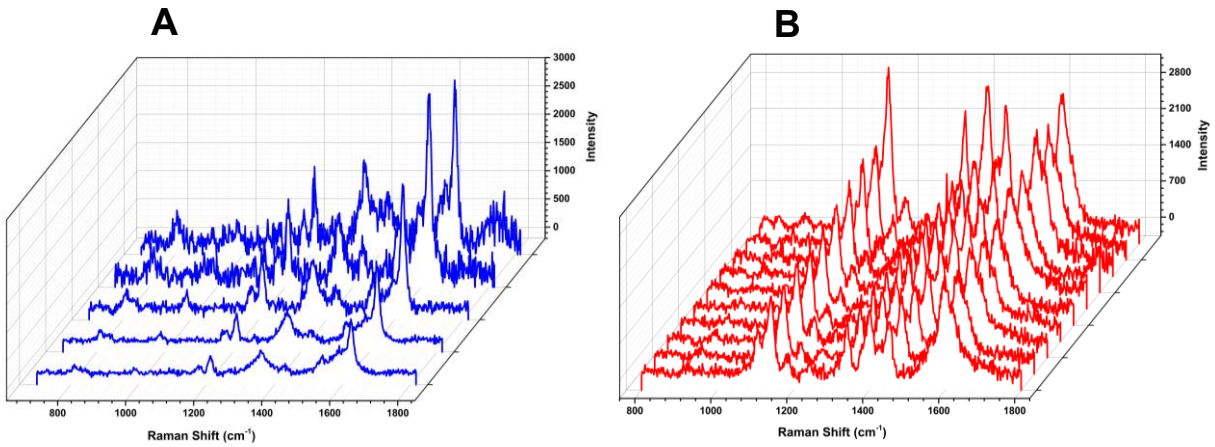

Figure 2.20. Raman spectra of (A) 4-nitrophenyl modified and (B) 4-nitroazobenzene modified CFRP composite specimens after a 7-day neutral salt spray test. The line scan spectra were collected on both modified specimens on the cylindrically oriented fibers in the composite.

A key question regards the stability of the diazonium adlayers during the 7-day salt spray exposure. Raman spectra presented in Figure 2.20 for NP and NAB modified CFRP composite edges reveal that indeed both organic adlayers are still present and are stable at least over 7 days. Raman spectra were recorded along an 80 μm line scan at 50×. Spectra were acquired at 1 μm distances and a select number of these are presented in the figure. The characteristic peaks for NP and NAB organic layers (see Table 2.1) are reflected in the spectra. There is some reduction in intensity of Raman peaks, as compared to the spectra in Figures 2.9 and 2.10 for modified specimens prior to the salt spray exposure. This suggests there may be some loss of admolecules from the surface during the testing period. Overall, though, the general finding is that the adlayers are stable during exposure to the continuous salt spray.

Carbon Corrosion. Microstructural damage and carbon corrosion were observed on the CFRP specimen edge after the 7-day neutral salt spray exposure. Carbon corrosion and composite degradation have previously been reported in galvanic corrosion studies of CFRP composites joined with metal alloys, and upon exposure to electrochemical conditions.[50,82-85] As can be seen in the SEM micrographs presented Figure 2.21, quite significant carbon fiber breakage and carbon corrosion occurred on the unmodified CFRP specimen during salt spray exposure (Figure 2.21B) as compared to the specimen before exposure (Figure 2.21A). Yellow arrows in Figure 2.21B identify regions of carbon fiber damage on the cylindrical and distal ends of the fibers. There is also detachment of the sizing material and epoxy matrix from some fibers as identified by the red arrows. While some carbon fiber damage is present on the NAB modified specimen (Figure 2.21C), the extent of the damage is less than that seen for the unmodified specimen after 7 days. There is some damage on the diazonium modified specimen, as the electrochemical data presented above suggest, the adlayer has defects or is not completely formed across the exposed carbon fibers such that dissolved oxygen can penetrate and be reduced at the underlying carbon surface. Of course, over a prolonged period, microstructural degradation and carbon corrosion could reduce the integrity and mechanical strength of the CFRP. We have previously reported significant epoxy debonding and degradation in the forms of cracks and fissures in CFRP composite specimens during a 7-day neutral salt spray exposure when electrically connected to an aluminum alloy.[50] There was, however, no apparent microstructural degradation of the carbon fibers or carbon corrosion. We believe that the degradation may result from the accumulation of hydrogen peroxide in the condensed solution layer at the interface between the CFRP and the TCP-coated aluminum alloy.[50] The hydrogen peroxide is produced from the reduction of dissolved oxygen by the 2 proton/2 electron pathway.[24-27,85] The molecule is a strong oxidation that chemically attacks both

the epoxy and carbon fibers. A second possible mechanism could be the alkaline pH of the condensed solution layer due to the proton consuming cathodic reactions. Carbon can undergo etching or dissolution in strongly alkaline media.[86-88]

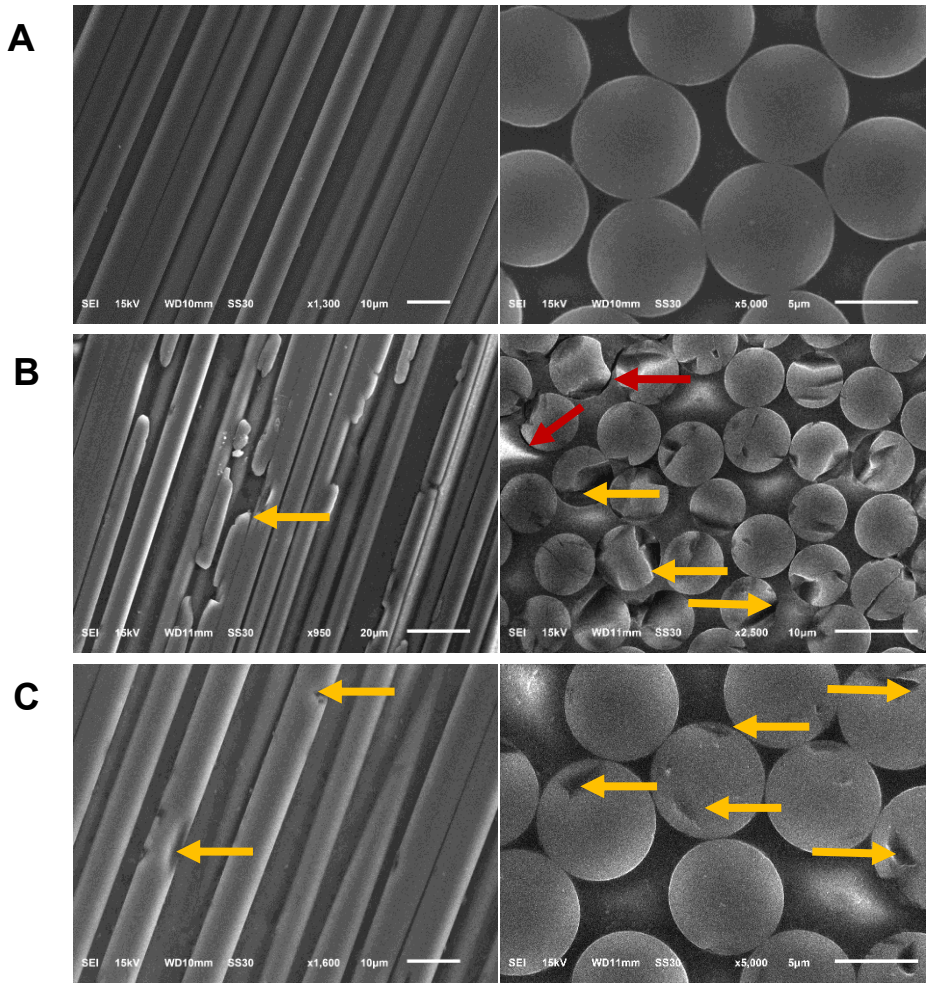

Figure 2.21. SEM micrographs of (A) polished unmodified CFRP composite before, (B) unmodified and (C) 4-nitroazobenzene modified CFRP composite specimens after a 7-day neutral salt spray test.

2.4 DISCUSSION

This study revealed that aryl diazonium adlayers can be covalently attached to the exposed carbon fibers of CFRP composites using an electrochemically assisted process, and that the surface pretreatment reduces the galvanic corrosion damage on TCP-coated aluminum alloy 2024-T3 specimens when joined with a modified CFRP and subjected to an accelerated degradation test.

The test used for assessment was a 7-day continuous neutral salt spray exposure. While there are many examples in the literature describing the surface modification of sp^2 and sp^3 carbon materials with diazonium adlayers for various electrochemical purposes, this is the first example of using the surface pretreatment to reduce the effects of galvanic corrosion on aerospace aluminum alloys and the associated carbon fiber degradation in CFRP composites. At least in a short-term neutral salt spray environment, both the 4-nitrophenyl (NP) and 4-nitroazobenzene (NAB) adlayers are stable on the carbon fiber surface and significantly reduce the alloy degradation by galvanic and crevice corrosion. The electrochemical reduction of either NP or NAB diazonium molecules by a one-electron reaction forms a phenyl radical and N_2. The phenyl radical then reacts with the carbon surface by covalent attachment to an unsatisfied valence or adding to a carbon-carbon double bond.[28-33] The surface modification can be accomplished in an electrochemically-assisted mode, as is the case for this work, or by spontaneous deposition (data to be reported separately).[89,90] In the electrochemically-assisted mode, a well-defined reduction peak is seen on the first scan that decreases in magnitude on the second and subsequent scans. This is because the exposed carbon fibers of the CFRP composite (edges and fastener hole wall) undergoes modification with the organic adlayer, which tends to inhibit further diazonium reduction. The adlayers will form on both the defects and graphitic edge plane sites as well as the basal plane sites of the exposed carbon fibers. [28,45,57]

The adlayers are quite stable and withstand at least 7 days of the neutral salt spray environment. This is expected as the diazonium adlayers on carbon are known to be stable with solution exposure, ultrasonication, temperature, etc.[33,40,63-65] Cyclic voltammetric measurements revealed about a 50% reduction in the kinetically controlled reduction current for dissolved O_2 reduction on both the NP and NAB surfaces and about 34% reduction on FL surfaces. Complete

inhibition was not achieved because the adlayer may not be fully covering the surface or may possess some defects through which O_2 can diffuse and reach the underlying carbon surface. Recent data for spontaneously formed (24 h soak) NP and NAB adlayers revealed near complete inhibition of the O_2 reduction current and even less galvanic corrosion damage than is reported herein for TCP-coated AA2024-T3 specimens. The digital microscopy and the weight loss metrics revealed significantly reduced galvanic and crevice corrosion of the aluminum alloy when joined with either NP or NAB modified CFRP specimens. The decrease in the rate of dissolved O_2 reduction on the more noble CFRP specimens by the aryl diazonium adlayers leads to a decrease in the rate of aluminum alloy oxidation and dissolution. This is attributed to the either blocking adsorption sites for the O_2 and/or reaction intermediates; the first step in the surface-mediated reduction reaction, or the adlayer produces an increased electron tunneling barrier to the O_2 molecule.

Interesting is the observation that the carbon fibers of the CFRP specimen undergo microstructural degradation and corrosion during the 7-day salt spray exposure. We have previously reported epoxy debonding and cracking in these composite specimens during a 7-day neutral salt spray exposure.[50] This damage is linked to electrochemical processes occurring at the exposed carbon fibers.[85] It was concluded that the damaged under the cathodic conditions is linked to H_2O_2 produced in the electrolyte solution layer from the reduction of dissolved O_2. In that work, carbon corrosion or microstructural degradation of the carbon fibers was not observed. Importantly, the carbon corrosion and microstructural degradation observed in the present work is significantly reduced by the diazonium adlayer.

During the salt spray test, a thin electrolyte solution layer, rich in O_2 from the atmosphere, is deposited continuously on the specimen surface.[91,92] A high diffusional flux of O_2 occurs through

the thin solution layer due to the large concentration gradient. The solution layer also serves as a reservoir for reduction and oxidation reaction products. The adlayer is not expected to affect the O_2 flux through the thin solution layer but does serve to inhibit the rate of the reduction reaction. Corrosion product accumulation can occur in the thin solution layer. In addition, pH changes and increases in the local concentration of pre-existing anions, like chloride, can occur to increase the anodic dissolution rate.[91,92] The general carbon corrosion reaction to produce CO_2 is shown in equation 3.

$$C + 2H_2O \rightarrow CO_2 + 4H^+ + 4e^- \qquad (3)$$

We suppose that carbon fiber corrosion can occur by one of two mechanisms. If O_2 reduction is occurring by the 2-electron/2-proton reduction (end-on) to produce H_2O_2, this strong oxidation could accumulate in the solution layer and oxidatively attack the carbon, the epoxy, and the interface between the two. Under neutral pH conditions, the redox rection proceeds according to equation 4,

$$O_2 + 2H_2O + 2e^- \rightarrow H_2O_2 + 2OH^- \qquad (4)$$

H_2O_2 accumulation in the thin solution layer could lead to carbon oxidation according to the following net redox reaction,

$$C + 2H_2O_2 \rightarrow CO_2 + 4H_2O \qquad (5)$$

Within the thin solution layer, there can be pH changes due to proton consuming cathodic reactions, such as the 2-electron/2-proton reduction to H_2O_2 shown in equation 4. The O_2 reduction reaction can also proceed by the 4-electron pathway to form hydroxide according to equation 6,

$$O_2 + 2H_2O + 4e^- \rightarrow 4OH^- \qquad (6)$$

Both reactions would lead to an increasing alkaline solution layer such that the following carbon oxidation reaction could occur,[86-88]

$$C + 6OH^- \rightarrow CO_3^{2-} + 3H_2O + 4e^- \qquad (7)$$

Finally, the reduced crevice corrosion underneath the CFRP composite seen for the diazonium modified specimens could result from greater physical interaction between the composite and the alloy. Exposure of the entire CFRP specimen in the diazonium acetonitrile solution used for the electrochemically assisted derivatization could soften up the outer region of the epoxy layer on the surface of the composite. When the composite is mechanically fastened to the aluminum alloy, a tighter seal with more physical interaction with the alloy may result. This serves to inhibit the penetration of solution into the crevice between the two.

2.5 CONCLUSIONS

We tested the hypothesis that the formation of covalently attached adlayers on the exposed carbon fiber surfaces of the CFRP composite edges by the electrochemically assisted reduction of para substituted aryldiazonium salts will inhibit the oxygen reduction reaction kinetics and thereby reduce the rate of galvanic corrosion of conversion-coated aluminum alloy when mechanically joined with the modified composite. Key findings from the work can be summarized as follows.

1. The electrochemically assisted reduction of 4-nitrophenyl and 4-nitroazobenzene diazonium salts generates stable adlayers on CFRP composite edges with apparent electrochemically active surface coverage of 14.2 ± 1.7 and 8.7 ± 1.8 nmol/cm^2, respectively for NP and NAB adlayers.
2. Cyclic voltametric data reveal reduced background current and capacitance for the diazonium modified CFRP edges consistent with the presence of an organic adlayer. Furthermore, the redox chemistry of the soluble, surface-sensitive $Fe(CN)_6^{-3/-4}$ redox couple is blocked by both NP and NAB adlayers.

3. Raman spectroscopy confirmed the presence of the adlayers after modification and their stability during exposure to the 7-day continuous neutral salt spray.
4. Cyclic voltametric data revealed that both NP and NAB adlayers reduced the current for dissolved oxygen reduction by 50%, and FL adlayer suppressed the current for oxygen reduction by 34% as compared to the unmodified specimen. Complete inhibition is not achieved because the adlayer may not be fully compact across the surface or may possess some defects through which O_2 can diffuse and reach the underlying carbon surface.
5. Both adlayers significantly reduce the galvanic, crevice and general corrosion of TCP-coated AA2024-T3 alloy specimens when a modified CFRP composite is joined during a 7-day continuous neutral salt spray exposure. Visible degradation and weight loss metrics (mass loss per cm^2 and corrosion intensity) are significantly reduced for the diazonium modified CFRP specimens.
6. The results indicate that this CFRP surface treatment is an effective approach for reducing the galvanic corrosion of aluminum alloys.

REFERENCES

1. Starke Jr, E. A., & Staley, J. T. (1996). Application of modern aluminum alloys to aircraft. *Progress in aerospace sciences*, *32*(2-3), 131.

2. Huda, Z., Taib, N. I., & Zaharinie, T. (2009). Characterization of 2024-T3: An aerospace aluminum alloy. *Materials Chemistry and Physics*, *113*(2-3), 515.

3. Jawalkar, C. S., & Kant, S. (2015). A review on use of aluminium alloys in aircraft components. *i-manager's Journal on Material Science*, *3*(3), 33.

4. Gokhan, O. Z. E. R., & Karaaslan, A. (2017). Properties of AA7075 aluminum alloy in aging and retrogression and reaging process. *Transactions of Nonferrous Metals Society of China*, *27*(11), 2357.

5. Dursun, T., & Soutis, C. (2014). Recent developments in advanced aircraft aluminium alloys. *Materials & Design (1980-2015)*, *56*, 862.

6. Traceski, F. T. (1999). Assessing industrial capabilities for carbon fiber production. *Aquisition Review Quarterly–Spring*, 180.

7. Dispenza, C., Alessi, S., & Spadaro, G. (2008). Carbon fiber composites cured by γ-radiation-induced polymerization of an epoxy resin matrix. *Advances in Polymer Technology: Journal of the Polymer Processing Institute*, *27*(3), 163.

8. Park, S. J. (2015). *Carbon fibers* (Vol. 210). Dordrecht, The Netherlands: Springer.

9. Chung, D. D. (2016). *Carbon composites: composites with carbon fibers, nanofibers, and nanotubes*. Butterworth-Heinemann.

10. Prasad, N. E., & Wanhill, R. J. (Eds.). (2017). *Aerospace materials and material technologies* (Vol. 1, pp. 29-52). Singapore: Springer.

11. Jiang, B., Chen, Q., & Yang, J. (2020). Advances in joining technology of carbon fiber-reinforced thermoplastic composite materials and aluminum alloys. *The International Journal of Advanced Manufacturing Technology*, *110*(9), 2631.

12. Liu, Z., Curioni, M., Jamshidi, P., Walker, A., Prengnell, P., Thompson, G. E., & Skeldon, P. (2014). Electrochemical characteristics of a carbon fibre composite and the associated galvanic effects with aluminium alloys. *Applied surface science*, *314*, 233.

13. Håkansson, E., Predecki, P., & Kumosa, M. S. (2015). Galvanic corrosion of high temperature low sag aluminum conductor composite core and conventional aluminum conductor steel reinforced overhead high voltage conductors. *IEEE Transactions on Reliability*, *64*(3), 928.

14. Håkansson, E., Hoffman, J., Predecki, P., & Kumosa, M. (2017). The role of corrosion product deposition in galvanic corrosion of aluminum/carbon systems. *Corrosion Science*, *114*, 10.

15. Bauer, A., Grundmeier, G., Steger, H., & Weitl, J. (2018). Corrosive delamination processes of CFRP-aluminum alloy hybrid components. *Materials and Corrosion*, *69*(1), 98.

16. Li, S., Khan, H. A., Hihara, L. H., Cong, H., & Li, J. (2018). Corrosion behavior of friction stir blind riveted Al/CFRP and Mg/CFRP joints exposed to a marine environment. *Corrosion Science*, *132*, 300.

17. Zhang, C., Zheng, D., Song, G. L., Guo, Y., Liu, M., & Kia, H. (2019). Corrosion behavior of the joints of carbon fiber reinforced polymers with DP590 steel and Al6022 alloy. *Anti-Corrosion Methods and Materials*, *66*(4), 479.

18. Sause, M. G., & Jasiūnienė, E. (2021). *Structural health monitoring damage detection systems for aerospace* (p. 284). Springer Nature.

19. Srinivasan, R., Nelson, J. A., & Hihara, L. H. (2015). Development of guidelines to attenuate galvanic corrosion between mechanically-coupled aluminum and carbon-fiber reinforced epoxy composites using insulation layers. *Journal of the Electrochemical Society*, *162*(10), C545.

20. Peng, Z., & Nie, X. (2013). Galvanic corrosion property of contacts between carbon fiber cloth materials and typical metal alloys in an aggressive environment. *Surface and coatings technology*, *215*, 85.

21. Srinivasan, R., & Hihara, L. H. (2016). Utilization of hydrophobic coatings on insulative skirts to attenuate galvanic corrosion between mechanically-fastened aluminum alloy and carbon-fiber reinforced polymer-matrix composites. *Electrochemistry Communications*, *72*, 96.

22. Feng, Z., Boerstler, J., Frankel, G. S., & Matzdorf, C. A. (2015). Effect of surface pretreatment on galvanic attack of coated Al alloy panels. *Corrosion*, *71*(6), 771.

23. Feng, Z., Frankel, G. S., Abbott, W. H., & Matzdorf, C. A. (2016). Galvanic attack of coated Al alloy panels in laboratory and field exposure. *Corrosion*, *72*(3), 342.

24. Morcos, I., & Yeager, E. (1970). Kinetic studies of the oxygen-peroxide couple on pyrolytic graphite. *Electrochimica Acta*, *15*(6), 953.

25. Xu, J., Huang, W., & McCreery, R. L. (1996). Isotope and surface preparation effects on alkaline dioxygen reduction at carbon electrodes. *Journal of Electroanalytical Chemistry*, *410*(2), 235.

26. Yang, H. H., & McCreery, R. L. (2000). Elucidation of the mechanism of dioxygen reduction on metal-free carbon electrodes. *Journal of the Electrochemical Society*, *147*(9), 3420.

27. Šljukić, B., Banks, C. E., & Compton, R. G. (2005). An overview of the electrochemical reduction of oxygen at carbon-based modified electrodes. *Journal of the Iranian Chemical Society*, *2*, 1-25.

28. Delamar, M., Hitmi, R., Pinson, J., & Saveant, J. M. (1992). Covalent modification of carbon surfaces by grafting of functionalized aryl radicals produced from electrochemical reduction of diazonium salts. *Journal of the American Chemical Society*, *114*(14), 5883.

29. Downard, A. J. (2000). Electrochemically assisted covalent modification of carbon electrodes. *Electroanalysis: An International Journal Devoted to Fundamental and Practical Aspects of Electroanalysis*, *12*(14), 1085.

30. Allongue, P., Delamar, M., Desbat, B., Fagebaume, O., Hitmi, R., Pinson, J., & Savéant, J. M. (1997). Covalent modification of carbon surfaces by aryl radicals generated from the electrochemical reduction of diazonium salts. *Journal of the american chemical society*, *119*(1), 201.

31. Ortiz, B., Saby, C., Champagne, G. Y., & Bélanger, D. (1998). Electrochemical modification of a carbon electrode using aromatic diazonium salts. 2. Electrochemistry of 4-nitrophenyl modified glassy carbon electrodes in aqueous media. *Journal of Electroanalytical Chemistry*, *455*(1-2), 75.

32. Ray, K., & McCreery, R. L. (1997). Spatially resolved Raman spectroscopy of carbon electrode surfaces: Observations of structural and chemical heterogeneity. *Analytical Chemistry*, *69*(22), 4680.

33. Delamar, M., Desarmot, G., Fagebaume, O., Hitmi, R., Pinsonc, J., & Savéant, J. M. (1997). Modification of carbon fiber surfaces by electrochemical reduction of aryl diazonium salts: Application to carbon epoxy composites. *Carbon*, *35*(6), 801.

34. Bath, B. D., Martin, H. B., Wightman, R. M., & Anderson, M. R. (2001). Dopamine adsorption at surface modified carbon-fiber electrodes. *Langmuir*, *17*(22), 7032.

35. Harnisch, J. A., Gazda, D. B., Anderegg, J. W., & Porter, M. D. (2001). Chemical modification of carbonaceous stationary phases by the reduction of diazonium salts. *Analytical chemistry*, *73*(16), 3954.

36. Dequaire, M., Degrand, C., & Limoges, B. (1999). Biotinylation of screen-printed carbon electrodes through the electrochemical reduction of the diazonium salt of p-aminobenzoyl biocytin. *Journal of the American Chemical Society*, *121*(29), 6946.

37. Ruffien, A., Dequaire, M., & Brossier, P. (2003). Covalent immobilization of oligonucleotides on p-aminophenyl-modified carbon screen-printed electrodes for viral DNA sensing. *Chemical communications*, (7), 912.

38. Ranganathan, S., Steidel, I., Anariba, F., & McCreery, R. L. (2001). Covalently bonded organic monolayers on a carbon substrate: a new paradigm for molecular electronics. *Nano Letters*, *1*(9), 491.

39. Anariba, F., DuVall, S. H., & McCreery, R. L. (2003). Mono-and multilayer formation by diazonium reduction on carbon surfaces monitored with atomic force microscopy "scratching". *Analytical Chemistry*, *75*(15), 3837.

40. Toupin, M., & Bélanger, D. (2007). Thermal stability study of aryl modified carbon black by in situ generated diazonium salt. *The Journal of Physical Chemistry C*, *111*(14), 5394.

41. Bahr, J. L., Yang, J., Kosynkin, D. V., Bronikowski, M. J., Smalley, R. E., & Tour, J. M. (2001). Functionalization of carbon nanotubes by electrochemical reduction of aryl diazonium salts: a bucky paper electrode. *Journal of the American chemical society*, *123*(27), 6536.

42. Heald, C. G., Wildgoose, G. G., Jiang, L., Jones, T. G., & Compton, R. G. (2004). Chemical derivatization of multiwalled carbon nanotubes using diazonium salts. *ChemPhysChem*, *5*, 1794.

43. Kuo, T. C., McCreery, R. L., & Swain, G. M. (1999). Electrochemical modification of boron-doped chemical vapor deposited diamond surfaces with covalently bonded monolayers. *Electrochemical and solid-state letters*, *2*(6), 288.

44. Wang, J., Firestone, M. A., Auciello, O., & Carlisle, J. A. (2004). Surface functionalization of ultrananocrystalline diamond films by electrochemical reduction of aryldiazonium salts. *Langmuir*, *20*(26), 11450.

45. Downard, A. J., & Prince, M. J. (2001). Barrier properties of organic monolayers on glassy carbon electrodes. *Langmuir*, *17*(18), 5581.

46. Saby, C., Ortiz, B., Champagne, G. Y., & Bélanger, D. (1997). Electrochemical modification of glassy carbon electrode using aromatic diazonium salts. 1. Blocking effect of 4-nitrophenyl and 4-carboxyphenyl groups. *Langmuir*, *13*(25), 6805.

47. Ortiz, B., Saby, C., Champagne, G. Y., & Bélanger, D. (1998). Electrochemical modification of a carbon electrode using aromatic diazonium salts. 2. Electrochemistry of 4-nitrophenyl modified glassy carbon electrodes in aqueous media. *Journal of Electroanalytical Chemistry*, *455*(1-2), 75.

48. McCreery, R. L. (2008). Advanced carbon electrode materials for molecular electrochemistry. *Chemical reviews*, *108*(7), 2646.

49. Kullapere, M., Jürmann, G., Tenno, T. T., Paprotny, J. J., Mirkhalaf, F., & Tammeveski, K. (2007). Oxygen electroreduction on chemically modified glassy carbon electrodes in alkaline solution. *Journal of Electroanalytical Chemistry*, *599*(2), 183.

50. Whitman, B. W., Miller, D., Davis, R., Brennan, J., & Swain, G. M. (2017). Effect of galvanic current on the physicochemical, electrochemical and mechanical properties of an aerospace carbon fiber reinforced epoxy composite. *Journal of The Electrochemical Society*, *164*(13), C881.

51. Ferrer, K. S., & Kelly, R. G. (2001). Comparison of methods for removal of corrosion product from AA2024-T3. *Corrosion*, *57*(02).

52. Osborn, K. (2010). Army Steps Up Plans to Fight Corrosion, U.S. Army Military Article #36266 (https://army.mil/article/36266/army_steps_up_plans_to_fight_corrosion).

53. Tuinstra, F., & Koenig, J. L. (1970). Raman spectrum of graphite. *The Journal of chemical physics*, *53*(3), 1126.

54. Nemanich, R. J., & Solin, S. A. (1979). First-and second-order Raman scattering from finite-size crystals of graphite. *Physical Review B*, *20*(2), 392.

55. Wang, Y., Alsmeyer, D. C., & McCreery, R. L. (1990). Raman spectroscopy of carbon materials: structural basis of observed spectra. *Chemistry of Materials*, *2*(5), 557.

56. Jawhari, T., Roid, A., & Casado, J. (1995). Raman spectroscopic characterization of some commercially available carbon black materials. *Carbon*, *33*(11), 1561.

57. Liu, Y. C., & McCreery, R. L. (1995). Reactions of organic monolayers on carbon surfaces observed with unenhanced Raman spectroscopy. *Journal of the American Chemical Society*, *117*(45), 11254.

58. Chen, P., & McCreery, R. L. (1996). Control of electron transfer kinetics at glassy carbon electrodes by specific surface modification. *Analytical Chemistry*, *68*(22), 3958.

59. Kariuki, J. K., & McDermott, M. T. (1999). Nucleation and growth of functionalized aryl films on graphite electrodes. *Langmuir*, *15*(19), 6534.

60. Kariuki, J. K., & McDermott, M. T. (2001). Formation of multilayers on glassy carbon electrodes via the reduction of diazonium salts. *Langmuir*, *17*(19), 5947.

61. Brooksby, P. A., & Downard, A. J. (2005). Multilayer nitroazobenzene films covalently attached to carbon. An AFM and electrochemical study. *The Journal of Physical Chemistry B*, *109*(18), 8791.

62. Liu, Y. C., & McCreery, R. L. (1997). Raman spectroscopic determination of the structure and orientation of organic monolayers chemisorbed on carbon electrode surfaces. *Analytical chemistry*, *69*(11), 2091.

63. Mahmoud, A. M., Bergren, A. J., Pekas, N., & McCreery, R. L. (2011). Towards integrated molecular electronic devices: Characterization of molecular layer integrity during fabrication processes. *Advanced Functional Materials*, *21*(12), 2273.

64. De Villeneuve, C. H., Pinson, J., Bernard, M. C., & Allongue, P. (1997). Electrochemical formation of close-packed phenyl layers on Si (111). *The Journal of Physical Chemistry B*, *101*(14), 2415.

65. D'Amours, M., & Bélanger, D. (2003). Stability of substituted phenyl groups electrochemically grafted at carbon electrode surface. *The Journal of Physical Chemistry B*, *107*(20), 4811.

66. Swain, G. M. (2007). Solid electrode materials: pretreatment and activation. In *Handbook of electrochemistry* (pp. 111-153). Elsevier.

67. DeClements, R., Swain, G. M., Dallas, T., Holtz, M. W., Herrick, R. D., & Stickney, J. L. (1996). Electrochemical and surface structural characterization of hydrogen plasma treated glassy carbon electrodes. *Langmuir*, *12*(26), 6578.

68. Chen, Q., & Swain, G. M. (1998). Structural characterization, electrochemical reactivity, and response stability of hydrogenated glassy carbon electrodes. *Langmuir*, *14*(24), 7017.

69. Doyle, M. P., Guy, J. K., Brown, K. C., Mahapatro, S. N., VanZyl, C. M., & Pladziewicz, J. R. (1987). Outer-sphere one-electron reductions of arenediazonium salts. *Journal of the American Chemical Society*, *109*(5), 1536.

70. Bowling, R. J., Packard, R. T., & McCreery, R. L. (1989). Activation of highly ordered pyrolytic graphite for heterogeneous electron transfer: relationship between electrochemical performance and carbon microstructure. *Journal of the American Chemical Society*, *111*(4), 1217.

71. Kneten, K. R., & McCreery, R. L. (1992). Effects of redox system structure on electron-transfer kinetics at ordered graphite and glassy carbon electrodes. *Analytical Chemistry*, *64*(21), 2518.

72. Li, L., Doran, K. P., & Swain, G. M. (2013). Electrochemical characterization of trivalent chromium process (TCP) coatings on aluminum alloys 6061 and 7075. *Journal of the Electrochemical Society*, *160*(8), C396.

73. Hirschorn, B., Orazem, M. E., Tribollet, B., Vivier, V., Frateur, I., & Musiani, M. (2010). Determination of effective capacitance and film thickness from constant-phase-element parameters. *Electrochimica acta*, *55*(21), 6218.

74. Dardona, S., Chen, L., Kryzman, M., Goberman, D., & Jaworowski, M. (2011). Polarization controlled kinetics and composition of trivalent chromium coatings on aluminum. *Analytical chemistry*, *83*(16), 6127.

75. Iyer, A., Willis, W., Frueh, S., Nickerson, W., Fowler, A., Barnes, J., Hagos, L., Escarsega, J., Scala, J. L., & Suib, S. L. (2010). Characterization of NAVAIR trivalent chromium process (TCP) coatings and solutions. *Plat. Surf. Finish*, *5*, 32.

76. Dong, X., Wang, P., Argekar, S., & Schaefer, D. W. (2010). Structure and composition of trivalent chromium process (TCP) films on Al alloy. *Langmuir*, *26*(13), 10833.

77. Li, L., Swain, G. P., Howell, A., Woodbury, D., & Swain, G. M. (2011). The formation, structure, electrochemical properties and stability of trivalent chrome process (TCP) coatings on AA2024. *Journal of The Electrochemical Society*, *158*(9), C274.

78. Guo, Y., & Frankel, G. S. (2012). Characterization of trivalent chromium process coating on AA2024-T3. *Surface and Coatings Technology*, *206*(19-20), 3895.

79. Guo, Y., & Frankel, G. S. (2012). Active corrosion inhibition of AA2024-T3 by trivalent chrome process treatment. *Corrosion, The Journal of Science and Engineering*, *68*(4), 045002-1.

80. Qi, J., Gao, L., Li, Y., Wang, Z., Thompson, G. E., & Skeldon, P. (2017). An optimized trivalent chromium conversion coating process for AA2024-T351 alloy. *Journal of The Electrochemical Society*, *164*(7), C390.

81. Pramanik, A., Basak, A. K., Dong, Y., Sarker, P. K., Uddin, M. S., Littlefair, G., Dixit, A. R., & Chattopadhyaya, S. (2017). Joining of carbon fibre reinforced polymer (CFRP) composites and aluminium alloys–A review. *Composites Part A: Applied Science and Manufacturing*, *101*, 1-29.

82. Gebhard, A., Bayerl, T., Schlarb, A. K., & Friedrich, K. (2009). Galvanic corrosion of polyacrylnitrile (PAN) and pitch based short carbon fibres in polyetheretherketone (PEEK) composites. *Corrosion science*, *51*(11), 2524.

83. Wu, X., Sun, J., Wang, J., Jiang, Y., & Li, J. (2019). Investigation on galvanic corrosion behaviors of CFRPs and aluminum alloys systems for automotive applications. *Materials and Corrosion*, *70*(6), 1036.

84. Hur, S. Y., Kim, K. T., Yoo, Y. R., & Kim, Y. S. (2020). Effects of NaCl concentration and solution temperature on the galvanic corrosion between CFRP and AA7075T6. *Corrosion Science and Technology*, *19*(2), 75.

85. Alias, M. N., & Brown, R. (1992). Damage to composites from electrochemical processes. *Corrosion*, *48*(05).

86. Kinoshita, K. (1988). Carbon: electrochemical and physicochemical properties.

87. DeClements, R., & Swain, G. M. (1997). The formation and electrochemical activity of microporous diamond thin film electrodes in concentrated KOH. *Journal of the Electrochemical Society*, *144*(3), 856.

88. Kiema, G. K., Ssenyange, S., & McDermott, M. T. (2004). Microfabrication of glassy carbon by electrochemical etching. *Journal of the Electrochemical Society*, *151*(2), C142.

89. Adenier, A., Cabet-Deliry, E., Chaussé, A., Griveau, S., Mercier, F., Pinson, J., & Vautrin-Ul, C. (2005). Grafting of nitrophenyl groups on carbon and metallic surfaces without electrochemical induction. *Chemistry of Materials*, *17*(3), 491-501.

90. Adenier, A., Barré, N., Cabet-Deliry, E., Chaussé, A., Griveau, S., Mercier, F., Pinson, J., & Vautrin-Ul, C. (2006). Study of the spontaneous formation of organic layers on carbon and metal surfaces from diazonium salts. *Surface Science*, *600*(21), 4801.

91. Usman, B. J., Scenini, F., & Curioni, M. (2020). The effect of exposure conditions on performance evaluation of post-treated anodic oxides on an aerospace aluminium alloy: Comparison between salt spray and immersion testing. *Surface and Coatings Technology*, *399*, 126157.

92. Policastro, S. A., Anderson, R. M., & Hangarter, C. M. (2021). Analysis of galvanic corrosion current between an aluminum alloy and stainless-steel exposed to an equilibrated droplet electrolyte. *Journal of The Electrochemical Society*, *168*(4), 041507.

CHAPTER 3. MITIGATION OF THE GALVANIC AND CARBON CORROSION IN AA2024-T3 ALUMINUM ALLOY - CARBON FIBER REINFORCED POLYMER COMPOSITE JOINTS BY SPONTANEOUS DEPOSITION OF DIAZONIUM ADLAYERS ON EXPOSED CARBON FIBERS

Chapter adapted from *J. Electrochem. Soc. 170*(9) 091503 (2023).© The Electrochemical Society. Reproduced with permission. All rights reserved.

Article: Isuri N. Dammulla and Greg M. Swain. *Inhibiting Metal Galvanic and Carbon Corrosion in Aluminum Alloy-Carbon Fiber Reinforced Composite Joints by Spontaneous Deposition of Diazonium Adlayers on Exposed Carbon Fibers.*

3.1 INTRODUCTION

The use of carbon fiber reinforced polymer (CFRP) composites as a structural component of military and civilian aircraft has increased over the years owing to their high strength to weight ratio, high damage tolerance, fatigue resistance, and corrosion resistance.[1-5] In the assembly of aircraft structures including wings, fuselages and horizontal and vertical stabilizers of the tail, CFRP composites are joined to metallic materials, such as aluminum alloys, by adhesive bonding or mechanical fastening using bolts and rivets.[6,7] Carbon fibers of the CFRP composite are more noble than aluminum alloy in the galvanic series. Therefore, when CFRP composites and aluminum alloys are assembled, a galvanic couple can result if a layer of moisture/electrolyte condenses over the contact area facilitating ion conduction. In such cases, the more noble carbon fibers of the composite will function as a cathode for the reduction of dissolved oxygen and accelerate the oxidation rate of the less noble aluminum alloy– so-called galvanic corrosion.[8,9] This is a significant problem on aerospace assets. The rate of galvanic corrosion can be reduced by eliminating the direct contact between the two materials,[9] using coating systems that provide a corrosion protection for the alloy surface[10,11] and/or applying coatings or adlayers on the CFRP composite to inhibit the cathodic oxygen reduction reaction.

The electrochemically assisted reduction of aryldiazonium salts is an extensively studied surface modification method for carbon electrode materials, which involves a reductive one-electron transfer to the aryldiazonium cation generating aryl radicals at the electrode interface that can covalently bind to carbon,[12,13] metal,[14,15] and semiconductor[16,17] surfaces. The properties of the organic adlayers grafted on conductive surfaces by this method can be tailored by simply varying the substituent groups on the aryl ring. We have previously reported that the galvanic corrosion of aluminum alloys is attenuated when joined with a CFRP composite surface treated with an organic adlayer via the electrochemically assisted reduction of aryldiazonium salts. This surface treatment inhibits the oxygen reduction reaction by blocking the active sites on exposed carbon fibers for O_2 chemisorption - the first step of oxygen reduction reaction (ORR) in aqueous media.[18] Even though the electrochemical reduction of aryldiazonium salts is a simple and rapid way of covalently attaching aryl groups to the carbon surface, grafting of diazonium salts on CFRP composites without any electrochemical assistance would be more practical for application in assembly or repair processes.

Spontaneous grafting of aryl groups to carbon and metallic surfaces by immersing the substrate in an appropriate diazonium salt solution has been reported in literature.[19-22] Spontaneous modification by immersion under open circuit conditions can produce a covalently attached and chemically stable adlayer similar to that produced by the electrochemically assisted process, but at a slower rate. The uniformity and thickness of the spontaneously grafted adlayers depend on the deposition conditions, such as immersion time, concentration of the diazonium salt solution and temperature and the state of the substrate surface.[19]

In the present work, we demonstrate the modification of exposed carbon fiber surfaces of CFRP composites by spontaneous covalent attachment of aryl diazonium adlayers and report on

their influence on the reduction of dissolved oxygen and the galvanic corrosion of conversion-coated AA2024-T3 alloys during a 14-day neutral salt spray exposure.

3.2 EXPERIMENTAL METHODS

Chemical and Reagents. Acetonitrile (Sigma Aldrich) was distilled and stored over activated 5 Å molecular sieves prior to use for removal of water impurity. Tetrabutylammonium tetrafluoroborate (NBu_4BF_4), 4-nitrophenyl diazonium tetrafluoroborate, and sodium sulfate (Na_2SO_4) were all purchased from a commercial supplier (Sigma Aldrich) and used as received. The 4-nitroazobenzene diazonium tetrafluoroborate and 2-fluorene diazonium tetrafluoroborate salts were provided by Professor Richard McCreery and his group at the University of Alberta. Turco 6849 (Henkel Technologies, Madison Heights, MI), after dilution to 20 % v/v, was used for degreasing the specimens. Turco Liquid Smut-Go (Henkel Technologies, Madison Heights, MI), after dilution to 20% v/v, was used to deoxidize the aluminum alloy specimens. Bonderite T-5900 RTU (Henkel Technologies, Madison Heights, MI) was the commercial trivalent chromium process (TCP) coating bath used as-received. All commercial solution dilutions and aqueous electrolyte solutions were prepared with ultrapure water (> 17 Ω-cm) from a Barnstead E-Pure water purification system.

Carbon Fiber Reinforced Epoxy (CFRP) Composite Specimens. A standard airframe composite panel (AS4/3501-6) was provided courtesy of the Polymer and Composites Division at the Naval Air Systems Command (Patuxent River, MD). The panel was a unidirectional cross-ply [0/90]4s laminate prepared with an intermediate modulus polyacrylonitrile (PAN) carbon fiber (7 μm diam.) and a toughened epoxy prepreg (3501-6) from Hexcel. The layup was an orthogonally oriented ply (0/90-degree direction). A symmetric layup at the mid-plane was used to keep the composite from warping due to differences in thermal expansion coefficients of the epoxy and

carbon fibers. The total layup was 16 plys (0/90/0/90/0/90/0/90/90/0/90/0/90/0/90/0). A phenolic sizing material was applied to the carbon fibers before preparing the composite to promote stronger bonding with the epoxy matrix. The composite specimen thickness was 0.25 cm. The CFRP composite panels were cut into 2.4 cm × 1.8 cm pieces for the laboratory tests. Electrical connection was made by inserting a copper wire into a hole drilled on one edge of the specimen and affixing it in place with conducting epoxy, as previously reported.[18,23] Good electrical connection with the carbon fibers was verified using the electrodeposition of Ag particles.[23] The geometric area of the exposed edge (a single edge) used in the electrochemical measurements was 0.45 cm^2. Currents and surface coverages are normalized to this area.

Pretreatment of CFRP Composite Electrodes. For the electrochemical measurements, the edge opposite that where electrical contact was made was first abraded for 3 min on P1500 grit aluminum oxide grinding paper wetted with ultrapure water. This was followed by a 10-min ultrasonic cleaning (40 kHz) in ultrapure water with the composite suspended in the solution. The edge was then mechanically polished with successively smaller grades of alumina powder (1, 0.3, and 0.05 μm) slurried in ultrapure water on separate felt polishing pads. After each polishing step, the composite was rinsed with and ultrasonically cleaned in ultrapure water for 15 min to remove polishing debris. A final ultrasonic cleaning was then performed in pure acetonitrile for 10 min. For the CFRP specimens used in the accelerated degradation testing, a lap joint configuration with the aluminum alloy was used for testing.[18,23] For these tests, all three sides, other than the one with the Cu wire contact, were pretreated by abrading, polishing and surface cleaning, as described above.

Surface Modification of CFRP Composite Specimens. The aryldiazonium salts studied were (i) 4-nitrophenyl diazonium tetrafluoroborate (NP), (ii) 4-nitroazobenzene diazonium tetrafluoroborate

(NAB), and 2-fluorene diazonium tetrafluoroborate (FL). The spontaneous surface modification was performed under open circuit conditions by immersing the pretreated CFRP composite specimen in a solution of 5 mM diazonium salt dissolved in acetonitrile for a specified time (1-24 h) at room temperature. For the electrochemical tests, just the one pretreated edge opposite the edge with the electrical connection was immersed in solution and modified. For the specimens used in the salt spray test, the entire specimen, except for the edge with the electrical connection, was immersed. The electrochemically assisted surface modification was performed using a three-compartment, three-electrode glass cell with a platinum (Pt) flag counter electrode, a silver wire quasi-reference electrode (AgQRE), and the pretreated CFRP composite working electrode. For this, the entire specimen, except for the edge with the electrical connection, was immersed in acetonitrile containing 5 mM of the diazonium salt and 0.1 M NBu_4BF_4 supporting electrolyte. Cyclic voltammetry was used for modification with the applied potential scanned from 0.6 to -0.5 V (vs. Ag QRE) at 50 mV/s for 25 cycles. After the modification, the specimens were thoroughly rinsed with acetonitrile. Raman spectroscopy was then performed to confirm the presence of the adlayer. The surface treated composite specimens were then used soon thereafter in either electrochemical measurements or accelerated degradation tests.

Electrochemical Measurements. All the electrochemical measurements were performed in a three-compartment, three-electrode glass cell with a platinum (Pt) flag counter electrode, a silver chloride reference electrode (Ag/AgCl, 4M KCl), and the CFRP specimen edge as the working electrode. The measurements were made at room temperature using a computer-controlled electrochemical workstation (Model 900, CH Instruments, Austin, TX). A meniscus was formed with the electrolyte solution contacting the edge to be examined electrochemically. The blocking properties of the adlayers were investigated by cyclic voltammetry in naturally aerated 0.5 mM

$K_4Fe(CN)_6$ + 0.5 M Na_2SO_4 at 50 mV/s. Cyclic voltammetric measurements were made in naturally aerated 0.5 M Na_2SO_4 (pH 5-6) at room temperature to assess the impact of the surface functionalization on the oxygen reduction reaction kinetics. Cyclic voltammograms were recorded at unmodified, electrochemically modified, and spontaneously modified CFRP composite edges in 1M KCl as a function of scan rate (from 0.1 to 0.5 V/s) to study the influence of diazonium modification on the magnitude of background charging current and capacitance. The capacitance was calculated from the slope of the background current-scan rate plots using the equation,

$$j = C_{dl}\nu \qquad (1)$$

where, j (A/cm^2) is the background current density, C_{dl} is the capacitance (F/cm^2), and ν is the scan rate (V/s). The assumption in the analysis is that all the background current is capacitive in nature, which is unlikely for the carbon fibers due to the expected presence of electroactive surface carbon-oxygen functional groups terminating the graphitic edge plane sites. Therefore, the capacitance values calculated and reported herein are apparent and overestimates of the true values.

Mixed Potential Theory. A wrought AA2024-T3 aluminum alloy (2.54 cm × 2.54 cm) specimen was first abraded on a P1500 grit aluminum oxide grinding paper for 4 min and ultrasonically cleaned in ultrapure water for 20 min. The specimen was then polished with 0.3 μm alumina for 4 min. This was followed by a 20-min ultrasonic cleaning in ultrapure water. The alloy specimen was then degreased, deoxidized and surface treated with TCP conversion coating by immersion, as described previously.[24,25] The electrochemical measurements were performed using a computer-controlled electrochemical workstation (Gamry Instruments, Inc., Reference 600, Warminster, PA). The counter electrode was a Pt flag, and the reference was an Ag/AgCl electrode (4 M KCl). All measurements were made in naturally aerated 0.5 M Na_2SO_4 + 0.01 M NaCl at room temperature. The TCP-coated alloy specimen was mounted at the bottom of a single-compartment

glass electrochemical cell with an O-ring defining the solution contact area (0.2 cm^2). The electrochemical testing proceeded as follows: (i) measurement of the open circuit potential (OCP) for 1 h (until stable); (ii) recording an anodic potentiodynamic polarization curve from -50 mV vs OCP to 1 V. The polarization measurements of the unmodified, electrochemically modified, and spontaneously modified CFRP composite specimens were made in a three-compartment, three-electrode glass electrochemical cell with the same counter and reference electrodes. The composites were modified electrochemically (25 potential cycles) and spontaneously with NP (24-h immersion). One modified edge, opposite that where the electrical contact was made, was contacted with the solution (0.45 cm^2). The electrochemical testing proceeded as follows: (i) measurement of OCP for 1 h (until stable); (ii) recording a cathodic potentiodynamic polarization curve from +50 mV vs OCP to -1 V. All the anodic and cathodic potentiodynamic polarization scans were recorded at 1 mV/s.

Rotating Disk Voltammetry. The rotating disk voltammetric measurements were performed using a glassy carbon disk electrode (GC RDE). The electrode diameter was 0.3 cm (0.07 cm^2). The electrode was pretreated prior to a measurement by mechanical polishing with successively smaller grades of alumina (1, 0.3 and 0.05 μm diam.) slurried in ultrapure water. Each polishing step was performed for 3 min on separate felt pads to avoid cross contamination of the polishing grit. After each step, the electrode was rinsed with and ultrasonically cleaned in ultrapure water for 10 min to remove polishing debris. A final ultrasonic cleaning in pure acetonitrile was performed for 10 min. The GC RDE was then spontaneously modified with NP, as described above, for 24 h under open circuit conditions. The electrochemical measurements were performed in the three-compartment, three-electrode glass cell. The OCP was initially measured for at least 30 min in naturally aerated 0.5 M Na_2SO_4. Cathodic polarization curves were then recorded at 0, 100, 200,

300, 400 and 500 rpm from the OCP to a more negative potential of -1.2 V. The scan rate was 1 mV/s.

Aluminum Alloy Preparation. Wrought aluminum alloy 2024-T3 was obtained as a 1 mm-thick sheet (www.onlinemetals.com) and cut into 5.5 cm × 3.6 cm pieces. The alloy specimens were then abraded, polished, degreased, deoxidized and surface treated with TCP, as described elsewhere.[24,25] The TCP coating was formed by a 10-min immersion at room temperature.

Neutral Salt Spray Testing (ASTM B117). TCP-coated aluminum alloy specimens were lap joined with spontaneously modified or unmodified CFRP composite specimens using a single stainless-steel 316L fastener. The torque applied was 45 lb-in. The composite specimen edges were spontaneously modified by full immersion in 5 mM diazonium salt dissolved in acetonitrile for 24 h under open circuit conditions. The specimens were then thoroughly rinsed with acetonitrile. The stainless-steel fastener threads were wrapped with Teflon tape to prevent direct electrical contact with the hole wall. The exposed bolt head and nut were covered with a commercial silicone sealant (DAP KWIK SEAL ULTRA) to repel moisture and electrically isolate the metal from the solution mist. The back side of the aluminum alloy specimen was covered with corrosion protection tape (Scotchrap™, 3M Co.) so that only the front surface and the edges of the alloy were exposed to the salt spray environment. Mechanically fastened aluminum alloy-CFRP composite lap joints were exposed to a continuous salt fog generated from 5 wt. % NaCl at 35 ± 1 °C in a commercial salt spray chamber (Associated Environmental Systems-MX 9204). The test period was 14 days according to ASTM B117 (Standard Practice for Operating Salt Spray (Fog) Apparatus). At the end of the test period, the joined specimens were removed, disassembled, and rinsed thoroughly with and ultrasonically cleaned in ultrapure water for 30 min to remove salt deposits. Additionally, the aluminum alloy specimens were ultrasonically cleaned in concentrated HNO_3 for 10 min

increments to dissolve corrosion product, dried thoroughly with N_2 gas, and weighed.[26] Ultrasonic cleaning in HNO_3 was repeated until the mass change of a specimen was small ($\leq$ 0.002 g). This was followed by a through rinsing in ultrapure water and drying under a stream of N_2 gas prior to any weight measurement or additional material characterization.

Galvanic Current Measurements. Galvanic current measurements were conducted with mechanically fastened aluminum alloy-CFRP composite lap joints subjected to neutral salt spray (ASTM B117, Standard Practice for Operating Salt Spray (Fog) Apparatus). The TCP-coated AA2024-T3 panels were joined with unmodified and spontaneously modified (NAB) CFRP composites as shown in Figure 3.1. A polyimide film cut into the size of the composite was inserted between the composite and the alloy specimen. Insulated wires ran from the aluminum alloy-CFRP composite assemblies out of the salt spray chamber. Current measurements were made by placing a digital multimeter (EX330, Extech Instruments) in the circuit with each aluminum alloy-CFRP composite lap joint several times over the course of the exposure period. The test period was 14 days.

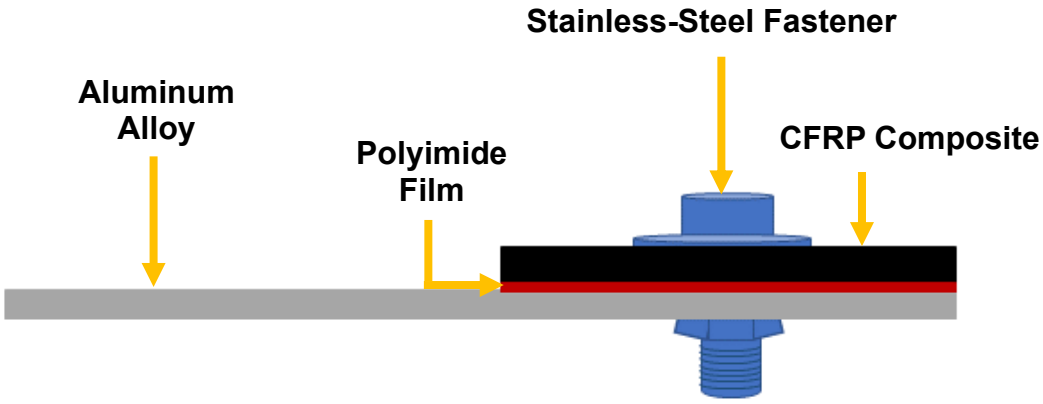

Figure 3.1. Configuration of the joined aluminum alloy-CFRP composite specimen subjected to 14-day neutral salt spray for galvanic current measurements. The geometric ratio of the cathode to anode exposed areas was 0.3 (5.3 cm^2 for the CFRP and 19.8 cm^2 for the aluminum alloy).

Material Characterization. The cleaned aluminum alloy specimens were analyzed by digital optical microscopy (Keyence VHX-6000) and laser confocal microscopy (Nikon C2) to assess the surface texture and corrosion damage. Scanning electron microscopy was performed at the Center for Advanced Microscopy (MSU) using a JSM-6610LV (JEOL USA) general purpose electron microscope. Accelerating voltages used were between 10-15 kV with a working distance of 10 – 13 mm. Raman spectroscopy was performed using an inVia™ confocal instrument(Renishaw). The instrument consisted of a confocal microscope connected to a continuous wave, diode-pumped solid-state laser (100 mW max. with 10 mW applied at the sample) having a fundamental emission at 532 nm. The CFRP composite specimen was positioned under the laser light using a motorized stage. The stage position was controlled, and spectral data acquired with instrument's software (WiREInterface). This software allows for control of the laser power, integration time, spectral range covered, and stage positioning for mapping a sample. A Leica (50×/0.75 N.A.) objective lens was used for focusing the excitation light and collecting the scattered radiation. A notch filter was used to remove the Rayleigh scattered laser light. Each spectrum was acquired using a *ca.* 1 μm spot size with an integration time of 10 s. Each spectrum presented represents an average of 5 spectral acquisitions at each point. An 1800 lines mm^{-1} holographic grating was used for separating the Raman scattered light into its component wavelengths. Wavenumber shift calibration was made using the 521 cm^{-1} phonon line of single crystal Si.

Corrosion Damage Evaluation. The following scale, proposed by the U.S. Army Material Command, was used to grade the alloy specimens after the neutral salt-spray exposure: Stage 0 – shows no visible corrosion; Stage 1 – sample discoloration and staining; Stage 2 – loose isolated rust or corrosion product and early stage pitting of the surface along with minor etching; Stage 3 – more extensive rust or corrosion product, minor etching, pitting and more extensive surface

damage; Stage 4 – extensive rust or corrosion product formation, extensive etching, blistering, deadhesion and pitting that has progressed to the point where the life of the specimen has been affected.[27]

3.3 RESULTS

Raman Spectroscopy. The bonding of a diazonium adlayer on the CFRP composite specimens, formed by immersion, was confirmed by Raman spectroscopy.

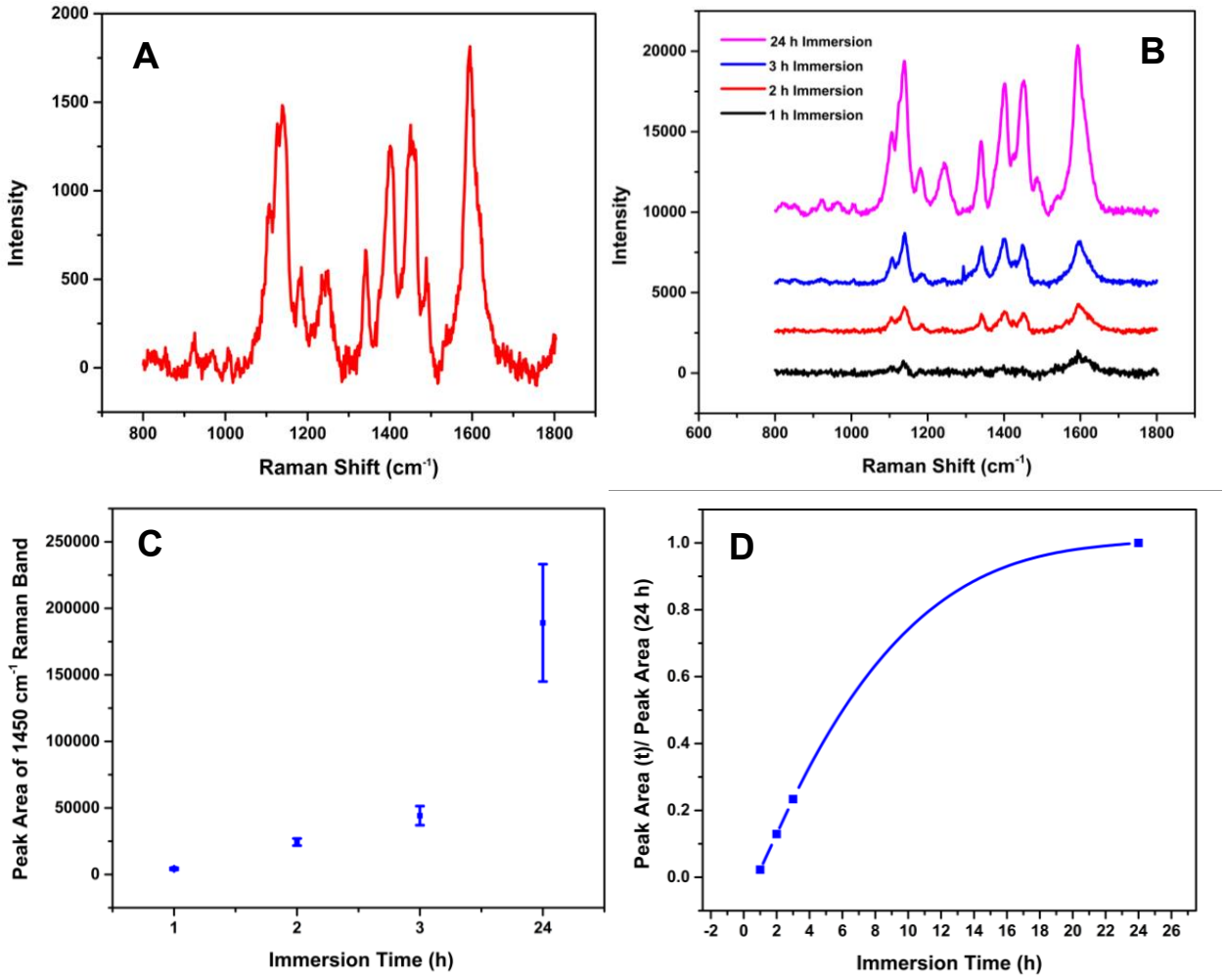

Figure 3.2. Raman spectra for (A) solid 4-nitroazobenzene diazonium salt and (B) CFRP composite edges after different immersion times (1-24 h) in a 5 mM 4-NAB salt + acetonitrile solution. The spectra in B have been background corrected for the spectral features arising from the underlying carbon. (C) Plot of 1450 cm^{-1} peak area vs. immersion time. Data are presented as mean ± std. dev. for n=3 specimens at each immersion time. (D) Plot of 1450 cm^{-1} peak area (t)/peak area (24 h) vs. immersion time.

The spectrum for a 4-nitroazobenzene diazonium tetrafluoroborate salt particle and spectra for CFRP composite specimens after immersion in 5 mM NAB dissolved in acetonitrile for 1, 2, 3 and 24 h are presented in Figure 3.2A and B. The spectral features for the salt are conserved when the admolecule is grafted on the composite surface. All the spectra for the modified composites exhibit Raman bands characteristic of the aryl diazonium molecule. The peak intensities increased with immersion time, as is presented in Figure 3.2B. The primary bands corresponding to NO_2 stretching, N=N stretching, and phenyl ring C=C stretching vibrations are observed at 1350, 1450, and 1598 cm^{-1} respectively.[36,37] The increase in Raman peak intensity with immersion time is indicative of an increasing surface coverage of NAB admolecules with time. Figure 3.2C presents the peak area of the Raman band at 1450 cm^{-1} as a function of immersion time. The peak area is related to the number of Raman scatterers on the surface and this coverage increases with time. Figure 3.2D shows how the normalized surface coverage of the aryl diazonium, (1450 cm^{-1} peak area (t)/peak area for 24 h) changes with time for one set of composite measurements. In fact, when pooling all the data, there was such a large variation in the mean value for the 24-h immersion that we do not yet know how long of an immersion time is needed to achieve maximum coverage.

In related work, the surface coverage of the 4-nitrophenyl admolecule as a function of immersion time has (i.e., film formation) been previously reported on using Fourier transform infrared reflection absorption spectroscopy (FT-IRRAS) and atomic force microscopy (AFM).[38] The FT-IRRAS spectra exhibited bands characteristic of nitrophenyl groups on an iron surface that increased in intensity with immersion time. The AFM analysis revealed the grafting of 4-nitrophenyl diazonium molecules in the first 5 min of immersion occurred through the formation of small islands on the electrode. After 30 min immersion, a homogeneous layer was formed. The adlayer became more compact as the immersion time was increased to 2 h. The substrate was no

longer visible by the dense adlayer formed after a 5-h immersion. Future work will focus on investigating how the surface coverage changes with immersion time and diazonium molecule concentration.

Blocking Properties. Molecular adlayer formation on the exposed carbon fibers was achieved under open circuit conditions by immersing the specimen in a solution of the aryl diazonium salt dissolved in acetonitrile. The surface coverage and blocking properties of the adlayer formed depends on the immersion time, as shown in Figure 3.3. The effect of the adlayer on the electrochemical properties of the carbon fibers was probed using the surface-sensitive ferri/ferrocyanide redox system. Cyclic voltammetric *i-E* curves for $[Fe(CN)_6]^{-3/-4}$ in 0.5 M Na_2SO_4 at a typical CFRP composite specimen edge, before and after the spontaneous modification with 4-nitrophenyl diazonium (NP), are presented. The immersion times were 5, 15, 30 and 60 min or 1 h. The curve for the unmodified specimen reflects quasi-reversible electron-transfer kinetics with well resolved oxidation and reduction peaks at 0.325 and 0.244 V, respectively, giving a ΔE_p of 81 mV. The 5-min immersion time produces an NP adlayer that suppresses the oxidation current by close to 35%. The oxidation peak is shifted positive to 0.493 V and the reduction peak shifted negative to 0.158 V giving a ΔE_p of 335 mV. The increased ΔE_p reflects a more sluggish electron transfer kinetics caused by the blocking effects of the adlayer.

The 15, 30, and 60-min immersion times suppress the oxidation and reduction reaction currents such that no oxidation or reduction peaks are seen for the 30-and 60-min immersed specimens. Figure 3.3B provides a better visualization of cyclic voltammetric *i-E* curves after 15-, 30- and 60-min immersion times. Immersion times of 30 min, or greater, allow for the spontaneous formation of NP adlayers that are low in defects (pin holes) and thicker such that the adlayer cannot be penetrated by the $[Fe(CN)_6]^{4-}$ ions. Additionally, the adlayer functions as a

barrier to electron tunneling between the redox probe and the exposed carbon fibers. This type of blocking behavior is commonly observed for this highly charged redox system at diazonium-modified carbon electrodes of various types[28-31] and metal electrodes.[32-35]

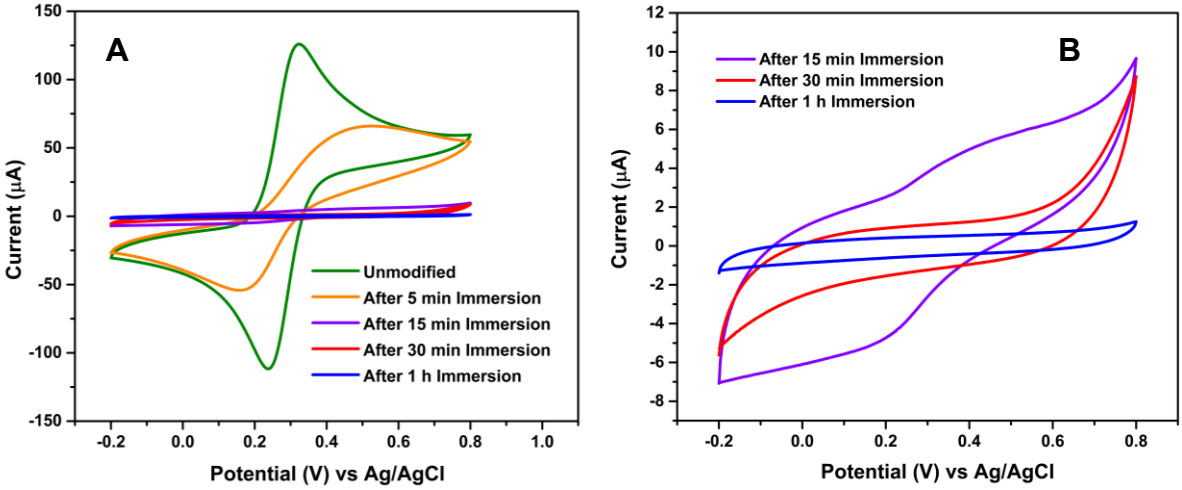

Figure 3.3. Cyclic voltammetric *i-E* curves recorded for (A) 0.5 mM $[Fe(CN)_6]^{-3/-4}$ in 0.5 M Na_2SO_4 at unmodified and spontaneously modified CFRP composite specimens after immersion for 5, 15, 30 and 60 min under open circuit conditions in a 5 mM 4-nitrophenyldiazonium (NP) solution. (B) Expanded axis *i-E* curves for 0.5 mM $[Fe(CN)_6]^{-3/-4}$ in 0.5 M Na_2SO_4 at spontaneously modified CFRP composite specimens after immersion for 15-, 30- and 60-min. Scan rate = 50 mV/s. Geometric area = 0.45 cm^2.

Oxygen Reduction Current. Figure 3.4 presents the cyclic voltammetric *i-E* curves for the reduction of dissolved oxygen at a typical CFRP composite edge before and after surface treatment with a NP adlayer. The curves were recorded in naturally aerated 0.5 M Na_2SO_4 between 1.0 and -0.8 V vs. Ag/AgCl (4M KCl) at 0.01 V/s. The reduction current for dissolved oxygen at -0.8 V is progressively attenuated for NP adlayers formed for 0.25, 0.5, 1, 6, and 24 h. The largest oxygen reduction current between -0.4 and -0.8 V (black curve) is seen for the unmodified CFRP edge with a current of *ca.* -155 μA at -0.8 V. Clearly, the current at all potentials is controlled by electron-transfer kinetics. Mass transfer-controlled currents are not achieved in this potential range. There is a progressive diminution in the current at this potential with increasing immersion time for

adlayer formation. It should be noted that the 15-, 30-, and 60-min immersion times did not produce adlayers compact enough for the total inhibition of the reduction current for the small, neutral O_2 molecule, as was observed for the highly charged $[Fe(CN)_6]^{-3/-4}$. Figure 3.4A reveals that the reduction current at -0.8 V decreased by 42, 55, and 74% after immersion times of 0.5, 1, and 6 h, respectively. The NP adlayer formed during the 24-h immersion, however, reduced the oxygen reduction reaction current by 99% (Figure 3.4A and B). The results indicate that a more compact, less defective adlayer preventing dissolved O_2 molecules from reaching the underlying carbon is formed by immersion for 24 h.

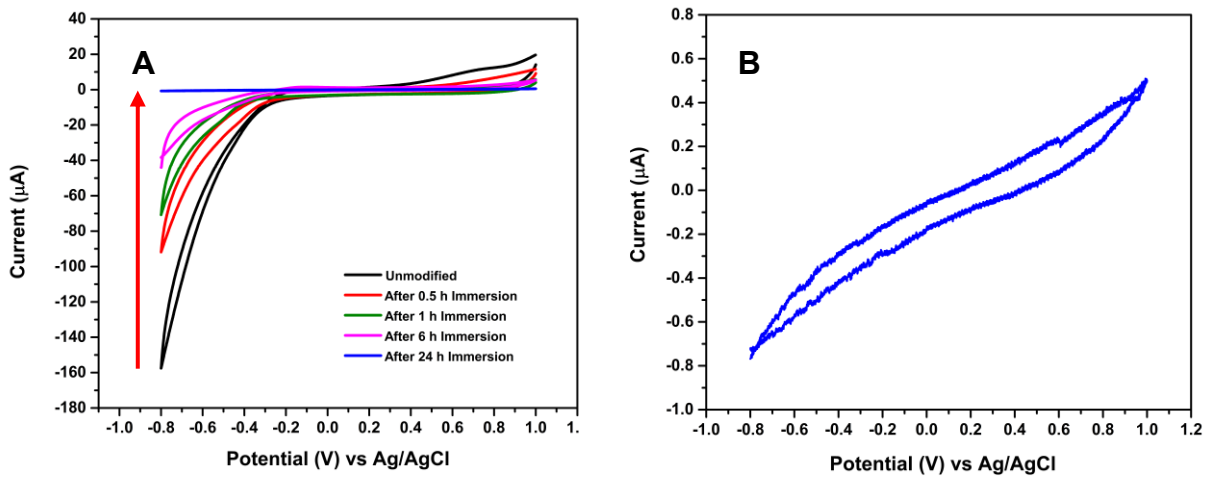

Figure 3.4. (A) Cyclic voltammetric *i-E* curves for dissolved oxygen reduction at unmodified and spontaneously modified CFRP composite specimens with 4-nitrophenyl diazonium (NP) for 0.5, 1, 6, and 24 h in naturally aerated 0.5 M Na_2SO_4. (B) Cyclic voltammetric *i-E* curve for a CFRP composite specimen spontaneously modified with NP for 24 h in naturally aerated 0.5 M Na_2SO_4. Scan rate = 0.01 V/s. Geometric area = 0.45 cm^2.

The decreased carbon fiber activity for oxygen reduction is not due to contamination by the acetonitrile as a 24-h immersion in pure solvent produced little change in the current at -0.8 V as compared to the unmodified specimen (*i.e.*, -150 µA). The results from this control experiment affirm that the decreased activity for the surface-sensitive oxygen reduction reaction arises from the site blocking effect of the NP adlayer. Mechanistically, we suppose the adlayer prevents

chemisorption of the O_2 molecule which is the initial step in the redox reaction in aqueous media. The chemisorption weakens the O=O double bond and lowers the activation energy for electron transfer.[39-41] In aqueous electrolyte solution, the oxygen reduction reaction involves a multi-step proton and electron transfer pathway to form water according to (neutral or alkaline media): $O_2 + 2H_2O + 2e^- \rightarrow H_2O_2 + 2OH^-$. Additionally, the compact, less defective adlayer acts as an effective tunneling barrier for electron transfer between the dissolved O_2 molecule and the underlying carbon fiber surface.

We recently reported that diazonium modification of the CFRP composite edge by an electrochemically assisted process inhibits the oxygen reduction reaction kinetics and leads to less galvanic corrosion on aluminum alloy-CFRP composite joints when tested during neutral salt-spray exposure.[18] The adlayer studied in the prior work was NP. The spontaneous modification for 24 h with NP more effectively inhibits the oxygen reduction reaction kinetics. This can be seen in the comparison data shown below. Figure 3.5 presents cyclic voltammetric *i-E* curves for dissolved oxygen reduction in naturally aerated 0.5 M Na_2SO_4 at unmodified, electrochemically modified and spontaneously modified CFRP composite specimens. The electrochemical modification was performed by cyclic voltammetry in acetonitrile containing 5 mM NP and 0.1 M NBu_4BF_4, as reported elsewhere.[18] No electrolyte salt was added to the acetonitrile solution for the spontaneous modification. The electrochemically formed NP adlayer attenuated the oxygen reduction current at -0.8 V by only 67% while the spontaneously formed adlayer totally inhibited the current. The NP adlayer spontaneously formed for 24 h is more compact, less defective, and perhaps thicker than the adlayer formed by the electrochemically assisted grafting. Future work will involve studies of the adlayer coverage and thickness across the electrode surface as a function of the diazonium concentration and immersion time.

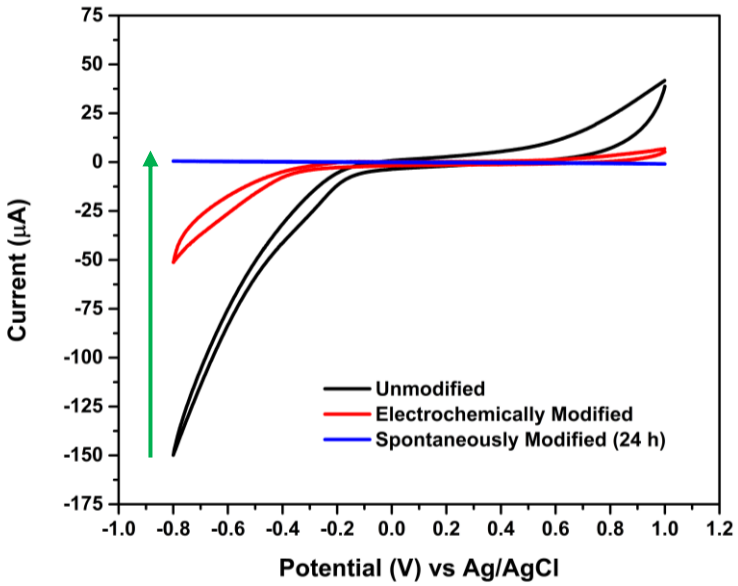

Figure 3.5. Cyclic voltammetric *i-E* curves recorded in naturally aerated 0.5 M Na_2SO_4 at unmodified, electrochemically modified, and spontaneously modified (24 h) CFRP composite specimens. The aryl diazonium used for the surface treatment was 4-nitrophenyldiazonium (NP). Scan rate = 0.01 V/s.

Evaluation of the effect of the diazonium admolecule type on the oxygen reduction reaction kinetics was also performed. Cyclic voltammetric *i-E* curves for CFRP composite specimens spontaneously modified with NP, NAB, and FL for 24 h are presented in Figure 3.6A. Both the NP and NAB modifications attenuated the current for dissolved oxygen reduction by *ca.* 99%. The FL modification, however, reduced the current by only 80%, as compared to the unmodified specimen. This suggests that the FL adlayer is not as compact and defect free as are the NP and NAB adlayers. The 2-fluorene diazonium cation has three rings covalently bonded together making it slightly bulkier than the NP and NAB admolecules. The bulkier nature may limit the coverage and or prevent the close packing of FL admolecules. Figure 3.6B shows the *i-E* curves for the NP and NAB modified composites are similar. Future work will involve more detailed studies of the effect of the diazonium admolecule structure on suppression of the oxygen reduction reaction kinetics.

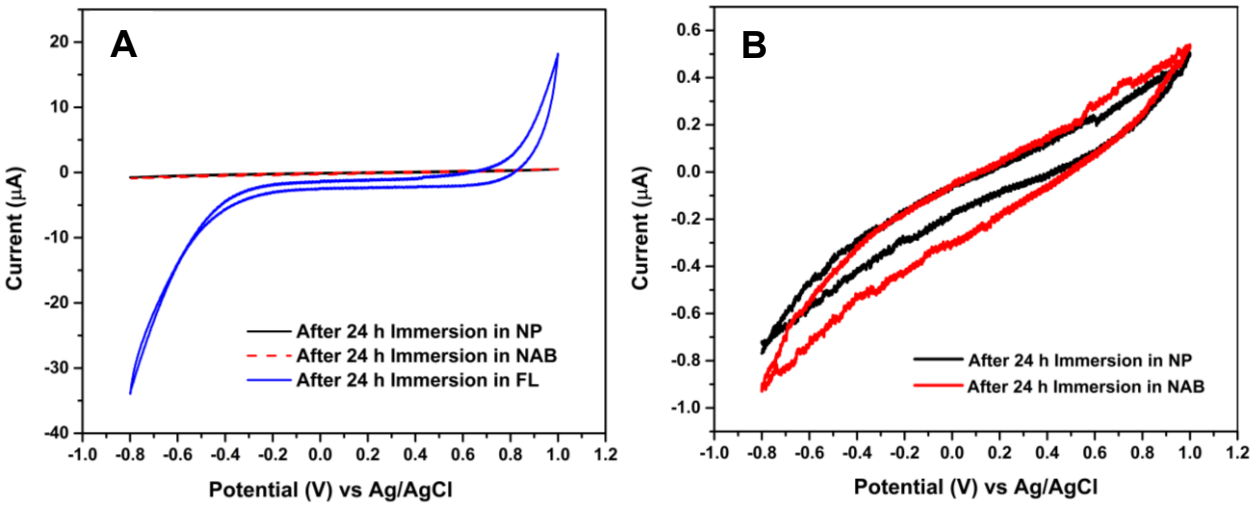

Figure 3.6. Cyclic voltammetric *i-E* curves for CFRP composite specimens spontaneously modified with 4-nitrophenyldiazonium (NP), 4-nitroazobenzenediazonium (NAB), and 2-fluorenediazonium (FL) adlayers for 24 h. The measurements were made in naturally aerated 0.5 M Na_2SO_4. Scan rate = 0.01 V/s. Geometric area = 0.45 cm^2.

Background Current and Capacitance. Figure 3.7A provides a comparison of background cyclic voltammetric *i-E* curves for unmodified, electrochemically modified, and spontaneously modified (24 h) CFRP composite specimens in 1 M KCl. Both the electrochemical and spontaneous modifications were performed using NP. The background current decreases in the following order: unmodified >>> electrochemically modified > spontaneously modified (24 h). The low background current is a result of the passivation of the composite surface by diazonium adlayer. The adlayer acts as a dielectric causing an increase in the separation distance between the charged electrode and the electrolyte solution, thereby decreasing the capacitance. The background current at 0.2 V vs. scan rate plots for unmodified, electrochemically modified and spontaneously modified (24 h) CFRP composite electrodes are presented in Figure 3.7B. The background current at 0.2 V increased linearly with the scan rate consistent with the current being capacitive in nature. In cyclic voltammetry, excess charge is formed on the electrode surface at each applied potential. This excess surface charge is compensated by the reorientation of solvent molecule dipoles at the

electrode surface and the movement of oppositely charged ions toward the surface. This movement of counterbalancing charge is the capacitive background current. The scan rate can be considered as the rate at which the excess charge on the electrode surface is changed. The excess charge density created per unit time increases with the scan rate thereby increasing the number of ions moving toward the electrode for charge compensation per unit time; in other words, increasing the current.

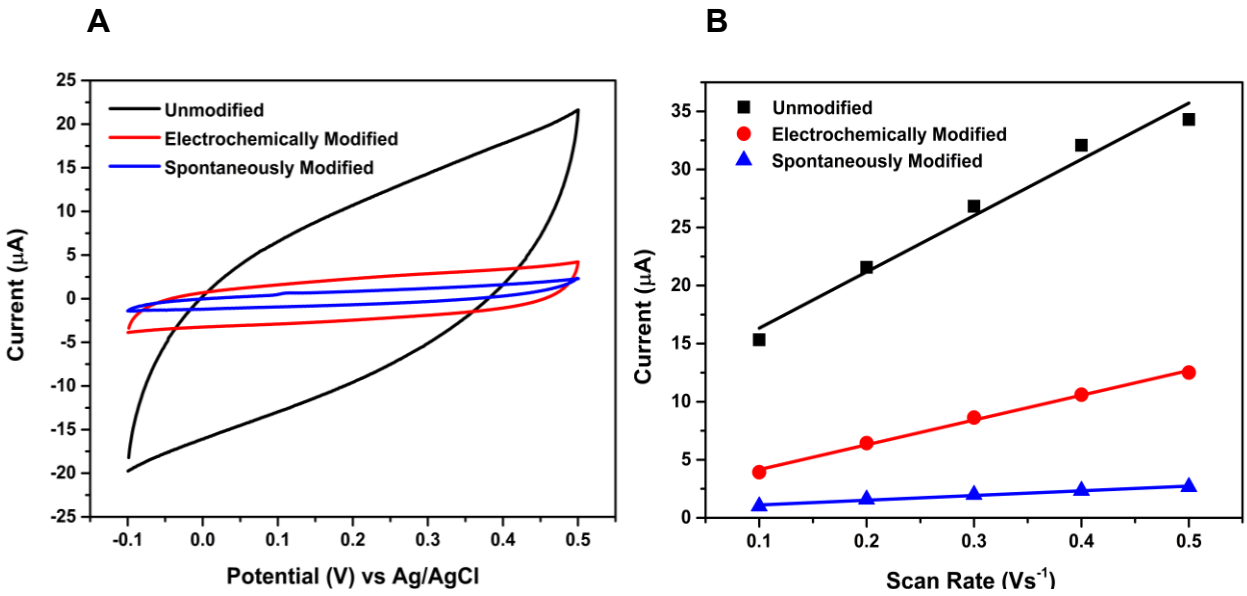

Figure 3.7. (A) Background cyclic voltammetric *i-E* curves recorded in 1M KCl at an unmodified, electrochemically modified, and spontaneously modified (24 h immersion) CFRP composite specimen. The diazonium salt used was NP. Scan rate = 50 mV/s. (B) Background current at 0.2 V vs scan rate plots for unmodified, electrochemically modified and spontaneously modified (24 h) composites. The linear regression equations for the unmodified, electrochemically modified, and spontaneously modified electrodes are y = 48.44x + 11.49, y = 21.33x + 2.02, and y = 4.07x + 0.70, respectively. The R^2 values are 0.9709, 0.9956, and 0.9785, respectively. Geometric area = 0.45 cm^2. Data reflect single measurements with each modified composite.

As mentioned above, the capacitance was calculated from the slope of the background current vs. scan rate plot according to Equation 1. The interfacial capacitance, C_{dl}, based on the current measured at 0.2 V, is estimated to be 108, 47 and 9 μF/cm^2, respectively, for an unmodified, electrochemically modified, and spontaneously modified (24 h) specimens (single specimens of each type). The capacitance is *ca.* 2× lower for the composite specimen electrochemically modified

with NP and *ca.* 12× lower for the CFRP composite electrode spontaneously modified with NP, as compared to the unmodified control. The decrease in interfacial capacitance arises from a more compact and less defective, and a thicker adlayer spacing the counterbalancing charge further away from the composite on the solution side of the interface.

Mixed Potential Theory. Figure 3.8 represents the cathodic and anodic polarization curves recorded with (i) unmodified and surface modified CFRP composites and (ii) a TCP-coated AA2024-T3 specimen in naturally aerated 0.5 M Na_2SO_4 + 0.01 M NaCl.

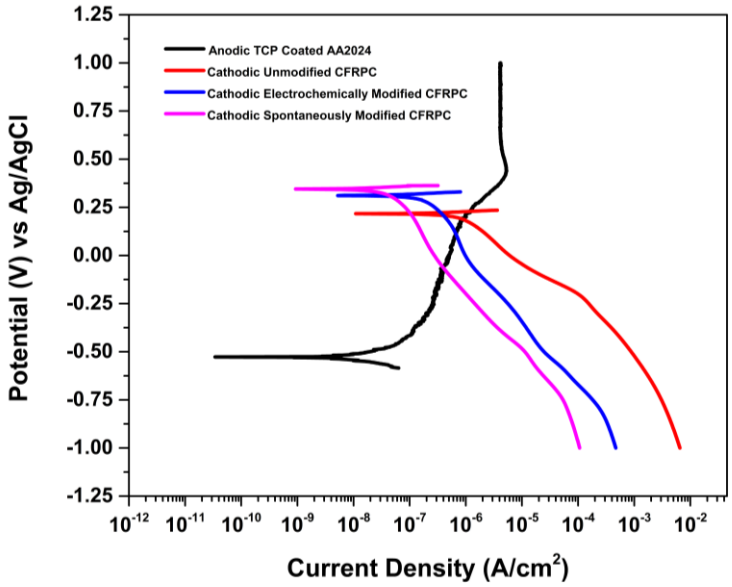

Figure 3.8. Anodic and cathodic potentiodynamic polarization curves recorded in naturally aerated 0.5 M Na_2SO_4 + 0.01 M NaCl at room temperature for the following specimens: TCP-coated AA2024 with (i) an unmodified CFRP composite, (ii) a CFRP composite modified electrochemically with NP and (iii) a CFRP modified spontaneously with NP. Scan rate=1 mV/s.

The data for replicate measurements are summarized in Table 3.1. As can be seen in the figure, the OCP of the unmodified CFRP composite is 0.220 V. The OCPs of the CFRP composites modified electrochemically and spontaneously with NP are more noble at 0.310 V and 0.347 V, respectively. The OCP shifts to more positive (noble) potentials upon diazonium surface modification because of the surface passivation by the NP adlayer. The cathodic reaction occurring at the unmodified/modified CFRP composite is oxygen reduction. This was confirmed from

cathodic polarization curves recorded after purging the electrolyte solution with N_2, which decreased the current in -0.25 to -1.0 V range.

Table 3.1. A summary of corrosion potential and corrosion current density data.

	Corrosion Potential (E_{corr}) / mV vs. Ag/AgCl	**Corrosion Current Density (J_{corr}) / Acm^{-2}**
Unmodified CFRP + TCP AA2024	250 ± 53	15.4 (± 5.5) × 10^{-7}
Echem. Mod. CFRP + TCP AA2024	113 ± 2	6.6 (± 0.2) × 10^{-7} (2.3× lower)
Spont. Mod. CFRP + TCP AA2024	-75 ± 16	3.7 (± 0.1) × 10^{-7} (4.2× lower)

Data are presented as mean ± std. dev. for n=3 specimens of each type.

The largest oxygen reduction current density of 3.8 ×10^{-3} A cm^{-2} at -0.8 V is observed for the unmodified CFRP composite. The oxygen reduction current density for the electrochemically modified and spontaneously modified CFRP composite specimens at -0.8 V is 2.5 × 10^{-4} A cm^{-2} and 6.7 × 10^{-5} A cm^{-2}, respectively. In other words, the oxygen reduction current density at -0.8 V for the composite electrochemically modified with NP is 15× lower and the current density for the composite spontaneously modified with NP is 56× lower than the unmodified composite. This can be attributed to the behavior of the NP adlayer as a physical blocking layer, which prevents dissolved O_2 molecules from reaching the underlying carbon and reduces the rate of electron transfer, hence the current. The lower current density for the spontaneously modified as compared to the electrochemically modified composite indicates the presence of a less defective NP adlayer. This is consistent with the capacitance measurements presented in Figure 3.7.

Potentiodynamic polarization curves are presented in Figure 3.8 for a typical TCP-coated AA2024-T3 panel and three different CFRP specimens: (i) unmodified, (ii) electrochemically modified with NP (25 cycles), and (iii) spontaneously modified with NP (24-h immersion). Using mixed potential theory, the crossing point of cathodic curves with the respective anodic curve is used to determine the corrosion potential, E_{corr}, and estimate the corrosion current density, J_{corr}, at

E_{corr}. At this intersection, $J_{anodic} = -J_{cathodic} = J_{corr}$. Corrosion is assumed to be uniform across the surface in this analysis, which is not the case for this alloy. Even so, the data in Table 1 reveal that J_{corr} decreases with the cathodic inhibitor, i.e., the diazonium adlayer, and E_{corr} decreases as the adlayer decreases the area available for oxygen reduction. J_{corr} is decreased by 2.3 and 4.2× for the electrochemically and spontaneously modified CFRPs. The negative shift of E_{corr} is also reflective of the cathodic reaction inhibition provided by the NP adlayer.

Rotating Disk Voltammetry. The inhibition of the oxygen reduction current was also studied using a GC rotating disk electrode after spontaneous modification with NP in naturally aerated 0.5 M Na_2SO_4. Figure 3.9 shows cathodic potentiodynamic polarization curves for unmodified, electrochemically modified (25 cycles), and spontaneously modified (24 h immersion) GC-RDEs at different rotation rates. It was confirmed that the current at potentials between -0.4 and -1.2 V is due to the reduction of dissolved oxygen based on the decreased current in this potential region observed under deaerated conditions (by N_2 purging). It can be seen in the curves presented that the OCP shifts negative and the oxygen reduction current increases with increasing rotation rate for the unmodified GC (Figure 3.9A). In contrast, there is much less of a change in the OCP and the oxygen reduction reaction current is changed little by the rotation rate for the electrochemically modified GC (Figure 3.9B). Distinctly, there is no change in the OCP or the current for the spontaneously modified GC with rotation rate (Figure 3.9C). These results clearly indicate that the reaction rate is not limited by mass transport and that NP diazonium adlayer functions as an electron transfer barrier for O_2. The current density for the spontaneously modified GC at -0.7 V at 0 rpm is 10× lower than for the electrochemically modified GC, and both are significantly lower than the current for the unmodified electrode. This is consistent with the spontaneous grafting by a 24-h immersion forming a more compact, better blocking adlayer.

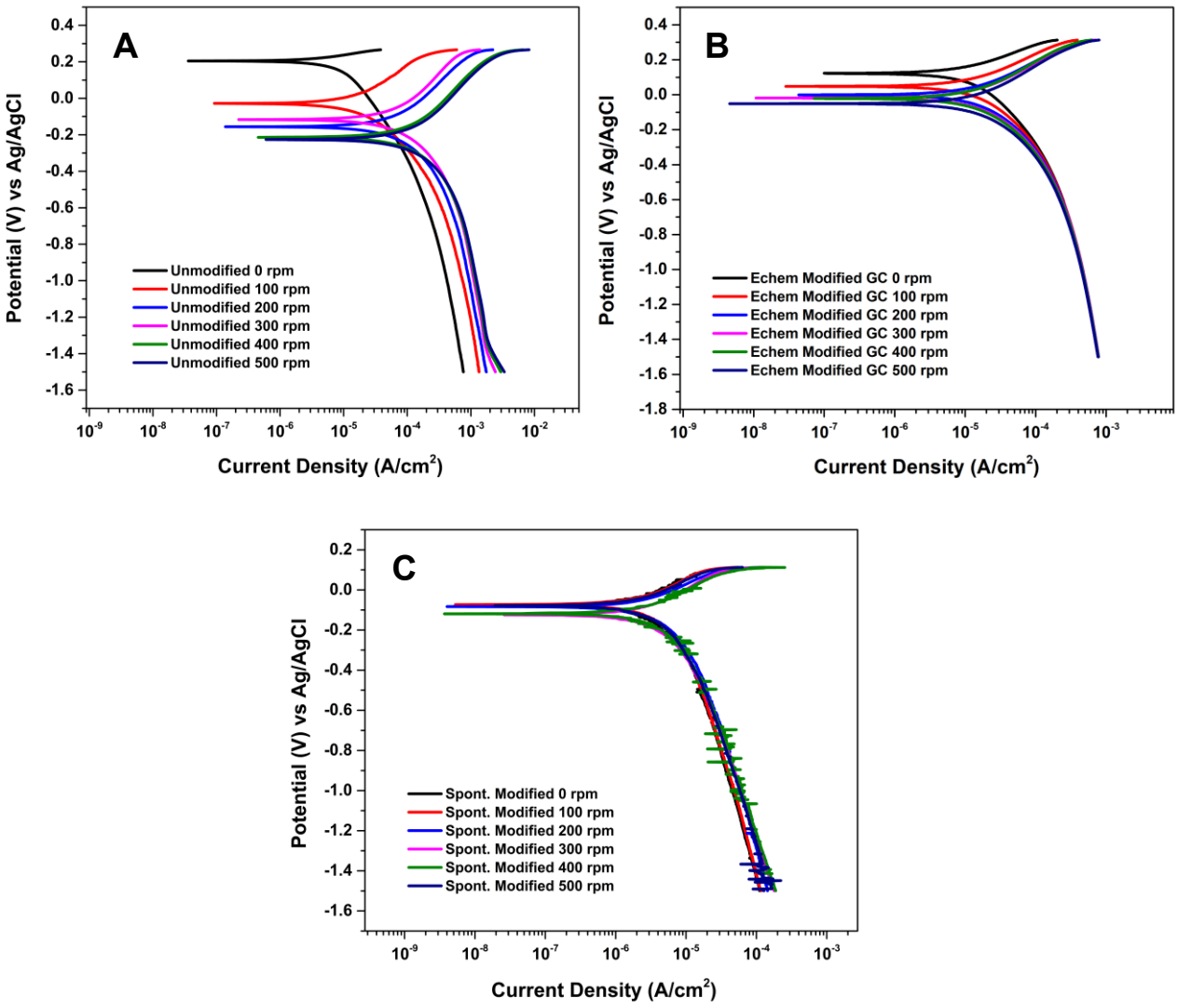

Figure 3.9. Cathodic potentiodynamic polarization curves recorded in naturally aerated 0.5 M Na_2SO_4 at room temperature for a glassy carbon rotating disk electrode: (A) unmodified, (B) electrochemically modified (25 cycles) and (C) spontaneously modified (24 h immersion). The GC RDE was modified with NP. Scan rate = 1 mV/s. Data for rotation rates up to 500 rpm are presented.

Figure 3.10 presents plots of the limiting current at -0.7 V for the (i) unmodified, (ii) electrochemically modified (25 cycles) and (iii) spontaneously modified (24 h immersion) GC RDE as a function of the rotation rate$^{1/2}$. For the unmodified electrode, the current increases linearly with the rotation rate$^{1/2}$ as predicted by the Levich equation (Equation 2).

$$i_l = 0.62nFAD_O^{2/3}\omega^{1/2}\nu^{-1/6}C_O^* \qquad (2)$$

in which i_l is the limiting current (A), A is the electrode area (cm^2), C is the concentration of dissolved oxygen (mol/cm^3), D is the diffusion coefficient for dissolved oxygen (cm^2/s), ν is the kinematic viscosity (cm^2/s), and ω is the electrode rotation rate (s^{-1}). n and F have their usual meanings. The linearity of the plot indicates that mass transfer-influenced oxygen reduction is occurring.

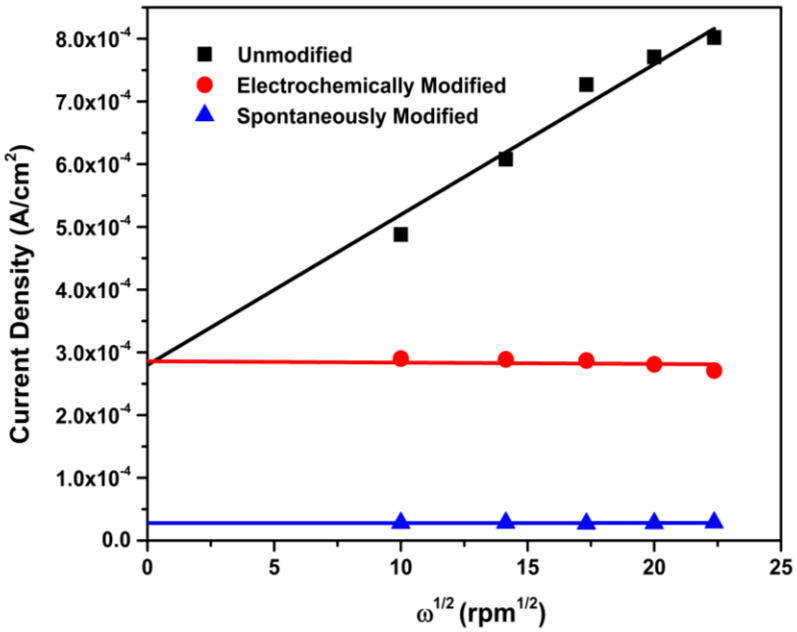

Figure 3.10. Plot of the current density at -0.7 V vs. Ag/AgCl as a function of the square root of the rotation rate ($\omega^{1/2}$) for a GC RDE (a) unmodified (black), (B) electrochemically modified (25 cycles) (red), and spontaneously modified (24 h immersion) (blue) in naturally aerated 0.5 M Na_2SO_4. The GC RDE was modified with NP. The linear regression equations for the unmodified, electrochemically modified and spontaneously modified electrodes are $y = 2.40\times10^{-5}x + 2.80\times10^{-4}$, $y = 2.13\times10^{-7}x + 2.86\times10^{-4}$, and $y = 6.42\times10^{-9}x + 2.79\times10^{-5}$, respectively The R^2 values are 0.9619, 0.6965, and -0.3250, respectively. Data are presented for one electrode of each type.

In contrast, the currents for the two modified electrodes are independent of the rotation rate$^{1/2}$. This means that the mass transfer kinetics are not limiting the current, *i.e.*, the redox reaction rate, but rather the electron transfer kinetics are. For a simple and reversible redox reaction with no electron-transfer kinetic complications at the potential, the limiting current data are expected to fall along a straight line that intercepts the vertical axis at zero. The plots for all three, but especially the ones for the two diazonium modified electrodes, have best-fit lines that intercept

the vertical axis above zero. This is an indication that the oxygen reduction reaction has an electron transfer kinetic limitation at this potential.

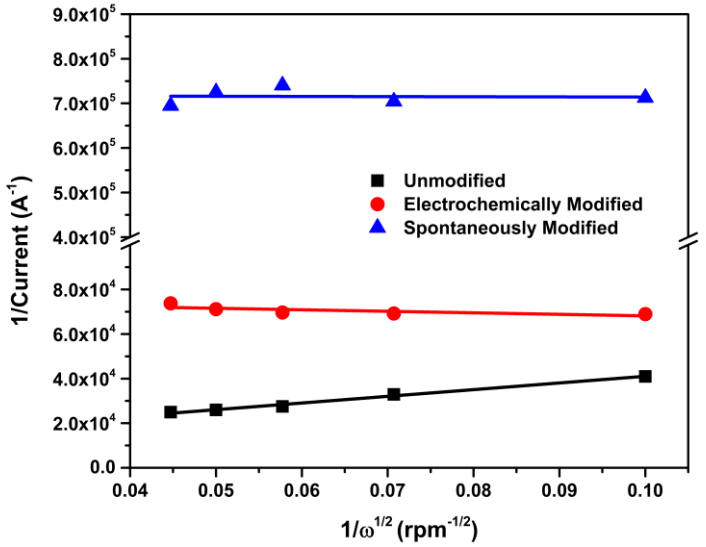

Figure 3.11. Variation of $1/i_k$ at -0.7 V vs. $1/\omega^{1/2}$ for unmodified, electrochemically modified (25 potential cycles) and spontaneously modified (24 h immersion) GC RDEs in naturally aerated 0.5 M Na_2SO_4. The diazonium salt used was NP. These are the data presented in Figure 9.

Figure 3.11 presents the Koutecký-Levich plots of the data (Fig. 3.10) for the unmodified, electrochemically modified and, spontaneously modified GC electrodes.

$$\frac{1}{i} = \frac{1}{i_K} + \frac{1}{0.62nFAD_O^{2/3}\omega^{1/2}\nu^{-1/6}C_O^*} \quad (3)$$

Equation 3 represents the Koutecký-Levich equation in which the kinetic current, i_K , is the current in the absence of any mass transfer effects. In other words, i_K is the current that flows under kinetic limitation when the mass transfer is efficient enough to maintain a constant concentration throughout the electrolyte solution. The i_K values extrapolated from the y-intercept ($1/\omega^{1/2} = 0$) of the Koutecký-Levich plots for the unmodified, electrochemically modified and, spontaneously modified GC RDEs are 9.03×10^{-5}, 1.33×10^{-5}, and 1.39×10^{-6} A, respectively. The electrochemically formed NP adlayer on GC lowers i_K by *ca.* 6× while the spontaneously grafted NP adlayer reduces i_K by *ca.* 65×, as compared to the unmodified electrode.

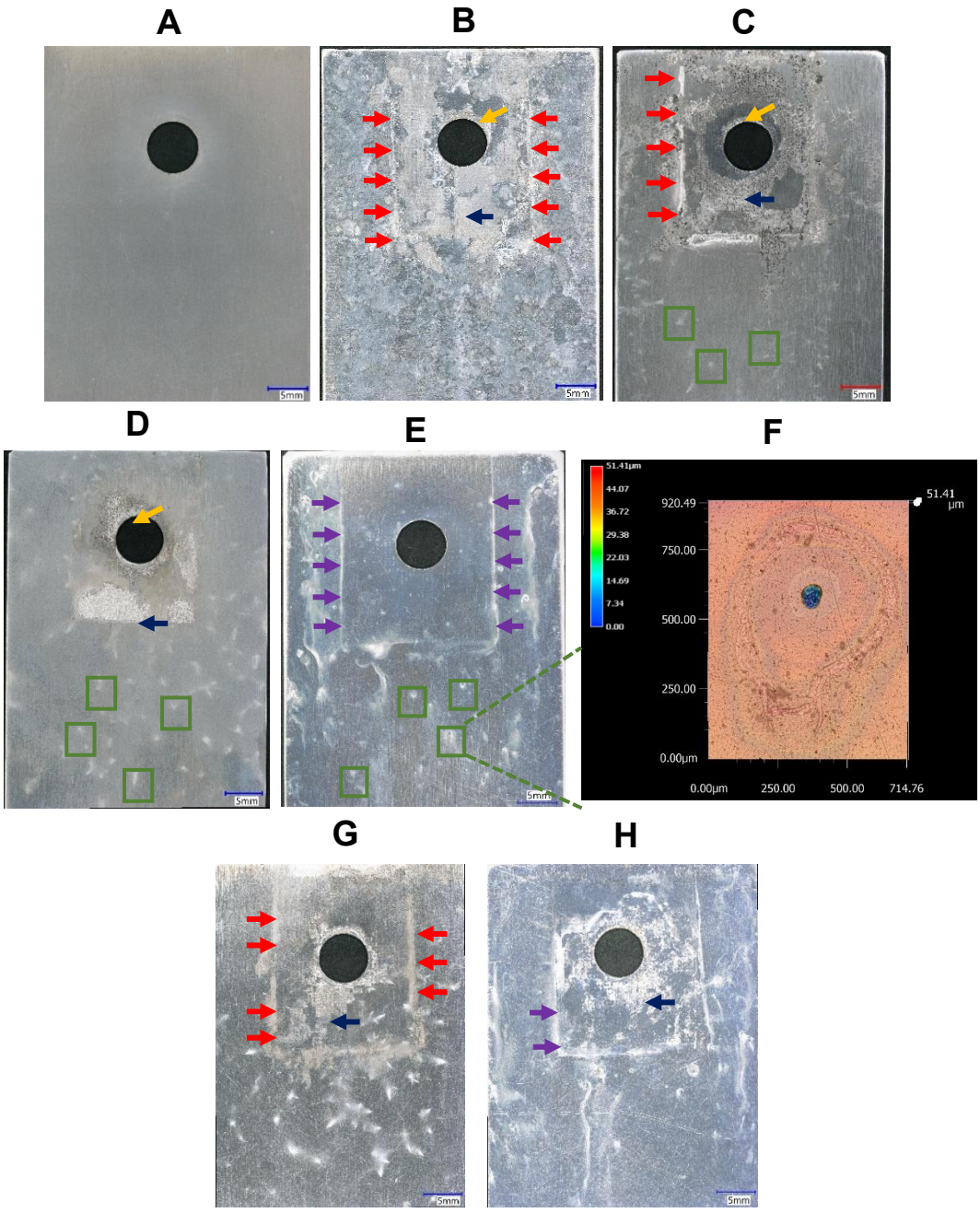

Figure 3.12. Digital optical micrographs of AA2024-T3 panels (5.5 cm × 3.6 cm) (A) with a TCP coating and before salt spray exposure, (B) uncoated and joined with an unmodified CFRP composite after just 3 days of neutral salt spray (NSS) exposure, (C) TCP-coated and joined with an unmodified composite, (D) TCP-coated and joined to a composite electrochemically modified with a 4-nitroazobenzene diazonium (NAB) adlayer, and (E) TCP-coated and joined to a composite spontaneously grafted with a 4-NAB adlayer after 14 days of NSS exposure. (F) Digital microscope 3D contour plot of a discolored region observed on the panel away from the CFRP position demarked by the green box in (E) at 1000×. (G) TCP-coated and joined to a composite electrochemically modified with a 2-fluorene diazonium (FL) adlayer and (E) TCP-coated and joined to a composite spontaneously grafted with a 2-FL adlayer after 14 days of NSS exposure.

Accelerated Degradation Testing. To assess how effective the diazonium surface treatment is at inhibiting galvanic corrosion on the TCP-coated AA2024-T3 alloy, lap joint specimens were assembled, as reported elsewhere[18], and subjected to a 14-day continuous neutral salt spray of 5 wt.% NaCl at 35 °C. The CFRP composites were modified spontaneously by a 24-h immersion in NAB solution under open circuit conditions and electrochemically by 25 potential cycles. Figure 3.12 presents digital optical micrographs of aluminum alloy specimens before and after exposure to the salt spray environment. The TCP-coated AA2024-T3 alloy specimen before exposure has no visible defects or discolorations (Stage 0) on the surface (Figure 3.12A). The uncoated AA2024-T3 alloy coupled with an unmodified CFRP composite (Figure 3.12B) developed extensive corrosion damage (Stage 3-4, see Experimental) after just 3 days into the test, as revealed by the micrograph. In the absence of the TCP conversion coating, widespread pitting corrosion damage can be seen on the panel away from where the composite was joined, while galvanic corrosion is predominant near where the edges of the composite were positioned (red arrows). Significant corrosion underneath the composite is also evident (blue arrow). Finally, there is significant corrosion damage around the through-hole (yellow arrow). The corrosion damage on the TCP-coated alloy joined with an unmodified CFRP specimen after 14 days is limited to trenching along where the edges of the composite was positioned (Stage 2) (red arrows).Crevice corrosion under the composite is evident (blue arrow), but the damage is far less than that seen on the uncoated alloy (Figure 3.12B). Corrosion damage is noticeable on the panel underneath where the composite was joined and around the fastener hole (yellow arrow), but both are less severe than that seen on the uncoated alloy after just 3 days. Importantly, the TCP coating formed by immersion does an effective job of inhibiting corrosion on the alloy panel away from where the composite was joined as only a few isolated regions of localized pitting were observed as marked by the green boxes.

Importantly, the micrographs reveal that modifying the edges of the composite with an NAB adlayer dramatically reduces the galvanic corrosion near the composite edges, crevice corrosion underneath the composite, and galvanic corrosion around the through-hole after 14 days. The TCP-coated aluminum alloy joined to a CFRP composite electrochemically modified with NAB (Figure 3.12D) does not show severe trenching along the perimeter of the composite (Stage 1-2). In other words, the trenching degradation caused by galvanic corrosion is attenuated when the CFRP edges are surface treated. There is, however, some crevice corrosion damage on the alloy panel where the composite was joined (blue arrow), but this damage is far less than that seen in Figure 3.12B and C for the unmodified composite. Furthermore, there is only minor corrosion damage around the through-hole (yellow arrow).

Importantly, consistent with the electrochemical data presented above, the least damaged alloy panel is the one joined to the CFRP composite that was spontaneously modified with a NAB adlayer for 24 h. This is apparent in the micrograph (Figure 3.12E) that shows discolorations (Stage 1) rather than metal dissolution. As identified by purple arrows, the discolorations are observed on the alloy along the perimeter of where the composite specimen was joined. The discoloration is an impression of the composite specimen left on the TCP-coated alloy. No trenching is observed. No corrosion damage is visible around the fastener hole or on the outer alloy panel away from where the composite was joined. There are a few discolored areas appearing as white spots (green squares) on the alloy away from where the composite was positioned. These discolorations were identified by SEM EDXS analysis (data not shown here) as regions where the TCP coating was compromised leading to corrosion pit formation. Figure 3.12F presents a 3D contour plot obtained by digital optical microscopy showing one such corrosion pit. The blue color represents a depression with a depth of ~50µm. For comparison, the digital optical micrographs of TCP-coated

AA2024-T3 panels joined to CFRP composites electrochemically and spontaneously modified with 2-fluorene diazonium (FL) adlayers after 14 days of salt spray exposure are presented respectively in Figures 3.12G and H. The corrosion damage is relatively higher compared to their counterparts joined with NAB modified composites. This is consistent with the ORR current data indicating that the FL adlayer is not as compact and defect free as is the NAB adlayer. The 2-fluorenediazonium cation has three rings covalently bonded together making it slightly bulkier than the NAB admolecules. The bulkier nature may limit the coverage and or prevent the close packing of FL admolecules.

A quantitative corrosion damage assessment was performed by comparing the weight loss and corrosion intensity metrics for the TCP-coated AA2024-T3 panels joined with unmodified, electrochemically modified, and spontaneously modified CFRP composites with NAB. Table 3.2 presents a summary of the data. The largest weight loss per cm^2 was observed for the TCP-coated alloy specimen joined with an unmodified CFRP composite due to the significant galvanic and crevice corrosion damage. Surface treating the composite with the electrochemically formed NAB adlayer reduces weight loss by 3×. Surface treating the composite with the spontaneously formed NAB adlayer (24 h) reduces weight loss by 16×. A similar trend is seen for the corrosion intensity data. These data are consistent with electrochemical data and optical micrographs. The spontaneously formed adlayer (24 h immersion) is the most compact and defect free and, as such, provides the best protection against galvanic corrosion on the aluminum alloy.

Table 3.2. A summary of weight loss and corrosion intensity data for aluminum alloy specimens after the 14-day NSS exposure.

CFRP Composite	Aluminum Alloy	Weight Loss per cm^2 (mg/cm^2)	Corrosion Intensity (g/m^2. y)
Unmodified	TCP-coated AA2024	3.02 ± 1.07	774.36 ± 274.23
4-NAB Echem. Modified	TCP-coated AA2024	1.01 ± 0.42 (3× lower)	259.00 ± 109.56
4-NAB Spont. Modified	TCP-coated AA2024	0.19 ± 0.14 (16× lower)	49.17 ± 35.61

Data are presented as mean ± std. dev. for n=3 specimens of each type.

A closer examination of the pattern/distribution of galvanic corrosion damage on the TCP-coated AA2024-T3 panels was performed to further determine how effective the galvanic corrosion inhibition is upon the spontaneous grafting of NAB on the exposed carbon fiber surfaces. Figure 3.13A is a schematic diagram of a TCP-coated panel. The black dashed outline represents the area where the composite was joined. Figure 3.13B and C are SEM micrographs of TCP-coated AA2024-T3 panels joined with unmodified and spontaneously modified composites after the 14-day salt spray test. The red box in Figure 3.13A designates the area on each panel where the micrographs were collected. The TCP-coated panel joined with the unmodified composite (3.13B) experienced greater corrosion damage that spread laterally and with depth into the alloy (red arrows). The TCP-coated panel joined with the spontaneously modified composite (3.13C), on the other hand, shows little corrosion damage. Figure 3.13D and E present 3D contour plots revealing the surface texture of TCP-coated panels joined with unmodified and spontaneously modified composites, respectively. It should be noted that the area analyzed by digital optical microscopy to generate the contour plots is 2500 μm × 2500 μm and is larger than the area shown in the SEM micrographs. Figure 3.13D reveals a highly roughened surface on the TCP-coated panel coupled with unmodified composite. In comparison, Figure 3.13E reveals a much smoother texture of a TCP-coated panel coupled with a composite spontaneously modified with NAB. The smoother surface texture is consistent with greatly reduced corrosion damage.

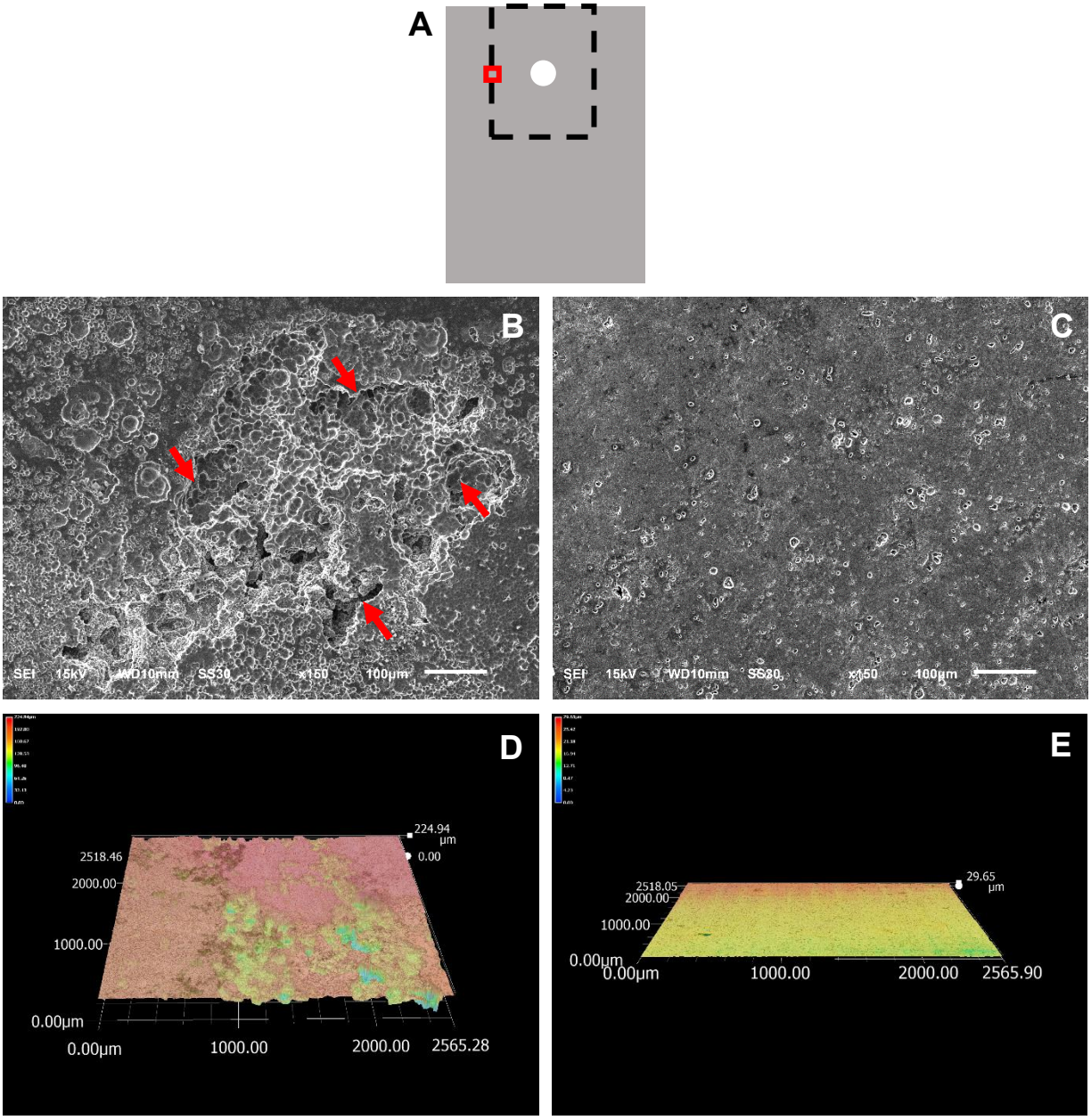

Figure 3.13. (A) Schematic diagram of a TCP-coated AA2024-T3 panel showing where the CFRP composite was joined and where the micrographs were collected. SEM micrographs of (B) a TCP-coated panel joined with an unmodified composite and (C) a TCP-coated panel joined with a composite spontaneously modified with 4-NAB (24 h immersion) after a 14-day salt spray test. 3D contour plots generated from stitched digital optical micrographs revealing the surface texture of (C) a TCP-coated panel joined with a composite spontaneously modified with 4-NAB (24 h immersion) after a 14-day salt spray test.

Digital optical microscopy was used to further quantify changes in the surface texture (roughness, peak-to-valley height) of the aluminum alloy specimens before and after the 14-day salt spray exposure. Table 3.3 shows the surface roughness and peak-to-valley height parameters for TCP-coated AA2024-T3 panels before and after salt spray exposure. The TCP-coated panels were joined with (A) unmodified, (B) electrochemically modified (25 cycles) and (C) spontaneously modified (24-h immersion) CFRP composite specimens using NAB. Data for the TCP-coated panel before exposure are presented for comparison. The surface texture analysis was performed at 5 different spots on each panel in the region adjacent to where the composite was joined (i.e., areas of greatest galvanic corrosion or trenching). The area analyzed per spot was 2500 µm × 2500 µm at a 1000× magnification. A schematic diagram is presented in Figure 3.14 showing the regions where the optical micrographs were collected on each panel.

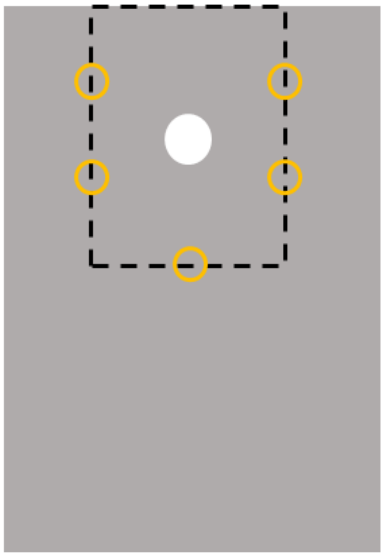

Figure 3.14. Schematic diagram showing the areas where the micrographs were collected on panel.

Table 3.3. Summary of surface texture analysis data for TCP-coated AA2024-T3 alloy specimens after 14-day salt spray testing.

	CFRP Composite	**Aluminum Alloy**	**Surface Roughness S_q (µm)**	**Peak-to-Valley Height S_z (µm)**
Before	-	TCP-coated AA2024	1.5 ± 0.1	7 ± 1
After	Unmodified	TCP-coated AA2024	44.7 ± 9.4	264 ± 45
	4-NAB Echem. Modified	TCP-coated AA2024	17.9 ± 5.8	151 ± 32
	4-NAB Spont. Modified	TCP-coated AA2024	8.0 ± 1.6	30 ± 9

Data are presented as mean ± std. dev. for n=15. Roughness data were recorded on 5 spots per specimen and 3 specimens of each type were used.

The TCP-coated panel joined with an unmodified CFRP composite showed a surface roughness increase by 30× and a peak-to-valley height increase by 37× from 7 to 264 µm, as compared to the control specimen, after 14 days of salt spray testing. This reflects the significant galvanic corrosion damage that occurs near the composite edge in the form of trenching. In contrast, the surface roughness and the peak-to-valley height for the TCP-coated panel increased by 12× when joined with a composite electrochemically modified with NAB (25 potential cycles) and by only 5× when joined with a composite spontaneously modified with NAB (24 h) after 14 days of salt spray testing. The respective peak-to-valley height changes are at 21× and 4×, respectively. In summary, the surface texture analysis reveals the significantly reduced galvanic corrosion on the TCP-coated alloy panels when mechanically joined to a CFRP composite spontaneously modified with an NAB adlayer.

Table 3.4 presents data for the widths of the galvanically corroded trench regions on the TCP-coated alloy panels adjacent to unmodified and spontaneously modified (NAB 24-h immersion) CFRP composite panels after 14-day salt spray testing. The lateral distribution of corrosion damage is approximately 18× less on the left side, 9× less on the bottom side, and 15× less on the right side of the panel coupled with a spontaneously modified composite.

Table 3.4. A summary of the widths of trench regions for TCP-coated AA2024-T3 aluminum alloy specimens after 14-day salt spray testing when mechanically joined with unmodified and spontaneously modified (24-h immersion) CFRP composites. The composites were modified with an NAB adlayer.

	Unmodified Composite (mm)	**Spontaneously Modified Composite (mm)**
Left Side	2.96 ± 2.57	0.16 ± 0.09
Bottom Side	2.86 ± 2.51	0.32 ± 0.58
Right Side	4.08 ± 1.70	0.26 ± 0.24

Data are presented as mean ± std. dev. for n=3 specimens of each type.

Galvanic corrosion occurs with depth into the trench regions as well. This was assessed by digital optical microscopy. Figure 3.15 presents line profiles for TCP-coated panels joined with unmodified and spontaneously modified CFRP composites (NAB 24-h immersion) after 14 days of salt spray testing. The schematic diagram in Figure 14A indicates in red color where the surface line profiles shown in Figure 3.15B, C, and D were collected on each alloy specimen. The line scans reveal the galvanic corrosion damage progresses deep into the alloy panel with a nominal depth of 229 ± 54 μm when joined with an unmodified composite. This damage results after 14 days. In contrast, the line scans reveal negligible dissolution with depth into the panel when joined with a spontaneously modified composite. Collectively, the data indicate that surface treating a composite with spontaneously formed NAB (24-h immersion) greatly reduces galvanic corrosion of TCP-coated AA2024-T3 under and around the mechanically joined composite.

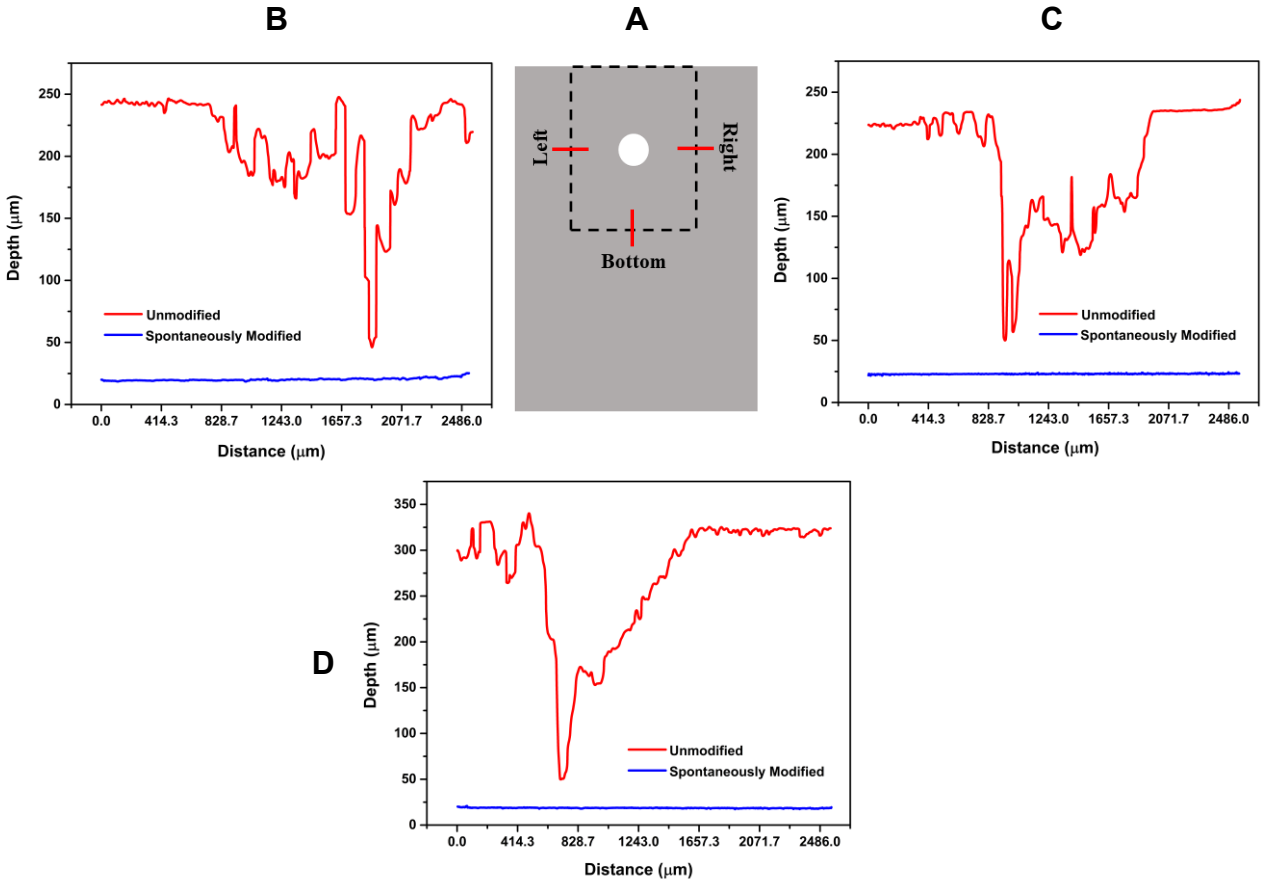

Figure 3.15. Digital optical microscopy surface texture line profiles on AA2024-T3 alloy panels after the 14-day neutral salt spray test revealing the depth of corrosion damage near the edges of the unmodified and spontaneously modified composites. (A) Schematic diagram showing where the line profiles were recorded on each type of panel. Line profiles on the TCP-coated alloy panel across where the (B) left, (C) right and (D) bottom edges of the unmodified and spontaneously modified CFRP composites were positioned on during the test. The surface line profiling was performed at 1000× over a 2.5 mm linear distance.

Inhibition of Carbon Corrosion. In addition to reducing the galvanic corrosion damage on the TCP-coated aluminum alloy, surface treatment of the CFRP composite edges also reduces carbon corrosion and epoxy debonding. In prior work, we observed degradation of the CFRP composite edges in specimens lap joined to TCP-coated alloys during salt spray exposure.[18] We hypothesize the damage is caused by hydrogen peroxide (H_2O_2) accumulation in the liquid layer that forms on a composite edge. The oxygen reduction reaction can proceed through either a $4e^-/4H^+$ or a $2e^-/2H^+$ pathway.[39-41] On carbon materials, the reaction proceeds by the latter pathway to produce the

strong oxidant, H_2O_2, in acidic and neutral media.

To test for the presence of H_2O_2 during the salt spray exposure, Water Works™ peroxide test strips were positioned near the edge of a CFRP specimen in a lap joint configuration where H_2O_2 accumulation is expected to occur. The test strips colorimetrically report on the presence of the oxidant in the concentration range from 0.5-100 ppm. If present, H_2O_2 reacts with peroxidase and an organic redox indicator on the test strip forming an oxidation compound that is blue in color. During the salt spray exposure, all test specimens turned dark blue qualitatively indicating the formation of H_2O_2. H_2O_2 is a strong oxidant, and its accumulation can cause CFRP composite degradation. The reaction between H_2O_2 and the CFRP composite could result in carbon fiber oxidation/corrosion and/or debonding of the epoxy and, over time, leading to material fatigue.[23] Degradation of the epoxy resins in acidic media, such as hydrochloric (HCl), nitric (HNO_3) and sulfuric (H_2SO_4,) have been reported in literature.[43-46] Because the epoxy resin is a thermosetting polymer with a highly cross-linked structure, once cured, it cannot be melted down or remodeled by applying temperature. [44,46] The decomposition of the epoxy resin matrix in HNO_3 solution at high temperature leads to the separation of the carbon fibers from the polymer matrix and is used as a chemical recycling method for carbon fiber reuse.[43]

Figure 3.16 presents the SEM micrographs of unmodified composite edges before and after 14 days of salt spray testing. The composites shown here were mechanically joined to uncoated AA2024-T3 alloy panels during the test. Figure 3.16A shows a polished and unmodified CFRP composite edge devoid of any detectable damage before testing. SEM micrographs of the unmodified composite edge coupled to an uncoated AA2024-T3 alloy panel during the accelerated degradation test reveal the most extensive damage (Figures 3.16B, C, and D). There is clearly significant epoxy degradation (red arrows) between the carbon fibers resulting in cracks and

fissures into the composite. Additionally, damage due to carbon corrosion is seen on some carbon fibers as indicated by yellow arrows. These observations are consistent with the uninhibited oxygen reduction, resulting in the accumulation of H_2O_2 at the composite and far greater galvanic corrosion damage on the uncoated AA2024-T3 alloy panel.

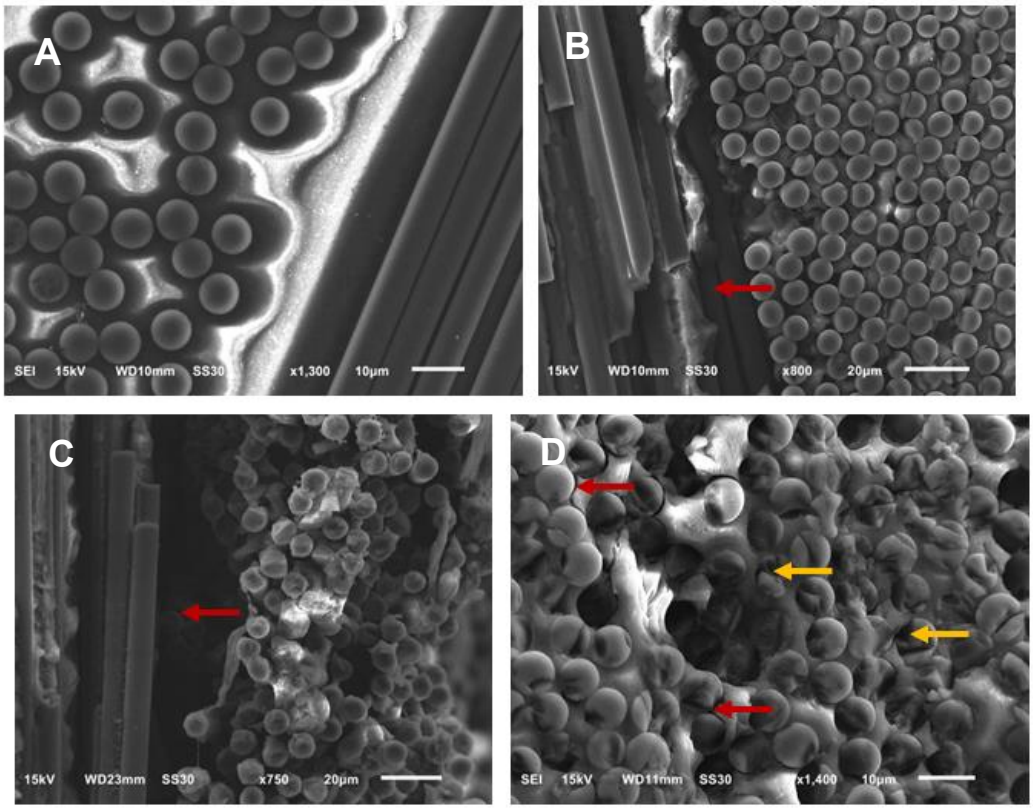

Figure 3.16. SEM micrographs of (A) a polished, unmodified CFRP composite edge before 14-day salt spray exposure and (B), (C), (D) an unmodified CFRP composite edge after 14-day salt spray exposure. During the test, the unmodified composite was mechanically joined with an uncoated AA2024-T3 panel. composite spontaneously modified with NAB (24 h immersion) after a 14-day salt spray test. During the test, the composite was mechanically joined with a TCP-coated AA2024-T3 panel.

Figure 3.17 presents the SEM micrographs of unmodified and diazonium-modified composite edges before and after 14 days of salt spray testing. During the test, the composites were mechanically joined to a TCP-coated AA2024-T3 alloy panel. A polished and unmodified CFRP composite edge before testing is shown in Figure 3.17A. The micrograph reveals the distal ends of the exposed carbon fibers, all undamaged. The interface between the epoxy matrix and the

carbon fibers is intact. Signs of significant degradation are noticeable in the SEM image of the unmodified CFRP composite edge after the 14-day NSS shown in Figure 3.17B. Loss of carbon leading to voids and pits due to carbon oxidation, gasification, and corrosion are observed on distal end carbon fibers as indicated by yellow arrows. The damage is most severe on the unmodified composite but reduced for the spontaneously modified composite such that few damage fibers are detected. Additionally, matrix debonding is observed on the unmodified specimen, as well. The degree of damage associated with debonding is reduced for the spontaneously modified composite. In summary, surface treating the exposed carbon fibers with a spontaneously formed NAB adlayer provides superior inhibition of galvanic corrosion on the TCP-coated aluminum alloy and superior protection against carbon corrosion and epoxy debonding than

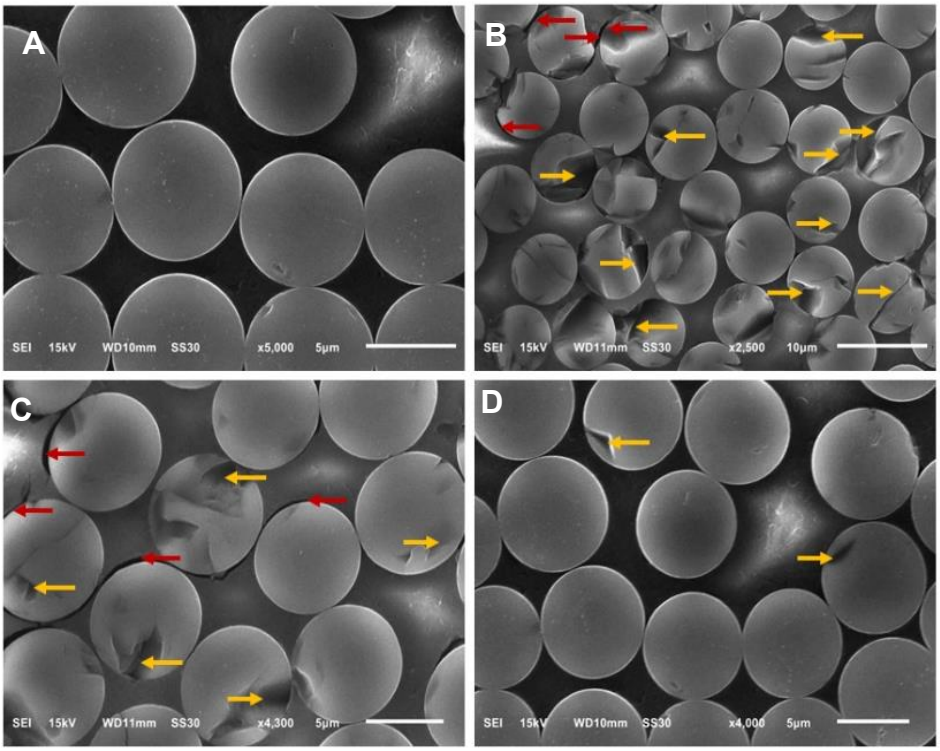

Figure 3.17. SEM micrographs of (A) an unmodified CFRP composite edge showing the distal ends of carbon fibers before a 14-day salt spray test. SEM micrographs of (B) an unmodified composite, (C) a composite electrochemically modified (25 cycles) with NAB, and (D) a composite spontaneously modified with NAB (24 h immersion) after a 14-day salt spray test. During the test, the composite was mechanically joined with a TCP-coated AA2024-T3 panel.

does surface treatment by an electrochemically formed adlayer. Prior work has shown that diazonium adlayers can protect carbon materials from corrosion and degradation.[18,47,48]

Galvanic Current During 14-Day Salt Spray Test. Galvanic current measurements were performed to further evaluate the galvanic corrosion inhibition of AA2024-T3 specimens by NAB adlayers formed spontaneously on CFRP composite edges during a different 14-day salt spray test. Figure 3.18 presents the plots of galvanic current measured. A polyimide film was introduced between the alloy and composite specimens to trap the electrolyte solution, NaCl in this case and establish a conducting medium. All AA202-T3 panels, regardless of the type of composite they were joined with, were coated with TCP. TCP coatings provide corrosion protection to the aluminum alloy. Consequently, when exposed to a continuous fog of NaCl, no galvanic current flow was detected until day 2. An uncoated AA 2024 + unmodified CFRP composite couple was also used in the test. This couple showed a current of 4.5 μA just after 24 hours, indicating the onset of galvanic corrosion due to the absence of a protective TCP coating on the AA202-T3 panel to delay the corrosion process. The galvanic current between unmodified CFRP composite and TCP-coated AA2024-T3 ranged from 3 to 11 μm over the test period. In contrast, noticeably lower galvanic current was measured between spontaneously modified CFRP composite and TCP-coated AA2024-T3 specimens and ranged from 0.5 to 2.5 μm over the test period. Initially, both plots displayed an increase in galvanic current. As the galvanic corrosion begins, the TCP coating becomes compromised, exposing the underlying aluminum alloy surface. This leads to the initiation of localized and pitting corrosion. The simultaneous occurrence of galvanic and pitting corrosions results in the observed increase in current. Subsequently, the current began to decrease due to the deposition of corrosion products. Overall, the current measured between spontaneously modified CFRP composite specimens and TCP coated AA2024-T3 panels was significantly lower

than the current measured between unmodified CFRP composite and TCP-coated AA2024-T3 couples throughout the duration of the test. This quantitative observation serves as an additional confirmation of the reduced galvanic corrosion resulting from the diazonium surface treatment of CFRP composites.

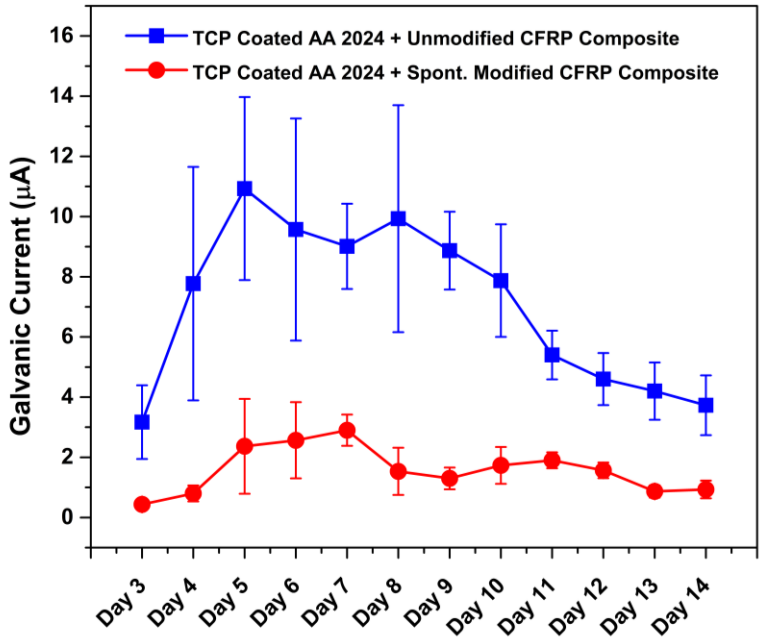

Figure 3.18. Galvanic currents measured between unmodified/spontaneously modified CFRP composite and TCP-coated AA2024-T3 panels at selected time points during the 14-day neutral salt spray exposure.

Figure 3.19 presents the digital micrographs of TCP-coated AA2024-T3 panels subjected to 14-day salt spray exposure for galvanic current measurements. Clearly, the alloy panel joined to unmodified CFRP composite reveals extensive galvanic corrosion damage. In contrast, the AA2024-T3 panel coupled with spontaneously modified composite during testing shows much reduced galvanic corrosion damage. Overall, the TCP-coated AA2024-T3 panels joined respectively to unmodified and CFRP composites and used for galvanic corrosion measurements show relatively higher damage after 14 days of salt spray exposure as compared to their counterparts presented in Figures 3.12C and E. One possible explanation could be the presence of the polyimide

membrane inserted between the alloy and composite during galvanic current measurements. This may have resulted in the high ionic strength of the salt-spray mist to produce an effective conducting medium in the polyamide membrane.

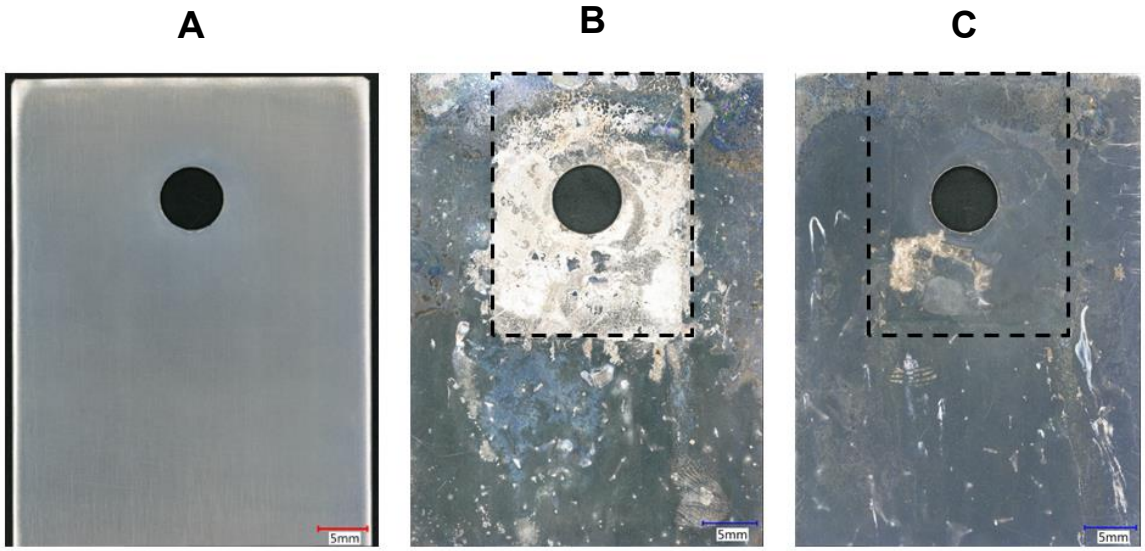

Figure 3.19. Digital optical micrographs of AA2024-T3 panels composite used for galvanic current measurements (A) with a TCP coating and before salt spray exposure, (B) TCP-coated and joined with an unmodified CFRP after 14-day neutral salt spray exposure, and (C) TCP-coated and joined with a CFRP composite spontaneously modified with NAB after 14 days of neutral salt spray exposure.

SEM micrographs of the CFRP composites after galvanic current measurements are presented in Figure 3.20. The unmodified CFRP composite edges (Figures 3.20A and B) reveal signs of carbon corrosion (yellow arrows) and epoxy debonding (red arrows) after galvanic corrosion measurements. The unmodified CFRP composite surface that was in contact with the polyimide membrane shows significant epoxy degradation exposing the carbon fibers (Figure 3.20E). Conversely, far less epoxy degradation and carbon corrosion damage was seen on the spontaneously modified composite (Figures 3.20C, D, and F. This is attributed to the inhibition of the oxygen reduction reaction that produces H_2O_2 by the spontaneously formed NAB adlayer.

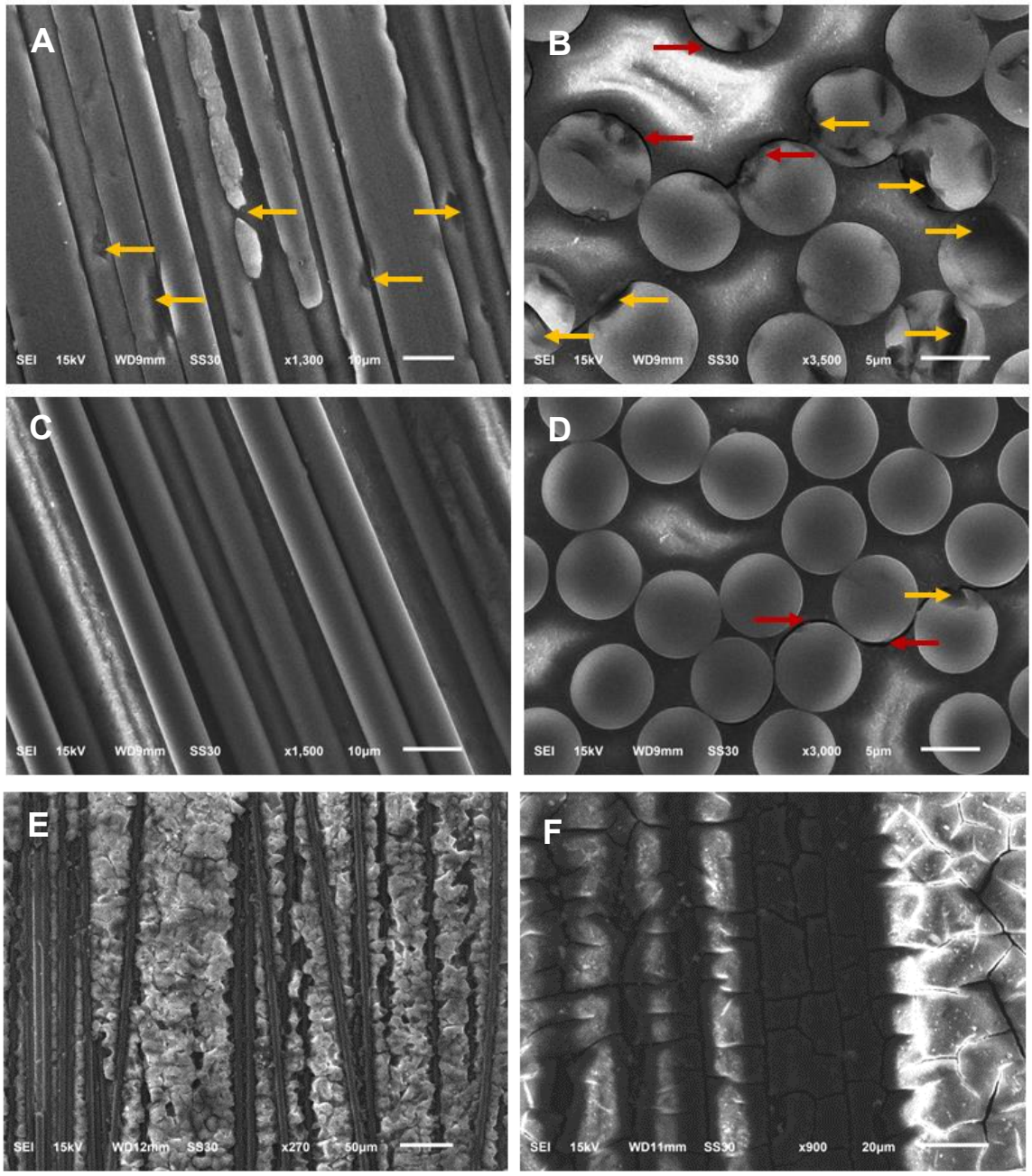

Figure 3.20. SEM micrographs of an unmodified CFRP composite edge showing the (A) cylindrical carbon fibers and (B) distal ends after galvanic current measurements, a composite edge spontaneously modified with NAB, showing the (C) cylindrical carbon fibers and (D) distal ends after galvanic current measurements, and the surfaces of the (E) unmodified and (F) spontaneously modified composites that were in direct contact with the polyimide membrane during galvanic current measurements.

3.4 DISCUSSION

Following up prior work showing the effectiveness of electrochemically formed diazonium adlayer[18], this study demonstrates that the spontaneously formed diazonium adlayer on the exposed edges of CFRP composites is even better at inhibiting the oxygen reduction reaction kinetics (*i.e.,* cathodic inhibitor) and provides greater suppression of both aluminum alloy galvanic corrosion and carbon fiber corrosion. This is the first time this surface treatment has been applied to CFRP exposed surfaces to reduce the rate of galvanic corrosion on mechanically joined aluminum alloy specimens. Fabrication and assembly of an aircraft involve a variety of detail part fabrication and assembly operations.[49] For example, fuselage assembly involves riveting and fastening operations at five major assembly levels. The wing has three major levels of assembly. We believe this surface treatment could be applied as part of the normal process flow for fabrication and assembly without significantly increasing the overall processing time.

The immersion of CFRP composites in aryl diazonium salt solutions under open circuit conditions leads to spontaneous formation of an organic adlayer that provides barrier protection against direct contact with the solution layer and kinetic inhibition of surface-sensitive electrochemical reactions, in this case, dissolved oxygen reduction. If there are electrons available in electronic states of the carbon that are higher in energy than the LUMO of the diazonium molecule, thermodynamically, electron transfer can occur from the electrode to the diazonium to produce the reactive radical species. This radical then reacts with the electrode surface to form a stable, covalently bonded admolecule. While the blocking effect of the (NP and NAB) adlayer formed at different immersion times was studied, further investigation of the formation kinetics is still needed to better inform on how parameters, such as diazonium concentration, temperature, and immersion time, affect the adlayer density, thickness, and performance. In other words, process

parameter optimization is needed. Nevertheless, the data presented herein reveal that the spontaneously formed adlayer provides better blocking and kinetic inhibition than does the electrochemically formed adlayer. The degree of kinetic inhibition for surface-sensitive electrochemical reactions provided by the adlayer depends on the soluble redox system – its size and charge. For example, a 5-min immersion of a CFRP composite in a 5 mM NP solution produces an adlayer that decreases the oxidation current for the $[Fe(CN)_6]^{-3/-4}$ redox system by *ca.* 35% and increases the cyclic voltammetric ΔE_p reflecting more sluggish electron transfer kinetics. The surface coverage, density, and thickness of the adlayer are proportional to the immersion time. The surface coverage effect is evidenced by the increase in the Raman spectroscopy peak intensities recorded for an admolecule (*e.g.*, NAB) with immersion time. The 15 and 30-min immersion times largely suppress $[Fe(CN)_6]^{-3/-4}$ redox chemistry. However, these immersion times do not fully inhibit the reduction current for the smaller and electrically neutral O_2 molecule. At least a 24-h immersion is needed to form a fully blocking adlayer. The existence of some reduction current at the shorter immersion times suggests there are defects in the adlayer or incomplete adlayer coverage such that the O_2 molecule can penetrate and reach the underlying carbon where it can undergo electron transfer at unmodified edge plane sites. Additionally, the O_2 molecule may undergo more effective electron tunneling (*i.e.*, closer approach) through the adlayer than does the highly charged $[Fe(CN)_6]^{-3/-4}$ so speculatively, longer immersion times are needed to increase the adlayer thickness. For long immersion times of 6 and 24 h, cyclic voltammetric measurements reveal about a 74% decrease in the kinetically controlled reduction current for dissolved O_2 after 6 h and near complete inhibition (99%) of the reduction current after 24 h. NP and NAB modified surfaces behaved similarly. This is attributed to the formation of a more compact and denser adlayer during the 24-h immersion that effectively blocks adsorption sites for the O_2 molecule on

the carbon surface, which is the first step in the surface-mediated reduction reaction.[39-41]

The near complete inhibition of the rate of dissolved O_2 reduction on the more noble CFRP specimens then leads to significantly lower galvanic corrosion damage on TCP-coated AA2024-T3 panels during a 14-day continuous neutral salt spray exposure owing to the decreased rate of aluminum alloy oxidation and dissolution. The weight loss and surface roughness data reveal that the metal dissolution and the length, width and depth of the galvanic corrosion damage is remarkably attenuated when TCP-coated AA2024-T3 is mechanically joined to a CFRP composite spontaneously modified with NAB (24-h immersion). The typical damage pattern on the alloy of trenching near the composite edges, crevice corrosion underneath the composite, and galvanic corrosion damage on the walls of the fastener through-hole are not seen during a 14-day salt spray exposure. We suppose the reduction in crevice corrosion on the panel underneath the joined composite is reduced because of a better seal between the two. When the composite specimen is immersed in the diazonium-containing acetonitrile solution, the epoxy is slightly softened so that when joined with the alloy panel, an interface is formed with greater contact area than is formed with a normal untreated composite which consist of a hard and irregularly shaped epoxy layer. The reduction in corrosion damage in the through-hole region is attributed to the treatment of the hole wall on the composited with a diazonium adlayer. This reduces the rate of dissolved oxygen reduction on the nearby carbon and lessens the metal dissolution. The tighter seal between the composite and the alloy panel also serves to prevent moisture and oxygen ingress to the through-hole region.

The kinetic inhibition of the diazonium adlayer (NP) on the O_2 reduction reaction was demonstrated clearly with the rotating disk voltammetric experiments using a modified glassy carbon working electrode. Unchanging i_l versus $\omega^{1/2}$ plots for both the electrochemically- and

spontaneously-modified electrodes with a non-zero y-axis intercept indicates the adlayer provides a kinetic barrier to the reduction of O_2. In other words, the rate of reaction is limited by the electron-transfer kinetics rather than mass transfer kinetics. The kinetic currents, i_K, obtained from extrapolation of the Koutecký-Levich plots to $\omega^{-1/2} = 0$ for the unmodified, electrochemically modified, and spontaneously modified glassy carbon RDEs are 9.03×10^{-5}, 1.33×10^{-5} (6× lower) and 1.39×10^{-6} A (65× lower), respectively, reflecting the kinetic inhibition provided by the adlayer.

The spontaneous formation of the diazonium adlayer (NAB) also has a dramatic effect at reducing carbon corrosion and epoxy debonding on the CFRP composite.[18] In the salt spray mist, dissolved O_2 molecules get reduced to H_2O_2, which is a strong oxidant. The concentration in mist droplets contacting the carbon edge increases over time, likely producing relatively high levels. H_2O_2 accumulation in the thin solution layer leads to carbon oxidation according to the following net redox reaction,

$$C + 2H_2O_2 \rightarrow CO_2 + 2H_2O \qquad (4)$$

The more compact, spontaneously formed NAB adlayer inhibits carbon oxidation/corrosion and epoxy debonding by acting as a barrier layer for direct solution contact with the surface and a kinetic inhibitor of H_2O_2 production.

Translational research is needed to (i) optimize the parameters for applying the surface treatment through a spontaneous formation process (solution immersion) so as to maximize the degree of galvanic corrosion suppression on the aluminum alloy while minimizing the overall processing time, (ii) investigating the application of the surface treatment using brush and spray-on applications, and (iv) subsystem demonstration of test assemblies in a service environment (*e.g.*, sea-side beach exposure).

3.5 CONCLUSIONS

Carbon fiber reinforced polymer (CFRP) composites and aluminum alloys are widely used as integrated structural components in military and civilian aircraft, military transport vehicles, automobiles for transportation, and marine vessels. Severe galvanic corrosion can develop at locations where these dissimilar materials are joined and become electrically connected by a condensed layer of atmospheric moisture. The more noble carbon fibers act as a cathode and support the electrochemical reduction of dissolved oxygen. The consumption of electrons in this cathodic reaction accelerates the electrochemical oxidation rate of the nearby aluminum alloy, so-called galvanic corrosion. Galvanic corrosion causes a metal to degrade at a faster rate than it otherwise would in the absence of a dissimilar material. Galvanic corrosion of aluminum alloy with carbon fiber materials is a serious and well-known issue. Strategies for more effectively mitigating galvanic corrosion at CFRP composite-metal alloy joints represent the unmet technological need.

We believe that the aryl diazonium surface treatment technology reported herein for treating exposed carbon fibers in CFRP composites joined with metal alloys will result in less galvanic corrosion damage to the alloy, and reduced costs for repair and maintenance. Cyclic voltammetric data revealed that both NP and NAB adlayers spontaneously grafted by a 24-h immersion reduces the current for dissolved oxygen reduction by 99%, as compared to the unmodified specimen. Complete inhibition was not achieved by the 2-FL grafting because the adlayer may not be fully compact across the surface or may possess some holes/defects through which O_2 can diffuse and reach the underlying carbon surface. The 4-NAB adlayer spontaneously grafted on the exposed carbon fiber surfaces of the composite by a 24-h immersion significantly attenuated the galvanic

corrosion of TCP-coated AA2024-T3 alloy specimens during a 14-day salt spray exposure when coupled together. The key findings from the work can be summarized as follows:

1. Diazonium adlayers can be formed on the exposed carbon fibers of CFRPs by spontaneous immersion. The adlayers are perhaps thicker but are certainly more defect free than adlayers formed by the electrochemically assisted method.
2. Immersion times of 30 min, or greater, allow for the spontaneous formation of NP adlayers that are low in defects (pin holes) and perhaps thicker such that the adlayer cannot be penetrated by the $[Fe(CN)_6]^{4-}$ ions.
3. The capacitance is *ca*. 2× lower for the composite specimen electrochemically modified with NP and *ca.* 12× lower for the CFRP composite electrode spontaneously modified with NP, as compared to the unmodified control. The decrease in interfacial capacitance arises from a more compact, less defective, and thicker adlayer spacing the counterbalancing charge further away from the composite on the solution side of the interface.
4. The electrochemically formed NP adlayer attenuated the kinetically controlled oxygen reduction current at -0.8 V by only 67% while the spontaneously formed adlayer totally inhibited the current. The NP adlayer spontaneously formed for 24 h is more compact, less defective, and perhaps thicker than the adlayer formed by the electrochemically assisted grafting.
5. The oxygen reduction current density at -0.8 V in potentiodynamic polarization curves for the composite electrochemically modified with NP is 15× lower and the current density for the composite spontaneously modified with NP is 56× lower than the unmodified composite. This is attributed to the behavior of the NP adlayer as a physical blocking layer, which prevents

dissolved O_2 molecules from reaching the underlying carbon and reduces the rate of electron transfer, hence the current.

6. In rotating disk voltammetric measurements, the current for dissolved oxygen reduction at a glassy carbon electrode was independent of the rotation when spontaneously modified with an NP adlayer. The electrochemically formed NP adlayer on GC lowers the kinetic current, i_K, by ca. 6× while the spontaneously grafted NP adlayer reduces i_K by ca. 64× as compared to the unmodified electrode.
7. Consistent with the electrochemical test data, results from a 14-day neutral salt spray exposure of CFRP composite/TCP-coated lap joint specimens revealed that surface treating the composite with an electrochemically formed (25 cycles) NAB adlayer reduces weight loss and corrosion intensity by 3×. Surface treating the composite with the spontaneously formed NAB adlayer (24 h) reduces weight loss and corrosion intensity by 16×.
8. All signs of carbon corrosion and epoxy debonding were absent on CFRP specimens when spontaneously modified (24 h immersion) with NAB after a 14-day salt spray exposure.

REFERENCES

1. Dursun, T., & Soutis, C. (2014). Recent developments in advanced aircraft aluminium alloys. *Materials & Design (1980-2015)*, *56*, 862.

2. Traceski, F. T. (1999). Assessing industrial capabilities for carbon fiber production. *Aquisition Review Quarterly–Spring*, 180.

3. Soutis, C. (2005). Fibre reinforced composites in aircraft construction. *Progress in aerospace sciences*, *41*(2), 143.

4. Dispenza, C., Alessi, S., & Spadaro, G. (2008). Carbon fiber composites cured by γ-radiation-induced polymerization of an epoxy resin matrix. *Advances in Polymer Technology: Journal of the Polymer Processing Institute*, *27*(3), 163.

5. Chung, D. D. (2016). *Carbon composites: composites with carbon fibers, nanofibers, and nanotubes*. Butterworth-Heinemann.

6. Pramanik, A., Basak, A. K., Dong, Y., Sarker, P. K., Uddin, M. S., Littlefair, G., Dixit, A. R., & Chattopadhyaya, S. (2017). Joining of carbon fibre reinforced polymer (CFRP) composites and aluminium alloys–A review. *Composites Part A: Applied Science and Manufacturing*, *101*, 1-29.

7. Jiang, B., Chen, Q., & Yang, J. (2020). Advances in joining technology of carbon fiber-reinforced thermoplastic composite materials and aluminum alloys. *The International Journal of Advanced Manufacturing Technology*, *110*(9), 2631.

8. Liu, Z., Curioni, M., Jamshidi, P., Walker, A., Prengnell, P., Thompson, G. E., & Skeldon, P. (2014). Electrochemical characteristics of a carbon fibre composite and the associated galvanic effects with aluminium alloys. *Applied surface science*, *314*, 233.

9. Srinivasan, R., Nelson, J. A., & Hihara, L. H. (2015). Development of guidelines to attenuate galvanic corrosion between mechanically-coupled aluminum and carbon-fiber reinforced epoxy composites using insulation layers. *Journal of the Electrochemical Society*, *162*(10), C545.

10. Peng, Z., & Nie, X. (2013). Galvanic corrosion property of contacts between carbon fiber cloth materials and typical metal alloys in an aggressive environment. *Surface and coatings technology*, *215*, 85.

11. Feng, Z., Boerstler, J., Frankel, G. S., & Matzdorf, C. A. (2015). Effect of surface pretreatment on galvanic attack of coated Al alloy panels. *Corrosion*, *71*(6), 771.

12. Delamar, M., Hitmi, R., Pinson, J., & Saveant, J. M. (1992). Covalent modification of carbon surfaces by grafting of functionalized aryl radicals produced from electrochemical reduction of diazonium salts. *Journal of the American Chemical Society*, *114*(14), 5883.

13. Downard, A. J. (2000). Electrochemically assisted covalent modification of carbon electrodes. *Electroanalysis: An International Journal Devoted to Fundamental and Practical Aspects of Electroanalysis*, *12*(14), 1085.

14. Adenier, A., Bernard, M. C., Chehimi, M. M., Cabet-Deliry, E., Desbat, B., Fagebaume, O., Pinson, J., & Podvorica, F. (2001). Covalent modification of iron surfaces by electrochemical reduction of aryldiazonium salts. *Journal of the American Chemical Society*, *123*(19), 4541.

15. Bernard, M. C., Chaussé, A., Cabet-Deliry, E., Chehimi, M. M., Pinson, J., Podvorica, F., & Vautrin-Ul, C. (2003). Organic layers bonded to industrial, coinage, and noble metals through electrochemical reduction of aryldiazonium salts. *Chemistry of Materials*, *15*(18), 3450.

16. De Villeneuve, C. H., Pinson, J., Bernard, M. C., & Allongue, P. (1997). Electrochemical formation of close-packed phenyl layers on Si (111). *The Journal of Physical Chemistry B*, *101*(14), 2415.

17. Pinson, J., & Podvorica, F. (2005). Attachment of organic layers to conductive or semiconductive surfaces by reduction of diazonium salts. *Chemical Society Reviews*, *34*(5), 429.

18. Dammulla, I. N., & Swain, G. M. (2022). Inhibiting the oxygen reduction reaction kinetics on carbon fiber epoxy composites through diazonium surface modification-impacts on the galvanic corrosion of coupled aluminum alloys. *Journal of the electrochemical society*, *169*(7), 071501.

19. Adenier, A., Cabet-Deliry, E., Chaussé, A., Griveau, S., Mercier, F., Pinson, J., & Vautrin-Ul, C. (2005). Grafting of nitrophenyl groups on carbon and metallic surfaces without electrochemical induction. *Chemistry of Materials*, *17*(3), 491.

20. Adenier, A., Barré, N., Cabet-Deliry, E., Chaussé, A., Griveau, S., Mercier, F., Pinson, J., & Vautrin-Ul, C. (2006). Study of the spontaneous formation of organic layers on carbon and metal surfaces from diazonium salts. *Surface Science*, *600*(21), 4801.

21. Chamoulaud, G., & Belanger, D. (2007). Spontaneous derivatization of a copper electrode with in situ generated diazonium cations in aprotic and aqueous media. *The Journal of Physical Chemistry C*, *111*(20), 7501.

22. Assresahegn, B. D., Brousse, T., & Bélanger, D. (2015). Advances on the use of diazonium chemistry for functionalization of materials used in energy storage systems. *Carbon*, *92*, 362.

23. Whitman, B. W., Miller, D., Davis, R., Brennan, J., & Swain, G. M. (2017). Effect of galvanic current on the physicochemical, electrochemical and mechanical properties of an aerospace carbon fiber reinforced epoxy composite. *Journal of The Electrochemical Society*, *164*(13), C881.

24. Li, L., & Swain, G. M. (2013). Formation and structure of trivalent chromium process coatings on aluminum alloys 6061 and 7075. *Corrosion*, *69*(12), 1205.

25. Li, L., Doran, K. P., & Swain, G. M. (2013). Electrochemical characterization of trivalent chromium process (TCP) coatings on aluminum alloys 6061 and 7075. *Journal of the Electrochemical Society*, *160*(8), C396.

26. Ferrer, K. S., & Kelly, R. G. (2001). Comparison of methods for removal of corrosion product from AA2024-T3. *Corrosion*, *57*(02).

27. Osborn, K. (2010). Army Steps Up Plans to Fight Corrosion, U.S. Army Military Article #36266 (https://army.mil/article/36266/army_steps_up_plans_to_fight_corrosion).

28. Saby, C., Ortiz, B., Champagne, G. Y., & Bélanger, D. (1997). Electrochemical modification of glassy carbon electrode using aromatic diazonium salts. 1. Blocking effect of 4-nitrophenyl and 4-carboxyphenyl groups. *Langmuir*, *13*(25), 6805.

29. Ortiz, B., Saby, C., Champagne, G. Y., & Bélanger, D. (1998). Electrochemical modification of a carbon electrode using aromatic diazonium salts. 2. Electrochemistry of 4-nitrophenyl modified glassy carbon electrodes in aqueous media. *Journal of Electroanalytical Chemistry*, *455*(1-2), 75.

30. Kariuki, J. K., & McDermott, M. T. (1999). Nucleation and growth of functionalized aryl films on graphite electrodes. *Langmuir*, *15*(19), 6534.

31. Downard, A. J., & Prince, M. J. (2001). Barrier properties of organic monolayers on glassy carbon electrodes. *Langmuir*, *17*(18), 5581.

32. Thomas, Y. R., Benayad, A., Schroder, M., Morin, A., & Pauchet, J. (2015). New method for super hydrophobic treatment of gas diffusion layers for proton exchange membrane fuel cells using electrochemical reduction of diazonium salts. *ACS applied materials & interfaces*, *7*(27), 15068.

33. İsbir-Turan, A. A., Üstündağ, Z., Solak, A. O., Kılıç, E., & Avseven, A. (2009). Electrochemical and spectroscopic characterization of a benzo [c] cinnoline electrografted platinum surface. *Thin Solid Films*, *517*(9), 2871.

34. Laforgue, A., Addou, T., & Bélanger, D. (2005). Characterization of the deposition of organic molecules at the surface of gold by the electrochemical reduction of aryldiazonium cations. *Langmuir*, *21*(15), 6855.

35. Mooste, M., Kibena-Põldsepp, E., Marandi, M., Matisen, L., Sammelselg, V., Podvorica, F. I., & Tammeveski, K. (2018). Surface and electrochemical characterization of aryl films grafted on polycrystalline copper from the diazonium compounds using the rotating disk electrode method. *Journal of Electroanalytical Chemistry*, *817*, 89.

36. Liu, Y. C., & McCreery, R. L. (1995). Reactions of organic monolayers on carbon surfaces observed with unenhanced Raman spectroscopy. *Journal of the American Chemical Society*, *117*(45), 11254.

37. Liu, Y. C., & McCreery, R. L. (1997). Raman spectroscopic determination of the structure and orientation of organic monolayers chemisorbed on carbon electrode surfaces. *Analytical chemistry*, *69*(11), 2091.

38. Adenier, A., Barré, N., Cabet-Deliry, E., Chaussé, A., Griveau, S., Mercier, F., Pinson, J., & Vautrin-Ul, C. (2006). Study of the spontaneous formation of organic layers on carbon and metal surfaces from diazonium salts. *Surface Science*, *600*(21), 4801.

39. Yeager, E. (1984). Electrocatalysts for O2 reduction. *Electrochimica Acta*, *29*(11), 1527.

40. Yang, H. H., & McCreery, R. L. (2000). Elucidation of the mechanism of dioxygen reduction on metal-free carbon electrodes. *Journal of the Electrochemical Society*, *147*(9), 3420.

41. Gara, M., & Compton, R. G. (2011). Activity of carbon electrodes towards oxygen reduction in acid: A comparative study. *New Journal of Chemistry*, *35*(11), 2647.

42. Uthaman, A., Xian, G., Thomas, S., Wang, Y., Zheng, Q., & Liu, X. (2020). Durability of an epoxy resin and its carbon fiber-reinforced polymer composite upon immersion in water, acidic, and alkaline solutions. *Polymers*, *12*(3), 614.

43. Liu, Y., Meng, L., Huang, Y., & Du, J. (2004). Recycling of carbon/epoxy composites. *Journal of Applied Polymer Science*, *94*(5), 1912.

44. Shen, M., & Robertson, M. L. (2020). Degradation behavior of biobased epoxy resins in mild acidic media. *ACS Sustainable Chemistry & Engineering*, *9*(1), 438.

45. Dang, W., Kubouchi, M., Yamamoto, S., Sembokuya, H., & Tsuda, K. (2002). An approach to chemical recycling of epoxy resin cured with amine using nitric acid. *Polymer*, *43*(10), 2953.

46. Ye, L., Wang, K., Feng, H., & Wang, Y. (2021). Recycling of carbon fiber-reinforced epoxy resin-based composites using a benzyl alcohol/alkaline system. *Fibers and Polymers*, *22*, 811.

47. Park, Y. B., You, E., Pak, C., & Min, M. (2018). Preparation and characterization of durable catalyst via diazonium reaction in PEMFC. *Electrochimica Acta*, *284*, 242.

48. Luong, S., Atwa, M., Valappil, M. O., & Birss, V. I. (2022). The influence of monolayer and multilayer diazonium functionalities on the electrochemical oxidation of nanoporous carbons. *Journal of The Electrochemical Society*, *169*(3), 031512.

49. Sarh, B., Buttrick, J., Munk, C., & Bossi, R. (2009). Aircraft manufacturing and assembly. *Springer handbook of automation*, 893.

CHAPTER 4. THE EFFECT OF SPONTANEOUS DERIVATIZATION OF CARBON FIBER REINFORCED POLYMER COMPOSITES ON THE GALVANIC CORROSION INHIBITION OF COUPLED AA7075-T6 ALUMINUM ALLOYS

Chapter adapted from the manuscript in preparation to be submitted to *Corrosion*.

Article: Isuri N. Dammulla and Greg M. Swain. *Spontaneous Modification of Carbon Fiber Composite Edges: Impacts on Galvanic Corrosion of Joined AA7075-T6 Aluminum Alloy During Neutral Salt Spray and Thin Layer Mist Accelerated Degradation Testing.*

4.1 INTRODUCTION

Recent efforts to achieve weight reduction of aircraft and automobile structures for improved fuel efficiency and reduced carbon dioxide (CO_2) emission have led to the extensive employment of carbon fiber reinforced polymer (CFRP) composites in the aerospace and automotive industries.[1-8] Owing to their lightweight, high strength and outstanding fatigue endurance, CFRP composites are used in long-range civilian aircraft, such as the Boeing 787 and Airbus A350, and German cars including BMW and Audi. Carbon fibers in CFRP composites are electrically conductive and more noble in the galvanic series than most metals. [9,10] Hence, when using dissimilar material assemblies encompassing composites and metal alloys, precautions must be taken to eliminate direct contact between the materials to prevent galvanic corrosion.[11-14] The general engineering practice involves keeping the dissimilar materials electrically isolated using interlayers of glass fiber-reinforced composites or protective coating systems.[15-17] Nevertheless, severe galvanic corrosion can develop when CFRP composite edges and aluminum alloys come into direct electrical contact through a condensed layer of atmospheric moisture.[18,19] In such situations, the more noble carbon fibers act as a cathode and facilitate the electrochemical reduction of dissolved oxygen or protons, depending on the pH of the moisture layer.[15,20,21] The consumption of electrons in this cathodic reaction accelerates the electro-oxidation or galvanic corrosion rate of the nearby aluminum alloy. Galvanic corrosion and degradation can adversely

affect the structural integrity of both materials.[9,14,22] One viable approach for mitigating galvanic corrosion entails the surface treatment of CFRP composites with aryldiazonium adlayers to inhibit the oxygen reduction reaction (ORR) kinetics by blocking the active sites on exposed carbon fibers for O_2 chemisorption; the initial step of the ORR mechanism.

A significant body of work has reported the grafting of covalently attached, organic adlayers on carbon, metal, and semiconductor surfaces using aryldiazonium salts.[23-27] The simple and rapid electrochemically-assisted reduction of aryldiazonium salts modifies substrates by generating aryl radicals near the electrode surface that then bind covalently to the surface, producing a stable adlayer.[28,29] Spontaneous grafting involves the immersion of substrates in aryldiazonium salt solutions under open circuit conditions with no electrochemical induction.[30-33] While both methods yield adlayers with similar characteristics, spontaneous grafting is more practical in real-world applications involving large component assemblies or repair processes. We have previously reported on the electrochemically-assisted and spontaneous grafting of diazonium adlayers on CFRP composites and showed that the galvanic corrosion of AA2024-T3 aluminum alloys is mitigated most effectively when joining with a surface-treated CFRP composite during neutral salt spray exposure (ASTM B117, 5 wt.% NaCl) due to the inhibition of cathodic ORR. [34, 35]

We investigated and compared the extent of galvanic corrosion damage on TCP-coated AA7075-T6 aluminum alloys when mechanically joined with NAB-treated CFRP composites during 14-day neutral salt spray (ASTM B117, 5 wt.% NaCl, at 35 °C) and 14-day thin layer mist (3.5 wt.% NaCl, 55 °C) exposures. In this work, we build upon past work on NAB adlayer formation on CFRP composites electrochemically and spontaneously and the effectiveness of the surface treatment at reducing galvanic corrosion on TCP-coated AA7075-T6 lap joint specimens

during exposure to neutral salt spray and thin layer mist tests. Thin layer mist accelerated degradation test is more aggressive than a continuous neutral salt spray and more resemble real environmental exposure by a coast mist wetting, evaporation, salt concentration changes and heating and cooling cycles.[36] The results demonstrate that the galvanic corrosion damage is significantly reduced on the alloy when the CFRP composite is surface treated with a spontaneously formed NAB adlayer, during an aggressive thin layer mist test. The reason for this is the blocking properties of the spontaneously formed adlayer that serve to inhibit the oxygen reduction reaction kinetics. The spontaneously formed adlayers appear more dense and compact, have fewer pinholes and defects, and may readily form multilayers. Clearly, the adlayers are stable during 14 days of neutral salt spray and thin layer mist testing. The results further portend the effectiveness of this surface treatment to reduce aluminum alloy galvanic corrosion rates and damage in aircraft structures.

4.2 EXPERIMENTAL METHODS

Chemicals and Reagents. Acetonitrile (Sigma Aldrich) was distilled and stored over activated 5 Å molecular sieves prior to use for water impurity removal. Tetrabutylammonium tetrafluoroborate (NBu_4BF_4) was purchased from a commercial supplier (Sigma Aldrich) and used as received. The 4-nitroazobenzene diazonium tetrafluoroborate (NAB) was provided by Professor Richard McCreery and his group at the University of Alberta. Bonderite C-AK 6849 AERO (Henkel Technologies, Madison Heights, MI) was the commercial solution used for degreasing the specimens. Bonderite C-IC SMUTGO NC AERO (Henkel Technologies, Madison Heights, MI) was the commercial solution used to desmut the aluminum alloy specimens. Bonderite T-5900 RTU (Henkel Technologies, Madison Heights, MI) was the commercial trivalent chromium process (TCP) coating bath used. All aqueous solutions were prepared with ultrapure water (> 17

Ω-cm) from a Barnstead E-Pure water purification system.

Pretreatment of CFRP Composite Specimens. A standard airframe composite panel (AS4/3501-6) was prepared by and provided courtesy of the Polymer and Composites Division at the Naval Air Systems Command (Patuxent River, MD). The panel was a unidirectional cross-ply [0/90]4s laminate prepared with an intermediate modulus polyacrylonitrile (PAN) carbon fiber (7 μm diam.) and a toughened epoxy prepreg (3501-6) from Hexcel. The layup was an orthogonally oriented ply (0/90-degree direction 4 times). The composite specimen thickness was 0.25 cm. Composite panels (1 Ft^2) cut into 2.4 cm × 1.8 cm pieces were used for testing. Electrical connection was made by inserting a copper wire into a hole drilled on one side of the specimen and affixing it with conducting epoxy, as previously reported.[34,35] All three sides, other than the one with the Cu wire contact, were first abraded for 3 min on P1500 grit aluminum oxide sandpaper wetted with ultrapure water. This was followed by a 10-min ultrasonic cleaning in ultrapure water with the composite suspended in solution. Each abraded edge was then polished for 5 min with successively smaller grades of alumina powder (1, 0.3, and 0.05 μm) slurried in ultrapure water on separate felt polishing pads. After each polishing step, the composite was rinsed with and ultrasonically cleaned in ultrapure water for 15 min to remove polishing debris. A final ultrasonic cleaning was then performed in pure acetonitrile for 10 min. For the CFRP specimens used in the accelerated degradation testing, a lap joint configuration with the aluminum alloy was used for testing, as has been described in other publications.[34,35].

Surface Modification of CFRP Composite Specimens. The aryldiazonium salt studied was 4-nitroazobenzenediazonium tetrafluoroborate (NAB). The electrochemically-assisted surface modification was performed as reported elsewhere by cyclic voltammetry.[34] The spontaneous surface modification was performed under open circuit conditions by immersing the pretreated

CFRP composite specimen in a solution of 5 mM NAB salt dissolved in acetonitrile for 24 h at room temperature.[35] After modification, the specimens were thoroughly rinsed with acetonitrile to remove any unbound diazonium molecules.

Contact Angle Measurements. The wettability of the CFRE composite specimens before and after surface modification was investigated by static contact angle measurements. The contact angles were recorded on the composite edge surfaces with ultrapure water using a VCA Optima™ (AST Products, Inc.) video contact angle system. The volume of a water droplet used was 0.5 μL. All measurements were made in a dry room with a relative humidity of ≤ 0.1 %.

Electrochemical Measurements. All the electrochemical measurements were performed using a Reference 600™ (Gamry Instruments, Inc.) computer-controlled workstation in a three-compartment, three-electrode glass cell. A platinum (Pt) flag was used as the counter electrode and a silver wire quasi-reversible electrode (AgQRE) was employed as the reference. The CFRP composite served as the working electrode. Only the edge opposite of that where the electrical contact was affixed was utilized in these measurements. The change in the open circuit potential (OCP) during which spontaneous adlayer formation occurred was recorded for abraded and polished CFRP composite electrodes in acetonitrile solutions containing 5 mM NAB + 0.1 M NBu_4BF_4. The electrochemically-active NAB admolecule coverage on the modified edge was determined by cyclic voltammetry in deaerated acetonitrile containing 0.1 M NBu_4BF_4. The potential was cycled between 0.4 and -1.2 V vs AgQRE at a scan rate of 50 mV/s.

Preparation of Aluminum Alloy (AA) Specimens. Commercial wrought aluminum alloy 7075-T6 was obtained as a 1 mm-thick sheet (www.onlinemetals.com) and cut into 5.5 cm × 3.0 cm pieces. The alloy specimens were mechanically abraded with a 1500 grit aluminum oxide sandpaper for 4 min and ultrasonically cleaned in ultrapure water for 20 min. The specimens were then fine

polished with 0.3 μm alumina powder (Buehler) slurried in ultrapure water on a felt polishing pad for 4 min and ultrasonically cleaned in ultrapure water for another 20 min to remove polishing debris. This was followed by a degreasing step at 55 °C for 10 min in 20% v/v Bonderite C-AK 6849 AERO alkaline degreaser. The specimens were then gently rinsed with flowing city tap water for 2 min. The specimens were then deoxidized by immersion in 20% v/v Bonderite C-IC SMUTGO NC AERO at room temperature for 2 min. This was followed by another 2-min tap water rinse. The alloy specimens were then surface treated with a trivalent chromium process (TCP) conversion coating by immersion in Bonderite T5900 (Henkel Technologies) at room temperature for 10 min. Finally, the coated specimens were immersion rinsed in a beaker full of city tap water for 2 min, a beaker of ultrapure water for 30 s, and air dried for at least 12 h in a covered dish before further use.

Configuration of the CFRP Composite and AA7075-T6 Specimens in Lap Joints. The TCP-coated AA7075-T6 specimens were joined with unmodified and modified CFRP composite specimens, as presented in Figure 4.1, using a stainless-steel fastener. The mechanical fastener was tightened with a torque of 45 lb-in. The threads of the stainless-steel fasteners were covered with Teflon tape to prevent direct electrical contact with the composite and through-hole wall. The bolt head and nut were wet sealed with a commercial silicon sealant (DAP KWIK SEAL ULTRA) to repel water and to electrically isolate the metal from the solution mist. The back side of each aluminum alloy specimen was covered with corrosion protection tape (Scotchrap™, 3M Company) so that only the front surface of the alloy was exposed during the accelerated degradation testing. The geometric cathode/anode are ratio was 0.36. (6.0 cm^2 for the CFRP composite and 16.5 cm^2 for the aluminum alloy).

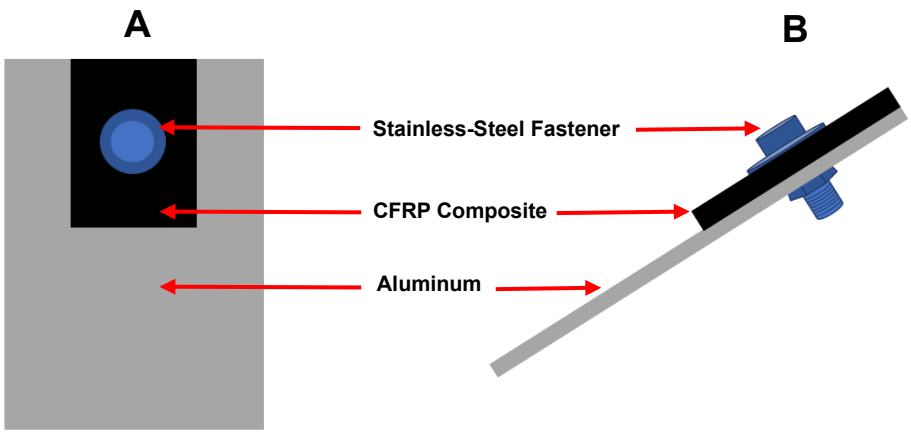

Figure 4.1. Configuration of the lap joined aluminum alloy-CFRP composite specimens used in the accelerated degradation testing. (A) Top view. (B) Side view. Dimensions: CFRP composite (2.4 × 1.8 × 0.25 cm), AA2024-T3 (5.5 × 3.0 × 0.1 cm).

Neutral Salt Spray Accelerated Degradation Test (ASTM B117). Mechanically fastened aluminum alloy-CFRP composite specimens were placed at a ~20° angle (with respect to the vertical axis) on plastic racks inside a commercial salt spray chamber (Associated Environmental Systems-MX 9204). The bolted end of the specimen was highest on the rack. The specimens were then exposed to a continuous salt fog generated with 5 wt.% NaCl at 35 ± 1 °C for 14 days according to ASTM B117 (Standard Practice for Operating Salt Spray (Fog) Apparatus). At the end of the 14-day test period, the coupled specimens were removed, disassembled, and rinsed thoroughly with and ultrasonically cleaned in ultrapure water for 30 min to remove salt deposits. The alloy specimens were then ultrasonically cleaned in concentrated HNO_3 for 10 min periods to dissolve corrosion product, dried thoroughly with N_2 gas, and weighed. Ultrasonic cleaning in HNO_3 was repeated until a constant weight was achieved.[51] The mass loss of the aluminum alloy provided a measure of the galvanic corrosion rate.

Thin Layer Mist Accelerated Degradation Test. Lap joint aluminum alloy-CFRP composite specimens were positioned horizontally on a platform above an ultrapure water layer inside a sealed polypropylene container, as shown in Figure 4.2. Separate containers were used for each

joined specimen. During a test, each specimen was misted with one spray (~1 ft distance) of 3.5 wt.% NaCl from a nebulizing spray bottle at room temperature. The closed polypropylene containers containing the joined specimens were then placed in an oven at 55°C. The water in the bottom of the container ensured that the relative humidity inside the container was at 100% during the test.

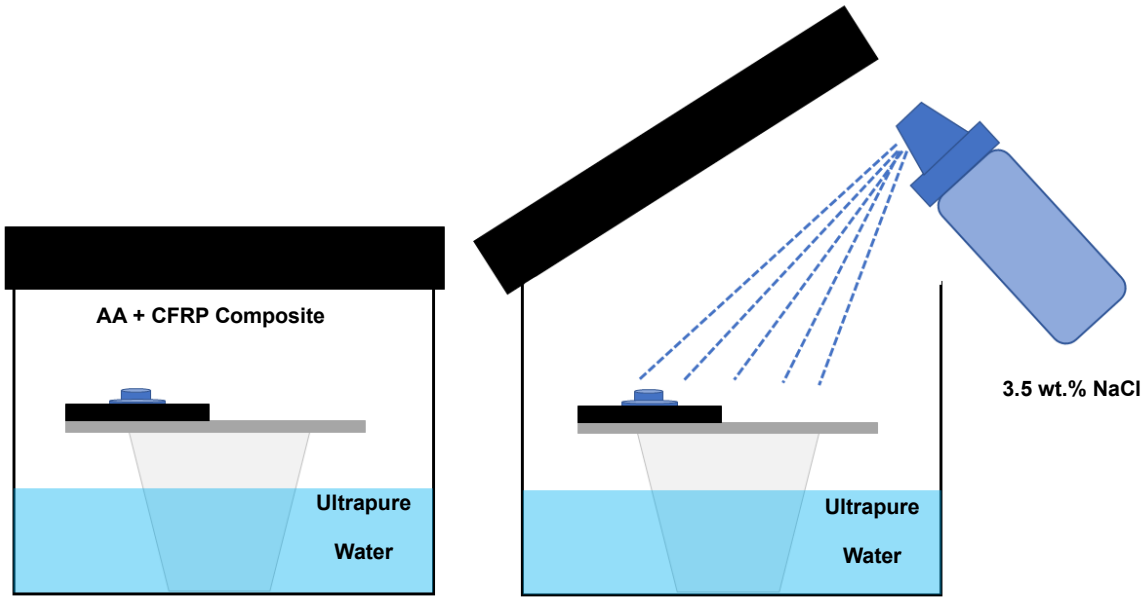

Figure 4.2. A schematic diagram of the thin layer mist (TLM) test configuration and specimen positioning.[36]

One test cycle was 24 h, during which the specimen surfaces experienced mist droplet evaporation, but did not completely dry out. After each 24 h test cycle, the containers were removed from the oven, cooled to room temperature for 30 min, and the specimens were resprayed with 3.5 wt.% NaCl. The containers remained open to the atmosphere for 15 min after applying 3.5 wt.% NaCl mist to replenish oxygen inside before being closed and placed back in the oven at 55 °C. The entire test lasted for 14 cycles. At the end of the 14-day test period, the coupled specimens were removed, disassembled, and rinsed thoroughly with and ultrasonically cleaned in ultrapure water for 30 min to remove salt deposits. The accumulated corrosion product on the alloy specimens was then removed by ultrasonically cleaning them in concentrated HNO_3 for 10 min

periods followed by thorough rinsing with ultrapure water and drying under a stream of N_2 gas. Ultrasonic cleaning in HNO_3 was repeated until the weight change of a specimen was negligible (≤ 0.002 g).[51]

Evaluation of Corrosion Damage. The galvanic corrosion damage on each AA7075-T6 panel was assessed both qualitatively and quantitatively. The surface texture and other corrosion damage on cleaned AA7075-T6 specimens were evaluated using a Keyence VHX 6000 digital optical and a Nikon C2 laser scanning confocal microscope. For higher resolution imaging, a JEOL 6610LV scanning electron microscope housed at the MSU Center for Advanced Microscopy was used. The weight loss of aluminum alloy panels due to corrosion damage was determined by comparing the weights measured before and after the accelerated degradation testing. The corrosion intensity (CI) was calculated using Equation 1, in which $y = 14\ day\ \times \frac{1\ yr}{365\ Day}$.

$$CI = \frac{g\ Loss}{m^2.y} \qquad (1)$$

The following scale, developed by the U.S. Army Material Command, was utilized to grade the corrosion damage on the aluminum alloy panels after the 14-day neutral salt spray and thin layer mist exposure. The grading scale is as follows: Stage 0- No visible corrosion, Stage 1- Simple discoloration and staining, Stage 2- Loose rust or corrosion product and early stage pitting along with minor etching, Stage 3- Rust or corrosion product, minor etching, pitting, and more extensive surface damage, Stage 4- Significant rust or corrosion product formation, extensive etching, blistering, and pitting that has progressed to the point where the life of the specimen has been affected.[41]

4.3 RESULTS

Surface Modification. Figure 4.3 presents the *E-t* curve of the OCP recorded during the spontaneous NAB adlayer formation on a pretreated CFRP composite. The immersion was for 24

h under ambient condition. The potential measurement began immediately upon immersion in the NAB diazonium salt solution. The OCP exhibits an initial negative shift from 0.346 V to *ca.* -0.440 V (vs AgQRE) within the first 3 h of the grafting process. Vautrin-UI et al. observed a similar shift in the OCP towards negative potentials during the spontaneous organic adlayer formation on carbon and metal surfaces using diazonium salts which can be attributed to a change in the accumulated charge on the electrode surface.[32] After 3 h, the OCP stabilizes at *ca.* -0.430 V (vs. AgQRE). The stable OCP indicates an unchanging condition at the electrode surface. This potential has no thermodynamic significance.

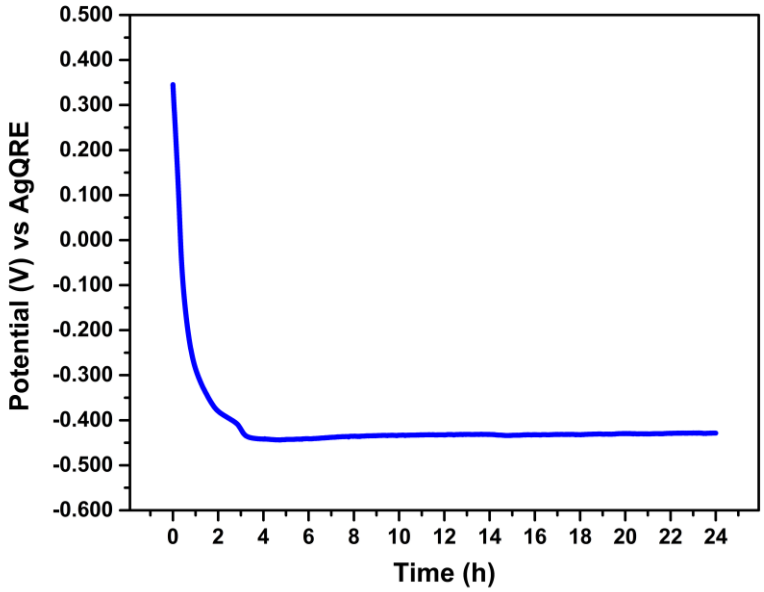

Figure 4.3. Plot of the OCP with time during a 24-h immersion of a polished CFRP composite electrode in acetonitrile + 0.1 M NBu_4BF_4 + 5 mM NAB under ambient condition.

The spontaneous grafting of an NAB adlayer on the CFRP composite electrode was achieved by immersing the specimen in a 5 mM diazonium salt solution under open conditions for 24 h. Prior work showed that the oxygen reduction reaction current was suppressed the most by an adlayer formed for this time.[35] The successful attachment of NAB admolecules on a CFRP composite surfaces in the absence of electrochemical assistance was confirmed by Raman spectroscopy in previous work.[35] The electrochemical characterization of the modified surface was

performed by cyclic voltammetry.[23,32,37-39] Figure 4.4 reveals the electrochemical response acquired for a typical spontaneously grafted CFRE composite electrode in acetonitrile containing 0.1 M NBu_4BF_4. The reduction and oxidation peaks observed, respectively, at -0.9 and -0.7 V (vs. AgQRE) correspond to the reversible $1e^-$ reduction of the pendant nitro ($-NO_2$) group on the grafted NAB admolecules to the radical anion ($-NO_2^{\bullet -}$).[37]

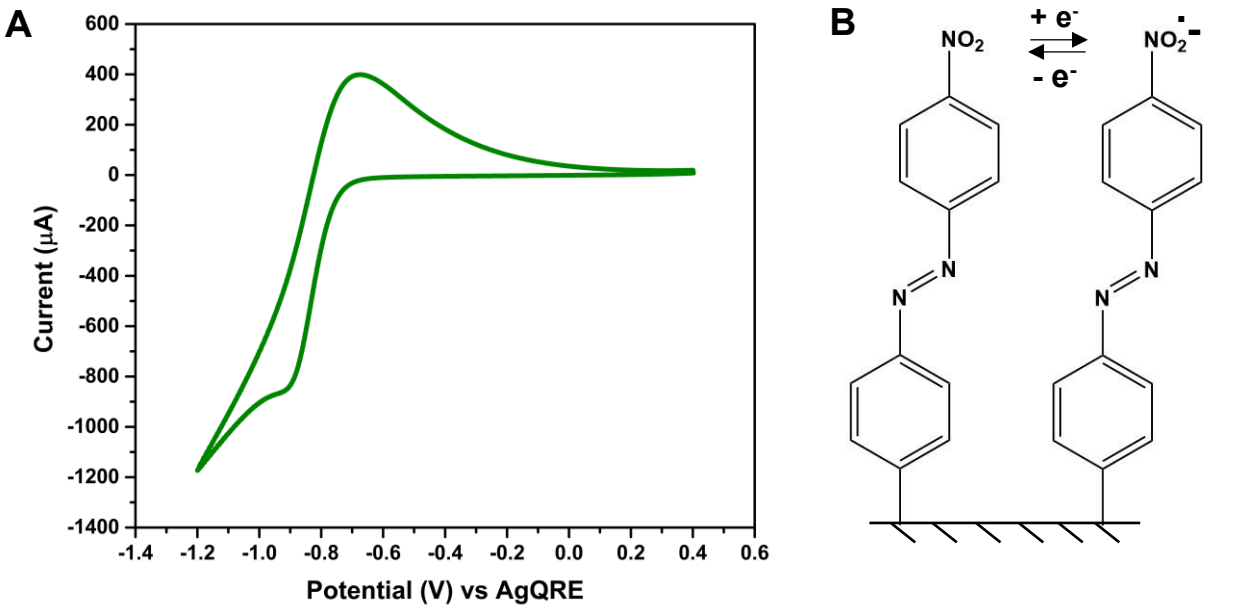

Figure 4.4. (A) Cyclic voltammetric *i-E* curve of a spontaneously modified CFRE composite electrode recorded in acetonitrile + 0.1 M NBu_4BF_4 at a scan rate of 50 mV/s. Grafting was performed by immersing the composite edge for 24 h in 5 mM NAB diazonium salt dissolved in deaerated acetonitrile. (B) The redox reaction of the pendant NO_2 functional group.

The electrochemically active surface coverage of the NAB adlayer was determined by integrating the oxidation peak, as reported elsewhere.[34] A nominal surface coverage of 4.3 ± 0.4 nmol/cm^2 was determined for the 24-h immersion. This surface coverage is about 50% of that for 4-NAB formed on the CFRP composite by the electrochemically-assisted method.[34] The surface coverage is reported as mean ± std. dev. for three different composites. The data are normalized to the geometric area of the composite edge. It should be noted that the surface coverage calculation by cyclic voltammetry only considers the electrochemically detected admolecules that are located at the electrode-adlayer interface.[31] Hence, the true surface coverage may be higher than the

electrochemically-active coverage. The theoretical coverage for a monolayer of closely packed NAB admolecules on a flat surface, assuming end-on bonding through the phenyl ring, is 1 nmol/cm^2.[40] The 4× larger apparent surface coverage may be caused by an underestimation of the true surface coverage of carbon fibers exposed on the edge or multilayer formation.

The ability of the adlayer to repel water is an important property. Figure 4.5 presents photographs of ultrapure water droplets on (A) unmodified and (B) spontaneously modified (24 h) CFRP composite edge surfaces. The nominal static contact angles for ultrapure water on an unmodified CFRP composite was 57.3 ± 1.6° while the contact angle on the spontaneously modified CFRP composite edge was higher at 74.5 ± 2.6°. The higher contact angle is attributed to the reduced wettability and increased hydrophobicity of the NAB modified carbon surface. Remember that the carbon fibers are embedded in epoxy so the contact angle measurement is affected by both the epoxy and the surface chemistry of the carbon fibers. In the absence of the NAB adlayer, the carbon surfaces are composed of the carbon-oxygen functional groups.

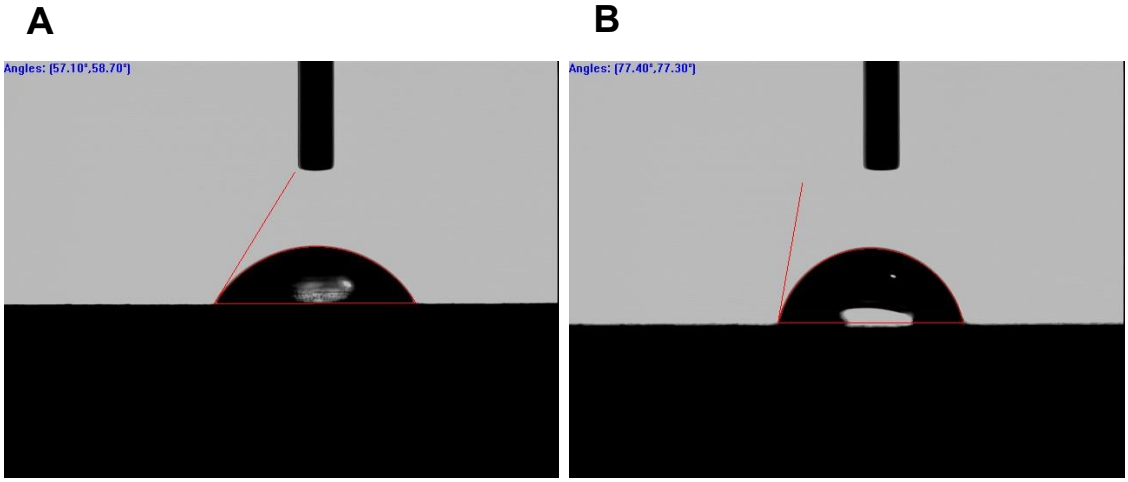

Figure 4.5. Photographs of water droplets and static contact angles for CFRP composite edges (A) unmodified and (B) spontaneously modified with NAB. The composites were spontaneously grafted by immersion in a 5 mM NAB diazonium salt + acetonitrile solution under open circuit condition for 24 h.

Neutral Salt Spray Accelerated Degradation Test (ASTM B117). To investigate the degree to which galvanic corrosion of a TCP-coated AA7075-T6 panel is reduced when it is mechanically joined to a CFRP composite treated with 4-NAB adlayer, the lap joined specimen was subjected to a continuous neutral spray of 5 wt.% NaCl at 35 ± 1 °C for 14 days. The corrosion damage on AA7075-T6 panels was graded according to the scale proposed by the U.S. Army Material Command.[41]

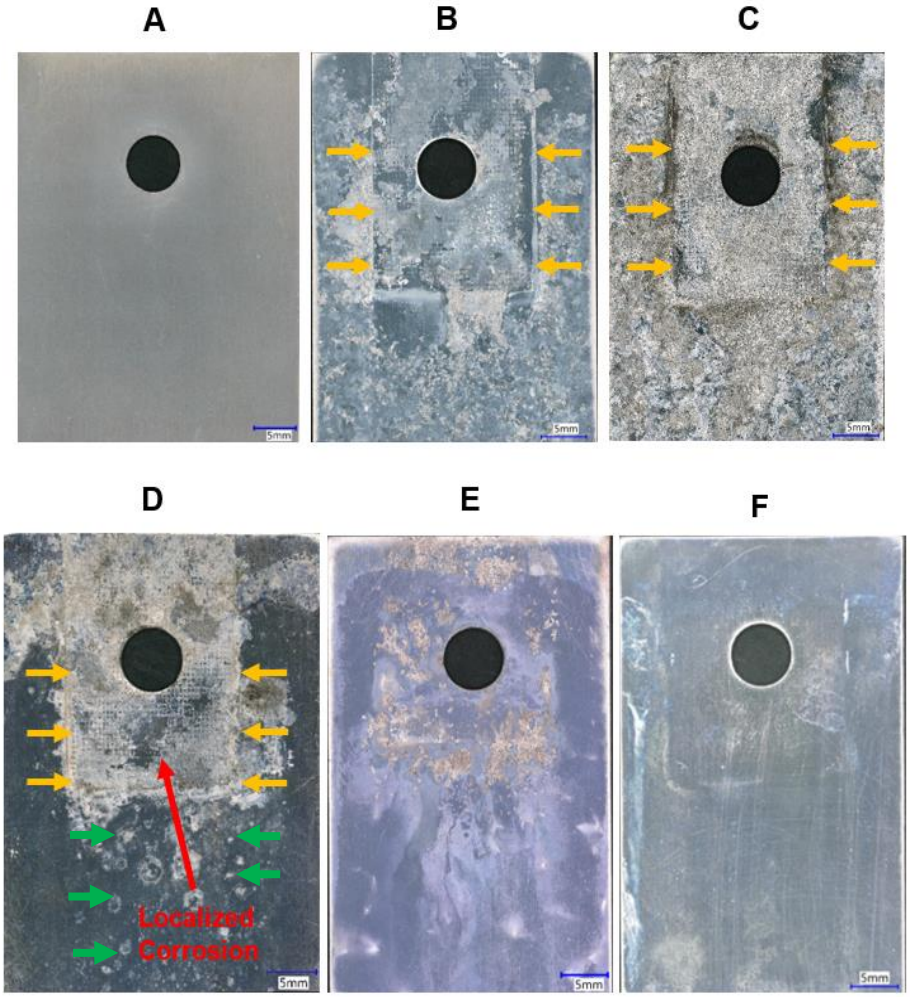

Figure 4.6. Digital optical micrographs of AA7075-T6 panels (A) TCP-coated and before neutral salt spray exposure, (B) uncoated and joined with an unmodified CFRP composite after just 3 days of NSS exposure, (C) uncoated and joined with an unmodified CFRP composite after 14 days of NSS exposure, (D) TCP-coated and joined to an unmodified composite after 14 days of NSS exposure, (E) TCP-coated and joined to an electrochemically-modified composite after 14 days of NSS exposure, and (F) TCP-coated with a spontaneously-modified CFRP composite after 14 days of NSS spray exposure at 30×.

Figure 4.6 presents the digital optical micrographs of the different AA7075-T6 panels before and after the 14-day neutral salt spray (NSS) exposure. The uncoated (Figure 4.6B and C) and TCP-coated (Figure 4.6D) alloy panels joined with an unmodified CFRP composite show widespread corrosion degradation, metal dissolution, and discoloration across the panels near and away from where the composite was joined. No visible of the TCP-coated AA7075-T6 panel prior to NSS exposure (Figure 4.6A). Figures 4.6B and C reveal the corrosion damage to uncoated AA7075-T6 panels that were joined to unmodified CFRP composites after 3 and 14 days of exposure. The uncoated AA7075-T6 panel in Figure 4.6B was exposed to neutral salt spray for only 3 days, while the uncoated A7075-T6 panel in Figure 4.6C was exposed for the entire test period of 14 days. Without either alloy panel or composite being surface treated, widespread corrosion damage (stage 3) is seen that results from a combination of galvanic, crevice underneath the composite specimen, and general corrosion, even after just 3 days. When exposed for 14 days, the corrosion damage develops to a point where there is extensive dissolution and corrosion product formation across the entire panel (stage 4). There is also trenching on both AA7075-T6 panels as indicated by the yellow arrows along where the edges of the unmodified composites were positioned. This trenching results from dissolution of the metal with depth into the alloy, driven galvanically by the oxygen reduction on the exposed CFRP composite edges. Figure 4.6D presents a TCP-coated AA7075-T6 panel that was joined to unmodified CFRP composite during the 14-day test. The TCP coating effectively inhibits general and pitting corrosion on the alloy panel away from the composite (green arrows), as compared to the widespread damage seen on the uncoated panel. When applied, the TCP conversion coating protects the AA7075-T6 alloy against corrosion through both anodic and cathodic protection mechanisms. The approximate composition of AA7075-T6 includes 5.1%-6.1% Zn, 2.1%-2.9% Mg, 1.2-2.0 % Cu and less than 0.5% of Si, Fe,

Mn, Ti, Cr etc.[42] The TCP coating (100-200 nm thick) provides cathodic protection by acting as a physical barrier to the transport of dissolved oxygen to surface Fe-rich and/or Cu-rich intermetallic sites.[43-50] The anodic protection is provided by coating the Al rich sites of the alloy (physical blocking), thereby inhibiting the metal oxidation reaction.[44-50] In other words, the TCP coating provided barrier layer protection to the underlying alloy prohibiting direct contact with the environment. The damage on the TCP-coated panel is more localized to trenching near where the edges of the composite were positioned and underneath the composite as crevice corrosion.

In contrast, micrographs in Figures 4.6E and F display a lower level of corrosion damage near the composite edges and underneath the composite, when the composites were modified with NAB adlayers. The TCP-coated AA7075-T6 panel joined to a CFRP composite electrochemically modified with NAB (Figure 4.6E) exhibits far less trenching along the perimeter of where the composite was positioned and significantly reduced corrosion damage (Stage 2) underneath the composite as compared to the TCP-coated AA7075-T6 panel joined to an unmodified composite (Figure 4.6D). No corrosion damage is visible on the panel away from where the composite was contacting. Importantly, neither trenching nor corrosion damage underneath the composite are present on the TCP-coated AA7075-T6 panel joined to a CFRP composite spontaneously modified with NAB for 24 h (Figure 4.6F). Only minor discoloration and staining (Stage 1) are observed on the AA7075-T6 panel. Clearly, the 24-h spontaneously formed NAB adlayer is more effective at inhibiting galvanic corrosion of the TCP-coated alloy. This is attenuated because of the decreased current for O_2 reduction, as has previously been reported.[35]

The galvanic corrosion damage was assessed quantitatively using surface texture analysis with a digital optical microscope. The surface texture analysis was performed at five different spots on each alloy panel in the region adjacent to where the composite was joined (i.e., areas of greatest

galvanic corrosion or trenching). The area analyzed per spot was 1000 µm × 1000 µm at a 500× magnification. A schematic diagram is presented in Figure 4.7A showing the regions where the 3D micrographs were collected on each panel. Figure 4.7B shows the average roughness and peak-to-valley height data for TCP-coated AA7075-T6 panels joined with unmodified, electrochemically-modified, and spontaneously-modified CFRP composites with NAB after 14 days of NSS exposure.

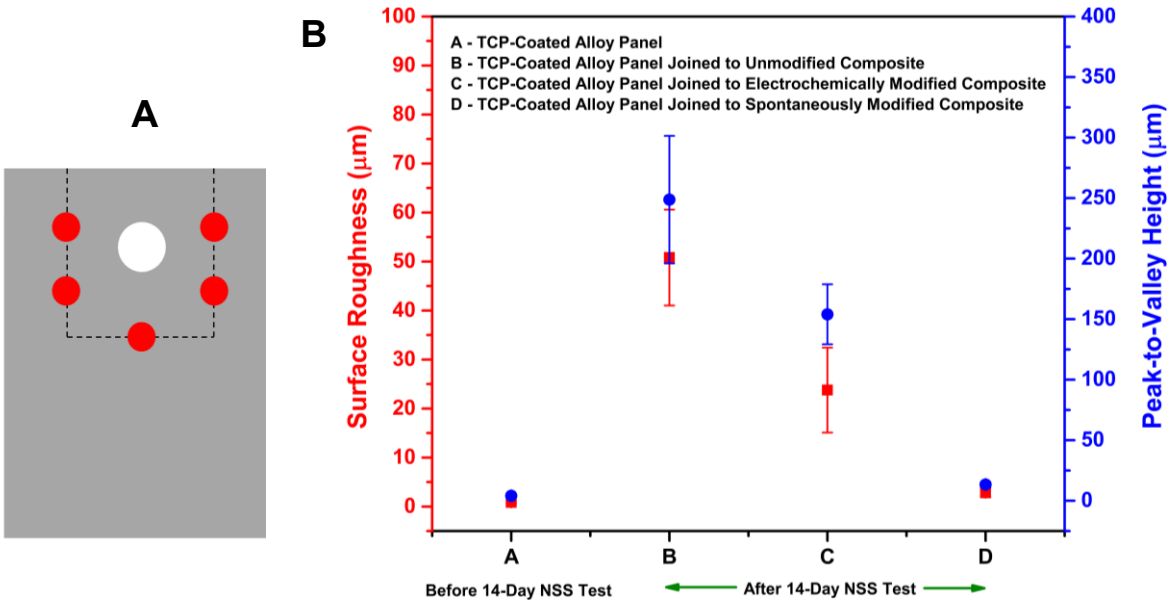

Figure 4.7. (A) Schematic diagram showing the areas where the surface texture analysis was performed on the TCP-coated AA7075-T6 panel and (B) the average surface roughness and peak-to-valley height data for specimens before and after 14 days of NSS exposure. Data are presented for TCP-coated AA 7075-T6 panels joined with CFRP composites unmodified, electrochemically modified, and spontaneously modified (24 h immersion) with NAB. Data are presented as mean ± std. dev for n=15, measurements per panel. Roughness data were recorded on 5 spots per AA7075-T6 panel and 3 panels of each type were used to generate the posted data.

The average surface roughness measured for TCP-coated AA7075-T6 panels prior to salt spray exposure was 0.9 ± 0.3 µm. The average surface roughness of TCP-coated AA7075-T6 panels joined to CFRP composites unmodified, electrochemically modified, and spontaneously modified with NAB after 14 days were 50.8 ± 9.8, 23.8 ± 8.7, and 2.8 ± 0.9 µm, respectively. The largest surface roughness is seen for the TCP-coated AA7075-T6 panels joined to unmodified

CFRP composites due to the extensive galvanic corrosion damage the specimens experienced. The surface roughness is 60× larger, as compared to the unexposed panel. The TCP-coated aluminum panels joined with electrochemically-modified composites showed a surface roughness increase of 28× with respect to the control panel and a surface roughness decrease of 2× as compared to the panels joined to unmodified composites. The lowest surface roughness is seen for the TCP-coated panels joined to spontaneously modified CFRP composites. The surface roughness increased by only 3× after the 14-day NSS test as compared to the unexposed panel.

The peak-to-valley height recorded for the unexposed alloy panel was 4.1 ± 0.7 μm. After 14 days of NSS exposure, TCP-coated panels joined to unmodified, electrochemically modified, and spontaneously modified CFRP composites had nominal peak-to-valley heights of 248.8 ± 52.6, 154.0 ± 24.8, and 13.4 ± 2.1 μm, respectively. These values reflect the galvanic corrosion that occurs leading to trench formation. The peak-to-valley height is approximately 61× higher for the TCP-coated AA7075-T6 panel joined to unmodified composite, 38× higher for the TCP-coated AA7075-T6 panel joined to electrochemically modified composite, and merely 3× higher for the TCP-coated AA7075-T6 panel joined to spontaneously modified composite, as compared to the unexposed control panel. Following a similar trend as the surface roughness, the TCP-coated AA7075-T6 panel joined to unmodified composite exhibited the largest peak-to-valley height reflective of significant galvanic corrosion damage that progressed deep into the alloy panel over 14 days. In contrast, the surface treatment of CFRP composites with an electrochemically-formed NAB adlayer decreased the peak-to-valley height of the TCP-coated AA7075-T6 panel by 2×. The TCP-coated AA7075-T6 panels joined to CFRP composites with spontaneously formed NAB adlayers remarkably lowered the peak-to-valley height by 19× during the14-day NSS test. In summary, the surface texture analysis provides evidence for the notably reduced galvanic corrosion

damage and negligible progression of metal dissolution with depth into the AA7075-T6 panel leading to trench formation when joined with a spontaneously modified CFRP composite.

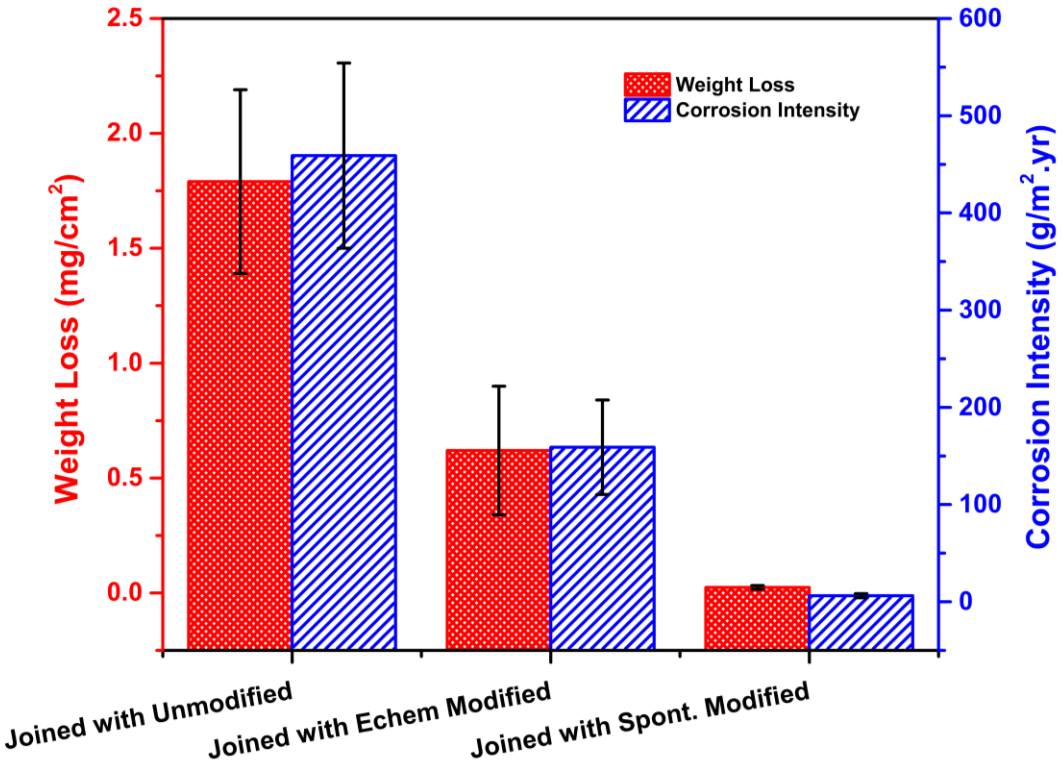

Figure 4.8. Weight loss and corrosion intensity data for TCP-coated AA7075-T6 panels joined with unmodified, electrochemically-modified (NAB) and spontaneously-modified (NAB) CFRP composites after 14 days of NSS exposure. Data are presented as mean ± std. dev. for n=3 specimens of each type.

Figure 4.8 presents weight loss and corrosion intensity data for TCP-coated AA7075-T6 panels joined with unmodified, electrochemically-modified, and spontaneously-modified CFRP composites after the 14-day NSS test. The TCP-coated AA7075-T6 panels joined with an unmodified CFRP composite exhibited the largest weight loss per unit area. The weight loss due to corrosion damage was lower 3× for the TCP-coated AA7075-T6 panels coupled to electrochemically-modified CFRP composites. The smallest weight loss was observed for the TCP-coated AA7075-T6 panels joined to CFRP composites surface treated with a spontaneously grafted NAB adlayer. This weight loss was 75× lower, as compared to the alloy joined with

unmodified CFRP composites. The corrosion intensity, defined as the weight loss of the aluminum alloy per m^2 per year, revealed the same trend as the weight loss data and decreased in the following order. TCP-coated AA7075-T6 coupled to unmodified CFRP composite > TCP-coated AA7075-T6 coupled to electrochemically-modified CFRP composite > TCP-coated AA7075-T6 coupled to spontaneously-modified CFRP composite. Collectively, the NAB adlayer spontaneously formed during a 24-h immersion provides superior inhibition of the ORR kinetics and therefore significantly attenuates the galvanic corrosion of the alloy panel.

Thin Layer Mist Accelerated Degradation Test. Figure 4.9 shows the digital micrographs of TCP-coated alloy panels before and after the 14-day thin layer mist (TLM) test. Since the CFRP composites modified with spontaneously grafted NAB adlayers through 24-h immersion exhibited ORR currents reduced by close to 99%, as compared to the unmodified composites, the TLM exposure was performed using TCP-coated alloy panels joined to unmodified and spontaneously modified composites. The TCP-coated AA7075-T6 specimens did not show any visible defects, surface imperfections or discolorations prior to the test (Figure 4.9A). Figures 4.9B and C reveal the extent of corrosion damage on TCP-coated alloy panels joined with unmodified and spontaneously modified CFRP composite specimens, respectively. On both panels, an outline of where the composite specimen was positioned can be seen. The TCP-coated alloy panel coupled to an unmodified composite (Figure 4.9B) is extensively corroded. Galvanic (nearby trenching) and crevice (underneath the composite) corrosion damage are seen on the surface. This damage is confined to the region in direct contact with the composite. The blue arrows identify the crevice corrosion damage on the alloy panel underneath the composite. Trenching due to severe galvanic corrosion was observed on the panel as indicated by red arrows along the three edges of the unmodified CFRP composite. This is expected since the ORR rate is greater at the exposed carbon

fibers of the unmodified composite edge. Another noteworthy observation, as designated by green arrows, is the corrosion damage on the TCP-coated AA7075-T6 panel that emanates from the trenches and spreads laterally on the alloy away from where the composite was joined. This lateral distribution of corrosion damage will be discussed later below.

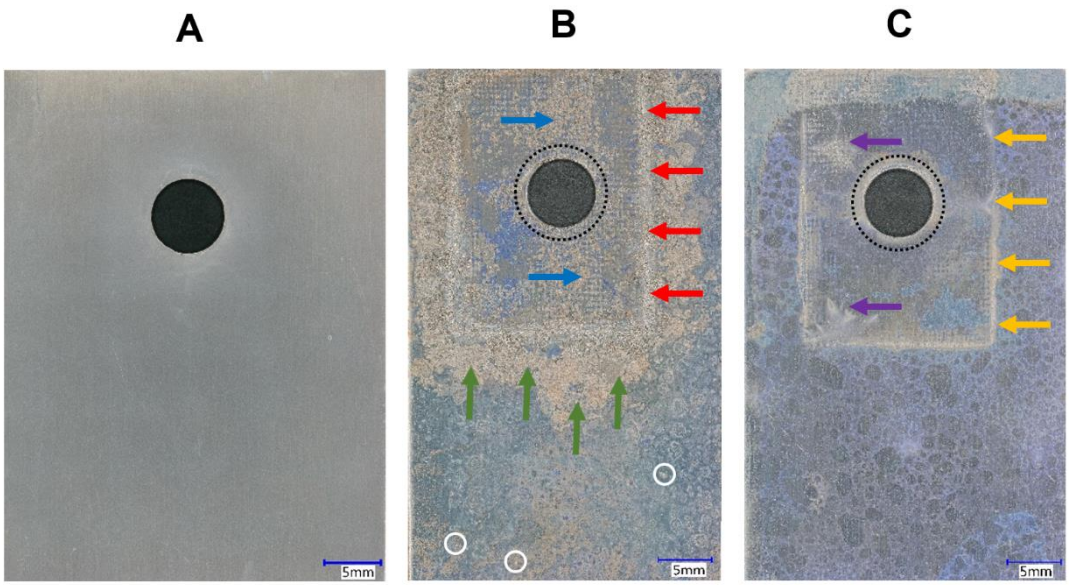

Figure 4.9. Digital micrographs of AA7075 panels (A) TCP-coated before testing, (B) TCP-coated and joined with an unmodified CFRP composite and (C) TCP-coated and joined with a spontaneously-modified (NAB) CFRP composite after 14 days of thin layer mist exposure at 30×.

Figure 4.9C shows a micrograph of the TCP-coated alloy specimen joined with a composite modified spontaneously with NAB. Clearly, there is far less galvanic and crevice corrosion damage on the alloy panel. The trenching degradation near the composite edges, as indicated by yellow arrows, is substantially reduced. The damage on the alloy panel along the three edges of the spontaneously modified CFRP composite resembles more of a discoloration of the composite perimeter rather than trenching degradation. This implies that the spontaneous modification of the CFRP composite by simple immersion for 24 h remarkably inhibits the cathodic ORR thereby attenuating the galvanic corrosion of the AA7075-T6. Additionally, the crevice corrosion underneath the composite is minimal. Only minor discolorations are present as

identified by purple arrows. These discolorations are a sign of a weakened TCP coating. This was confirmed by comparing EDS spectra collected over discolored regions after 14-days of TLM exposure and freshly TCP-coated AA7075-T6 panels. This results suggest a tighter seal of the composite with the aluminum panel. The immersion in the acetonitrile makes the surface epoxy slightly softened so that a tight seal results after joining with the metal.

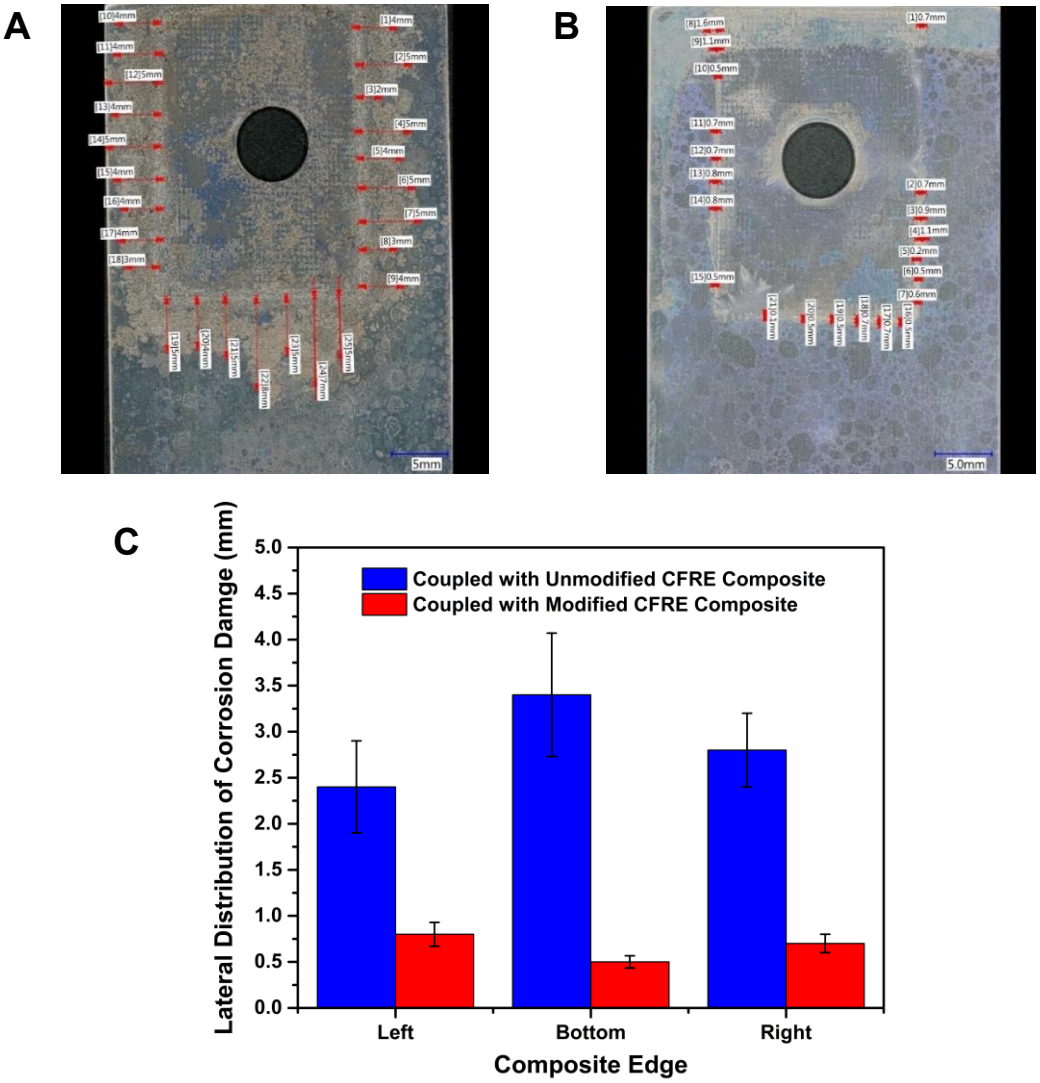

Figure 4.10. Digital micrographs of A) a TCP-coated AA7075-T6 specimen joined to an unmodified CFRP composite and B) a TCP-coated AA7075-T6 specimen joined to a spontaneously-modified CFRP composite showing the lateral distribution of corrosion damage on the AA panels. (C) Lateral corrosion distribution data for TCP-coated AA7075-T6 specimens joined to unmodified and spontaneously modified CFRP composites. Data are presented as mean ± SEM for n=9 measurements per edge.

Digital microscopy was used to measure the lateral distribution of corrosion damage on alloy panels in the trenching areas. Data are presented in Figures 4.10A and B. A comparison of the lateral distribution of the trenches is presented graphically in Figure 4.10C. The AA7075-T6 panel joined to unmodified CFRP composite shows a considerably higher lateral distribution of corrosion. The galvanic corrosion damage originates on the aluminum alloy panel adjacent to the unmodified CFRP composite edges consisting of exposed cathodic carbon fiber sites and progresses laterally away from the composite edge during the 14-day TLM test. The lateral corrosion distribution is approximately 3×, 7×, and 4× higher, respectively, on the left, bottom, and right sides of the alloy panel coupled with the unmodified composite as compared to that of the aluminum alloy specimen coupled with the spontaneously modified composite. With CFRP composite edges spontaneously modified to block the exposed carbon fibers, the lateral corrosion distribution on the TCP-coated AA7075-T6 panel is significantly mitigated.

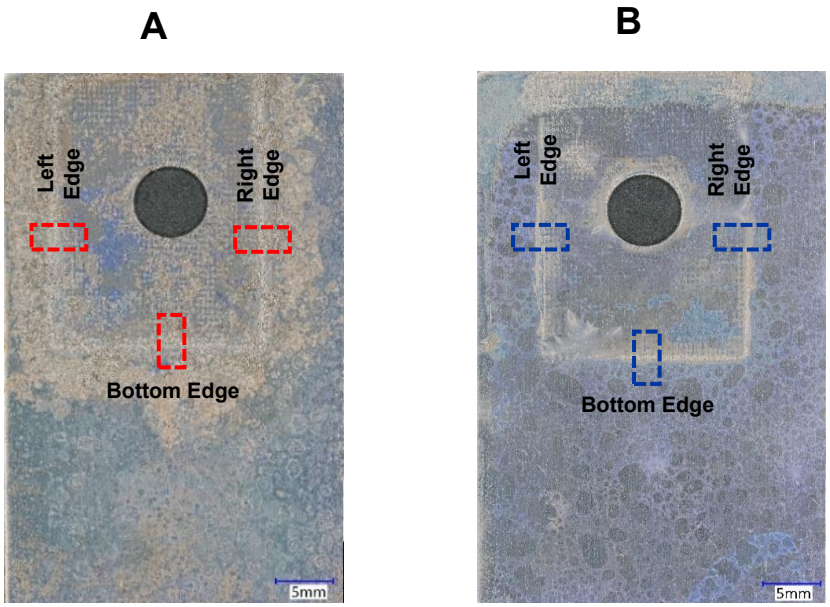

Figure 4.11. Digital micrographs of (A) TCP-coated AA7075-T6 joined to an unmodified CFRP composite and (B) TCP-coated AA7075-T6 joined to a spontaneously modified CFRP composite at 30× showing the areas on each specimen analyzed during the surface texture study.

The galvanic corrosion of an aluminum alloy panel joined to a CFRP composite tends to occur more rapidly near composite edges, prompting trench formation. Such vertical and localized corrosion can severely reduce the mechanical strength of the metal. The surface topography profiles were mapped using stitched 3D micrographs collected at 500× to assess the extent to which the more problematic vertical distribution of galvanic corrosion damage into the AA7075-T6 panel is attenuated due to composite surface treatment after the 14-day TLM test. The galvanic corrosion damage in the form of trenching mainly occurs on the AA7075-T6 panel along where the three edges (two sides and bottom) were sitting on during the degradation test. Hence, the areas indicated by red and blue rectangles in Figure 4.11 were specifically selected for analysis for the purpose of illustrating the difference between the surface profiles across these trenching-prone areas of the two sets of AA7075-T6 panels joined respectively with unmodified and spontaneously modified CFRP composites.

Figure 4.12 reveals the surface topography plots for TCP-coated AA7075-T6 panels joined with unmodified and spontaneously modified CFRP composites after 14 days of TLM exposure. The surface topography plots of the TCP-coated AA7075-T6 panel joined to an unmodified composite shown in Figures 4.12A, C, and E reveal extensive galvanic corrosion damage and metal dissolution leading to trench formation, as indicated by green arrows. In contrast, the surface topography plots of the TCP-coated AA7075-T6 panel joined to spontaneously modified composite exhibit no such trenching and possess a low surface roughness after the TLM exposure.

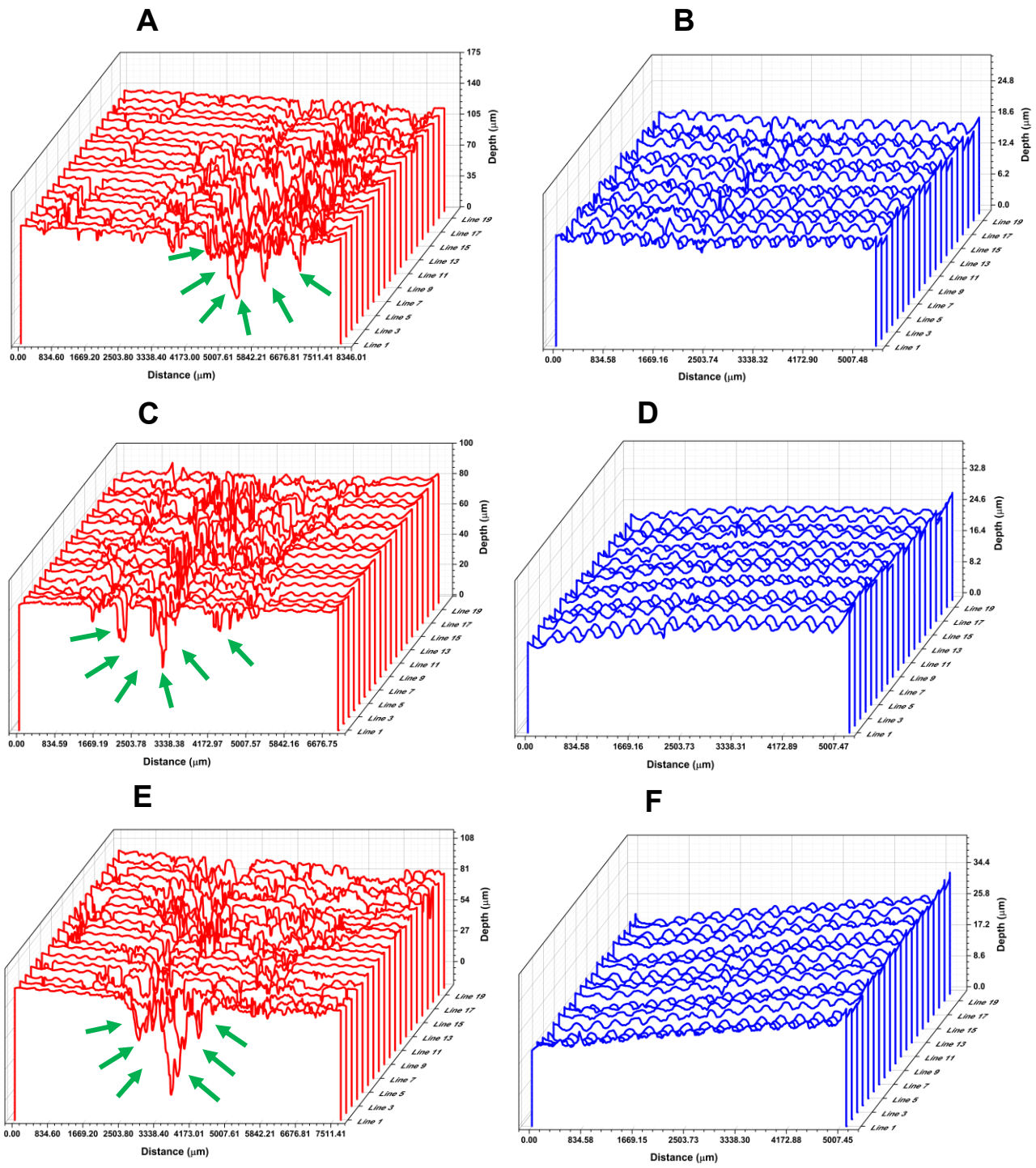

Figure 4.12. Surface topography plots of a TCP-coated AA7075-T6 panel joined to an unmodified CFRP composite in areas indicated in red in Figure 4.11A. (A) left, (B) right and (C) bottom. Surface topography plots of a TCP-coated AA7075-T6 panel joined to a spontaneously modified CFRP composite in areas indicated in blue in Figure 4.11B. (D) left, (E) right and (F) bottom. Plots were acquired after the 14-day TLM test.

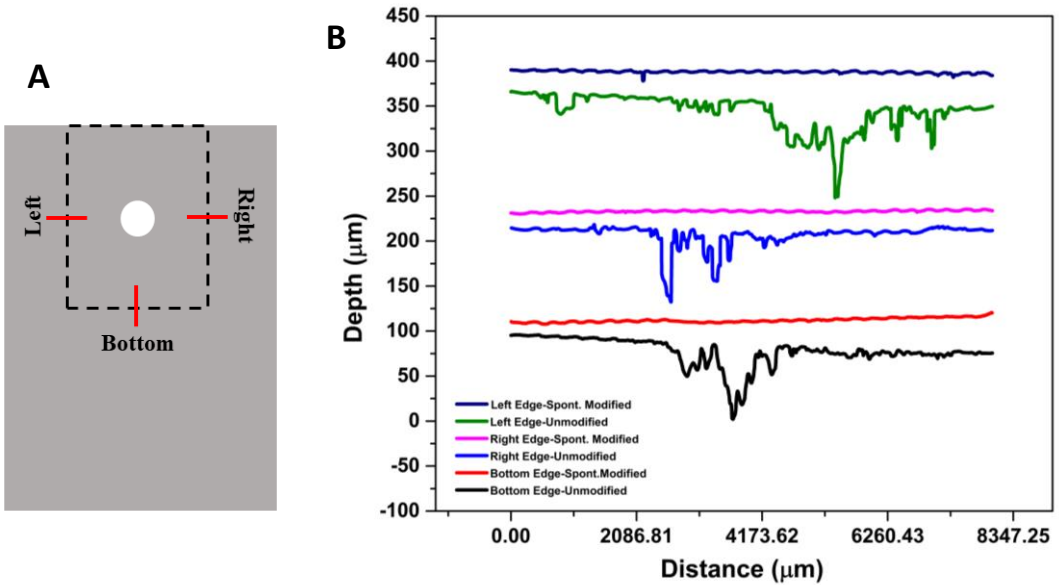

Figure 4.13. Digital optical microscopy surface topography line profiles after the 14-day TLM test revealing the depth of corrosion damage on AA panels near the edges of the unmodified and spontaneously-modified composites. (A) Schematic diagram showing where the line profiles were recorded on each type of AA panel. (B) Line profiles on the TCP-coated AA7075-T6 panels at the left, right and bottom edges of the unmodified and spontaneously-modified CFRP composites were sitting on during the TLM test.

A better representation of the depth of corrosion damage after 14 days of TLM exposure on TCP-coated AA7075-T6 specimens joined respectively with unmodified and spontaneously modified CFRP composites is provided by Figure 4.13. The surface line scans were probed across three regions of each AA7075-T6 panel as shown by the schematic diagram in Figure 4.13A. The distance profiled was 8 mm at 500×.The surface topography line profiles for TCP-coated AA7075-T6 panels joined with unmodified composites demonstrate the galvanic corrosion damage progresses into the alloy panel with a nominal depth of 113.0 ± 22.9 μm. On the contrary, the TCP-coated AA7075-T6 panels coupled with spontaneously modified CFRP composite specimens reveal no such damage. The surface texture of the AA7075-T6 panels near the edges of the CFRP composite was further examined by confocal laser scanning microscopy using the reflection mode with 488 nm laser at 10×. The confocal micrographs acquired for TCP-coated AA7075-T6 joined to unmodified and spontaneously modified CFRP composites are presented in Figure 4.14

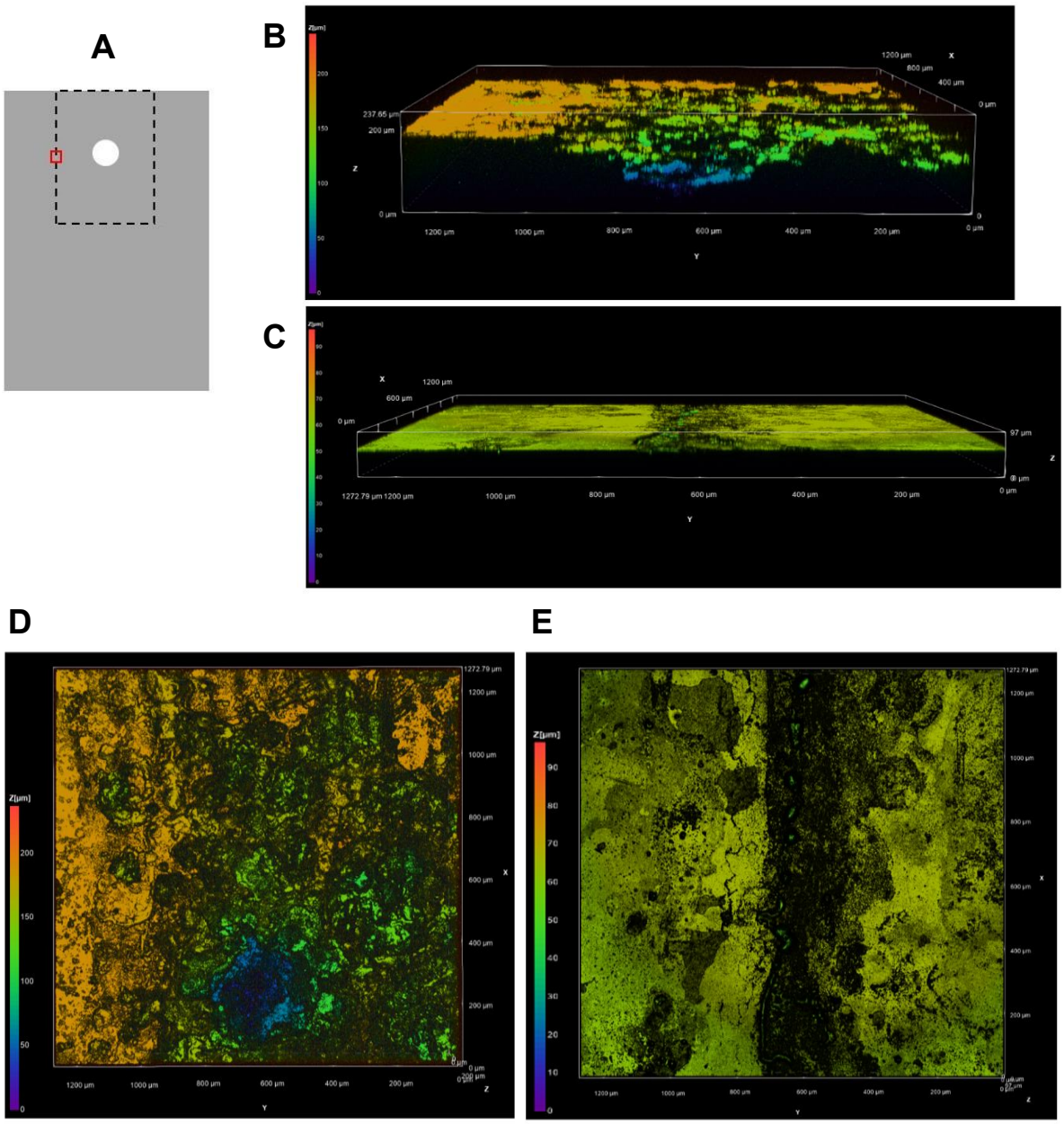

Figure 4.14. (A) Schematic diagram showing where the confocal imaging was performed on the alloy panel. Maximum intensity projection (MIP) images acquired by confocal laser scanning microscopy showing the (B) side view of a TCP-coated AA7075-T6 joined to an unmodified CFRP composite when the 3D profile is rotated by 90° around y axis, (C) side view of a TCP-coated AA7075-T6 joined to a spontaneously-modified CFRP composite when the 3D profile is rotated by 90° around y axis, (D) top view of a TCP-coated AA7075-T6 joined to an unmodified CFRP composite and (E) top view of a TCP-coated AA7075-T6 joined to a spontaneously-modified CFRP composite. The confocal micrographs were collected over the area indicated in red in A at 10× with reflective 488 nm laser.

The schematic diagram in Figure 4.14A indicates in red box where the confocal imaging was performed on each alloy specimen. The maximum intensity projection (MIP) projection images for TCP-coated AA7075-T6 panel coupled to unmodified CFRP composite (Figures 4.14D and E) clearly show the deep pitting due to substantial metal dissolution after the test period while the MIP projection images for TCP-coated AA7075-T6 joined with spontaneously modified CFRP composite reveal a comparatively smoother surface texture over the same area.

Figure 4.15 presents surface line scan profiles recorded from confocal laser scanning microscopy over the same area shown in Figure 4.14 for each aluminum alloy specimen. It should be noted that the confocal micrographs in Figure 4.14 represent only a fraction of a trench region due to the limited field of view, as compared to the digital optical microscope. Hence, the line profile in Figure 4.15 represent the surface texture across only a portion of a trench region. It, however, reveals how corrosion damage has formed a valley on the alloy specimen due to the vertical metal dissolution.

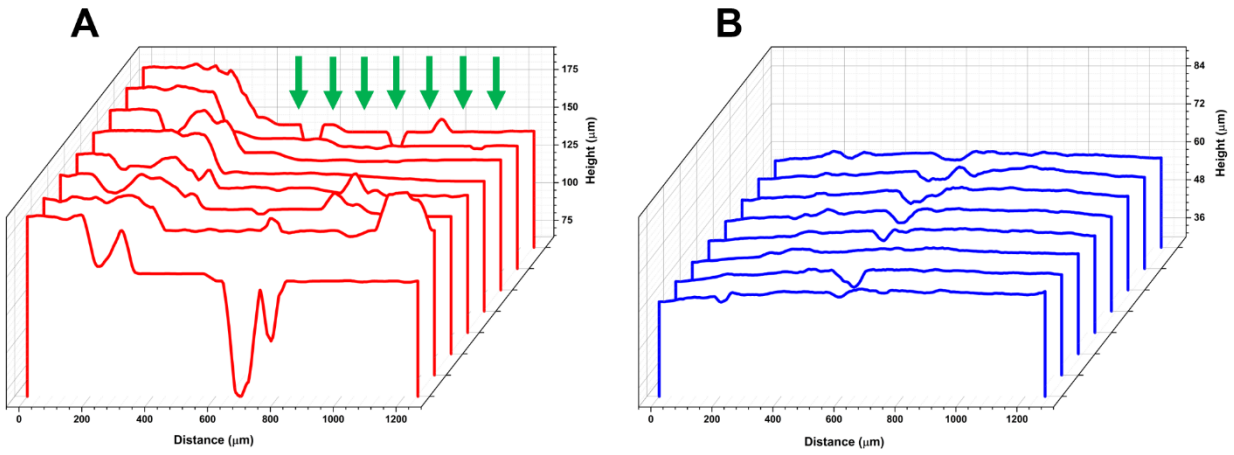

Figure 4.15. Surface line scan profiles generated from the confocal laser scanning microscope over a 1200 µm distance for (A) TCP-coated AA 7075-T6 joined to an unmodified CFRP composite and (B) TCP-coated AA 7075-T6 joined to a spontaneously modified CFRP composite at 10×.

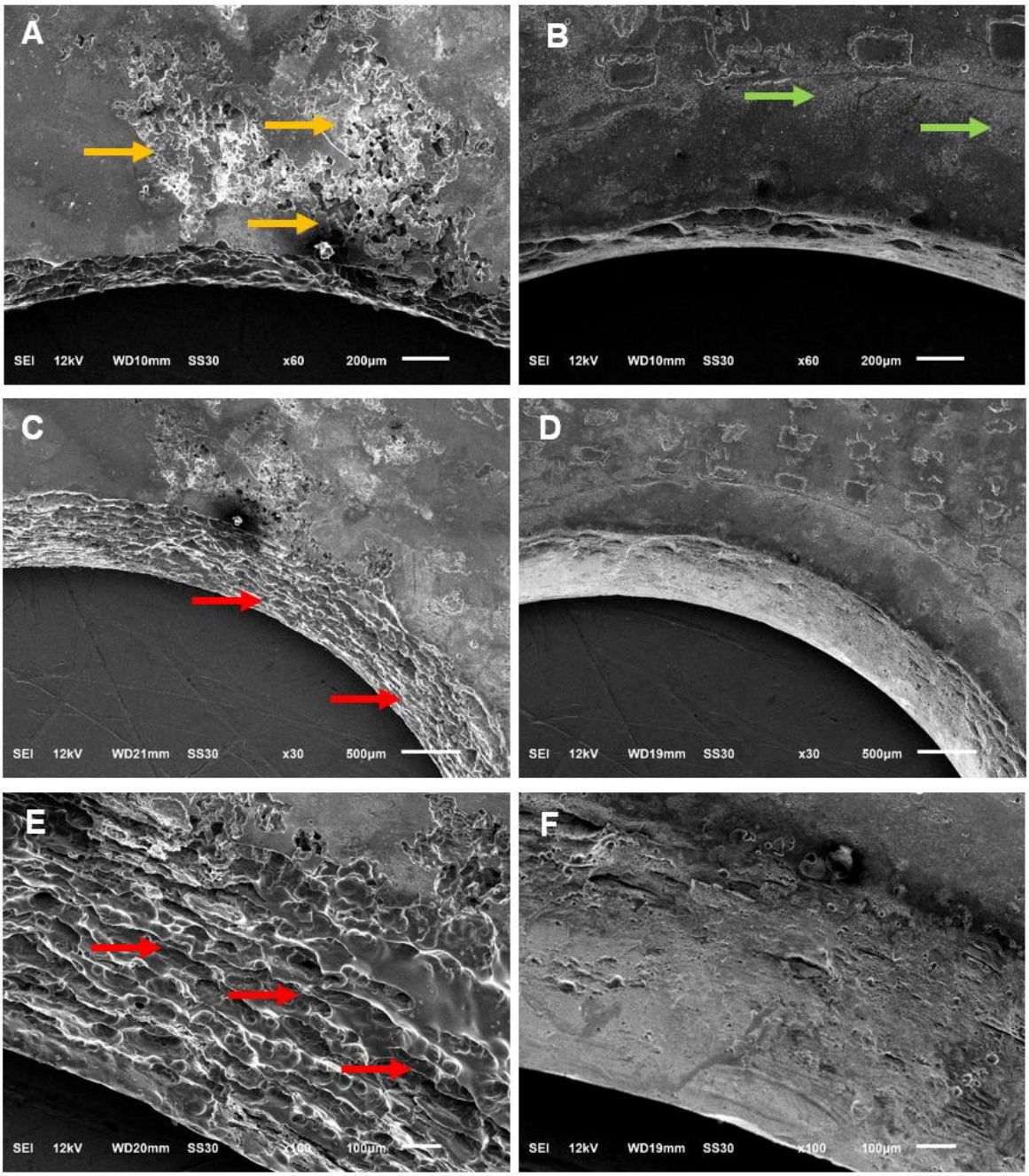

Figure 4.16. SEM micrographs of (A) a top view of the fastener hole on the surface of an AA7075-T6 panel joined to an unmodified CFRP composite, (B) a top view of the hole on the surface of an AA7075-T6 panel joined to a spontaneously-modified composite, (C) the hole wall of the alloy joined to an unmodified composite at a 28˚ tilt angle, (D) the hole wall of the alloy joined to a spontaneously-modified composite at a 28˚ tilt angle, (E) the hole wall of the alloy joined to an unmodified composite at a 40˚ tilt angle, (F) the hole wall of the alloy joined to a spontaneously-modified CFRP composite at a 40˚ tilt angle.

Figure 4.16 shows the SEM micrographs of the through-hole surface and walls on TCP-coated alloy panels joined with unmodified and spontaneously-modified composites after the 14-day TLM exposure. The top view of the hole on an alloy pane joined with an unmodified composite is presented in Figure 4.16A. Significant corrosion damage is present on the panel surface near the hole, under the composite, as indicated by yellow arrows. In contrast, there is no such damage near the hole of an alloy panel joined to a spontaneously modified composite, as shown in Figure 4.16B. A slight discoloration can be noticed on the panel near the hole as indicated by green arrows. According to the damage scale established by the U.S. Army Corrosion Control and Prevention Group, the TCP-coated alloy panel joined to spontaneously-modified composite shows Stage 1 damage in the form of sample discoloration and staining whereas the alloy panel joined to the unmodified composite exhibits Stage 3 damage with more extensive corrosion product formation, minor etching, pitting and more extensive surface damage.

During the degradation test, TCP-coated alloy and composite specimens were joined together using a stainless-steel metal fastener in which the threads were covered with Teflon tape to prevent direct electrical contact of the metal fastener with the alloy or composite. It should be noted, however, that stainless-steel is less susceptible to galvanic corrosion when coupled with carbon composites, but has the risk of undergoing pitting or crevice corrosion. Although the metal fastener threads were wrapped with Teflon tape, the hole walls of the AA panels showed signs of degradation after the TLM test. The hole wall damage for an alloy panel joined to an unmodified composite is indicated by red arrows in Figures 4.16C and E. The two SEM micrographs show extensive degradation in the hole wall. The damage is more extensive for the alloy joined to an unmodified composite. The hole wall damage on the alloy coupled to the spontaneously-modified composite is much less and the hole wall texture is much smoother. Figures 4.16D and F show the

SEM micrographs of the hole wall damage at different tilt angles. The diazonium modification of the composite edges reduces the galvanic corrosion in the form of trenching, and the modification of the composite through-hole reduces the galvanic corrosion damage in and around the through hole.

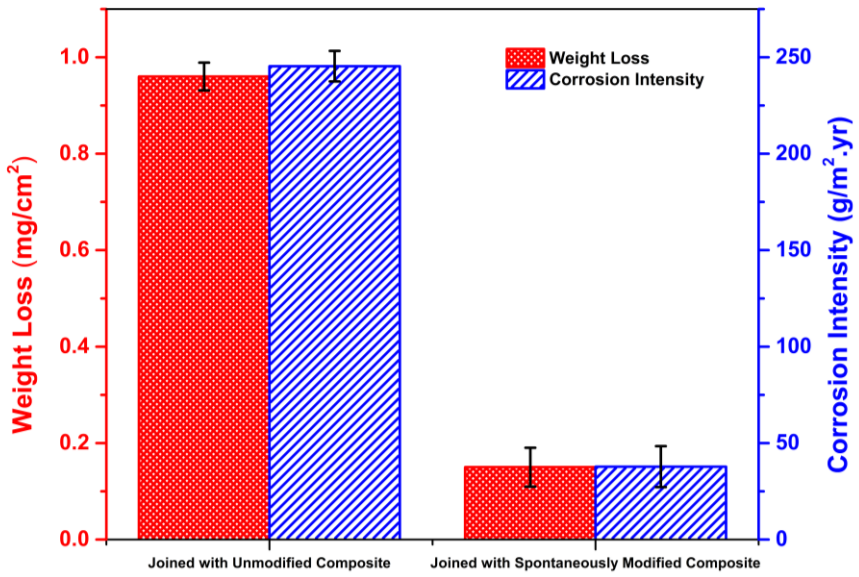

Figure 4.17. Weight loss and corrosion intensity of TCP-coated AA7075-T6 panels joined with an unmodified and spontaneously-modified (NAB) CFRP composites after 14 days of TLM exposure. Data are presented as mean ± std. dev. for n=3 specimens of each type.

The weight loss and corrosion intensity data after the 14-day (14, 24 h cycles) TLM exposure for the TCP-coated alloy panels joined with unmodified and spontaneously-modified composites are presented in Figure 4.17. The TCP-coated alloy joined with an unmodified composite exhibited weight loss and corrosion intensity values 84% greater than the values for the TCP-coated alloy joined with the spontaneously-modified composite. Both the weight loss and corrosion intensity values are 6× lower with the composite surface treated with the NAB adlayer.

4.4 DISCUSSION

Following up prior work, we investigated the surface treatment of CFRP composites spontaneously grafted with NAB adlayers and how effective these adlayers are at mitigating the

galvanic corrosion of AA7075-T6 aluminum specimens through inhibition of the cathodic oxygen reduction reaction when exposed to NSS and TLM accelerated degradation tests. We believe that the spontaneous grafting of substituted aryldiazonium cations can be developed into a more convenient, low cost, environmentally friendly surface treatment process for reduced galvanic corrosion in aluminum alloy-CFRP composite hybrids. The immersion of CFRP composite edges under open circuit conditions in aryl diazonium salt solutions lead to the formation of bonded, aryl adlayers. In a previous study, we showed that the immersion of CFRP composites in solutions of 4-nitroazobenzene and 4-nitrophenyl diazonium salt for 24 h respectively yield compact NAB and NP adlayers with the ability to suppress oxygen reduction current by 99%.[35] In this study, we further explored the characteristics and effectiveness of NAB adlayers spontaneously grafted on CFRP composites during 24-h immersion. Cyclic voltammetry data confirmed the spontaneous attachment of NAB admolecules on the CFRP composite edges and provided evidence of multilayer formation. An electrolyte to aid ion conduction is a key element necessary for galvanic corrosion. The isolation of substrate from electrolytes to prevent galvanic corrosion is commonly accomplished by the application of water repellent paints, coating, oils, and greases with barrier properties. The static contact angle measurements for water revealed that the spontaneously formed NAB adlayers decrease the wettability and improve the hydrophobicity of the CFRP composite exhibiting a greater moisture repulsion potential. The level of hydrophobicity imparted by the adlayer can be tailored as needed by changing the substituent groups of the aryl diazonium salt used. The ability to attain a wide variety of adlayers from commercially available and inexpensive reagents is a major advantage afforded by this surface treatment.

When in service aluminum alloy-composite hybrids interact with various atmospheric environments. The continuous exposure of these hybrid components to humid air, droplets of

spray, condensation, and precipitation can lead to the initiation and growth of different forms of corrosion including galvanic, pitting, and crevice corrosion. The efficiency of CFRP composite surface treatment on galvanic corrosion mitigation of AA7075-T6 was assessed by performing 14-day (i) neutral salt spray and (ii) thin layer mist accelerated degradation tests. During the neutral salt spray test, the specimens are exposed to a continuous fog of 5 wt.% NaCl at 35 ± 1 °C. The electrochemically formed adlayers on CFRP composites resulted in a moderate mitigation of galvanic corrosion after 14-day neutral salt spray exposure as revealed by the digital optical micrographs, surface texture parameters, and weight loss metrics. This observation is attributed to an incompletely packed adlayer with holes and defects through which small, neutral O_2 molecules can tunnel and reach the underlying carbon surface initiating chemisorption, the first step of oxygen reduction mechanism.[34] In contrast, the surface treatment of CFRP composites with spontaneous grafted adlayers provides superior galvanic corrosion protection to the TCP coated AA7075-T6 panels upon joining in this environment. The thin layer mist test employs a less aggressive salt solution (3.5 wt.% NaCl) than the neutral salt spray test (5 wt.% NaCl) and involves thermal cycling between 55 °C and room temperature with solution evaporation. Widespread galvanic corrosion damage was seen on the TCP coated AA7075-T6 panels joined to unmodified composites after 14 days of thin layer mist exposure. In contrast, the metal dissolution due to galvanic corrosion damage was significantly lower on the TCP coated AA7075-T6 panels joined to spontaneously modified CFRP composites after the 14-day thin layer mist exposure. This was further confirmed by the weight loss and corrosion intensity data. The surface texture analysis revealed substantially reduced lateral distribution of galvanic corrosion damage and remarkably attenuated galvanic corrosion progression into the aluminum panel. Further, the galvanic corrosion damage on the walls of the fastener through-hole was not seen when joined with spontaneously

modified composites.

Overall, the surface treatment of CFRP composites with spontaneously grafted NAB adlayers exceptionally mitigates the galvanic corrosion leading to trenching near the composite edges and the crevice corrosion on the AA7075-T6 panel underneath the composite during both neutral salt spray and thin layer mist degradation tests. The slow grafting rate in the absence of electrical induction enables the development of a more compact, closely packed adlayer over time with outstanding barrier properties towards O_2 molecules, as evident by the nearly complete suppression of oxygen reduction current, [35] ultimately inhibiting the galvanic corrosion. Future work will focus on optimizing the surface treatment parameters and investigating the surface treatment through brush and spray-on applications.

4.5 CONCLUSIONS

The NAB adlayer spontaneously grafted on the exposed carbon fiber surfaces of the composite by a 24-h immersion significantly attenuated the galvanic corrosion of TCP-coated AA7075-T6 alloy specimens when coupled together during 14-day neutral salt spray and thin layer mist exposures. The key findings from the work can be summarized as follows:

1. Diazonium adlayers can be spontaneously formed on the exposed carbon fibers of CFRP composites by immersion without electrochemical induction.
2. The spontaneously formed NAB adlayers after 24 h immersion improve the hydrophobicity of the CFRP composite by functioning as a moisture repellent barrier.
3. NAB organic adlayers formed spontaneously during a 24h immersion are more compact, have fewer defects, and higher apparent coverages than adlayers formed by electrochemically-assisted derivatization.

4. Spontaneously formed NAB adlayers (24 h immersion) provide much improved resistance to galvanic, crevice, and general alloy corrosion, as compared to the electrochemically-formed NAB adlayers during 14-day neutral salt spray exposure.
5. The weight loss metrics all indicate substantial reductions in mass loss, mass loss per cm^2, and corrosion intensity (g/m^2-yr) on TCP-coated AA7075-T6 alloys when joined with a CFRP modified with a more compact spontaneously formed adlayer during both 14-day neutral salt spray and 14-day thin layer mist exposures.
6. The weight loss (mg/cm^2) and corrosion intensity (g/m^2-yr) of TCP coated AA 7075-T6 joined with spontaneously modified CFRP composites are 6× lower compared to that of TCP coated AA7075-T6 joined with unmodified CFRP composites.
7. The progression of galvanic corrosion damage (lateral and vertical/trenching) on the aluminum alloy near the CFRP composite edges as well as the through-hole damage were greatly inhibited when joined with spontaneously modified CFRP composites.

REFERENCES

1. Ishikawa, T., Amaoka, K., Masubuchi, Y., Yamamoto, T., Yamanaka, A., Arai, M., & Takahashi, J. (2018). Overview of automotive structural composites technology developments in Japan. *Composites Science and Technology*, *155*, 221.

2. Zhang, J., Lin, G., Vaidya, U., & Wang, H. (2023). Past, present and future prospective of global carbon fibre composite developments and applications. *Composites Part B: Engineering*, *250*, 110463.

3. Choi, J. Y., Jeon, J. H., Lyu, J. H., Park, J., Kim, G. Y., Chey, S. Y., Quan, Y. J., Bhandari, B., Prusty, B. G., & Ahn, S. H. (2023). Current applications and development of composite manufacturing processes for future mobility. *International Journal of Precision Engineering and Manufacturing-Green Technology*, *10*(1), 269.

4. Parveez, B., Kittur, M. I., Badruddin, I. A., Kamangar, S., Hussien, M., & Umarfarooq, M. A. (2022). Scientific advancements in composite materials for aircraft applications: a review. *Polymers*, *14*(22), 5007.

5. Hagnell, M. K., Kumaraswamy, S., Nyman, T., & Åkermo, M. (2020). From aviation to automotive-a study on material selection and its implication on cost and weight efficient structural composite and sandwich designs. *Heliyon*, *6*(3).

6. Timmis, A. J., Hodzic, A., Koh, L., Bonner, M., Soutis, C., Schäfer, A. W., & Dray, L. (2015). Environmental impact assessment of aviation emission reduction through the implementation of composite materials. *The International Journal of Life Cycle Assessment*, *20*, 233.

7. Pervaiz, M., Panthapulakkal, S., Sain, M., & Tjong, J. (2016). Emerging trends in automotive lightweighting through novel composite materials. *Materials sciences and Applications*, *7*(01), 26.

8. Khalil, Y. F. (2017). Eco-efficient lightweight carbon-fiber reinforced polymer for environmentally greener commercial aviation industry. *Sustainable Production and consumption*, *12*, 16.

9. Whitman, B. W., Miller, D., Davis, R., Brennan, J., & Swain, G. M. (2017). Effect of galvanic current on the physicochemical, electrochemical, and mechanical properties of an aerospace carbon fiber reinforced epoxy composite. *Journal of The Electrochemical Society*, *164*(13), C881.

10. Hur, S. Y., Kim, K. T., Yoo, Y. R., & Kim, Y. S. (2020). Effects of NaCl concentration and solution temperature on the galvanic corrosion between CFRP and AA7075T6. *Corros. Sci. Technol.*, *19*(2), 75.

11. Kleinbaum, S., Jiang, C., & Logan, S. (2019). Enabling sustainable transportation through joining of dissimilar lightweight materials. *MRS Bulletin*, *44*(8), 608.

12. Montemor, M. F. (2016). Corrosion issues in joining lightweight materials: A review of the latest achievements. *Physical Sciences Reviews*, *1*(2), 20150011.

13. Liu, M., Guo, Y., Wang, J., & Yergin, M. (2018). Corrosion avoidance in lightweight materials for automotive applications. *NPJ Materials Degradation*, *2*(1), 24.

14. Wu, X., Sun, J., Wang, J., Jiang, Y., & Li, J. (2019). Investigation on galvanic corrosion behaviors of CFRPs and aluminum alloys systems for automotive applications. *Materials and Corrosion*, *70*(6), 1036.

15. Srinivasan, R., Nelson, J. A., & Hihara, L. H. (2015). Development of guidelines to attenuate galvanic corrosion between mechanically-coupled aluminum and carbon-fiber reinforced epoxy composites using insulation layers. *Journal of the Electrochemical Society*, *162*(10), C545.

16. Peng, Z., & Nie, X. (2013). Galvanic corrosion property of contacts between carbon fiber cloth materials and typical metal alloys in an aggressive environment. *Surface and coatings technology*, *215*, 85.

17. Feng, Z., Boerstler, J., Frankel, G. S., & Matzdorf, C. A. (2015). Effect of surface pretreatment on galvanic attack of coated Al alloy panels. *Corrosion*, *71*(6), 771.

18. Ireland, R., Arronche, L., & La Saponara, V. (2012). Electrochemical investigation of galvanic corrosion between aluminum 7075 and glass fiber/epoxy composites modified with carbon nanotubes. *Composites Part B: Engineering*, *43*(2), 183.

19. Håkansson, E., Hoffman, J., Predecki, P., & Kumosa, M. (2017). The role of corrosion product deposition in galvanic corrosion of aluminum/carbon systems. *Corrosion Science*, *114*, 10.

20. Srinivasan, R., & Hihara, L. H. (2016). Utilization of hydrophobic coatings on insulative skirts to attenuate galvanic corrosion between mechanically-fastened aluminum alloy and carbon fiber reinforced polymer matrix composites. *Electrochemistry Communications*, *72*, 96.

21. Mandel, M., & Krüger, L. (2012). Electrochemical corrosion studies and pitting corrosion sensitivity of a self-pierce rivet joint of carbon fibre reinforced polymer (CFRP)–laminate and EN AW-6060-T6. *Materialwissenschaft und Werkstofftechnik*, *43*(4), 302.

22. Liu, J., Huang, X., Ren, Y., Wong, L. M., Liu, H., & Wang, S. (2022). Galvanic corrosion protection of Al-alloy in contact with carbon fibre reinforced polymer through plasma electrolytic oxidation treatment. *Scientific Reports*, *12*(1), 4532.

23. Delamar, M., Hitmi, R., Pinson, J., & Saveant, J. M. (1992). Covalent modification of carbon surfaces by grafting of functionalized aryl radicals produced from electrochemical reduction of diazonium salts. *Journal of the American Chemical Society*, *114*(14), 5883.

24. Downard, A. J. (2000). Electrochemically assisted covalent modification of carbon electrodes. *Electroanalysis: An International Journal Devoted to Fundamental and Practical Aspects of Electroanalysis*, *12*(14), 1085.

25. Adenier, A., Bernard, M. C., Chehimi, M. M., Cabet-Deliry, E., Desbat, B., Fagebaume, O., ... & Podvorica, F. (2001). Covalent modification of iron surfaces by electrochemical reduction of aryldiazonium salts. *Journal of the American Chemical Society*, *123*(19), 4541.

26. Bernard, M. C., Chaussé, A., Cabet-Deliry, E., Chehimi, M. M., Pinson, J., Podvorica, F., & Vautrin-Ul, C. (2003). Organic layers bonded to industrial, coinage, and noble metals through electrochemical reduction of aryldiazonium salts. *Chemistry of Materials*, *15*(18), 3450.

27. Pinson, J., & Podvorica, F. (2005). Attachment of organic layers to conductive or semiconductive surfaces by reduction of diazonium salts. *Chemical Society Reviews*, *34*(5), 429.

28. Boukerma, K., Chehimi, M. M., Pinson, J., & Blomfield, C. (2003). X-ray photoelectron spectroscopy evidence for the covalent bond between an iron surface and aryl groups attached by the electrochemical reduction of diazonium salts. *Langmuir*, *19*(15), 6333.

29. Li, D., Luo, Y., Onidas, D., He, L., Jin, M., Gazeau, F., Pinson, J., & Mangeney, C. (2021). Surface functionalization of nanomaterials by aryl diazonium salts for biomedical sciences. *Advances in Colloid and Interface Science*, *294*, 102479.

30. Adenier, A., Cabet-Deliry, E., Chaussé, A., Griveau, S., Mercier, F., Pinson, J., & Vautrin-Ul, C. (2005). Grafting of nitrophenyl groups on carbon and metallic surfaces without electrochemical induction. *Chemistry of Materials*, *17*(3), 491.

31. Adenier, A., Barré, N., Cabet-Deliry, E., Chaussé, A., Griveau, S., Mercier, F., ... & Vautrin-Ul, C. (2006). Study of the spontaneous formation of organic layers on carbon and metal surfaces from diazonium salts. *Surface Science*, *600*(21), 4801.

32. Chamoulaud, G., & Belanger, D. (2007). Spontaneous derivatization of a copper electrode with in situ generated diazonium cations in aprotic and aqueous media. *The Journal of Physical Chemistry C*, *111*(20), 7501.

33. Assresahegn, B. D., Brousse, T., & Bélanger, D. (2015). Advances on the use of diazonium chemistry for functionalization of materials used in energy storage systems. *Carbon*, *92*, 362.

34. Dammulla, I. N., & Swain, G. M. (2022). Inhibiting the oxygen reduction reaction kinetics on carbon fiber epoxy composites through diazonium surface modification-impacts on the galvanic corrosion of coupled aluminum alloys. *Journal of The Electrochemical Society*, *169*(7), 071501.

35. Dammulla, I. N., & Swain, G. M. (2023). Inhibiting Metal Galvanic and Carbon Corrosion in Aluminum Alloy-Carbon Fiber Reinforced Composite Joints by Spontaneous Deposition of Diazonium Adlayers on Exposed Carbon Fibers. *Journal of The Electrochemical Society*, *170*(9), 091503.

36. Munson, C. A., McFall-Boegeman, S. A., & Swain, G. M. (2018). Cross comparison of TCP conversion coating performance on aluminum alloys during neutral salt-spray and thin-layer mist accelerated degradation testing. *Electrochimica Acta*, *282*, 171.

37. Liu, Y. C., & McCreery, R. L. (1995). Reactions of organic monolayers on carbon surfaces observed with unenhanced Raman spectroscopy. *Journal of the American Chemical Society*, *117*(45), 11254.

38. Allongue, P., Delamar, M., Desbat, B., Fagebaume, O., Hitmi, R., Pinson, J., & Savéant, J. M. (1997). Covalent modification of carbon surfaces by aryl radicals generated from the electrochemical reduction of diazonium salts. *Journal of the American Chemical Society*, *119*(1), 201.

39. Delamar, M., Desarmot, G., Fagebaume, O., Hitmi, R., Pinsonc, J., & Savéant, J. M. (1997). Modification of carbon fiber surfaces by electrochemical reduction of aryl diazonium salts: Application to carbon epoxy composites. *Carbon*, *35*(6), 801.

40. Liu, Y. C., & McCreery, R. L. (1997). Raman spectroscopic determination of the structure and orientation of organic monolayers chemisorbed on carbon electrode surfaces. *Analytical chemistry*, *69*(11), 2091.

41. Osborn, K. (2010). Army Steps Up Plans to Fight Corrosion, U.S. Army Military Article #36266 (https://army.mil/article/36266/army_steps_up_plans_to_fight_corrosion).

42. Munson, C. A., & Swain, G. M. (2017). Structure and chemical composition of different variants of a commercial trivalent chromium process (TCP) coating on aluminum alloy 7075-T6. *Surface and Coatings Technology*, *315*, 150.

43. Li, L., Doran, K. P., & Swain, G. M. (2013). Electrochemical characterization of trivalent chromium process (TCP) coatings on aluminum alloys 6061 and 7075. *Journal of the Electrochemical Society*, *160*(8), C396.

44. Dardona, S., Chen, L., Kryzman, M., Goberman, D., & Jaworowski, M. (2011). Polarization controlled kinetics and composition of trivalent chromium coatings on aluminum. *Analytical chemistry*, *83*(16), 6127.

45. Iyer, A., Willis, W., Frueh, S., Nickerson, W., Fowler, A., Barnes, J., ... & Suib, S. L. (2010). Characterization of NAVAIR trivalent chromium process (TCP) coatings and solutions. *Plat. Surf. Finish*, *5*, 32.

46. Dong, X., Wang, P., Argekar, S., & Schaefer, D. W. (2010). Structure and composition of trivalent chromium process (TCP) films on Al alloy. *Langmuir*, *26*(13), 10833.

47. Li, L., Swain, G. P., Howell, A., Woodbury, D., & Swain, G. M. (2011). The formation, structure, electrochemical properties and stability of trivalent chrome process (TCP) coatings on AA2024. *Journal of The Electrochemical Society*, *158*(9), C274.

48. Guo, Y., & Frankel, G. S. (2012). Characterization of trivalent chromium process coating on AA2024-T3. *Surface and Coatings Technology*, *206*(19-20), 3895.

49. Guo, Y., & Frankel, G. S. (2012). Active corrosion inhibition of AA2024-T3 by trivalent chrome process treatment. *Corrosion, The Journal of Science and Engineering*, *68*(4), 045002-1.

50. J. Qi, L. Gao, Y. Li, Z. Wang, G. E. Thompson, and P. Skeldon, An optimized trivalent chromium conversion coating process for AA2024-T351 Alloy. *J. Electrochem. Soc.,* 164, C390 (2017).

51. Ferrer, K. S., & Kelly, R. G. (2001). Comparison of methods for removal of corrosion product from AA2024-T3. *Corrosion*, *57*(02).

CHAPTER 5. MATERIAL CHARACTERIZATION AND ELECTROCHEMICAL CORROSION BEHAVIOR OF TITANIUM ALLOY TI-5553 PREPARED BY SELECTIVE LASER MELTING

Chapter adapted from the manuscript in preparation to be submitted to *ACS Omega.*

Article: Isuri N. Dammulla, Ryan Weston, Zia Uddin Mahmud, Sujoy Saha, Sarah McFall-Boegeman, Luke Rice, Jonathan H. Dwyer, Taylor Kmetz, Carl J. Boehlert, and Greg M. Swain. *Material Characterization and Electrochemical Properties of Titanium alloy Prepared by Selective Laser Melting As-Processed and After Abrading and Polishing.*

5.1 INTRODUCTION

Titanium alloys (Ti) are widely used in the aerospace (e.g., landing gear) and biomedical (e.g., implants) fields owing to their excellent mechanical properties such as high strength, high fracture resistance, good formability, high temperature properties, and corrosion resistance.[1-8] The increased demand for these alloys and the high cost of conventional Ti components prepared using subtractive machining have driven interest in the bottom-up fabrication of intricate Ti parts needed for these applications using additive manufacturing (AM) techniques.[9-16]

AM, also known as 3D printing, is a process whereby parts and components are fabricated from the bottom up using a layer-by-layer approach following a three-dimensional computer-aided design (3D CAD). This fabrication method contrasts with the conventional subtractive and formative manufacturing techniques, such as extrusion, forging, shape casting, machining, etc.[14-21] The notable advantages of AM fabrication include the ability to design and prepare geometrically complex, lightweight structures with improved performance, reduced design-to-manufacture time, minimized waste production, and lower cost.[12-15,20,21] Two broad classes of metal AM technologies are powder bed fusion (PBF) and directed energy deposition (DED). PBF methods enable manufacturing of geometrically complex products using a heat source, mainly laser or electron beams, to fuse powder particles layer-by-layer, forming a solid part. There are different types of

PBF methods including selective laser sintering (SLS), selective laser melting (SLM), and electron beam melting (EBM). DED AM technologies, on the other hand, inject the metal powders to a substrate where a high energy density heat source, such as a laser, electron beam or plasma electric arc, is focused and these are more appropriate for manufacturing larger parts with a coarser finish.[9,17,20-22] DED processes involve adding material alongside the heat input simultaneously.

Selective laser melting (SLM) employs a high-power laser beam to raster scan and melt the metal powder particles preplaced on a build platform. The melting of the regions of interest in a layer-by-layer manner fuses the molten metal into the desired structure upon cooling and solidification.[12-15,20-25] The process is repeated until the final part geometry is achieved. The powder particle fusion depends on multiple process variables including laser power, scanning speed, scanning pattern, and part geometry. These parameters influence the size of the melt pool around the scanning laser beam and the thermal gradient experienced by nearby particles.[15] Ti-6Al-4V (wt.%) is one of the Ti alloys most frequently prepared using SLM. [26-43]

A less-studied alloy, particularly in terms of its electrochemical properties, is Ti-5Al-5V-5Mo-3Cr (wt.%) (Ti-5553). This near-β phase alloy has several manufacturing advantages, such as castability and weldability.[44-45] This alloy exhibits excellent hardenability through thermal treatment[45] and high strength (up to 1300 MPa) with more than 10% elongation.[43,46] Given these desirable properties, efforts are underway within the scientific community to prepare this alloy using AM technologies.

Fundamental research is needed to better understand (i) how the fabrication parameters influence the material density, defects, microstructure, and electrochemical corrosion susceptibility, and (ii) how different surface pretreatments and finishes can be optimally applied to mitigate corrosion. These structure-function relationships are well established for wrought and die-

cast alloys, but have yet to be established for AM parts. Some work has been published describing the microstructure and mechanical properties of SLM processed Ti-5553.[13,14,47-53] However, there is very little published research regarding the electrochemical characterization of this SLM or die cast Ti-5553 alloy.[11,54-56] To address this knowledge gap, we report herein on the material characterization and electrochemical properties of SLM-prepared Ti-5553 specimens as-processed (i.e., with their native surface roughness and oxide film) and after abrading and polishing to smooth the surface texture thereby reducing the surface roughness and enabling the formation of a less defective and more compact oxide film.

5.2 EXPERIMENTAL METHODS

Chemicals and Reagents. All chemicals used were of analytical grade quality or better. Sodium chloride (NaCl) was purchased from a commercial supplier (Sigma Aldrich) and used as received. The BONDERITE C-AK 6849 AERO and BONDERITE C-IC SMUTGO NC AERO solutions were provided by Henkel Technologies, Inc. (Madison Heights, MI). Both were diluted with ultrapure water to 20% (v/v) before use. All aqueous solutions were prepared with ultrapure water (> 17 Ω-cm) from a Barnstead E-Pure water purification system.

Fabrication of AM Ti-5553. An Additive Industries (AI) MetalFab1 laser powder bed fusion (LPBF) system was used to manufacture the specimens using Ti-5553 powder purchased from AP&C (Montreal, Canada). MetalFab1 is a four-laser system, each of which is full-field. The lasers were ytterbium (Yb)-doped fiber type with a maximum power of 500 W, a fundamental output wavelength of 1070 nm, and spot size of 100-105 μm. The specimens were built via a continuous wave exposure strategy involving scan-path striping for each layer. Scan-path striping is a laser scanning strategy that divides the area to be consolidated into smaller sets of laser raster vectors. Each build layer is rotated 67 degrees to avoid stacking scan corners and interior seams (this is a

common build practice). The laser power during the build ranged from 120 to 160 W and the laser scan speed varied between 600 to 950 mm/s, depending on the cross-sectional geometry and layer. The powder layer thickness remained a constant 40 µm. All specimens were built with long dimensions perpendicular to the surface of the plate to minimize the area needed to be cut for removal. The parts were removed from the build plate by wire electrical discharge machining and cleaned by an in-house process, including media blasting, to remove the excess powder. The media blast step removed semi-sintered particles from the specimen and provided a matte finish to the exterior. The specimens were sand blasted at a pressure between 50-70 psi. Cleaning consisted of the five steps: (i) high pressure spray with detergent followed by water rinsing, (ii) multifrequency (40-280 kHz) ultrasonication in detergent followed by water rinsing, (iii) ultrasonication (40 kHz) in deionized water and drying with a stream of N_2 gas, (iv) vacuum oven drying (10^{-2} torr), and (v) packaging the cooled specimens into nylon bag for shipment to Michigan State University. No thermal annealing was applied. These specimens are referred to as-processed. The powder used for the alloy preparation is proprietary but had the following general composition in wt.% as indicated in Aerospace Material Specification AMS7026: Al (4.4-5.7), V (4.0-5.5), Mo (4.0-5.5), Cr (2.5-3.5), with the balance as Ti. The particle size used in the builds had a diameter ranging from 20 – 63 µm. Two batches of material were used: Batch #1 (2021) and Batch #2 (2022). The deposition conditions were adjusted leading to less surface roughness and porosity in the Batch #2 specimens. Specifics on the differences in fabrication conditions are proprietary. Material characterization was performed on both batches, while the electrochemical measurements were performed using Batch #2 specimens only.

Digital Optical Microscopy. The surface texture of the as-processed Ti-5553 specimens, before and after smoothing by mechanical abrading and polishing, was investigated using a VHX-6000

(Keyence Corp. USA) optical microscope. The as-processed specimen was abraded with P1500 grit aluminum oxide grinding paper for 4 min on a polishing wheel and then ultrasonically cleaned in ultrapure water for 10 min. The specimen was then polished by hand for 5 min using 0.3 μm alumina powder (Buehler) slurried in ultrapure water on a felt pad and then was ultrasonically cleaned in ultrapure water for 10 min. This was followed by polishing with 0.05 μm alumina powder (Buehler) slurried in ultrapure water on a separate felt pad by hand for 5 min and ultrasonic cleaning in ultrapure water for 10-20 min. Optical microscopy was then used to image the specimen and to quantitatively assess the surface texture. The root-mean-square of the surface roughness (S_q) and the maximum peak-to-valley height (S_z) were calculated by analyzing five spots on three specimens from each batch (area of a single spot = 1000 × 1000 μm^2).

Scanning Electron Microscopy (SEM). SEM was performed using JSM-6610LV (JEOL USA, Inc.) and TESCAN MIRA3 FEG-SEM (TESCAN USA, Inc.) scanning electron microscopes. The as-processed specimens were characterized before and after abrading and polishing. The abrading and polishing steps are described in section 2.7 and were slightly different from the procedure used to smooth the specimens for optical microscopy. A smoother surface provides a better visualization of the grain boundaries, second-phase particles, microvoids and other defects that might be present. These specimens were imaged using both secondary (SE) and backscattered electrons (BSE) detectors at an accelerating voltage of 20 kV and a working distance of approximately 11 mm.

X-Ray Diffraction Analysis. A 1" × 1" as-processed specimen was ultrasonically- cleaned in ethanol for 15 min. The specimen was then air dried. A Rigaku SmartLab X-ray diffractometer was used to characterize the crystallographic structure of the specimen. A Cu (K-α) X-ray source (1.54 Å) was used at 40 kV and 44 mA over a 2θ scan range of 20-90 degrees. The scan speed was 3.03 degrees/min with a step width of 0.01 degrees. The spot size was 0.4 mm × 12.0 mm.

Microhardness Measurements. As-processed specimens were first abraded on a wet P1500 grit aluminum oxide grinding paper for 10 min and ultrasonically cleaned in ultrapure water for 20 min. The specimens were then polished on a polishing wheel with 1.0 and 0.3 μm alumina powder/H_2O slurries. Each polishing step was performed for 10 min. After each, the specimens were both rinsed and ultrasonically cleaned in ultrapure water for 20 min. The Vickers microhardness measurements were then performed on three smoothed specimens using the pyramidally-shaped diamond indenter of a Clark CM-800AT microhardness tester (Figure 5.1). Measurements were made at 5 different spots (four corner regions and center) on each specimen by applying an indentation load of 500 gf for 15 s. The measurements and analysis were performed according to ASTM E384 (Standard Test for Microhardness of Materials).

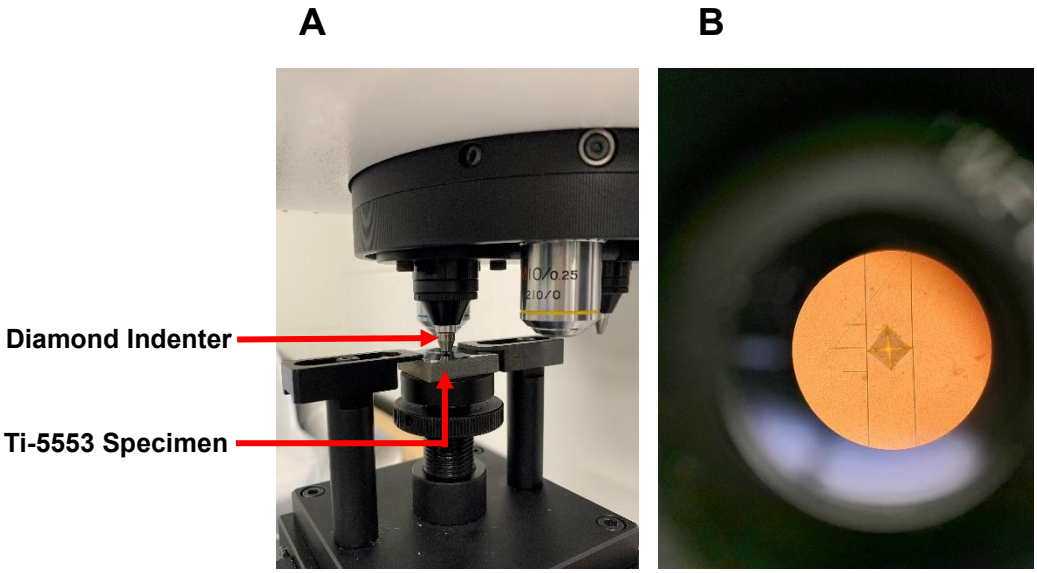

Figure 5.1. Photographs of (A) the diamond indenter making an indentation on a Ti 5553 and (B) the indentation imprint at 50×. The indentation load was 500 gf and the dwelling time was 15s.

Specimen Preparation for Microstructure Analysis. The sample preparation method used for the metallographic analysis of the specimens involved a series of abrading and polishing steps followed by wet chemical etching was. The specimens were first mechanically abraded on wet 12 and 8 μm aluminum oxide grinding paper, respectively, for 20 min each. This was followed by

ultrasonic cleaning in ultrapure water (10 min) before sequentially polishing with 6, 3, 1 and 0.25 μm alumina/H_2O slurries. Each polishing step was performed for 20 min on a polishing wheel. The specimens were rinsed with and ultrasonically cleaned in ultrapure water after each polishing step. The specimens were then polished with 0.04 μm colloidal silica for 40 min on a polishing wheel and rinsed with and ultrasonicated in ethanol for 10 min. Kroll's solution was then used as the etchant. Kroll's solution is specifically used for Ti alloys. It has a composition of 6 wt.% HNO_3 and 1 wt. % HF, with the balance as water. The etching was performed by immersion of the sample for 30 s at room temperature. After etching, the specimens were removed, rinsed with ultrapure water and isopropanol, respectively, and dried with N_2 gas flow.

Electrochemical Measurements. The specimens were electrochemically characterized using open circuit potential (OCP) measurements, linear polarization resistance (R_p) measurements, anodic and cathodic potentiodynamic polarization curves, and full frequency electrochemical impedance spectroscopy (EIS) at the OCP. The electrolyte was naturally aerated 3.5 wt.% NaCl.

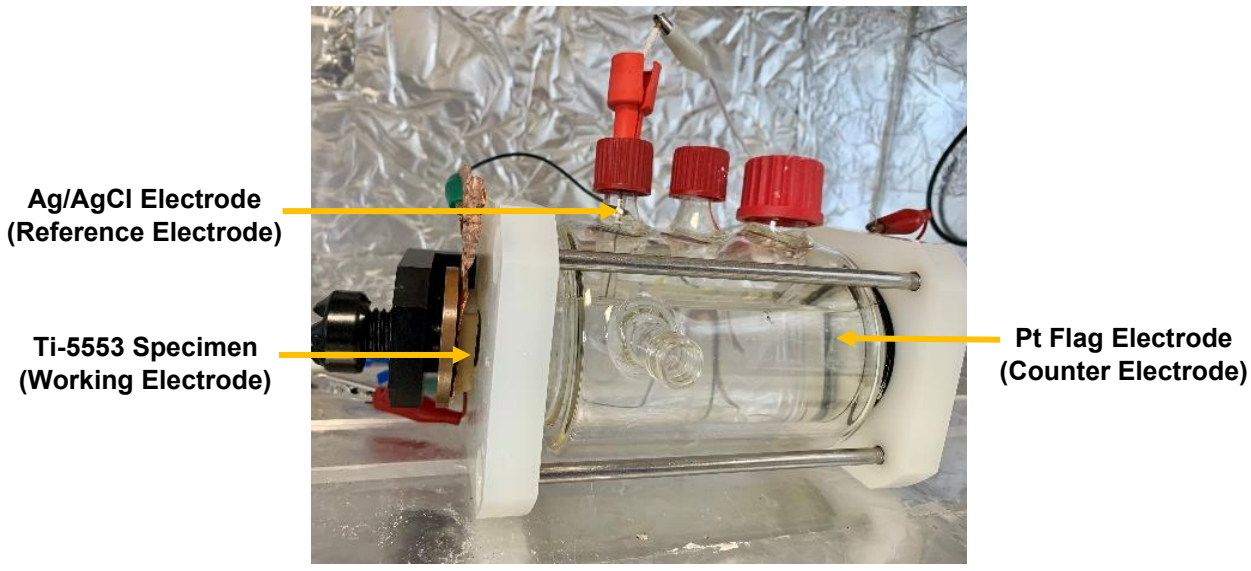

Figure 5.2. Cell set-up used for electrochemical measurements.

All electrochemical measurements were made at room temperature using a 1 cm^2 flat cell as shown in Figure 5.2. (BioLogic Science Instruments, France) design in combination with a

computer-controlled electrochemical workstation (Gamry Instruments, Inc, Reference 600, Warminster, PA). A specimen was mounted in the cell against a Viton® O-ring that defined the exposed geometric area, 1 cm^2. All currents reported herein are normalized to this geometric area. The counter electrode was a Pt flag, and the reference was a home-made silver chloride electrode (Ag/AgCl, 4M KCl) that was housed in a Luggin capillary with a cracked glass tip.

The OCP was measured for at least 1 h after the initial alloy contact with the electrolyte solution. Linear polarization resistance measurements were performed using linear sweep voltammetry over a ΔE of ± 20 mV relative to the OCP. The scan rate was 1 mV/s. The reciprocal slope of the *i-E* curve is the polarization resistance, R_p.[57]

$$\left(R_p = \frac{\Delta E}{\Delta i}\ as\ \Delta E \to 0\right) \qquad (1)$$

Potentiodynamic polarization curves were recorded from ± 0.050 V vs. OCP to either a positive limit of 1.0 V vs. Ag/AgCl for the anodic curves or to a negative limit of -1.0 V vs. Ag/AgCl for the cathodic curves. The scan rate was 1 mV/s. These curves provided insight on the anodic (oxide formation and localized pitting corrosion) and cathodic (oxygen and water reduction) reaction rates as a function of electrode potential. EIS measurements were made at the stable OCP using a 10-mV sine wave with seven points per decade of frequency collected for analysis. A range from 10^5 to 10^{-2} Hz was employed to determine the frequency dependence of the real (ohmic) and imaginary (capacitive) components of the total impedance. The experimental data were analyzed by fitting to an appropriate equivalent circuit using the ZView software (version 3.5a). This was performed to determine the numerical magnitudes of the circuit components (*i.e.*, the electrochemical parameters). The measurements were repeated with at least three specimens of each type (as processed and abraded and polished) to assess response reproducibility. The electrochemical analyses were performed using as-processed, and abraded and polished

specimens. As-processed specimens were only degreased and deoxidized, as described below, prior to use in the electrochemical measurements. The as-processed specimens were smoothed by first abrading (by hand) on P1500 grit aluminum oxide grinding paper for 4 min followed by ultrasonic cleaning in ultrapure water for 20 min. The specimens were then polished (by hand) with a 0.3 μm alumina powder/H_2O slurry on a felt pad for 20 min. This was followed by ultrasonic cleaning in ultrapure water for 20 min. The as-processed and polished specimens were degreased by immersion in an alkaline cleaner (BONDERITE C-AK 6849 AERO, Henkel Technologies) for 10 min at 55 °C followed by a 2-min flowing city tap water rinse. The degreased specimens were then deoxidized (BONDERITE C-IC SMUTGO NC AERO, Henkel Technologies) by immersion for 2 min at room temperature. The specimens were rinsed again in flowing city tap water for 2 min, dried with a low pressure N_2 gas flow, and tested immediately thereafter. All specimens were used immediately afterward in the electrochemical measurements.

5.3 RESULTS

Density Measurements. The density of as-processed Ti-5553 specimens (Batch #2) was determined from (i) weight and volume measurements and (ii) water volume displacement. Both methods returned similar values of the density. The average density for five different specimens determined from weight and volume measurements was 4.55 ± 0.02 g/cm³. The density determined using the volume displacement method for three specimens from a different batch was 4.70 ± 0.03 g/cm^3. The volume displacement method value is statistically similar to the value reported for the fully dense die-cast alloy (4.65 g/cm^3).[48,58] This indicates the as-processed SLM alloy was nearly fully densified or at most possessed 1-2% porosity.

Specimen Texture and Morphology. Figure 5.3 presents optical micrographs of an as-processed specimen (Batch #1) surface before and after abrading on a wet P1500 grit aluminum oxide

grinding paper and polishing with decreasing grades of alumina powder. The yellow arrow in Figure 5.3A shows the build direction. The micrograph of the specimen before any abrading and polishing (Figure 5.3A) revealed a rough surface texture characteristic of the SLM fabrication process. As-processed surface roughness was reduced by the abrading and polishing steps. The abrading on wet P1500 grit aluminum oxide grinding paper produced a smoother surface texture with visible striations, as indicated by the black arrows in Figure 5.3B. An even smoother, striation-free surface resulted after the abrading and the alumina powder polishing, as shown in Figure 5.3C.

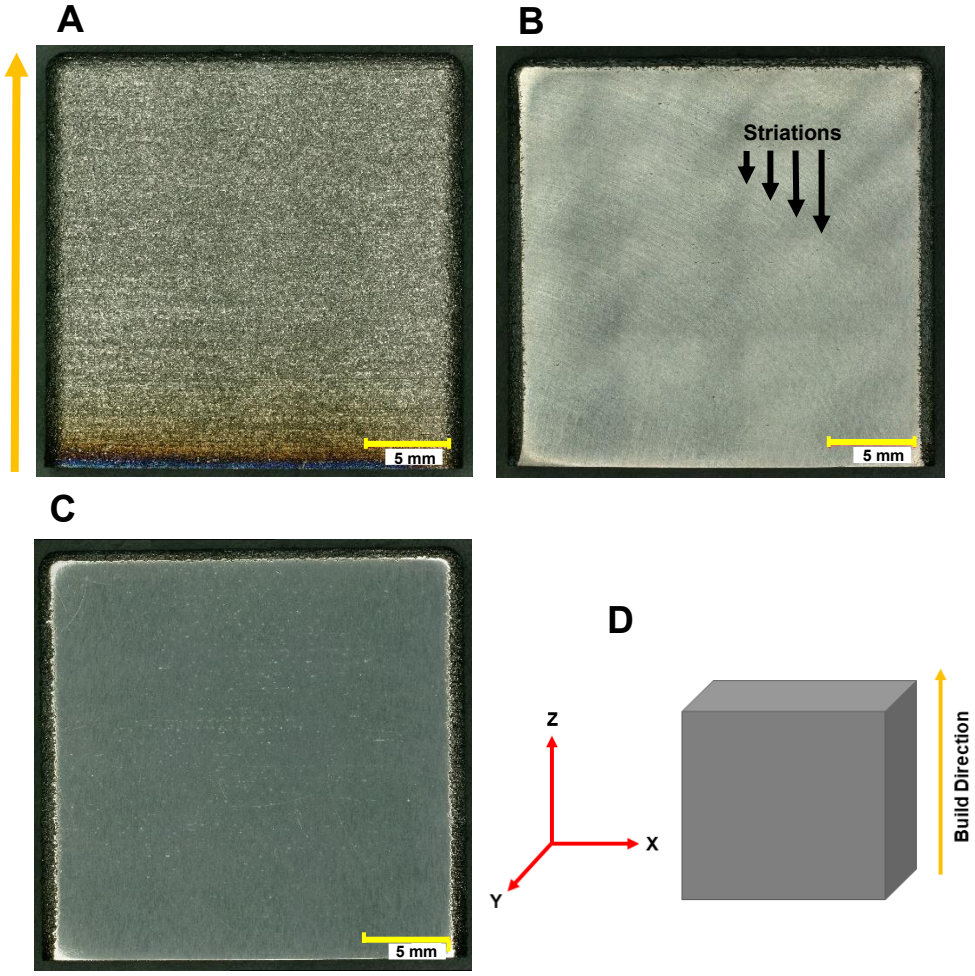

Figure 5.3. Optical micrographs of a typical specimen (Batch #1) (A) as-processed, (B) after mechanically abrading on wet P1500 grit aluminum oxide grinding paper, and (C) after mechanical abrading and polishing with decreasing grades of alumina powder. The full 2.54 × 2.54 cm^2 specimen is shown. The yellow arrow shows the build direction. The micrographs are of the XZ plane orthogonal to the build plane. The scale bar in the micrographs is 5 mm. (D) Schematic diagram indicating the build direction and X,Y, and Z axes.

Figure 5.3D illustrates the build direction and the X, Y, Z axes of the specimens. In the present example, the abrading and polishing were performed by hand using alumina powder. While the abrading does smooth the surface, polishing by hand for less than 20 min under these conditions had less of an effect on the surface texture. Better surface finishes were achieved using the polishing wheel for periods of time $\geq$ 20 min (see below).

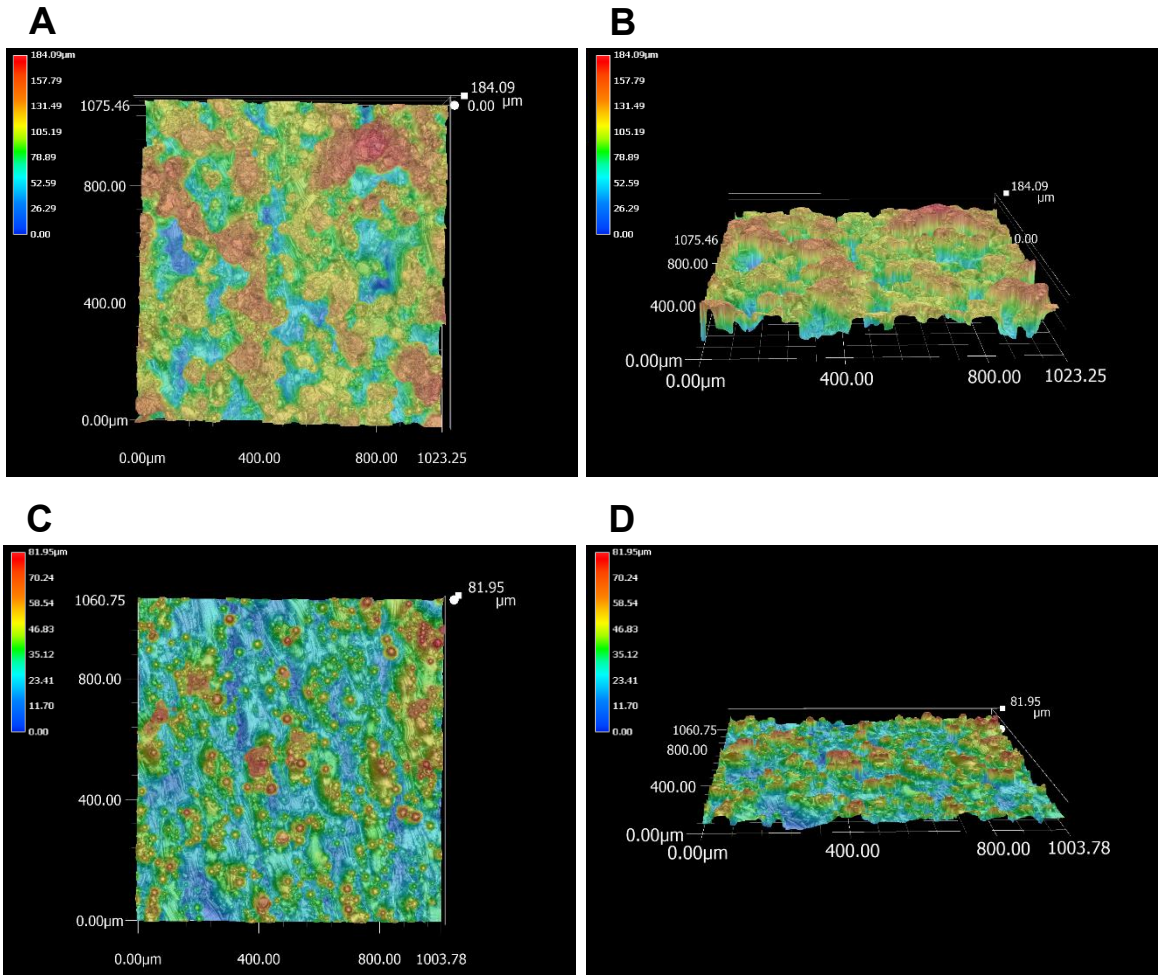

Figure 5.4. Height color maps of the surface topography of the two batches of as-processed (no abrading or polishing) Ti-5553 alloy specimens: (A and B) and (C and D) Batch #2. The maps were generated from 3D images collected at 1000×. The XZ plane is shown.

Figure 5.4 height color plots of the surface topography of as-processed specimens from (A and B) Batch #1 and (C and D) Batch #2. The plots reveal a rough surface texture for both specimen types with the red regions being elevated and blue regions being valleys. In Figure 5.4A and B, the

maximum in the color scale is 184 μm. In Figure 5.4C and D, the maximum in the color scale is 82 μm. Table 1 presents a summary of the surface texture analysis of the 3D raw images. The data reveal that the arithmetical mean height (S_a), maximum peak-to-valley height (S_z), and surface roughness (S_q) of the Batch #2 specimens were lower than those from the Batch #1 specimens. In other words, the Batch #2 specimens exhibited a smoother native surface texture. All surface texture parameters were 2× lower for the Batch #2 specimens. The Batch #2 specimens were exclusively used for the XRD, density, microhardness, and electrochemical measurement data presented herein given the smoother surface texture.

Table 5.1. Surface texture analysis of the 3D image data of as-processed specimens from the two different batches.

Surface Texture Parameter	Batch #1	Batch #2
S_a, Arithmetical Mean Height	25.5 ± 2.4 μm	13.3 ± 4.3 μm
S_z Maximum Peak-to-Valley Height	189 ± 21 μm	111 ± 29 μm
S_q, Root Mean Square Height (Surface Roughness)	31.6 ± 2.8 μm	16.7 ± 5.3 μm

Data are reported as mean ± std. dev. for five spots each on three different specimens from each batch. The 3D images were collected at 1000× and the surface texture data are for regions 1000× 1000 μm^2. Values were determined using the Keyence microscope software.

3D optical micrographs are presented in Figure 5.5 for a small area (1000 × 200 μm^2) of the same alloy specimen (Batch #1) presented in Figure 5.3. The micrographs reveal differences in the surface texture for as-processed (Fig. 5.5A), abraded (Fig. 5.5B), and abraded and polished (Fig. 5.5C) specimens. The surface texture parameters are presented in Table 5.2. The as-processed specimen exhibited some balling. This is a common defect and arises due to competition between melt spreading and solidification during the laser heating. In other words, melted droplets solidify before spreading completely to create a flat layer.[12-16,59] Clearly, the surface was smoothed by abrading with P1500 grit alumina grinding paper on a mechanical polisher as both the surface roughness and maximum peak-to-valley height were reduced by an order of magnitude.

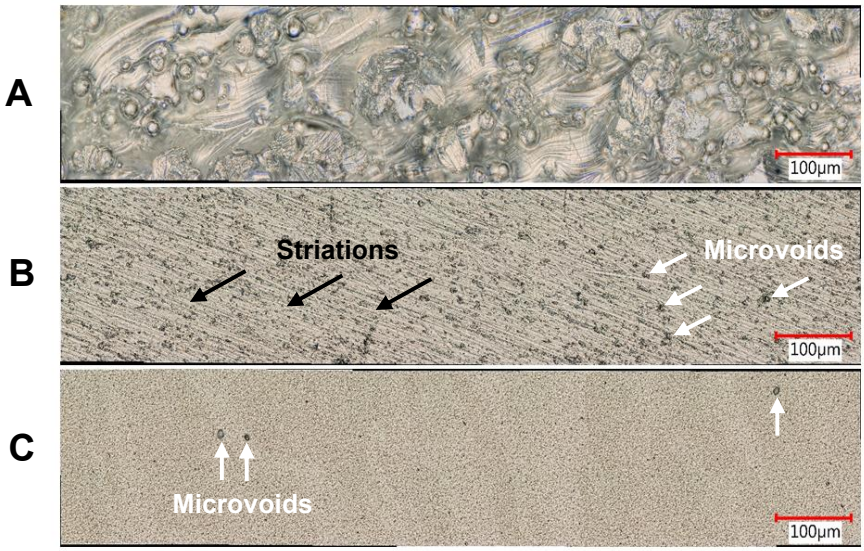

Figure 5.5 Optical micrographs of a specimen (Batch #1) (A) as-processed, (B) the same specimen a in A after mechanically abrading on wet P1500 grit aluminum oxide grinding paper using a polishing wheel , and (C) the same specimen and in B after polishing with decreasing grades of alumina powder by hand. All micrographs were obtained at 2000× magnification. The XZ plane is shown. The scale bar in all the micrographs is 100 µm.

Table 5.2. Surface texture analysis of the 3D image data of the Batch #2 alloy specimens in Figure 3 as-processed, after abrading on a wheel, and after abrading and polishing by hand.

Batch #2 Specimen	**As Processed**	**After Abrading on a Polishing Wheel**	**After Abrading and Polishing by Hand**
S_q, Root Mean Square Height (Surface Roughness)	29 ± 7 µm	1.8 ± 0.1 µm	1.5 ± 0.1 µm
S_z Maximum Peak-to-Valley Height	127 ± 25 µm	6.4 ± 0.4 µm	5.6 ± 0.2 µm

The table shows compiled data for S_q and S_z over five spots on a single specimen. Area of a single spot = 1000 × 200 µm^2. Values were determined using the Keyence microscope software.

The striations or scratches produced by the mechanical abrading are apparent in Figure 5.5B. The grit diameter was 13 µm and the striation widths are this dimension. The abrading revealed some microvoids and pores in the material that were not visible on the rough, as-processed specimen. Micropores are another type of defect commonly found in SLM alloys. Such defects result from the layer-by-layer build. It is likely that this results from the entrapment of residual gas

during the fabrication process.[12-15,19,20,59] This prohibits particle fusion and packing, and leads to voids during the solidification process. Figure 5.5C demonstrates that further polishing by hand with 0.3 and 0.05 μm alumina grit does not lead to much additional smoothing. The alloy was so hard that a few minutes of hand polishing with alumina powder does not alter the surface texture much. The hand polishing did reveal some of the native pores characteristic of the alloy.

The striations produced by the mechanical abrading can be seen in the secondary electron (SE) SEM micrograph of a specimen (Batch #1) presented in Figure 5.6A. The surface texture across the specimen was homogeneous after the abrading. Striations from the abrading formed directionally from the upper left to lower right across the micrograph (Fig. 5.6A). There were also a few brighter particulates decorating the surface that originated from contamination during the abrading step. Cracks and fissures formed on the specimen (XZ plane) as seen in Figure 5.6A. These defects only observed on some of the Batch #1 specimens were visible only after smoothing the surface by abrading and or polishing. The fissure was 100 μm in length and 2-3 μm wide. High heating (laser power) and cooling (scan speed) rates experienced locally in the specimen during fabrication can lead to thermal or residual stress. The relief of this stress sometimes manifests itself in the form of cracks and fissures.[6,59] Figure 5.6B shows another type of defect that is referred to as a fusion hole. These fusion holes result from incomplete melting and fusion of powder particles.[13-16,59] These were better revealed on the smoother surface texture. There were balling features and powder particles in the hole. Some of the particles might have resulted from the accumulation of grinding debris that was not fully removed by the ultrasonic cleaning. This grit might “fill in” the depression as depicted in the schematic provided in Figure 5.6C. Another possibility is smearing from displacement and spreading of material across the surface during the abrading and polishing steps.[60] Such debris could obscure morphological features and be

detrimental to the formation and adhesion of surface finishes used for appearance and corrosion control.

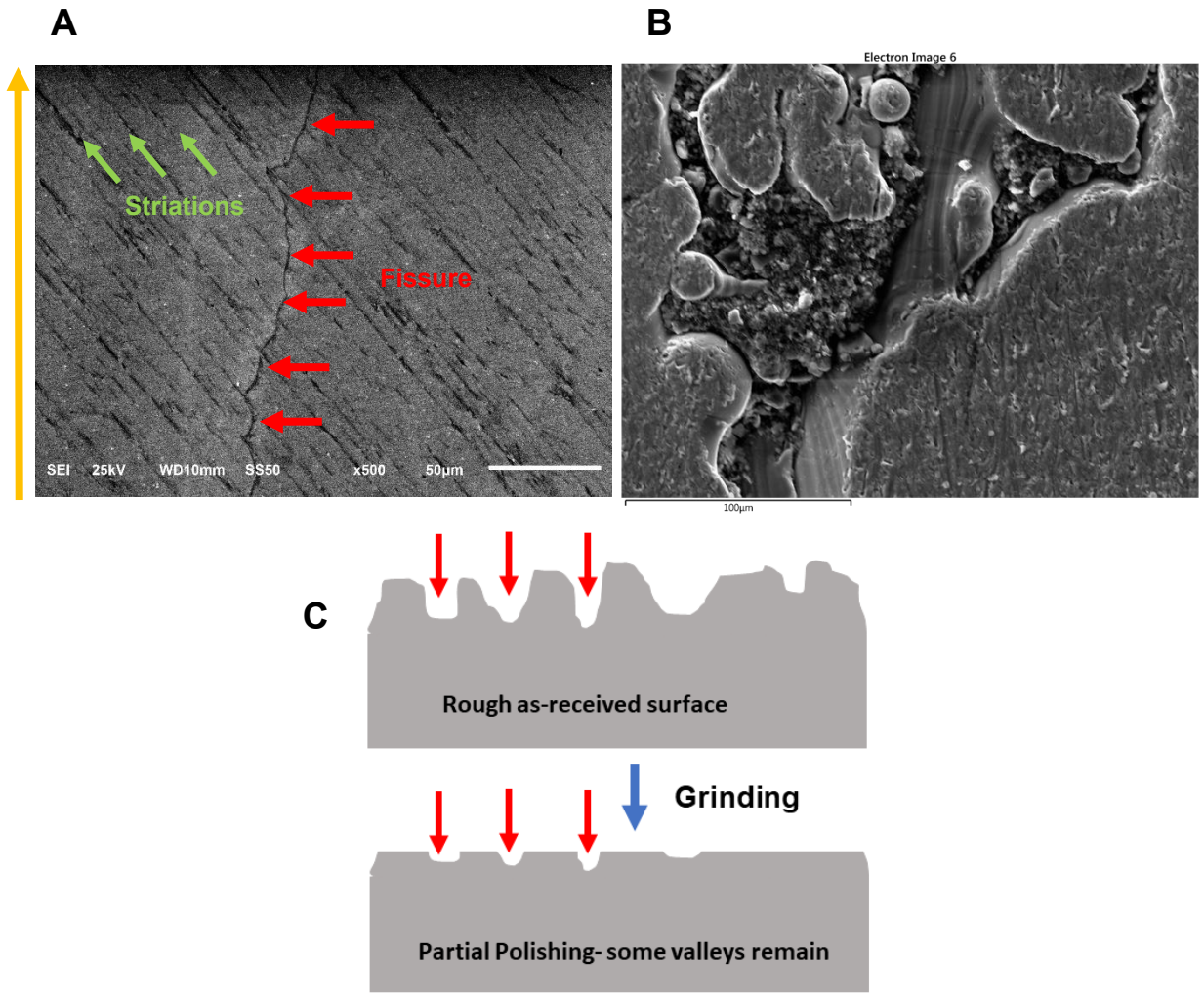

Figure 5.6. Secondary electron (SE) SEM micrographs of a specimen (Batch #1, XZ plane) after (A) mechanical abrading on wet P1500 grit aluminum oxide grinding paper on a polishing wheel showing the presence of striations (green arrows) and a fissure (red arrows) at 500×. The yellow arrow indicates the build direction. (B) SE SEM micrograph revealing depressions and valleys on the surface after abrading. The scale bar in the micrograph is 100 µm. (C) A schematic showing how the abrading smooths down high points on the surface and fills in depressions and valleys with grinding debris that was not removed by ultrasonic cleaning. The presence of the debris can obscure morphological features.

Scanning electron microscopy was used to further compare the morphological and microstructural differences between the two batches of alloys and the effect of mechanical abrading with wet P1500 grit aluminum oxide paper had on each. Figure 5.7 presents SEM

micrographs at two magnifications showing the differences in surface texture of as-processed specimens from the two batches. Figure 5.7A and B show a specimen from Batch #1 and C and D show a specimen from Batch #2. The micrographs reveal a similar surface morphology for both. Rough surface textures are seen for both alloys with partially melted and fully melted powder particles. The ball features reflect powder particles that have only been partially melted during the laser scanning process. These powder particles, while not fully melted adhere to the surface. Both surfaces are largely devoid of micropores and cracks that, at least in these regions, that develop in SLM prepared alloys.[13-16]

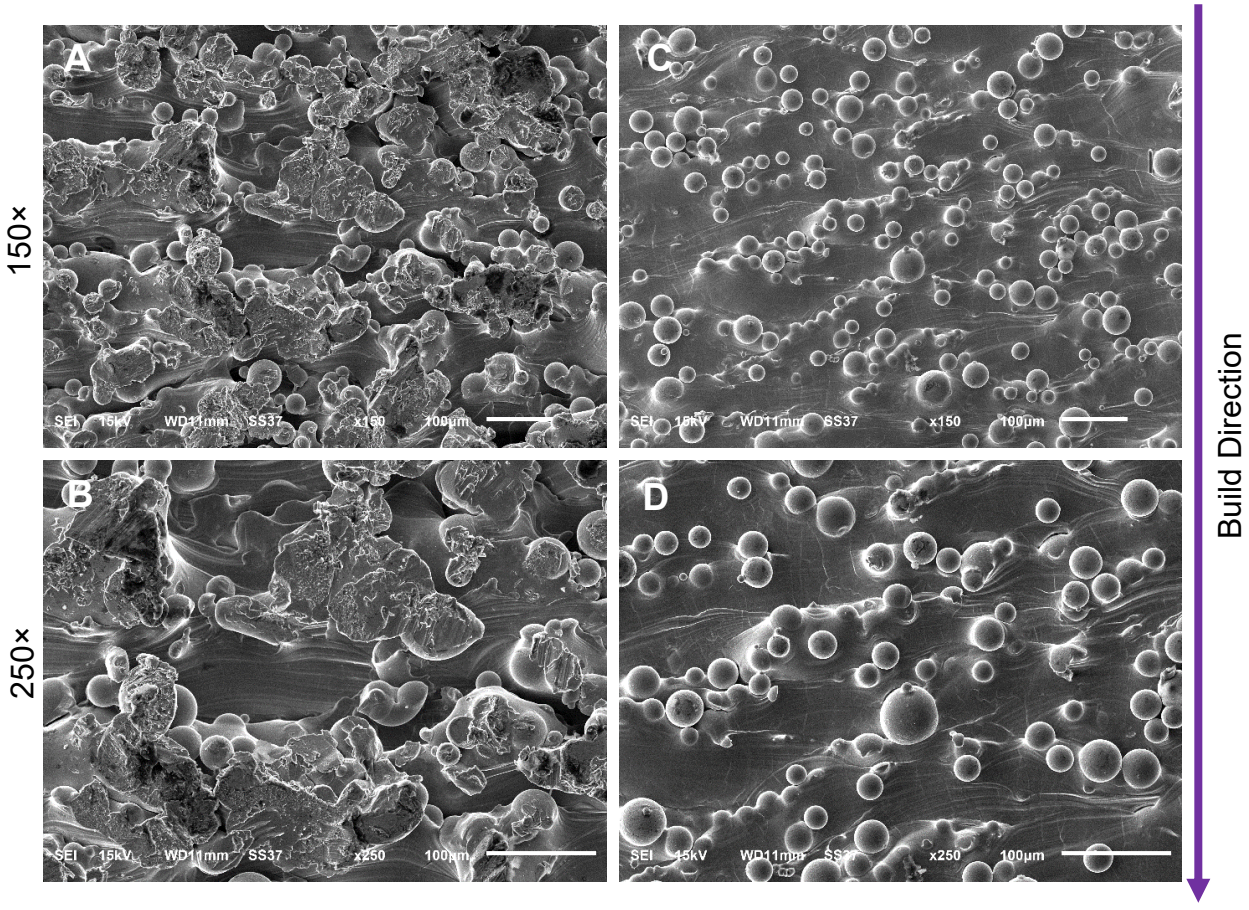

Figure 5.7. SEM micrographs (secondary electron images) of as-processed specimens (A and B) from Batch #1 and (C and D) from Batch #2. The XZ plane is shown. The scale bar is 100 µm.

Figure 5.8 presents SEM micrographs of specimens from the two batches after abrading with P1500 grit alumina grinding paper for 4 min on a polishing wheel. This was followed by a 20-min ultrasonic cleaning in ultrapure water. Figure 6A and B show a specimen from Batch #1 and Figure 5.8C and D show a specimen from Batch #2. After abrading, differences in the surface morphology can be seen. The Batch #1 specimen exhibits plateaus where the surface features were smoothed down along with remaining multiple fusion pores, some of which were long (i.e., tens of micrometers) and deep. In contrast, the smoothed Batch #2 specimen exhibited smaller fusion pores. This is consistent with the Batch #2 specimens being denser than the Batch #1 specimens.

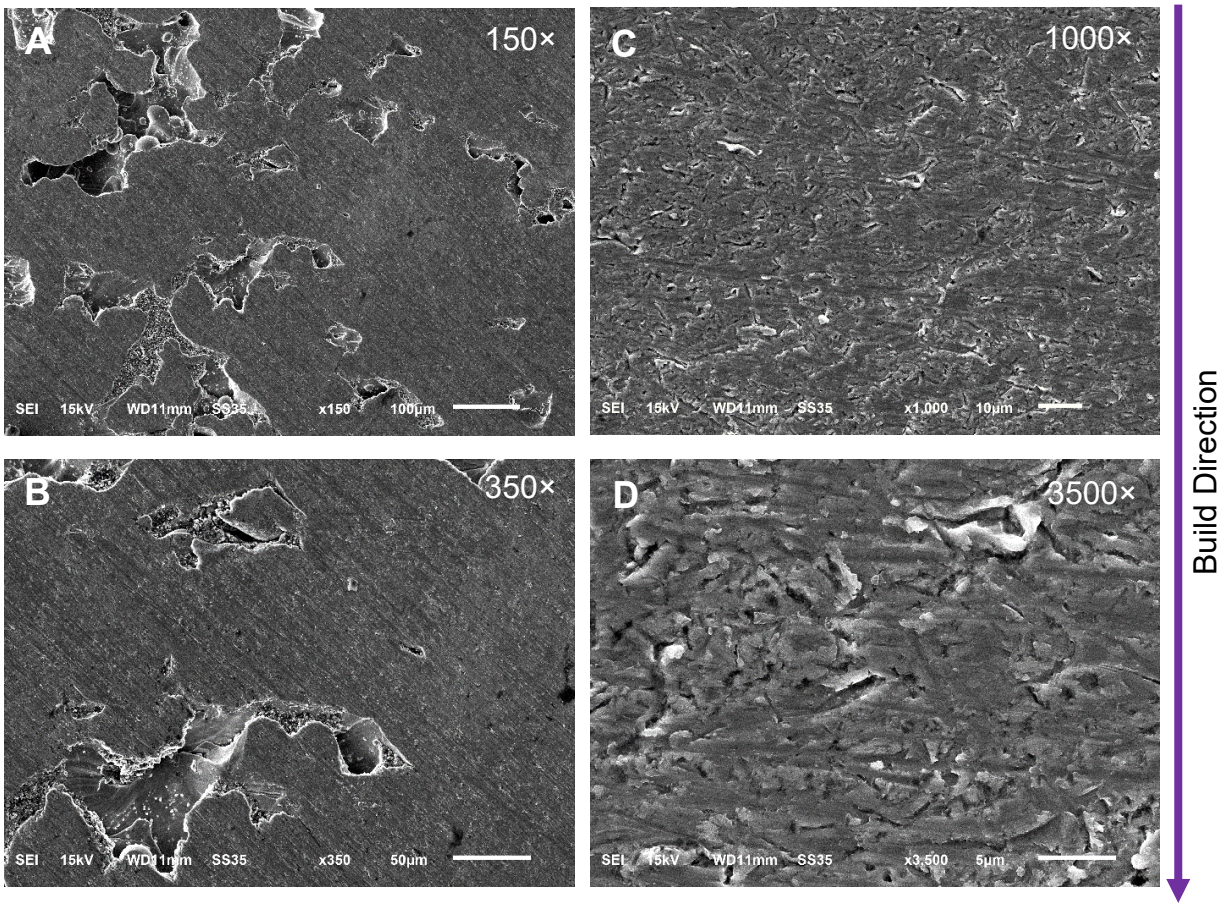

Figure 5.8. SEM micrographs (secondary electron images) of a Batch #1 specimen (A and B) and a Batch #2 specimen (C and D) after abrading. The XZ plane is shown. The micrographs (C and D) for the Batch #2 specimen were obtained at 10× higher magnifications than the micrographs for the Batch #1 specimen. The scale bars on Figures 6A, B, C, and D are 100 µm, 50 µm, 10 µm, and 5 µm, respectively.

Figure 5.9 presents an SEM micrograph for an as-processed Batch #2 specimen along with associated EDXS elemental maps for Ti, Al, Mo, V, Cr and O from the imaged area. Semi-quantitative x-ray analysis revealed weight percents of the alloying elements as the following: Al (4.1%), Mo (4.4%), V (5.3%) and Cr (2.1%), were close to the expected weight percents of Al (5%), Mo (5%), V (5%) and Cr (3%). The measured Ti content was 78%, while the measured O content (5.6%) arises from the surface oxide layer. The maps provide some confirmation of the alloy composition.

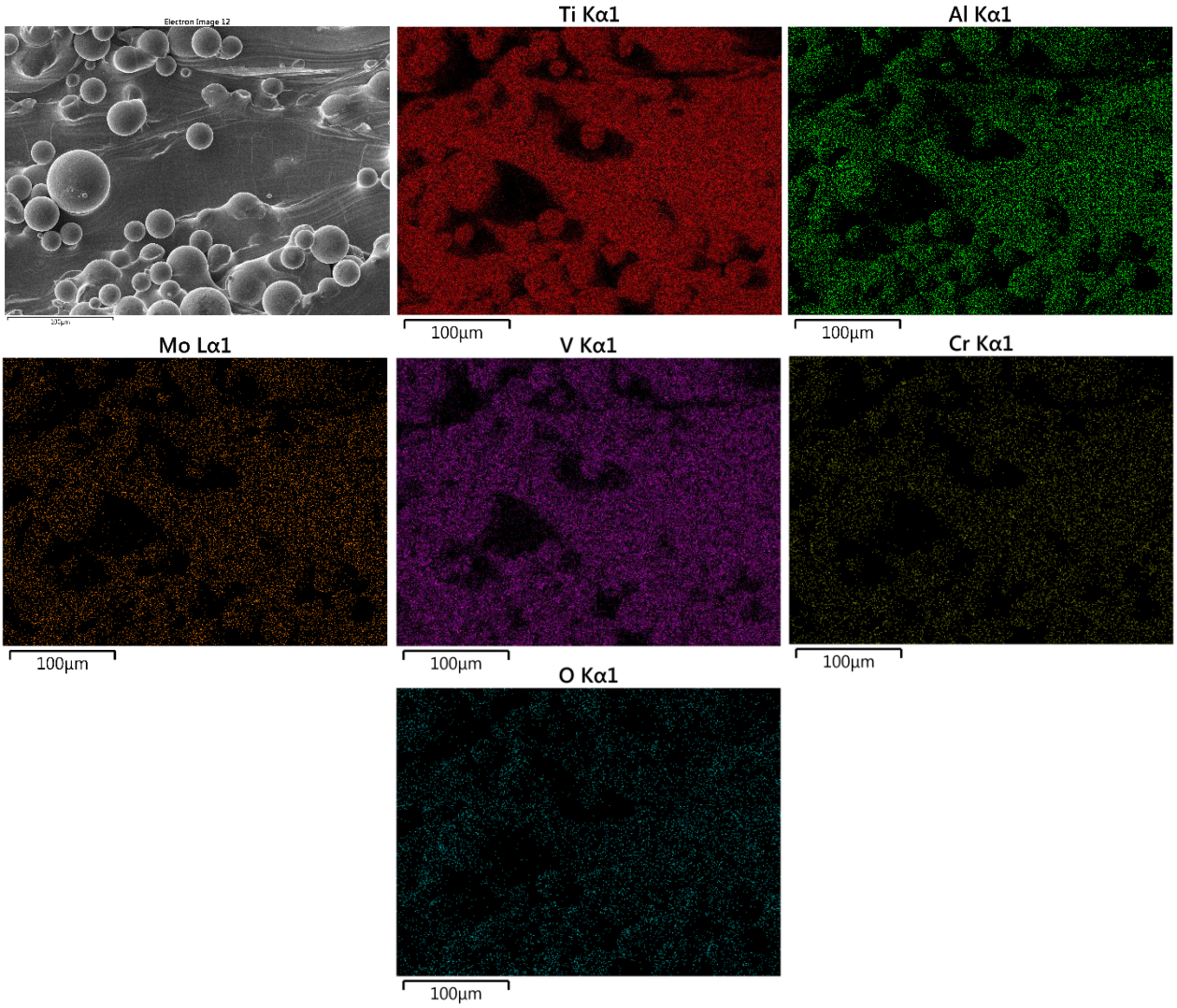

Figure 5.9. SEM micrograph (secondary electron image) of an as-processed specimen from Batch #2. The XZ plane is shown. The EDXS elemental maps for Ti, Al, Mo, V, Cr and O were obtained from the same area shown in the micrograph.

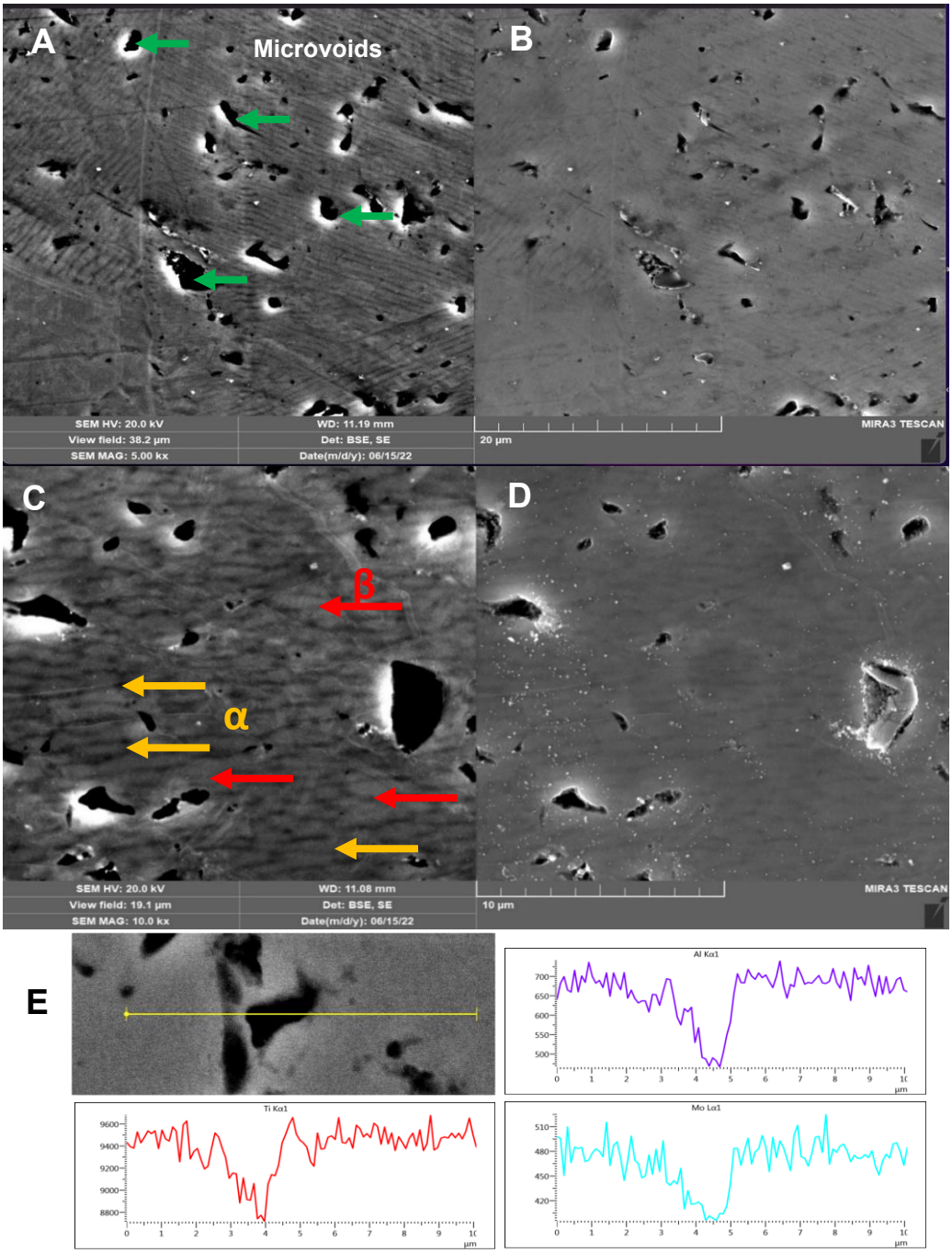

Figure 5.10. SEM micrographs of the same area for a specimen (Batch #2, XZ plane) in the (A) BSE image at 5000×(scale bar =20 µm), (B) SE image at 5000× (scale bar =20 µm), (C) BSE image at 10,000× (scale bar =10 µm), and (D) SE image at 10,000× (scale bar =10 µm), imaging modes after wet grinding on P1500 grit aluminum oxide grinding paper for 4 min followed by ultrasonic cleaning in ultrapure water for 20 min, polishing with a 0.25 µm alumina/H_2O slurry on a polishing wheel for 30 min, rinsing with ultrapure water, polishing with a 0.04 µm a colloidal silica/H_2O slurry on a polishing wheel for 40 min, rinsing with ethanol, rubbing on a felt pad wetted with ethanol to remove polishing debris and a final ultrasonic cleaning in ethanol for 10 min. The specimen was then etched in Kroll's solution. The β phase is brighter while the α phase is darker in the BSE images. (E) EDXS line spectra collected across a microvoid.

SEM micrographs for a specimen after abrading, polishing and wet chemical etching are presented in Figure 5.10. Figures 5.10A and B reveal some irregularly shaped microvoids and circular pores across the surface. Some of these pores were localized corrosion pits formed during the etching step. Areas consisting of heavier elements (higher atomic number) appear brighter in BSE SEM micrographs, while areas with higher concentration of lighter elements (lower atomic number) appear darker in BSE SEM micrographs. Higher magnification SE and BSE SEM micrographs for an abraded, polished, and etched specimen (XZ plane) are presented in Figures 5.10C and D. Pores and microvoids in the material were evident. Dark rod-like regions, as indicated by the yellow arrows, may represent the α phase. The brighter regions, indicated with the red arrows, are the β phase. The fine α precipitates dispersed in the β matrix strengthen the alloy. To confirm that the larger dark regions observed in the micrographs are microvoids and pores, energy dispersive x-ray (EDXS) line scan analysis was performed across one of these regions, The data are presented in Figure 5.10E.

X-Ray Diffraction Analysis. A typical x-ray diffraction spectrum for an as-processed specimen is shown in Figure 5.11. High intensity and symmetric diffraction peaks corresponding to the β phase were present at 2θ values (deg) of 39.45 (172,771 counts, 0.52 deg FWHM), 58.54 (10,855 counts, 1.47 deg), and 72.02 (6,248 counts, 2.19 deg FWHM). The weakly intense, symmetric peak at a 2θ value of 35.45 deg (1,632 counts, 0.49 deg FWHM) and asymmetric peak at a 2-θ value of 85.40 deg (3,254 counts, 1.33 deg FWHM) are associated with α and α" phases, respectively. The peak assignments are based on comparison of diffraction pattern data for this alloy.[2,6,63-65] The high intensity of the peak at a 2θ of 39.45 deg indicated that the alloy has a considerable amount of β phase. This is expected because Ti-5553 consists of high atomic levels of the β phase stabilizing elements Mo, V and Cr.

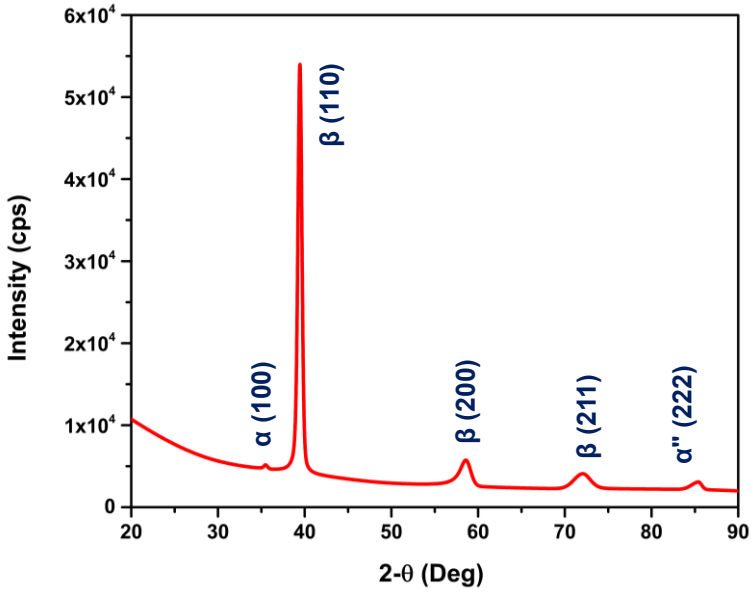

Figure 5.11. X-ray diffraction pattern for an as-received Ti-5553 alloy specimen (Batch #2).

Vickers Microhardness. The microhardness data revealed good reproducibility across multiple points in a single specimen and from specimen to specimen (n=5). For measurements performed at multiple spots in a single 1" × 1" specimen (Dwell time = 15 s. Load = 500 gf), a nominal hardness of 287 ± 5 HV was determined. This hardness is lower than the value reported for heat treated, die-cast Ti-5553 specimens (*i.e.*, 311 ± 8 HV).[14,15,64,66] This high hardness value is consistent with the near full density of the materials (*i.e.*, low porosity). The nominal hardness over three different 1" × 1" specimens (Batch #2) was 292 ± 2 HV (Dwell time = 15 s. Load = 200 gf). The lower value for the specimens used in this work was attributed to the microporosity (~2% porosity from the density measurement) and voids that are not present in the die-cast counterpart. Increasing hardness for Ti-5533 has been correlated with increasing aging temperature.[14,15,64,66]

Electrochemical Properties of As-Processed and Abraded and Polished Alloys. The main purpose for this paper is to present a body of electrochemical data for this SLM alloy before and after smoothing the surface texture. All the electrochemical data reported below are for Batch #2 specimens. Potentiodynamic polarization curves, both anodic and cathodic, were recorded for

multiple as-processed specimens to assess the reproducibility of the electrochemical behavior from specimen to specimen.

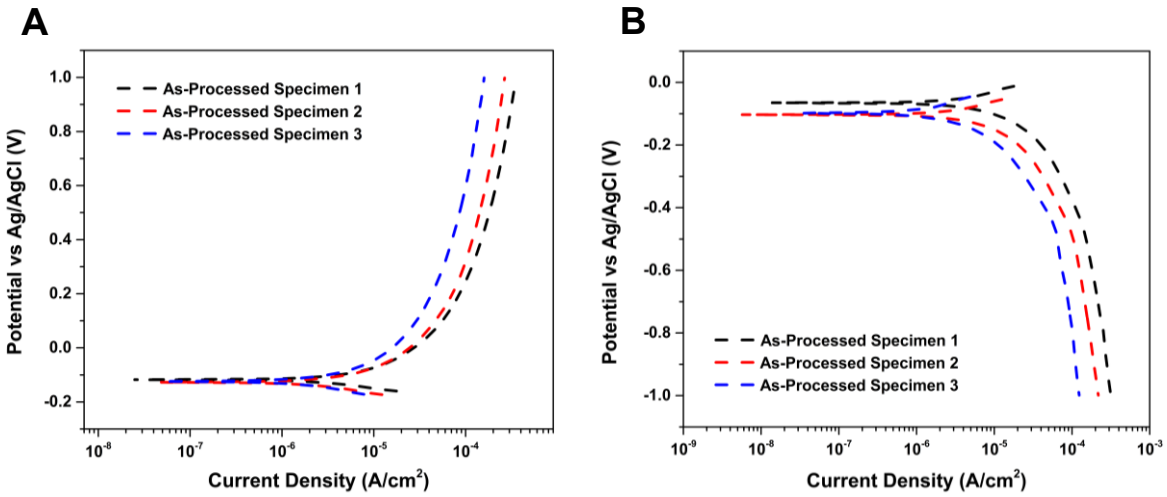

Figure 5.12. (A) Anodic and (B) cathodic potentiodynamic polarization curves for as-processed specimens (Batch #2) in naturally aerated 3.5 wt.% NaCl. Scan rate = 1 mV/s. Three specimens were used for both the anodic and cathodic measurements.

Figure 5.12 presents anodic (left) and cathodic (right) curves for three separate specimens. The same specimens were used to record both curves with the cathodic ones being recorded first. Importantly, the curve shapes were reproducible from specimen to specimen. The anodic curves were scanned from 0.050 V negative of the OCP, which ranged from 0 to 0.050 V, to 1.0 V vs. Ag/AgCl. A special focus was given to detecting oxide film breakdown and the development of localized pitting. The current increased significantly with increasing potential immediately positive of the OCP. A steady-state passivation current, i_{pass}, was quickly reached by ca. 0.2 V for all three specimens with a value of ca. 1×10^{-4} A/cm^2 at 0.8 V. The current was normalized to the geometric and not the true surface area, so the actual current density was less. The steady-state current was associated with the formation of a passivating oxide film (TiO_2). Below 0.2 V, the alloy was actively oxidizing to form Ti^{+4} ions that then react with H_2O in the interfacial layer to form TiO_2 ($Ti + 2H_2O \rightarrow TiO_2 + 4H^+ + 4e^-$).[67] The passivation current in this naturally aerated

aggressive electrolyte was stable out to at least 1.0 V with no evidence of oxide film breakdown or initiation of stable pit formation and growth. In fact, some specimens were polarized out to 2.4 V with no oxide film breakdown observed. In other words, well-defined transition from passive to active behavior was not observed up to 1.0 V vs. Ag/AgCl in this high chloride electrolyte.

The cathodic curves were recorded from 0.050 V positive of the OCP to -1.0 V vs. Ag/AgCl. The cathodic current increases steeply with increasing negative potential with a near steady-state current reached by -0.6 V. The steady-state current is associated, at least in part, with the diffusion-controlled reduction of dissolved oxygen. This was confirmed by observing a decrease in the steady-state current at these potentials after deaerating the electrolyte solution with N_2 gas. Some of the current at negative potentials in this neutral pH electrolyte is likely due to the reduction of the passivating TiO_2 to hydrated $Ti(OH)_3$ ($TiO_2 + 2H_2O + e^- \rightarrow Ti(OH)_3 + OH^-$). The oxygen reduction reaction on TiO_2 is complicated and can involve both a 2-electron/2-proton or a 4-electron/4-proton pathway.[68] More research is needed to better understand the oxygen reduction reaction mechanism in this alloy but we suppose the reaction proceeds following the 2-electron/2-proton pathway ($1/2O_2 + H_2O + 2e^- \rightarrow 2OH^-$).

The impact of smoothing the rough alloy surface texture on the electrochemical properties was investigated next. Specimens for these measurements were prepared by first abrading and polishing, and then degreasing and deoxidizing. As evident in Figure 5.13A and B, which presents anodic and cathodic curves for three separate abraded and polished specimens, the behavior is reproducible. In the anodic potentiodynamic polarization curves (Fig. 5.13A), as the potential is scanned positive, there is a gradual increase in the anodic current up to about 0.6 V than was observed for the as-processed specimens. A steady-state or passivation current, i_{pass}, was reached at 0.6 V with a value of ca. 2×10^{-6} A/cm^2. This current is about 100× lower than that seen for the

as-processed specimens. No breakdown of the passivation layer or onset of localized pitting corrosion was observed on any of three specimens out to at least 1.0 V vs. Ag/AgCl. The smoothed specimens were passivated by a low defect and continuous, electrochemically formed, oxide layer (TiO_2) that is likely on the order of a few nanometers thick. The oxide formed on the smoothed surface passivates the alloy better than does the oxide layer formed on the rough as-processed surface making the alloy more resistant to corrosion. The passivating oxide layer can form more continuously and with fewer defects on smoother surfaces. The alloying elements are mainly dissolved in the Ti matrix. However, over time, the dissolution of the alloying elements may impact the corrosion resistance by degrading the overall integrity of the oxide.[68] As the potential was scanned toward lower values in the cathodic polarization curves (Figure 5.13B), there is a gradual increase in current up to about -0.5 V, at which point a steady-state current is reached. The reproducible current magnitude at this potential is *ca*. 2×10^{-5} A/cm^2. This current is associated with dissolved oxygen reduction. Figure 5.13C compares anodic potentiodynamic polarization curves for representative as-processed and abraded and polished specimens in naturally aerated 3.5 wt.% NaCl. A steady-state passivation current was reached at 0.6 V for both specimens, but the magnitude for the as-processed specimen, ca. 1×10^{-4} A/cm^2, is 100× larger than the magnitude for the abraded and polished specimen, ca. 2×10^{-6} A/cm^2. Additionally, the OCP values for the as-processed specimens are about 100 mV less noble (more negative) than the values for the abraded and polished specimens. This together with the passivating current differences is consistent with the abraded and polished specimens being more passivating by the oxide layer than are the rough as-processed specimens. Figure 5.13D compares cathodic potentiodynamic polarization curves for an as-processed and an abraded and polished specimen in naturally aerated 3.5 wt.% NaCl. The cathodic current increases with increasing negative potential, with respect to

the OCP, for both specimens with a near steady-state current reached by -0.6 V. This current is associated with the reduction of dissolved oxygen. The steady-state current for the as-processed specimen is *ca*. 2×10^{-4} A/cm^2. In contrast, the current for the abraded and polished specimen is an order of magnitude lower at ca. 2×10^{-5} A/cm^2. The higher surface area of the as-processed specimen leads to higher rates of oxygen reduction as there are more active sites available for the reaction to occur. Thus, the morphology and roughness of the Ti-5553 surface can affect the rate of oxygen reduction.

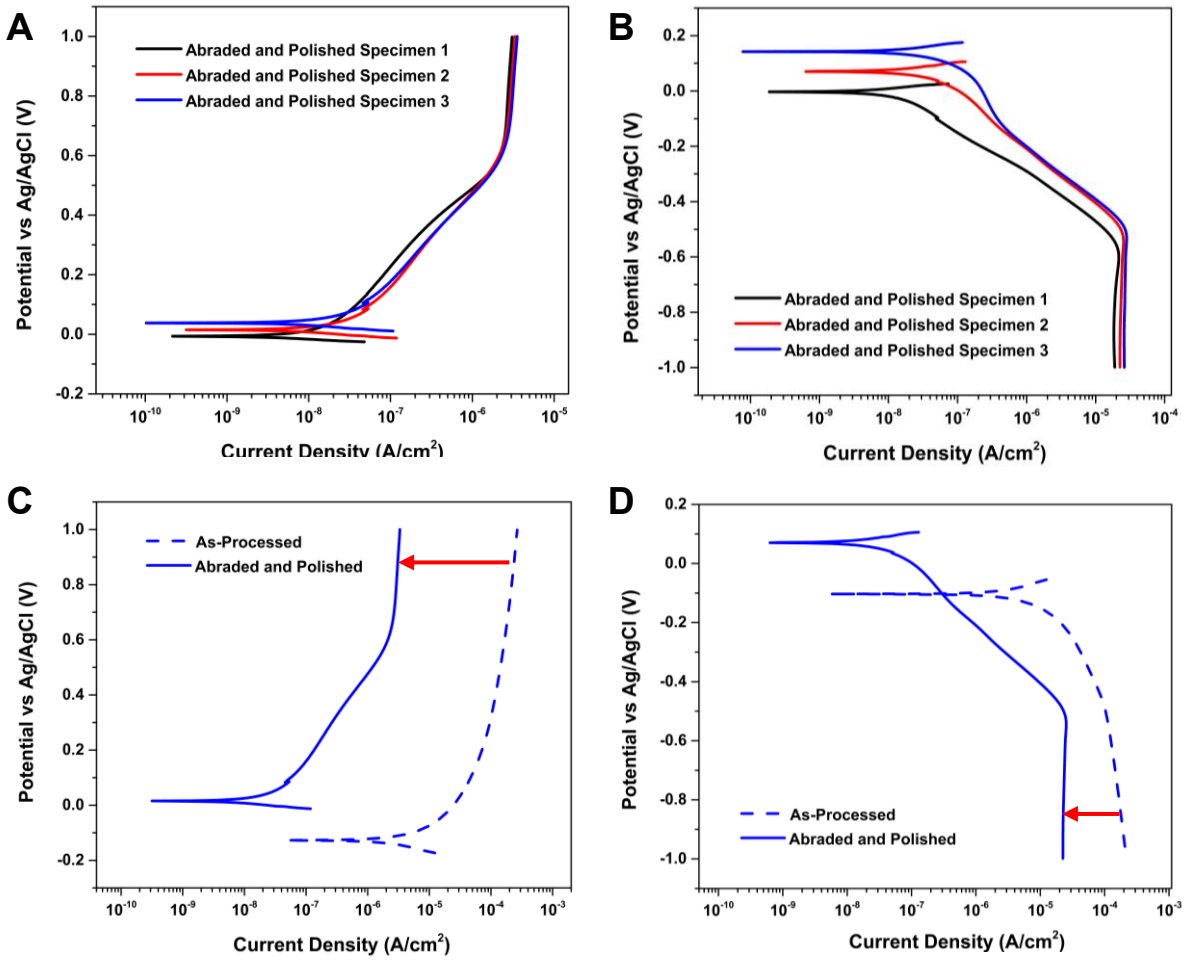

Figure 5.13. (A) Anodic and (B) cathodic potentiodynamic polarization curves for abraded and polished specimens (Batch #2) in naturally aerated 3.5 wt.% NaCl. Scan rate = 1 mV/s. Three specimens were used for both the anodic and cathodic measurements. Comparison of (C) anodic and (D) cathodic potentiodynamic polarization curves for an as-processed and an abraded and polished specimen in naturally aerated 3.5 wt.% NaCl. Scan rate = 1 mV/s. All specimens were degreased and deoxidized similarly.

Numerical electrochemical data obtained from the polarization curves are summarized in Table 5.3. The nominal OCP value for the abraded and polished specimens is more noble by 200 Mv as compared to the value for the as-processed specimens. The nominal polarization resistance (R_p) value was larger for the abraded and polished specimens at 1.99 (± 0.77) × 10^6 Ω-cm^2 versus 4.67 (± 1.78) × 10^3 Ω-cm^2 for the as-processed specimens. Thus, the R_p value for the abraded and polished specimens was *ca.* 3 orders of magnitude larger than the value for the as-processed specimens. The nominal anodic current in the polarization curves at 0.8 V for the abraded and polished specimens was 2 orders of magnitude smaller than the value for the as-processed specimens, 2.92 (± 0.19) × 10^{-6} vs. 2.10 (± 0.77) × 10^{-4} A/cm^2, respectively. Finally, the nominal cathodic current in the polarization curves at -0.8 V for the abraded and polished specimens was one order of magnitude lower than the value for the as-processed specimens, 2.26 (± 0.38) × 10^{-5} vs. 1.75 (±0.77) × 10^{-4} A/cm^2, respectively.

Table 5.3. A summary of numerical electrochemical parameters for specimens in the as-processed and after abrading and polishing conditions in naturally aerated 3.5 wt.% NaCl .

	As-Processed	**Abraded and Polished**
OCP (mV vs. Ag/AgCl)	-118 ± 7	107 ± 26
R_p - LPR (Ω-cm^2)	4.67 (± 1.78) × 10^3	1.99 (± 0.77) × 10^6
***j* at 0.8 V (A/cm^2)**	2.10 (± 0.77) × 10^{-4}	2.92 (± 0.19) × 10^{-6}
***j* at -0.8 V (A/cm^2)**	1.75 (± 0.77) × 10^{-4}	2.26 (± 0.38) × 10^{-5}

Data are presented as mean ± std. dev for n ≥ 3 specimens. Potentials are reported versus Ag/AgCl (4 M NaCl).

Electrochemical impedance spectroscopy measurements were performed at the OCP in naturally aerated 3.5% NaCl using as-processed and abraded and polished Ti-5553 specimens. Figure 5.14 presents impedance spectra in the forms of Bode diagrams for (A) as-processed and (B) abraded and polished specimens. A high degree of reproducibility between the replicate curves for each specimen type. At high frequencies, the Bode diagrams for both specimen types exhibit

a constant impedance of *ca.* 20 Ω cm^2 with a phase angle near 0°. This corresponds to the series resistance which is the sum of the ohmic resistances of the metal alloy and electrolyte solution. At middle frequencies, the impedance increases linearly with decreasing frequency while the phase shift approaches -70° for the as-processed and -80° for the abraded and polished specimens. The slope of the log Z vs. log frequency plot is close to -1. These trends are reflective of ideal capacitive behavior of the surface oxide film. The larger phase angle for the abraded and polished specimens and the fact that the phase angle remains near -80° to lower frequencies is consistent with the formation of a more compact and less defective oxide on these specimens.

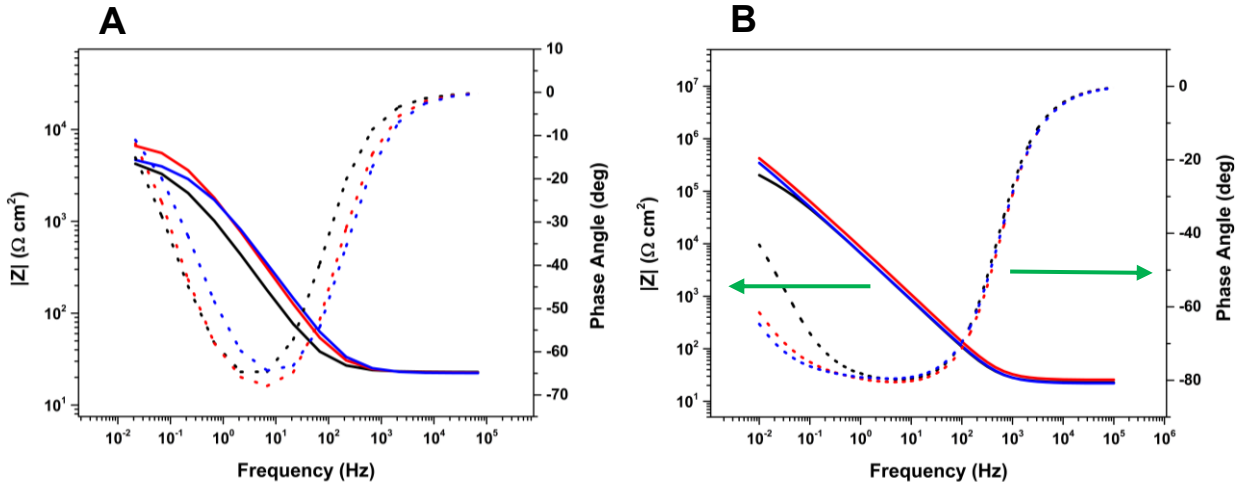

Figure 5.14. Bode plots of electrochemical impedance data recorded at the OCP for specimens (A) as-processed and (B) abraded and polished in naturally aerated 3.5 wt.% NaCl. All specimens were degreased and deoxidized similarly. AC amplitude = 0.010 V.

At low frequencies, the phase angle decreases toward 0° and the impedance reaches a maximum. Importantly, the magnitude of the impedance at 0.01 Hz (see Table 5. 4) is 35× larger for the abraded and polished specimens as compared to the as-processed specimens, 1.84 (± 0.49) ×10^5 vs. 5.19 (± 1.29) × 10^3 Ω-cm^2, respectively. The low frequency impedance magnitude if reflective of the polarization or charge transfer resistance and therefore the corrosion resistance of the alloy. The increased low frequency impedance for the abraded and polished specimens is consistent with the trends in R_p and the anodic and cathodic polarization currents; all reflective of

increased alloy corrosion resistance after smoothing the surface texture.

The EIS data were then fit to a simple Randles equivalent circuit consisting of an e resistance equivalent series (R_s) in series with the parallel combination of a constant phase element, in place of a capacitor, and a polarization resistance (R_p). The equivalent series resistance is the sum of the ohmic resistance of the electrolyte solution, electrode, and electrical contact. These values were

$$C_{eff} = \left(\frac{R_s R_p}{R_s + R_p}\right)^{\frac{1-\alpha}{\alpha}} Q^{\frac{1}{\alpha}} \qquad (2)$$

then be used to calculate the effective capacitance using the following equation[69].

The CPE components were expressed by mathematical parameters, Q, and α, where Q is the quasi-capacitance and α is the so-called homogeneity factor (α = 1 for an ideal capacitor).

Table 5.4. A summary of numerical EIS parameters for specimens in the as-processed condition and after abrading and polishing in naturally aerated 3.5 wt.% NaCl.

	As Processed	**Abraded and Polished**
Polarization Resistance - R_p (Ω-cm^2)	5.21 (±1.33) × 10^3	1.66 (±0.97) × 10^6
Equivalent Series Resistance - R_s (Ω)	22.20 ± 0.40	24.30 ± 1.98
Effective Capacitance - C_{eff} (F/cm^2)	5.29 (± 2.61) × 10^{-5}	1.05 (± 0.12) × 10^{-5}
Impedance Modulus - Z_{Mod} at 0.01 Hz (Ω-cm^2)	5.19 (± 1.29) × 10^3	1.84 (± 0.49) × 10^5

Data are presented as mean ± std. dev. for n = 3 specimens of each type. EIS measurements were made at the OCP. χ^2 values for the as-processed and the abraded and polished specimens 5.1 × 10^{-4} and 4.2 × 10^{-4}, respectively.

Table 5.4 presents a summary of the numerical parameters extracted from the EIS analysis. The nominal R_p value for the abraded and polished specimens was 300× larger than the value for the as-processed specimen, 1.66 (± 0.97) × 10^6 vs. 5.21 (± 1.33) × 10^3 Ω-cm^2. This is consistent with R_p values determined from the LPR measurements presented in Table 5.3, and indicates the increased corrosion resistance of the alloy with reduced surface roughness. The equivalent series resistance, R_s, is the same for both specimens. This is expected because the magnitude of R_s is dominated by the electrolyte resistance. The effective capacitance, C_{eff}, is lower for the abraded

and polished specimens, 1.05 (± 0.12) $\times 10^{-5}$ vs. 5.29 (± 2.61) $\times$ 10^{-5} F/cm^2. This is due to the improved dielectric properties of the passivating oxide layer on the abraded and polished specimens. A thicker or more dielectric oxide layer would reduce C_{eff}.

Effect of Deoxidation on Electrochemical Properties. The data show that the abraded and polished specimens exhibit improved corrosion resistance. The specimens were also degreased and deoxidized with commercial solutions as a final surface pretreatment prior to the electrochemical measurements. An important question is, "does this surface pretreatment alter the surface chemistry of the alloy and impact the electrochemical properties in any significant way?" The deoxidizer or desmutter employed was designed for use with aluminum alloys to dissolve smut and other contaminants from the alloy surface. Smut refers to solid products, typically aluminum oxide, and other impurities, that form on the alloy surface during material processing. These surface contaminants can negatively impact the formation of coatings and surface finished used to mitigate corrosion and therefore must be removed. This can be done with a deoxidizing acidic bath, such as the Smut-go bath used herein. The solution is free of chromate and is ideal for processing aluminum alloys that require low surface resistance, prior to anodizing, conversion coating, bonding, or welding. The solution will pit and etch aluminum alloys during the chemical dissolution process for control over contact time is critical. It is unknown how this surface pretreatment affects the surface morphology, microstructure, and chemistry of Ti-5553. Preliminary studies were therefore conducted to learn its effect on the electrochemical properties.

All alloy specimens used in these measurements were abraded and polished, as follows, using slightly different from the protocol listed in the Experimental section for the specimens used in the electrochemical measurements. As-processed specimens were smoothed by first abrading on P1500 grit aluminum oxide grinding paper for 20 min using the polishing wheel followed by

ultrasonic cleaning in ultrapure water for 30 min. The specimens were then polished (by hand) using 1 and 0.3 alumina powder/H_2O slurries for 30 min each. After each polishing step, the specimens were ultrasonically cleaned in ultrapure water for 30 min. As a final step, the specimens were polished with a 0.05 μm alumina powder/H_2O slurry followed by ultrasonic cleaning in ultrapure water for 30 min. One set of three received no additional surface pretreatment (i.e., no degreasing and deoxidation) and were used immediately in the electrochemical measurements. Another set of three was degreased and deoxidized (2 min), as described in the Experimental section, and then used in the electrochemical measurements.

Table 5.5. A summary of numerical electrochemical parameters for abraded and polished Ti-5553 specimens before and after degreasing and deoxidation in naturally aerated 3.5 wt.% NaCl.

Electrode Pretreatment	**OCP (mV vs. Ag/AgCl 3 M NaCl)**	***j* at 0.6 V (A/cm^2)**	***j* at -0.6 V (A/cm^2)**	**R_p ($\Omega\ cm^2$) × 10^6**
Polished and Abraded (naturally aerated)	-214 ± 49	5.59 (±0.48) × 10^{-6}	5.59 (±0.48) × 10^{-6}	0.85 ± 0.48
Polished and Abraded (deaerated)	-458 ± 41	5.49 (±0.86) × 10^{-6}	3.97 (±0.45) × 10^{-7}	1.64 ± 0.21
Polished and Abraded Plus Degreased and Deoxidized (naturally aerated)	-25 ± 6	3.95 (±1.06) × 10^{-6}	3.38 (±0.77) × 10^{-5}	4.97 ± 0.08

Data are presented as mean ± std. dev. for n = 3 specimens of each type.

Table 5.5 presents a summary of some preliminary electrochemical data obtained from OCP measurements, anodic and cathodic potentiodynamic polarization curves, and linear polarization resistance measurements in 3.5 wt. % NaCl at room temperature. These preliminary data reveal that the Smut-go deoxidation does affect the alloy chemistry in such a way as to cause a slight noble shift in the OCP and a five-fold increase in R_p. The anodic and cathodic polarization curve currents at the selected potentials are similar for naturally aerated conditions with the degreased and desmutted alloy being a little more active for oxygen reduction at the selected potential of -

0.6 V. Future work will examine the electrochemical properties in more detail as well as morphology and microstructure of the alloy after different deoxidation times using digital optical and scanning electron microscopy. Future work will also investigate the surface chemistry changes to alloy using x-ray photoelectron spectroscopy.

5.4 DISCUSSION

Given the lack of scientific literature reports on the electrochemical properties of Ti-5553 alloys prepared by SLM processing, the results reported herein address this knowledge gap. In this work, the electrochemical properties of alloy specimens as-processed and after mechanical abrading and polishing to renew and smooth the surface texture. Metal alloys prepared by SLM tend to possess significant surface roughness. The surface roughness can vary depending on several factors including the SLM processing parameters, powder characteristics, laser parameters, and post-processing techniques. The as-processed specimens used in this work had surface roughness, S_q, and maximum peak-to-valley height, S_z, values of 16.7 ± 5.3 and 111 ± 29 μm, respectively (n=5 spots on three specimens). The specimens were comprised of balling features with some micropore and fusion pore defects. After abrading and polishing the S_q and S_z values decreased to 1.8 ± 0.1 and 6.4 ± 0.4 μm, respectively. Given the hardness and density of this alloy, 287 ± 5 HV and 4.70 ± 0.03 g/cm^3, respectively, smoothing the surface texture is most effectively accomplished using a polishing wheel with a series of alumina grit sizes. It's important to optimize these build parameters based on specific material requirements and the desired surface finish for a particular application. A key finding from the results reported herein is that reducing the surface roughness by abrading and polishing, coupled with the degreasing and deoxidation pretreatments, improves the corrosion resistance of the alloy. In general, Ti and Ti alloys have excellent resistance against corrosion even in concentrated Cl^- electrolyte solutions. They are susceptible, however, to

erosion corrosion, stress corrosion cracking, corrosion fatigue, and crevice corrosion. The corrosion resistance of Ti and its alloys is due to the formation of a protective oxide layer, consisting of TiO_2, with a morphology that depends on the surface condition of the alloy on which it forms.[68,70] The improved corrosion resistance of the alloy after smoothing is attributed to the removal of the native and more defective oxide film on the as-processed alloy and reforming a more compact and less defective oxide on the smoothed surface. The surface area of the metal alloy exposed to the solution is also reduced after abrading and polishing. This also serves to make the alloy more corrosion resistant as decreasing the surface area exposed lessens the rate of corrosion processes. Reducing the surface area will generally produce lower corrosion rates due to decreased reaction site density, decreased mass transport pathways, and a diminished susceptibility to localized corrosion processes.

The native defects and surface microstructure will impact the electrochemical properties and corrosion susceptibility of the Ti-5553 alloy. Microvoids and pores are defects inherent to the SLM alloy because of incomplete annealing and particle fusion.[70] These defects represent sites where solution could penetrate the alloy and cause localized corrosion. These are also sites where there would be incomplete coverage of a passivating native oxide layer on the Ti. Some microvoids and pores were revealed on the alloy specimens used in this work, although from a bulk perspective, the specimens are nearly fully dense based on comparison of the measured density with the value reported for the die cast alloy. We estimate about a 1% porosity based on density measurements and detailed scanning electron micrographs that have been analyzed to yield a void volume. It is unclear at present how much of this surface porosity is native to the SLM alloy versus how much is introduced by the Smut-go deoxidation pretreatment and or the wet chemical etching by the Kroll's solution used as part of the metallographic finishing process. This needs to be

investigated further as these defects will deleteriously impact the formation of coatings and other surface finished for corrosion mitigation.

A detailed microstructural characterization of the SLM Ti-5553 alloys was not part of this work, but a significant body of literature exists on this. The crystal structure of pure Ti at ambient temperature and pressure is close-packed hexagonal, known as the α phase. At about 890 ºC, the Ti undergoes an allotropic transformation to a body-centered cubic structure, known as the β phase.[8,9,13-15,61,62] This β phase remains stable to the melting temperature (1700 ºC). The alloying elements can be categorized according to their stabilizing effect on the α and β phases.[8,9,13-15,61,62] Some alloying elements, such Al, are α stabilizers, while other elements, such as Mo, Nb, Ta, V and Cr, are β stabilizers. The presence of the α and β phases depends on the relative amounts of the respective stabilizers. Ti-5553 is a near-β phase alloy consisting of some α phase within a matrix of the β phase. Ti-5553 that was multi-directionally forged in the two-phase α+β phase field, exhibits microstructures containing large globular and rod-like, needle-shaped α precipitates within the β phase matrix.[72] The XRD data for Ti-5553 specimens used in this work indicate a largely β phase alloy based on higher intensity of the β phase peaks relative to the α phase ones.

The electrochemical properties of as-processed alloy specimens in naturally aerated 3.5% NaCl can be improved by abrading and polishing. OCP values were shifted to more noble potentials, R_p values increased by 2-3 orders of magnitude (10^6 Ω-cm^2), anodic and cathodic currents at selected potentials in potentiodynamic polarization curves decreased by 1-2 orders of magnitude, and the low frequency impedance modulus at 0.01 Hz increased by at least one order of magnitude after smoothing. Taken together, the data indicate that surface pretreatment to reduce the surface roughness and smooth the surface texture of the as-processed Ti-5553 alloy renders the metal less susceptible to corrosion. There are two related reasons for this. First, the abrading,

polishing, degreasing, and deoxidizing steps remove smut, impurities and the native oxide, thus exposing a fresh surface, and reducing the surface roughness. This allows for the formation of a less defective, more passivating oxide layer on the smooth surface.[9] This chemically stable oxide layer is primarily composed of titanium dioxide (TiO_2). It serves a crucial role by providing barrier layer and corrosion resistance to underlying metal and protecting it from further oxidation or chemical attack. The smoother the metal surface is and the more devoid it is of defects such as pores, cracks, and voids, the less defective the passivating oxide film will be and the better the corrosion protection it will provide. Second, as mentioned above, smoothing the surface reduces the area available for anodic and cathodic reactions. A larger surface area provides more pathways for the diffusion of reactants to the metal surface and removal of reaction produces and more sites for localized degradation; all of which impact corrosion rates.

5.5 CONCLUSIONS

The electrochemical behavior and corrosion susceptibility of Ti-5553 alloys prepared by selective laser melt (SLM) fabrication can be improved by abrading and polishing. Abrading and polishing produces a surface finish that renders Ti-5553 more resistant to electrochemical corrosion due to the removal of the defective native oxide on the as-processed specimens and formation of a more compact and less defective oxide film on the refreshed and smoothed surfaces. Additionally, the abrading and polishing reduce the surface area exposed to the solution leading to diminished corrosion susceptibility. Preliminary results indicate that the deoxidizing Smut-go pretreatment of the smoothed alloy, designed for desmutting aluminum alloys, has an impact on the electrochemical behavior by apparently altering the surface chemistry in such a way as to slightly enhance the corrosion resistance.

The key findings from the work are summarized as follows:

1. The surface roughness, S_q, and maximum peak-to-valley height, S_z, values of the as-processed specimens were 16.7 ± 5.3 and 111 ± 29 μm, respectively (n=5 spots on three specimens). The specimens were comprised of balling features, micropore and fusion pore defects. After abrading and polishing S_q and S_z decreased to 1.8 ± 0.1 and 6.4 ± 0.4 μm, respectively.
2. The nominal density of the as-processed specimens ranged from 4.55 ± 0.02 to 4.70 ± 0.03 g/cm^3 depending on the batch processed. Based on comparison with the reported density for the die-cast alloy, the specimens were 98-100% dense with 1-2% porosity. Vickers microhardness measurements revealed a nominal value of 292 ± 2 HV, a value slightly lower than the reported value for the die cast alloy of 311 ± 8 HV.
3. The open circuit potential (OCP) for the abraded and polished specimens in naturally aerated 3.5% NaCl was more noble or positive of the value for the as-processed specimens, 107 ± 26 vs. -118 ± 7 mV vs. Ag/AgCl (4 M NaCl). The nominal polarization resistance (R_p) obtained from linear polarization resistance measurements for the abraded and polished specimens was two orders of magnitude higher than the value for the as-processed specimens, 2×10^6 vs. 5×10^4 Ω-cm^2. Both are consistent with the corrosion resistance of the alloy being improved by the abrading and polishing.
4. Anodic potentiodynamic polarization curves revealed an anodic current of 1×10^{-4} A/cm^2 at 0.8 V vs. Ag/AgCl (4M NaCl) for the as-processed specimens that decreased to 2×10^{-6} A/cm^2 after abrading and polishing. The cathodic current in the potentiodynamic polarization curves at -0.8 V was one order of magnitude lower than the value for the as-processed specimens, 2.3×10^{-5} vs. 1.8×10^{-4} A/cm^2, respectively. Both indicate reduced oxidation and reduction reaction rates.

5. EIS data revealed a nominal low frequency impedance modulus at 0.01 Hz that was 35× larger and a polarization resistance from equivalent circuit fitting that was 300× larger (1.7×10^6 vs. 5.1×10^3 Ω-cm^2) for the abraded and polished specimens as compared to the rougher as-processed specimens. This is reflective of the improved corrosion resistance after smoothing the alloy.

REFERENCES

1. Welsch, G., Boyer, R., & Collings, E. W. (Eds.). (1993) Materials properties handbook: titanium alloys. ASM international.

2. Sha, W., & Malinov, S. (2009) Titanium alloys: modelling of microstructure, properties and applications. *Elsevier*.

3. Veiga, C., Davim, J. P., & Loureiro, A. J. R. (2012) Properties and applications of titanium alloys: a brief review. *Rev. Adv. Mater. Sci*. *32*(2), 133.

4. Banerjee, D., & Williams, J. C. (2013) Perspectives on titanium science and technology. *Acta Mater*. *61*(3), 844.

5. Sun, F., Jin-Ying Zhang, Matthieu Marteleur, C. Brozek, E. F. Rauch, M. Veron, P. Vermaut, P. J. Jacques, and F. Prima. (2015) A new titanium alloy with a combination of high strength, high strain hardening and improved ductility. *Scr. Mater.* 2015, 94, 17.

6. Zhao, Q., Yang, F., Torrens, R., & Bolzoni, L. (2019) Comparison of the cracking behavior of powder metallurgy and ingot metallurgy Ti-5Al-5Mo-5V-3Cr alloys during hot deformation. *Materials*, 2019, *12*(3), 457.

7. You, S. H., Lee, J. H., & Oh, S. H. (2019) A study on cutting characteristics in turning operations of titanium alloy used in automobiles. *Int. J. Precis. Eng. Manuf.* 2019, *20*, 209.

8. Kang, L., & Yang, C. (2019) A review on high-strength titanium alloys: microstructure, strengthening, and properties. *Adv. Eng. Mater.* 2019, *21*(8), 1801359.

9. Froes, F. H., & Dutta, B. The additive manufacturing (AM) of titanium alloys. *Adv. Mat. Res*. 2014, *1019*, 19.

10. Townsend, A.; Senin, N.; Blunt, L.; Leach, R. K.; Taylir, J. S. (2016) Surface texture metrology for metal additive manufacturing: a review. *Precis. Eng*. 2016, *46*, 34.

11. Sander, G.; Tan, J.; Balan, P.; Gharbi, O.; Feenstra, D. R.; Singer, L.; Thomas, S.; Kelly, R. G.; Scully, J. R.; and Birbilis, N. (2018) Corrosion of additively manufactured alloys: a review. *Corrosion.* 2018, *74*, 1318.

12. Blakey-Milner, B., Gradl, P., Snedden, G., Brooks, M., Pitot, J., Lopez, E., Leary, M., Berto, F., & Du Plessis, A. (2021) Metal additive manufacturing in aerospace: A review. *Mater. Des*. 2021, *209*, 110008.

13. Sharma, D.; Kada, S. R.; Fabijanic, D.; Parfitt, D.; Chen, B.; Roebuck, B.; Fitzpatrick, M. E.; Barnett, M. R. (2021). The ageing of direct laser deposited metastable β-Ti alloy, Ti-5Al-5Mo-5V-3Cr. *Addit. Manuf. 48*, 102384.

14. Ahmed, M.; Obeidi, M. A.; Yin, S.; and Lupoi R. (2022) Influence of process parameters on density, surface morphologies and hardness of as-built Ti-5Al-5Mo-5V-3Cr alloy manufactured by selective laser melting. *J. Alloys Compd. 910*, 164760.

15. Kuntoğlu, M.; Salur, E.; Canli E.; Aslan, A.; Gupta, M. K.; Waqar, S.; Krolczyk, G. M.; Xu, J. (2023) A state of the art on surface morphology of selective laser-melted metallic alloys. *Int. J. Adv. Manuf. Technol.* 2023, *127*, 1103.

16. Frazier, W. E. (2014) Metal Additive Manufacturing: A Review. *J. Mater. Eng. Perform.* 2014. *23*, 1917.

17. Lathabai, S. (2018) Additive Manufacturing of Aluminum-Based Alloys and Composites. *Fundamentals of aluminium metallurgy*, 2018. 47-92.

18. Bahnini, I., Rivette, M., Rechia, A., Siadat, A., & Elmesbahi, A. (2018) Additive manufacturing technology: the status, applications, and prospects. *Int. J. Adv. Manuf. Technol.* 2018, *97*, 147.

19. Aboulkhair, N. T., Simonelli, M., Parry, L., Ashcroft, I., Tuck, C., & Hague, R. (2019) 3D printing of Aluminium alloys: Additive Manufacturing of Aluminium alloys using selective laser melting. *Prog. Mater. Sci.* 2019, *106*, 100578.

20. Bandyopadhyay, A., Zhang, Y., & Bose, S. (2020) Recent developments in metal additive manufacturing. *Curr. Opin. Chem. Eng*. 2020. *28*, 96.

21. Sames, W. J., List, F. A., Pannala, S., Dehoff, R. R., & Babu, S. S. (2016) The metallurgy and processing science of metal additive manufacturing. *Int. Mater. Rev.* 2016, *61*(5), 315.

22. Svetlizky, D., Das, M., Zheng, B., Vyatskikh, A. L., Bose, S., Bandyopadhyay, A., Schoenung J. M., Lavernia, E. J., & Eliaz, N. (2021) Directed energy deposition (DED) additive manufacturing: Physical characteristics, defects, challenges and applications. *Mater. Today*. 2021, *49*, 271.

23. Louvis, E., Fox, P., & Sutcliffe, C. J. (2011). Selective laser melting of aluminium components. *J. Mater. Process. Technol*. 2011, *211*(2), 275.

24. Bremen, S., Meiners, W., & Diatlov, A. (2012) Selective laser melting: A manufacturing technology for the future? *Laser Tech. J.* 2012, *9*(2), 33.

25. Yap, C. Y., Chua, C. K., Dong, Z. L., Liu, Z. H., Zhang, D. Q., Loh, L. E., & Sing, S. L. (2015). Review of selective laser melting: Materials and applications. *Appl. Phys. Rev.* 2015, *2*(4), 041101.

26. Song, B., Dong, S., Zhang, B., Liao, H., & Coddet, C. (2012). Effects of processing parameters on microstructure and mechanical property of selective laser melted Ti6Al4V. *Mater. Des. 35*, 120.

27. Vrancken, B., Thijs, L., Kruth, J. P., & Van Humbeeck, J. (2012). Heat treatment of Ti6Al4V produced by Selective Laser Melting: Microstructure and mechanical properties. *J. Alloys Compd*. *541*, 177.

28. Rafi, H. K., Karthik, N. V., Gong, H., Starr, T. L., & Stucker, B. E. (2013). Microstructures and mechanical properties of Ti6Al4V parts fabricated by selective laser melting and electron beam melting. *J. Mater. Eng. Perform*. *22*, 3872.

29. Qiu, C., Adkins, N. J., & Attallah, M. M. (2013). Microstructure and tensile properties of selectively laser-melted and of HIPed laser-melted Ti–6Al–4V. *Mater. Sci. Eng. A*. *578*, 230.

30. Simonelli, M., Tse, Y. Y., & Tuck, C. (2014). On the texture formation of selective laser melted Ti-6Al-4V. *Metall. Mater. Trans. A*. *45*, 2863.

31. Wauthle, R., Vrancken, B., Beynaerts, B., Jorissen, K., Schrooten, J., Kruth, J. P., & Van Humbeeck, J. (2015) Effects of build orientation and heat treatment on the microstructure and mechanical properties of selective laser melted Ti6Al4V lattice structures. *Addit. Manuf*. *5*, 77.

32. Yang, J., Han, J., Yu, H., Yin, J., Gao, M., Wang, Z., & Zeng, X. (2016) Role of molten pool mode on formability, microstructure and mechanical properties of selective laser melted Ti-6Al-4V alloy. *Mater. Des. 110*, 558.

33. Zhao, X., Li, S., Zhang, M., Liu, Y., Sercombe, T. B., Wang, S., Hao, Y., Yang, R., & Murr, L. E. (2016). Comparison of the microstructures and mechanical properties of Ti–6Al–4V fabricated by selective laser melting and electron beam melting. *Mater. Des. 95*, 21.

34. Han, J., Yang, J., Yu, H., Yin, J., Gao, M., Wang, Z., & Zeng, X. (2017). Microstructure and mechanical property of selective laser melted Ti6Al4V dependence on laser energy density. *Rapid Prototyp. J*. *23*(2), 217.

35. Liang, Z., Sun, Z., Zhang, W., Wu, S., & Chang, H. (2019). The effect of heat treatment on microstructure evolution and tensile properties of selective laser melted Ti6Al4V alloy. *J. Alloys Compd*. *782*, 1041.

36. Jin, N., Yan, Z., Wang, Y., Cheng, H., & Zhang, H. (2021). Effects of heat treatment on microstructure and mechanical properties of selective laser melted Ti-6Al-4V lattice materials. *Inter. J. Mech. Sci*. *190*, 106042.

37. Zheng, Z., Jin, X., Bai, Y., Yang, Y., Ni, C., Lu, W. F., & Wang, H. (2022). Microstructure and anisotropic mechanical properties of selective laser melted Ti6Al4V alloy under different scanning strategies. *Mater. Sci. Eng. A. 831*, 142236.

38. Dai, N., Zhang, L. C., Zhang, J., Zhang, X., Ni, Q., Chen, Y., Wu, M., & Yang, C. (2016). Distinction in corrosion resistance of selective laser melted Ti-6Al-4V alloy on different planes. *Corros. Sci. 111*, 703.

39. Dai, N., Zhang, L. C., Zhang, J., Chen, Q., & Wu, M. (2016). Corrosion behavior of selective laser melted Ti-6Al-4 V alloy in NaCl solution. *Corros. Sci. 102*, 484.

40. Dai, N., Zhang, J., Chen, Y., & Zhang, L. C. (2017). Heat treatment degrading the corrosion resistance of selective laser melted Ti-6Al-4V alloy. *J. Electrochem. Soc. 164*(7), C428.

41. Kao, W. H., Su, Y. L., Horng, J. H., & Chang, C. Y. (2018). Tribological, electrochemical and biocompatibility properties of Ti6Al4V alloy produced by selective laser melting method and then processed using gas nitriding, CN or Ti-C: H coating treatments. *Surf. Coat. Technol. 350*, 172.

42. Yan, X., Shi, C., Liu, T., Ye, Y., Chang, C., Ma, W., Deng, C., Yin, S., Liao, H., & Liu, M. (2020). Effect of heat treatment on the corrosion resistance behavior of selective laser melted Ti6Al4V ELI. *Surf. Coat. Technol. 396*, 125955.

43. Jiang, J. U., Li, J. J., Jiang, M., Li, M. Y., Yang, L. X., Wang, K. M., Chao, Y. A. N. G., Kang, M. D., & Jun, W. A. N. G. (2021). Microstructure and electrochemical corrosion behavior of selective laser melted Ti− 6Al− 4V alloy in simulated artificial saliva. *T. Nonferr. Metal. Soc. 31*(1), 167.

44. Bartus, S. D. Evaluation of Titanium-5Al-5Mo-5V-3Cr (Ti-5553) alloy against fragment and armor-piercing projectiles. Army Research Laboratory Report, #ARL-TR-4996.

45. Donachie, M. J., Jr. (2000). Titanium: A Technical Guide; 2nd ed.; ASM International, Materials Park, OH.

46. Cotton, J.D., Briggs, R.D., Boyer, R.R.; Tamirisakandala, S.; Russo, P.; Shchetnikov, N. & Fanning, J.C. (2015). State of the art in beta titanium alloys for airframe applications. *JOM. 67*, 1281.

47. Schwab, H., Palm, F., Kühn, U., & Eckert, J. (2016). Microstructure, and mechanical properties of the near-beta titanium alloy Ti-5553 processed by selective laser melting. *Mater. Des.105*, 75.

48. Zopp, C., Blümer, S., Schubert, F., & Kroll, L. (2017). Processing of a metastable titanium alloy (Ti-5553) by selective laser melting. *Ain Shams Eng. J. 8*(3), 475.

49. Schwab, H., Bönisch, M., Giebeler, L., Gustmann, T., Eckert, J., & Kühn, U. (2017). Processing of Ti-5553 with improved mechanical properties via an in-situ heat treatment combining selective laser melting and substrate plate heating. *Mater. Des. 130*, 83.

50. Grove, T., Denkena, B., Maiß, O., Krödel, A., Schwab, H., & Kühn, U. (2018). Cutting mechanism and surface integrity in milling of Ti-5553 processed by selective laser melting. *J. Mech. Sci. and Technol. 32*, 4883.

51. Carlton, H. D., Klein, K. D., & Elmer, J. W. (2019). Evolution of microstructure and mechanical properties of selective laser melted Ti-5Al-5V-5Mo-3Cr after heat treatments. *Sci. Technol. Weld. Join. 24*(5), 465.

52. Ahmed, M., Obeidi, M. A., Yin, S., & Lupoi, R. (2022). Influence of processing parameters on density, surface morphologies and hardness of as-built Ti-5Al-5Mo-5V-3Cr alloy manufactured by selective laser melting. *J. Alloys Compd*. *910*, 164760.

53. Yan, D., & Bolzowski, R. Investigation to Density and Metallurgical Characteristics of Selective Laser Melted Ti-5Al-5 V-5Mo-3Cr Versus Ti-6Al-4 V. In *TMS 2023 152nd Annual Meeting & Exhibition Supplemental Proceedings* (pp. 539-547). Cham: Springer Nature Switzerland.

54. Sangali, M.; Opini, V. C.; Fatichi, A. Z.; Mello, M. G.; Fanton, L.; Caram, R.; and Cremasco, A. (2023). Nb modified Ti-5553 alloy: effects of heating rate on mechanical properties, corrosion behavior, and crystallographic texture. *J. Mater. Res. Technol. 23*, 5310.

55. Muñoz, J. M. J.; Gaona-Tiburcio, C.; Cabral Miramontes, J.A.; López, F. E.; Zambrano Robledo, P. C.; Saucedo, R.; Calderon, F.A. (2021). Electrochemical behavior of titanium alloys using potentiodynamic polarization. *ECS Trans.* 2021, *101*, 173.

56. Luis de Assis, S.; Wolynec, S.; and Costa, I. (2006). Corrosion characterization of titanium alloy by electrochemical techniques. *Electrochem. Acta.* 2006, *51*, 1815.

57. Aslam, R. (2023). Potentiodynamic Polarization Methods for Corrosion Measurement, In Electrochemical and Analytical Techniques for Sustainable Corrosion Monitoring; Aslam, J., Verma, C. and Hussain, C.M. eds. Elsevier, pp.25-37.

58. Meier, B., Petrusa, J. and Waldhauser, W. (2024). L-PBF of the metastable β titanium alloy Ti-5553: microstructure and mechanical properties. *Berg. Huettenmaenn. Monatsh. 169*, 17.

59. Zhou, X.; Liu, X.; Zhang, D.; Shen, Z.; Liu W. (2015). Balling phenomena in selective laser melted tungsten. *J. Mater. Process. Technol. 222*, 33.

60. Franklyn, C. B. and Merkle, R. K. W. (2001). Surface contamination by smearing during polishing – A PIXE study. *Nuclear Instruments and Methods in Physics Research Section B: Beam Interactions with Materials and Atoms* 2001, *181*, 140.

61. Kalienko, M.; Volkov, A.; Leder, M.; Zhelnina, A.; and Panfilov, P. (2019). Study of lamination in beta-phase of Ti-5553 titanium alloy. *IOP Conf. Series: Materials Science and Engineering* 2019, *461*, 012033.

62. Chanfreau, N.; Poquillon, D.; Stark, A.; Maawad, E.; Mareau, C.; and Dehmas, M. (2022). Phase transformation of the Ti-5553 titanium alloy subjected to rapid heating. *J. Mater. Sci. 57*, 5620.

63. Schwab, H., Palm, F., Kühn, U., and Eckert, J. (2016). Microstructure and mechanical properties of the near-beta titanium alloy Ti-5553 processed by selective laser melting. *Mater. Des. 105*, 75.

64. Salvador, C.A.F.; Opini, V. C.; Mello, M. G. and Caram, R. (2019). Effects of double-aging heat-treatments on the microstructure and mechanical behavior of an Nb-modified Ti-5553 alloy. *Mater. Sci. Eng. A. 743*, 716.

65. Bakhshivash, S., Asgari, H., Russo, P., Dibia, C. F., Ansari, M., Gerlich, A. P., and Toyserkani, E. (2019). Printability and microstructural evolution of Ti-5553 alloy fabricated by modulated laser powder bed fusion. *Int. J. Adv. Manuf. Technol.103*, 4399.

66. Campo, K. N.; Andrade, D. R.; Opini,V. C.; Mello, M. G.; Lopes, E. S. N. and Caram, R. (2016). On the hardenability of Nb-modified metastable beta Ti-5553 alloy. *J. Alloys Compd*. *667*, 211.

67. Mirshekari, G. R. and Shirvanian, A. P. (2018). Electrochemical behavior of titanium oxide nanoparticles for oxygen reduction reaction environment in PEM fuel cells. *Mater. Today Energy*. *9*, 235.

68. Gudić S.; Vrsalović L.; Kvrgić D.; and Nagode, A. (2021). Electrochemical behaviour of Ti and Ti-6Al-4V alloy in phosphate buffered saline solution. *Materials. 14*, 7495.

69. Hirschorn, B.; Orazem, M. E.; Tribollet, B.; Vivier, V.; Frateur, I. and Musiani, M. (2010). Determination of effective capacitance and film thickness from constant-phase-element parameters. *Electrochim. Acta.* 55, 6218.

70. Thomas, N.T.; and Nobe K. (1969). The electrochemical behavior of titanium. *J. Electrochem. Soc: Electrochem. Technol. 116*(12), 1748.

71. Nudelis, N.; and Mayr, P. (2021). A novel classification method for pores in laser powder bed fusion. *Metals*. *11*(12), 1912.

72. Fan, J., Li, J., Zhang, Y., Kou, H., Ghanbaja, J., Gan, W., Germain, L., and Esling, C. (2017). The origin of striation in the metastable β phase of titanium alloys observed by transmission electron microscopy. *J. Appl. Crystallogr. 50*(3), 795.

CHAPTER 6. CONCLUSIONS AND FUTURE WORK

6.1 CONCLUSIONS

Carbon fiber reinforced polymer (CFRP) composites and aluminum alloys serve as integral structural elements in aircraft, automobiles, marine vessels, and military transport vehicles. When these two materials are assembled, a galvanic couple can result when a conducting solution layer condenses on the surfaces. The more noble carbon fibers in the galvanic series will act as a cathode and effectively support the reduction of dissolved oxygen or water. The cathodic reaction rate escalates the oxidation rate of the less noble aluminum alloy– so-called galvanic corrosion. Corrosion of the aluminum alloy can be inhibited by decreasing the rate of the metal oxidation, decreasing the rate of the cathodic reaction, or decreasing the rate of both. This dissertation work primarily investigates the effectiveness of the surface treatment of CFRP composite edges with substituted phenyl diazonium adlayers towards the inhibition of cathodic oxygen reaction kinetics by blocking the active sites on the carbon fibers for O_2 chemisorption; the first step of oxygen reduction. The purpose of the surface treatment is to reduce the extent of galvanic corrosion on a trivalent chromium process (TCP) conversion-coated aluminum alloy when the two materials are mechanically joined.

The two surface treatment approaches discussed herein are (i) electrochemically-assisted and (ii) spontaneous grafting of organic adlayers through reduction of para substituted aryldiazonium salts. Raman spectra of the chemically modified composites confirmed that the electrochemically-assisted and spontaneous reduction of aryldiazonium salts generate stable covalently attached adlayers on CFRP composite edges. The adlayers are believed to function as physical barriers and reduce the rate of dissolved oxygen reduction on the more noble carbon by blocking reactive surface sites for O_2 chemisorption thereby mitigating the rate of galvanic

corrosion on the more active metal alloy. Electrochemically-formed adlayers suppressed the current for ORR by 50%, as compared to the unmodified CFRP composite specimen. Spontaneously-formed adlayers (24h immersion) reduced the current for ORR by 99%. The organic adlayers formed spontaneously during a 24h immersion are more compact, have fewer defects, and higher apparent coverages than adlayers formed by electrochemically-assisted derivatization. Results reveal that the adlayers are stable during accelerated degradation tests and the extent of galvanic corrosion on trivalent chromium process (TCP) conversion-coated aluminum alloys is significantly reduced when joined with a surface treated composite. Spontaneously formed adlayers provide much improved resistance to galvanic, crevice and general aluminum alloy corrosion, as compared to the electrochemically-formed adlayers. The weight loss metrics all indicate substantial reductions in mass loss, mass loss per cm^2 , and corrosion intensity (g/m^2-yr) on both TCP-coated alloys when joined with a CFRP modified with a more compact spontaneously formed adlayer. The extent of carbon corrosion and microstructural degradation of carbon fibers is also attenuated by the organic adlayers. Carbon corrosion damage seen on the unmodified CFRP specimens after a degradation test joined with a TCP-coated aluminum alloy is somewhat reduced by the electrochemically-formed adlayers, but is significantly reduced by the spontaneously formed adlayers. The research highlights that the spontaneously formed adlayers by 24h immersion offer superior inhibition of galvanic corrosion on aluminum alloy and greater resistance to carbon corrosion than do adlayers formed through an electrochemically assisted process. The diazonium surface treatment holds a promising potential for reduced corrosion in CFRP composite/metal hybrids.

Fabrication of advanced titanium alloys via additive manufacturing (AM) techniques including selective laser melting (SLM), has sparked a newfound interest over recent years.

Although the enhanced flexibility in producing parts with greater complexity and reduced waste offered by AM is highly sought after, structure-function relationships are yet to be established for new AM titanium alloy materials through in-depth testing. Chapter 5 of this dissertation work focuses on investigating the material properties and understanding the influence of surface pretreatments on the electrochemical corrosion behavior of titanium alloys prepared by SLM. The surface pretreatment consists of abrading and polishing to reduce the surface roughness and smooth the surface texture. The specimens were comprised of balling features, micropore and fusion pore defects. The results reveal that the abrading and polishing improve the corrosion and degradation resistance of the SLM titanium alloys specimens. The open circuit potential was 225 mV more noble, the anodic current in potentiodynamic polarization curves were two orders of magnitude lower, and the cathodic current was one order of magnitude lower for abraded and polished titanium alloy specimens compared to as-processed specimens. The polarization resistance increased by 425× after smoothing the surface texture. The superior electrochemical properties are attributed to a less defective and more continuous passivating oxide layer that formed on the surface-pretreated specimens.

6.2 FUTURE WORK

The surface treatment of exposed carbon fibers in CFRP composites with diazonium adlayers resulted in substantially suppressed oxygen reduction currents and notably reduced galvanic corrosion damage to the aluminum alloy coupled. The adlayers achieved by spontaneous grafting during 24-h immersion in particular exhibited near complete inhibition of the oxygen reduction reaction. Further work is needed to optimize the spontaneous grafting parameters such as diazonium concentration, temperature, and immersion time for improved performance of the adlayers. Additionally, the stability and performance of the adlayers should be evaluated during

long term exposure in the field (i.e. beach exposure). Another avenue worth exploring for practical applications is the spontaneous deposition of adlayers through spray application of diazonium salt solutions on CFRP composite edges. A deeper understanding of the surface treatment parameters and performance of the diazonium adlayers will advance the development of more effective, environmentally friendly corrosion protection coatings.